NUMERICAL SIMULATIONS OF HYDRODYNAMIC PARTICLE INTERACTIONS AT LOW PARTICLE REYNOLDS NUMBER

By

Salvador Vargas-Díaz

Thesis Submitted for the degree of

Doctor of Philosophy

The University of Edinburgh

2008

ABSTRACT

Two-phase flows are of considerable importance in industry and in nature. Examples include: pneumatic transport in coal fired power stations; rockslides and avalanches; sandstorms; particle transport in the atmosphere, rivers and channels; flow in grain silos and of powdered pharmaceutical and food ingredients. Despite the ubiquity of such flows, many of the phenomena associated with them are poorly understood. When solid particles are suspended in the fluid and are not in a jammed state, a fruitful approach to modelling the system can be to describe it as a system of particles interacting both with each other and with an external field. In the specific case when the particles are far enough apart, the dominant interactions between particles are those mediated by the surrounding fluid rather than direct particle-particle interactions, possible only when the particles are touching.

One of the most important phenomena observed in this regime is particle roping – rather than being evenly dispersed throughout the fluid, particles congregate in one or more 'ropes' aligned with the flow direction. This can be a serious problem in coal fired power stations, which require coal dust to be evenly distributed to operate at maximum efficiency. This thesis presents a basic numerical study of particle-fluid-particle interactions under conditions characteristic of the roping phenomenon found after bends in the pneumatic transport systems of coal fired power plants. The main objectives of this work are to:

1. Obtain a pair potential hydrodynamic force field from computational fluid dynamics simulations of two fixed spherical particles at low particle Reynolds number
2. Estimate the magnitude of errors introduced by the pair potential approximation by comparing the two-particle system results with CFD simulations of systems of three fixed spherical particles
3. Use many-particle Monte Carlo simulations to investigate the conditions under which clustering or roping occurs.

ACKNOWLEDGEMENTS

First, I would like to gratefully acknowledge to Professor William J. Easson for all his academic and non-academic support during this project. His appropriate observations and comments during our meetings always gave me new ideas and push me forward to the right direction to successfully develop this thesis. I also want to thank Dr. Tom Bruce, my second supervisor for his invaluable comments at some stages of this work, Dr. Philip J. Camp from The School of Chemistry for his help and advice with the Monte Carlo simulations. He was very willing to share his Monte Carlo code with me, for which I am most grateful. I also want to thank Dr. Jorge Rojas from The Energy Research Centre in Mexico (CIE - Centro de Investigación en Energía, México) for his earliest motivation to pursue my PhD research in fluid mechanics.

Far too many people to mention individually, whose have helped me in so many ways during my PhD at The University of Edinburgh, so they all have my sincere gratitude. I especially want to thank Dr. William Lee for his outstanding proofreading of my first draft and some suggestions and comments.

Without any doubt the person I have to thank the most is my wife, Elizabeth Cabana Navarro for all her support and companionship throughout this work, certainly she was the key person for the completion of this degree. I am also grateful to my parents-in-law Alfredo Cabana and Elizabeth Navarro my sisters-in-law Sandra Catalina and Martha Sofia, my nice Margarita Pedraza Vargas and all my friends, particularly to Pedro Rivera, Nubia Herrera and Gloria Rendón for all their support during this work. Finally, I want to dedicate this work to my whole family, especially to my son Alfredo Andres, my daughter Andrea Sofia and my parents, Epifania and J. Cayetano Vargas.

This work was funded by the Mexican Council for Science and Technology (CONACyT – Consejo Nacional de Ciencia y Tecnología, México).

TABLE OF CONTENTS

TABLE OF FIGURES

TABLE OF TABLES

NOMENCLATURE

ACRONYMS

BBO	Basset-Boussinesq-Oseen equation
CCTs	Clean Coal Technologies
CCD	Charge-Couple Device
CFB	Circulating Fluidised Bed
CFD	Computational Fluid Dynamics
DEM	Discrete-Element-Method
DKT	Two particles Drafting, Kissing and Tumbling phenomenon
DNS	Direct Numerical Simulation
DSMC	Direct Simulation Monte Carlo
ECT	Electrical Capacitance Tomography
E-E	Eulerian-Eulerian model
FCC	Face Centre Cubic unit
FDM	Finite Difference Method
FEM	Finite Element Method
GR	Growth rate in a grid size function (GAMBIT)
IEA/AIE	International Energy Agency/Agence Internationale De L'énergie
KE	Kinetic Energy
KTGF	Kinetic Theory of Granular Flow
LBM	Lattice-Boltzmann Method
LDA	Laser Doppler Anemometry
L-E	Lagrangian-Eulerian model
LGA	Lattice-Gas-Automata method
MC	Monte Carlo method
MD	Molecular Dynamics simulation
MIC	Minimum Image Convention
NVT	Canonical Monte Carlos Ensemble (Constant Number of particles-Volume-Temperature)

PBC	Periodic Boundary Condition
PDA	Phase Doppler Anemometry
PF	Pulverized Fuel
PIV	Particle Image Velocimetry
RANS	Reynolds time-Averaged Navier-Stokes equations
RMS, rms	Root Mean Square
RNGs	Random Number Generators
TFM	Two-Fluid Model
UK	United Kingdom
WSS	Wall Shear Stress [Pa]

ROMAN SYMBOLS

A	Area	$[m^2]$
A_{xx}	Autocorrelation function	[-]
C	Mass concentration	[-]
C_d, C_D	Drag coefficient	[-]
C_{df}	Drag friction	[-]
C_{ds}	Drag coefficient for a single particle	[-]
C_{Dm}	Multiparticle drag coefficient	[-]
C_{dp}	Drag form or pressure coefficient	[-]
C_i	Interaction coefficient	[-]
$C_n(r)$	Legendre polynomial coefficients, eq. (5.4)	[-]
C_p	Pressure coefficient	[N]
C_s	Wall shear stress coefficient	[N]
$\frac{D}{Dt}$	Material derivative	[-]
D_o	Dimensionless particle separation (l/d_p, r/d_p)	[-]
d_p	Particle diameter	[m, μm]
dr_{max}	Maximum particle displacement in MC simulations	[-]
F	Force	[N]

F_{basset}	Basset force	[N]
F_d, F_D	Drag force	[N]
F_f	Friction drag force	[N]
F_g	Gravity force	[N]
F_i	Interaction force between particles	[N]
F_L	Force perpendicular to the flow, lift force	[N]
F_p	Form drag force, Pressure force	[N]
F_{vm}	Virtual force	[N]
f_{coll}	Frequency of collisions	$[s^{-1}]$
g	Gravity constant	$[ms^{-2}]$
g(r)	Radial distribution function	[-]
g_1	Constant, eq. (5.5)	[-]
g_2	Constant, eq. (5.5)	[-]
h_1	Constant, eq. (5.5)	[-]
h_2	Constant, eq. (5.5)	[-]
k	Boltzmann constant (1.38066×10^{-23})	[J/°K]
l, r	Interparticle separation	[m]
$L_{f,c}$	Characteristic length for fluid	[m]
M_p	Total mass of the dispersed phase (particles)	[kg]
$\dot{M}_f$	Total fluid mass flow rate	$[kgm^{-2}s^{-1}]$
$\dot{M}_p$	Total particle mass flow rate	$[kgm^{-2}s^{-1}]$
M_f	Total mass of the continuous phase (fluid)	[kg]
m_p	Mass of a single particle	[kg]
$\dot{m}_f$	Fluid mass flux at a local region	$[kgm^{-2}s^{-1}]$
$\dot{m}_p$	Particle mass flux at a local region	$[kgm^{-2}s^{-1}]$
N_b	Number of particles in a bin in MC simulations	[-]
N_{block}	Monte Carlo blocks in MC simulations	[-]
N_{id}	Average number of atoms in an ideal gas	[-]
N_p	Number of particles	[-]
N_{step}	Monte Carlo steps in MC simulations	[-]
n_p	Density number	$[particles/m^3]$

P_{acc}	Probability of acceptance in MC simulations	[-]
$P_n(x)$	Legendre polynomial	[-]
p	Pressure	[Pa]
p_∞	Pressure reference ($p_\infty = 0$)	[N]
Re	Reynolds number	[-]
Re_p	Particle Reynolds number	[-]
St_p	Stokes number	[-]
T	Temperature	[K]
T_g	Granular temperature	[kg m^2 s^{-2}]
T^*	Reduced temperature (T_g/U_{min})	[-]
U	Velocity vector, Energy	[m s^{-1}], [J]
U_∞	Free stream velocity	[m s^{-1}]
$U(r,\theta)$	Pairwise potential energy function	[J]
U_{min}	Minimum energy (-2.07×10^{-11})	[J]
$U_n(r)$	Legendre polynomial coefficients	[-]
u'	Velocity fluctuations	[ms^{-1}]
u_f	Fluid velocity	[ms^{-1}]
$u_{f,c}$	Characteristic velocity of the fluid	[ms^{-1}]
u_{mean}	Local mean velocity	[ms^{-1}]
u_p	Particle velocity	[ms^{-1}]
$u_{p,r}$	Particle relative velocity	[ms^{-1}]
u_{rms}	Root mean square velocity ($\sqrt{\overline{u'^2}}$)	[ms^{-1}]
V	Velocity vector in the y axis direction	[m s^{-1}]
V	Volume	[m^3]
V_f	Volume of the fluid (continuous phase)	[-]
V_p	Volume of the total number of particles	[-]
v_p	Volume of a spherical particle	[m^3]
W	Velocity vector in the z axis direction	[m s^{-1}]
x	Cross-stream direction	[-]
y	Streamwise direction	[-]
z	Spanwise direction	[-]

GREEK SYMBOLS

α	Angle ($\alpha = 0$ at the downstream stagnation point)	[deg]
α_f	Fluid (continuous phase) volume fraction	[-]
α_p	Particle volume fraction	[-]
Δ	Difference	[-]
∇	Nabla or "del" operator	[-]
λ	Local mass loading	[-]
Λ	Total mass loading	[-]
μ_a	Dynamic air viscosity (1.7894×10^{-5})	[kg $m^{-1}s^{-1}$]
μ_f	Fluid dynamic viscosity	[kg $m^{-1}s^{-1}$]
π	Constant (3.14159)	[-]
ρ_f	Fluid density	[kgm^{-3}]
$\overline{\rho}_f$	Bulk density of the continuous phase (fluid)	[kgm^{-3}]
$\overline{\rho}_p$	Particle bulk density or particle concentration (solid)	[kgm^{-3}]
ρ_a	Air density (1.225)	[kg m^{-3}]
ρ_m	Mixture density	[kgm^{-3}]
ρ_p	Particle density	[kgm^{-3}]
σ_x^2	Covariance	[-]
θ	Angle between particles	[deg]
τ_{coll}	Time of collisions	[s]
τ_f	Characteristic time of the fluid	[s]
τ_p	Particle relaxation time, particle response time	[s]
τ_w	Shear wall stress or skin friction	[N]

OTHER ABBREVIATIONS

NO_x	Oxides of Nitrogen
SO_x	Oxides of Sulphur
CO_2	Carbon dioxide

CHAPTER 1

1 INTRODUCTION

This chapter describes the importance of dispersed multiphase flows in both industry and nature. Particular emphasis is given to coal pneumatic transport in the power generation industry, with emphasis on the so-called roping phenomenon, commonly found in coal pneumatic transport. Roping phenomenon has been described as one of the most relevant problems and limiting factor in the reduction of NO_x in the power generation industry. In order to obtain a better understanding of particle aerodynamic (or hydrodynamic) interactions, local study of particle-fluid-particle interactions is required. The main problem in studying multiple particle interactions is the long computing time required to simulate a large number of particles. To overcome this problem a basic two particle interaction correlation is proposed to simulate multiple particles using a statistical mechanics approach, such as the Monte Carlo Method. Finally, the objectives and approach to studying the multiple particle interactions through using the results obtained from interacting particle pairs is described.

1.1 Motivation

Most multiphase flows are considered as two-phase flows, which are frequently found in nature and industrial processes. Pollutant transport in the atmosphere, dust storms, rain formation, volcanic ash eruptions, sediment transport in rivers and channels and blood transport in the human body are some examples of multiphase

flows in nature. On the other hand, industrial applications include particle exhaust gases, fluidised beds, drug aerosol delivery, cyclone separators, bubble columns, and pneumatic transport of granular materials in food and chemical processes, and in coal-fired power generation.

Particle pneumatic transport is an important subject in multiphase flows especially in coal-fire electricity generation where pulverized coal (pulverised fuel – PF) is transported pneumatically from mills to the burners via complicated pipeline systems connected by elbows and at the end it is split into two or more branches. The presence of elbows leads to regions of high particle concentration in the outer wall of the pipe due to inertial effects as shown in Figure 1.1. These high particle concentration regions are commonly know in power generation industry as particle roping (rope-like structures).

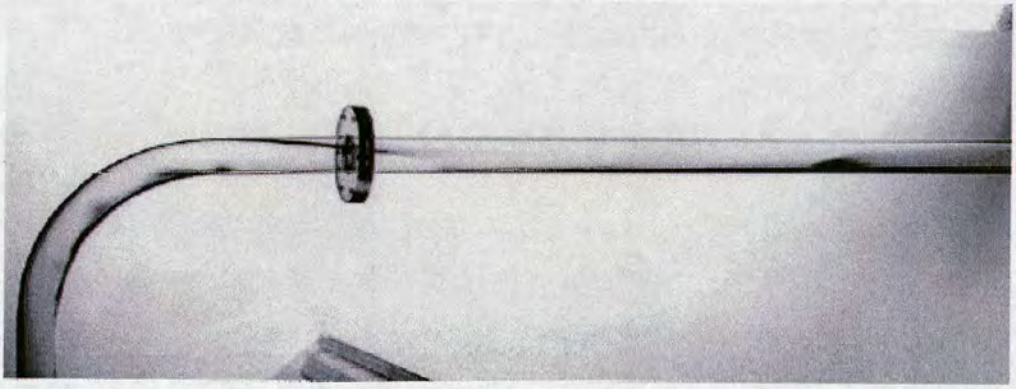

Fig. 1.1 Typical rope formations after a 90° bend in a pulverized fuel pipe model, McCluskey *et al.* (1989).

The rope-like structure holds together for long distances and disintegrates further downstream into large and discontinuous clusters. Particle roping structures can cause a poor distribution of coal over the cross section of the pipe entering a splitter. A badly balanced distribution of coal in pipes increases the levels of unburned carbon and consequently higher rates of pollution. For this reason the study of rope-like structures in coal pneumatic transport in the broader field of multiphase flows has received great attention. But the stability and patterns of particle ropes and

clusters in coal pneumatic transport and in general the local particle-fluid-particle interaction is a challenging research area.

Even though there are many studies of the particle roping phenomenon, to the best of our knowledge no attention has been paid to the local particle-air-particle interactions: the attraction-repulsion mechanism between particles due to their high concentration at low particle Reynolds numbers, which is believed could play an important role in the particle roping phenomenon patterns. Therefore a fundamental study of aerodynamic (or hydrodynamic) particle-fluid-particle interactions in two-phase flows to better understand the physics of roping stability in complex flows, such as coal-fire pneumatic transport, is of great importance.

1.2 Coal-fire electricity generation

Electricity is a very important factor in a country's economic development and in its people's quality of life among other benefits. Access to electricity can help to increase production rates in industry, to reduce the infant mortality in hospitals, to facilitate education and to illuminate millions of homes. Worldwide electricity generation is achieved by different technologies and fuels: gas, coal, nuclear, oil, hydro and several other alternatives, such as solar energy, biomass, wind, geothermal and tidal-waves.

At the present, coal provides over 24% of global primary energy needs and generates 39% of the total world's electricity, compared to 19% for gas, 17% nuclear, 16% hydro, 7% oil and 2% "renewables", IEA/AIE (2004). Possibly, coal-fire electricity generation will fall slightly in developed countries, but certainly new coal-fire power plants will be built in developing countries, mainly in developing Asia. Hence coal will remain as the principal fuel in electricity generation for many decades because of its large reserves and low cost production. At the present time, some countries, such as Poland, South Africa, China, Australia, Israel, India, Czech Republic,

Greece, Germany and United States of America generate over 50% of their total electricity in coal-fire power plants.

Electricity demand has increased strongly in the last few decades and will continue to increase because of the growth of population and industry, especially in developing countries where energy is needed to fuel economic growth and supply people's requirements, such as heating, lighting, air conditioning and electrical appliances. All kind of fuels will be needed to satisfy these demands, but coal will play the major role in the near future electricity generation. All sources of electricity have positive as well as negative impacts, but taking into account their availability, reserves and low cost of production coal will be the predominant source of electricity for the next decades, IEA/AIE (2004).

As mentioned before all forms of electricity production have their benefits and drawbacks. There is no free-risk way to produce energy, whether in terms of human health, safety and environmental impact. In general, the combustion of coal in power plants produces some particulates such as flying ash: particulates can affect human respiratory systems; toxic elements such as mercury and arsenic are very harmful to the environment and to human health; oxides of nitrogen, NO_x, contribute to smog, acid rain and greenhouse gases; oxides of sulphur, SO_x, generally as sulphur dioxide, SO_2, which are produced from the sulphur contained almost in all types of coals; oxides of sulphur produce acid rain and acidic aerosols; oxides of carbon such as carbon dioxide, CO_2, which is produced when coal is burnt: CO_2 is a greenhouse gas with significant impact on the climate change and global warming. As a result coal has to face very important technical and engineering challenges to reduce the amount of pollutants. In order to meet these challenges, the coal industry along with the coal-fire power plants must significantly reduce their greenhouse and particulates emissions. This goal can be achieved by improving the coal-fire power plant efficiency: improving the coal transport and also reducing the amount of coal; and by eliminating or capturing pollutant emissions.

Some technologies have been already developed to reduce these human and environmental problems. These technologies are well known as clean coal technologies (CCTs). CCTs are those which can be used in coal combustion to reduce different environmental problems in the most viable economic way. Some of these technologies have been already employed in developed countries. At the present time CCTs are becoming more important, as they can provide a possible alternative to meet the different environmental restrictions imposed by local and worldwide environmental organizations.

1.3 Roping phenomenon in coal pneumatic transport

In a typical coal-fire power plant, coal is transported from the mines to the hopper in the power plant; coal is then pulverized in a mill. In many coal-fire power plants coal is transported pneumatically from 5 - 8 mills to 30 - 50 burners located in different furnaces, Malmgren *et al.* (2003). The pipe system that conveys coal pneumatically from the mill to the burners is at different levels and has different geometries and lengths. It consists of horizontal and vertical sections connected by bends and elbows. The main pneumatic pipeline that carries the pulverised coal from the mill to the furnace is commonly divided into two or more outlet small pipes to feed four or eight burners in the furnace. Figure 1.2 shows a general outline of the pipe coal conveying from The Kingsnorth Power Station, PowerGen Ltd., UK.

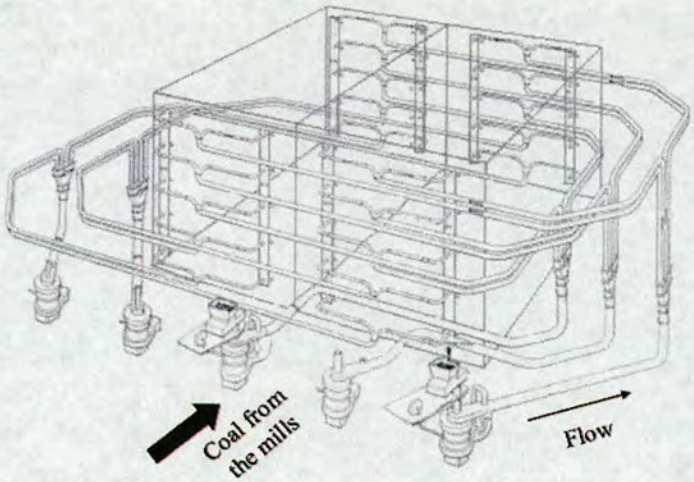

Fig. 1.2 Coal-fire power plant schematic pipe layout, Malmgren *et al.* (2003).

Thus, in order to guarantee an efficient combustion in the furnace each individual burner must be provided with the same amount of fuel (coal/air mixture), so a homogeneous cross-section distribution of coal/air mixture must be obtained just in front of the split section. If an inhomogeneous distribution is present before the splitter, some burners will receive more coal than the others. This imbalance of coal/air mixture can notably affect the efficiency of the combustion process and increase the production of NO_x, Losenno (2004). Even circumstances where only a small imbalance exists (5%) split of fuel occurs at the first bifurcation in one pipeline and all the other bifurcations result in 50:50 per cent splits, can add up to considerable waste of fuel, Barnes *et al.* (1995). The common air velocities found in coal pneumatic conveying at coal-fire power plants are in the range of 15-40 m/s and typical particle/ air mass ratios between 0.5:1 and 5:1 kg of solids/kg of air, which is approximately equivalent to solids concentration of 0.05% and 0.5% with separations between 10 and 5 particle diameters, in pipes ranging typically from 300 mm to1000 mm in diameter.

As it is shown in Figure 1.2, the pipe system that carries the coal and primary air from the bunkers to the burners consists of a series of vertical and horizontal pipe sections connected by elbows. The presence of elbows can cause an inhomogeneous distribution of the PF in the pipes due to inertial effects, creating the so-called roping

and cluster flow regimes, Figure 1.3, with regions of relative high particle concentration from 12 to 30 kg/m^3 at the bend exit, which correspond to solids concentration of 0.8% and 2%. The rope-like structure, high concentration corresponds to approximately to 4.0 and 3.0 particle diameters in particle separation distance, Yilmaz & Levi (1998), Bilirgen & Levy (2001), and Akilli *et al.* (2005).

In a recent report about multiphase flows in the UK with application to coal-fired power generation, power generators reported that roping is one of the five most relevant problems found in coal-fired power generation industry, Azzoparrdi *et al.* (2001). Particle coal roping has been claimed as the main limiting factor in the reduction of NO_x due to unequal distribution at the points where the PF is split into separate pathways, causing uneven feed of pulverised coal to the burners.

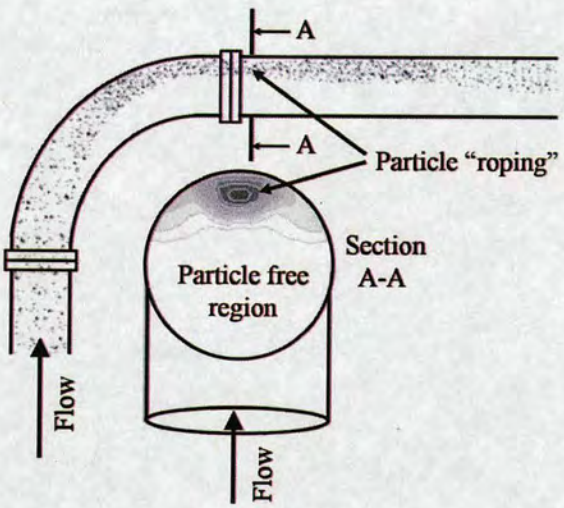

Fig. 1.3 Schematic picture of roping phenomenon after a 90° elbow in a coal transport.

The study of rope-like formations after bends in coal-fire power generation goes back to papers published in the late 1950s and early 1960s, Patterson (1959), Weintraub (1959), Whitney (1959) and Zipse (1966). However, most of the work on roping has been done in the last two decades both numerically and experimentally by McCluskey *et al.* (1989), McCluskey (1992), Levy & Mason (1998), Bilirgen *et al.*

(1998), Bilirgen & Levy (2001), Yilmaz & Levy (2001), Schaller & Levy (2000), Akilli *et al.* (2001), Fokeer *et al.* (2004), Giddings *et al.* (2004), Lee *et al.* (2004), Akilli *et al.* (2005) and Yan & Kuan (2006). Most of these works have been limited to study some specific aspects of the roping phenomenon at particle Reynolds numbers between 9 and 50. From the previous works, a broad classification of the roping studies can be made: (1) particle concentration measurements, (2) particle and gas velocity measurements, (3) particle-wall collision simulations, (4) simulations of particle-particle collisions, (5) bend to pipe radius ratio and (6) rope dispersion methods.

1.4 Hydrodynamic particle interactions

In most fluid mechanics studies fluid-particle interactions is referred to as hydrodynamics interactions because water is the most common example, in this work, the reader could find the word "*hydrodynamics*" as synonym of "*aerodynamics*". Most of dispersed two-phase flows are turbulent due to the presence of particles, which affect the mean motion of the flow. In order to acquire a better understanding of these processes and to improve the efficiency of industrial applications, it is important to study the particle interactions in these types of flow.

Most of the particle-fluid-particle interaction studies have been carried out at intermediate and high particle Reynolds numbers ($50 < Re_p < 1000$), focusing on the turbulence modulation. Turbulence modulation is an important research area in two-phase flows but this topic is beyond the scope of this work. For studies on this subject the reader is referred to the works of Sato *et al.* (2000), Crowe (2000), Tashiro *et al.* (2001), Kussin & Sommerfeld (2002), Tanaka *et al.* (2002), Aliseda *et al.* (2002), Kajishima & Takiguchi (2002), Pan *et al.* (2002), Ljus *et al.* (2002), Lain & Sommerfeld (2003) and Rani *et al.* (2004).

On the other hand, local particle dynamic interaction studies are performed at very low particle Reynolds numbers ($0 < Re_p < 1$) and low-intermediate particle Reynolds numbers ($1 < Re_p < 300$). The works related to this topic will be discussed in subsequent chapters.

1.5 Objectives and Approach

A particular consideration has been made to the complex roping phenomenon found after bends in coal transport in power plants, but there are still some open questions on this topic, limiting the knowledge of this complex phenomenon. The goal of the present research is to facilitate a better understanding of the local particle-air-particle interactions in the roping phenomenon and their role in the stability of the rope-like structure via two numerical approaches: a two fixed spherical particles system at low particle Reynolds number, using a Computational Fluid Dynamics (CFD) commercial code and a multi-particle system by Monte Carlo (MC) simulations. The CFD simulations were carried out at particle Reynolds number of 15 based on the extensive experimental work of McCluskey (1992) and Losenno (2004), a fundamental work in a model of pulverized fuel pipes of air-particle flow fields where the experimental parameters are characteristic of coal-fired electricity generating stations and the experimental study of air-particle interactions of free falling particles with mean diameters varying from 60 to 300 μm, respectively.

The CFD simulations are carried out using a widely accepted finite volume commercial program, FLUENT. CFD simulations focused on the pressure and viscous forces to define the interaction forces between two fixed particles. The results from two interactive particles are used to find an energy pair potential in order to simulate several particles using Monte Carlo (MC) method. A homemade MC program developed by Dr. P. J. Camp from the School of Chemistry at the Edinburgh University is used to simulate multiple particles. Particle Image Velocimetry (PIV) and Laser Doppler Anemometry (LDA) results for free falling spherical particles in

air from Losenno (2004) are used to obtain RMS particle velocity fluctuations to used in MC simulations. Some MC simulations are compared with PIV particle images from Losenno's work. CFD simulations of three fixed particles are used to study the influence of a third particle in the pair particle interactions.

1.6 Thesis outline

The general lay-out of the thesis is as follows, an overview of the theoretical background of multiphase flows, particle dynamics, and previous experimental and numerical work in the field of dynamic particle interactions available in the literature is given in chapter 2. The focus of this review is on two-phase classification, properties and previous many-particle hydrodynamic interaction studies. Two and three particles hydrodynamic interactions are given in subsequent chapters. In chapter 3 a detailed CFD study of two fixed spherical particles immersed in a fluid flow is given in terms of velocity profiles, pressure coefficients, wall shear stress coefficients, drag forces and interaction coefficients. The influence of a third fixed spherical particle on a pair of fixed spherical particles, based on the drag and lift forces comparison is presented in chapter 4. From two fixed spherical particle dynamic interactions the pair potential energy is obtained to be used in the multiple particle Monte Carlo simulations and the results are reported in chapter 5. In the same chapter, PIV images from previous experimental work are also reported and compared with multiple particle MC simulations. Finally, in chapter 6, a discussion and main conclusion of this work can be found, as well as some recommendations for future studies in this field.

CHAPTER 2

2 MULTIPHASE FLOW THEORY AND PARTICLE DYNAMICS

The objective of this chapter is to provide basic background information of multiphase flows and particle dynamics, such as definitions, classification, properties, equations and previous experimental and numerical studies of multiple particles immersed in a fluid flow. Some representative illustrations of two-phase flows in industry are also shown in this chapter. In order to understand the complexity of fluid dynamics around bodies, the equation of a single spherical particle is presented as well.

2.1 Introduction

Multiphase flows are found frequently in nature and many engineering applications. Most of the multiphase flows are two-phase flows, but three-phase flows can be also found. So, because most multiphase flows found in nature and industrial process are two-phase flows, the terms "multiphase" and "two-phase" are taken as synonymous in this work. A multiphase flow could be described as a fluid flow containing more than one phase, two in the case of two-phase flows. A phase refers to the state of the matter, which can be solid, liquid or gas. Figure 2.1 shows the three states of matter and the possible combinations to form the different types of multiphase flows. Four of these five combinations are two-phase flows (gas-solid, gas-liquid, liquid-solid

and liquid-liquid) and one of them is a three-phase flow. Three-phase flows are less frequent than two-phase flows and are not discussed in this work, but are no less important. This work is focused only on the particle-fluid-particle dynamic interactions in the dispersed two-phase flows.

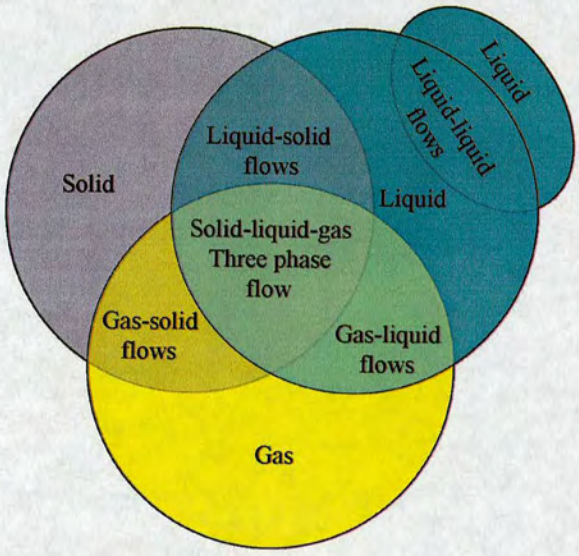

Fig. 2.1 Types of multiphase flows.

Numerical and experimental approaches have been used to study two-phase flows; however a complete understanding of two-phase flows is yet to be attained. The study of these flows represents a challenging and potentially productive area of knowledge for engineers and scientists. Due to the complexity of these flows, most of the work done on this topic has been applied to very specific problems. This research is focused mainly on the local hydrodynamic particle-fluid-particle interactions at low particle Reynolds number with specific application to the roping phenomenon found in the pneumatic transport in coal-fire power plants.

2.2 Multiphase flow classification and examples

Multiphase flows imply two or more phases coexisting in motion. The classification of multiphase flows depends on several factors, such as particle loading, particle and fluid Reynolds numbers, particle properties, type of fluids and size and configuration of the pipe system. Consequently, there is not a single classification that can adequately describe the large diversity of multiphase flows. A general classification is to divide two-phase flows into four groups, as shown in Figure 2.1. The four groups are gas-liquid flows (bubbly flows, separated flows, gas-droplet flows), gas-solid flows (gas-particle flows, fluidised beds), liquid-solid flows (slurry flows, sediment transport) and immiscible liquid-liquid (oil in water or water in oil). The last case is technically not a two-phase flow, it is rather a single-phase with two component flow, but for practical purposes it can be considered as a two-phase flow. Ishii (1975) gave another classification using the interfacial structure and the phenomenological description of the geometry distribution of the two phases. Figure 2.2 shows this classification, which is divided into three classes; separated flows, transitional or mixed flows and dispersed flows. In dispersed flows the particles, drops or bubbles are well distributed and maintained in a nearly homogeneous state in the continuous phase (gas or liquid). In separated flows the two phases are clearly distinguished, e.g., stratified flows, jet flows or film flows. Transient flows with a transition from pure liquid to a vapour flow as a result of external heating, e.g., gas core with droplets and liquid film in a steam generator. Dispersed two-phase flows are the main concern of the present study, which are encountered in numerous technical and industrial processes, are discussed in more detail in the next section.

class	Typical regimes	Geometry	Configurations	Examples
Separated flows	Film flow		• Liquid film in gas • Gas film in liquid	• Film cooling • Film boiling
	Annular flow		• Liquid core and gas film • Gas core and liquid film	• Film boiling • Condensers
	Jet flow		• Liquid jet in gas • Gas jet in liquid	• Atomization • Jet condenser
Transitional flows	Slug flow		• Liquid film in gas • Gas film in liquid	• Film cooling • Film boiling
	Bubbly annular flow	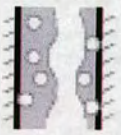	• Gas bubbles in liquid with gas core	• Evaporators with wall nucleation
	Droplet annular flow		• Gas core with droplets and liquid film	• Steam generator
	Bubbly droplet annular flow		• Gas core with droplets and liquid film with gas bubbles	• Nuclear reactor channel
Dispersed flows	Bubbly flow		• Gas bubbles in liquid	• Chemical reactors • Bubble columns
	Droplet flow		• Liquid droplets in gas	• Spray cooling
	Particulate flow		• Solid particles in gas or liquid	• Pneumatic transport • Falling particles in gas or liquid • Cyclone separators

Table 2.1 Two-phase flows classification, taken from Adrianov (2003).

2.2.1 Dispersed two-phase flows

In dispersed two-phase flows, the word "particles" refers to all dispersed phases, i.e., solid particles, bubbles or droplets and "fluid" refers to the continuous phase, gas or liquid.

Dispersed two-phase flows are a subcategory of the multiphase flow classification. Two-phase flows are classified in terms of the different phases being present; examples of important industrial processes of two-phase flows are summarised in Figure 2.2. Pneumatic transport of particles is widely applied in the chemical, food, mining, pharmaceutical and coal-fired power industries. Particle-fluid-particle dynamic interactions at low particle Reynolds number, applied to the roping phenomenon commonly found in the coal pneumatic transport in coal-fire power plants, is the main subject of this work.

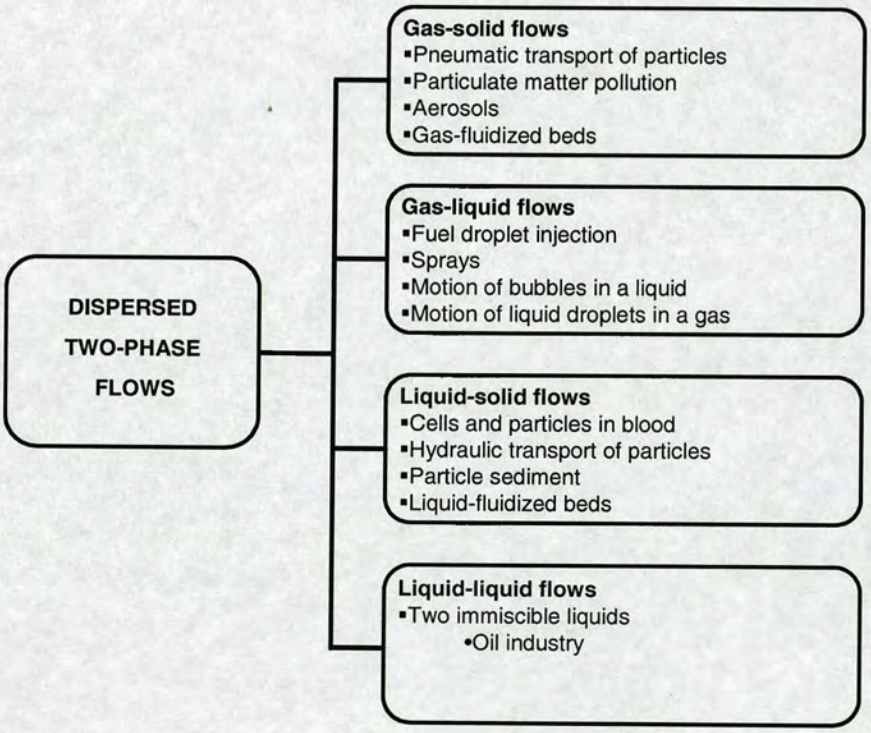

Fig. 2.2 Dispersed two-phase flows classification and important technical processes.

Gas-solid flows. Figure 2.3 show some examples of gas-solid flows. Gas-solid flows are generally gas with suspended solid particles; representative examples of these flows are pneumatic transport, cyclone separators and fluidised beds, as shown in Figure 2.3. Particle pneumatic transport is used extensively in several industrial applications, transport of cement, grains, coal, medical and food powders. The flow patterns found in particle pneumatic transport depend on many factors, such as solid loading, particle and gas velocities, pipe layout and particle properties, Figure 2.3(a), shows a typical particle pneumatic transport pattern in a vertical to horizontal pipe joined by a 90^{o} elbow. Cyclone separators are used to remove solid particles and droplets (~ 5 μm) from industrial exhaust. In cyclones, gas-particles enter into the cyclone in a tangential direction as shown in Figure 2.3(b). The particles are unable to follow the spiral air and continue to the wall where they lose momentum and fall to the bottom where they can be removed. The "clean" gas converges to the centre and exits the device through the top. Another important industrial application of gas-solid flows is the gas-fluidised bed. A fluidised bed consists of a vertical particle container where gas is introduced through the bottom of the device as shown in Figure 2.3(c). Fluidised beds are commonly used in many chemical processes such as coal gasification and disposal of organic and toxic waste.

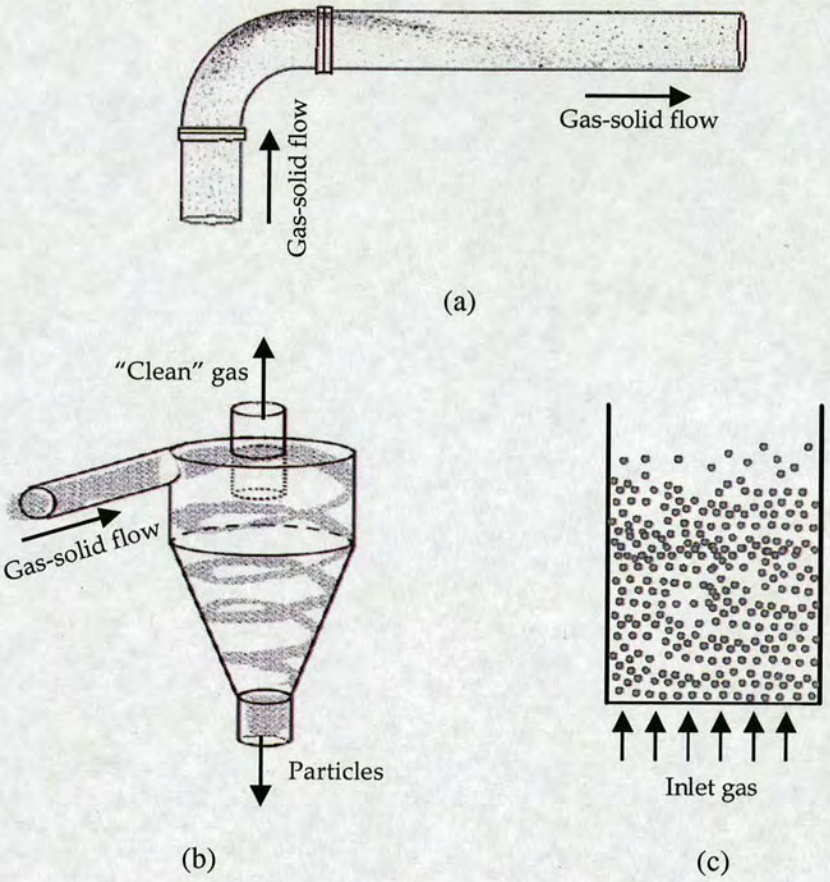

Fig. 2.3 Gas-solid two-phase flows, (a) pneumatic transport, (c) cyclone separator and (b) fluidised bed.

Gas-liquid flows. Dispersed gas-liquid flows can be the motion of liquid droplets in a gas or the motion of bubbles in a liquid. Figure 2.4 shows two good examples of gas-liquid two-phase flows; a ceiling fire suppression sprinkler system and bubble columns. Fire suppression sprinkler systems have been used for several decades to extinguish the fire in factories, warehouses and residencies. Two-phase phenomena associated with the water spray are very complex: droplets are projected toward the fire; they interact dynamically with themselves; and later they interact with the hot plume of the fire. Some droplets evaporate in the gas plume while others penetrate the fire and evaporate there. Fire suppression by droplets is an important research area at the present time. Bubble columns are another typical example of gas-liquid flows; bubble columns have been applied to different industrial applications such as

absorption and coal liquefaction. In bubble columns the gas bubbles flow through the liquid interacting dynamically between themselves and also with the continuous phase.

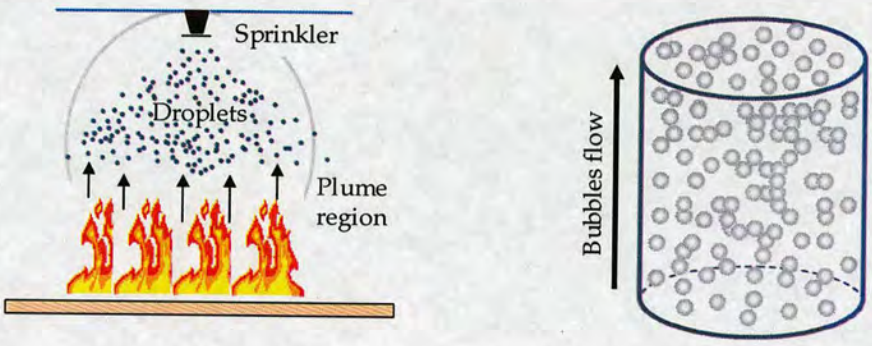

Fig. 2.4 Gas-liquid two-phase flows, a) sprinkler fire suppression system and (b) bubbly column.

Liquid-solid flows. Liquid-solid and gas solid flows are very similar with only a few differences, e.g., in a dispersion of very small particles (> 10 μm) in liquids, electrostatic forces play a more important role. On the other hand, large Stokes numbers can never be obtained in liquid-solid flows due to the physical properties of the liquids, Kleinstreuer (2003). Three good examples of liquid-solid flows are the cells/platelets in blood flows, particle sedimentation and liquid-fluidised beds, these three typical examples are shown in Figure 2.6. Figure 2.5(a) shows the blood flow, which has three main different types of particles: red blood cells, white blood cells and platelets. The study of local homodynamic of blood flows is a very important subject in the diagnosis and treatment of patients of cardiovascular diseases, Boryczko *et al.* (2003). Particle sedimentation is another good example of liquid-solid two-phase flow. Particle sedimentation is a common process found in nature, e.g., migration of biological matter in water systems and particle sedimentation in oceans, lakes, rivers and channels. It is also used in many industrial processes, for example, in waste water treatment systems, and the petroleum and chemical industries as a means of separating particles, Kusela, (2005) and Thelen & Ramirez, (1999)]; Figure 2.5(b) and 2.5(c) shows schematic pictures of a particle

sedimentation system and a liquid-fluidised bed, respectively. Particle sedimentation systems are commonly used in potable and waste water treatment. Liquid-fluidised beds are less common than gas-fluidised beds, but they have some important applications in industry: particle separation, wastewater treatment and bioreactors, for more information see Eptein, (2003) and Thelen & Ramirez, (1999).

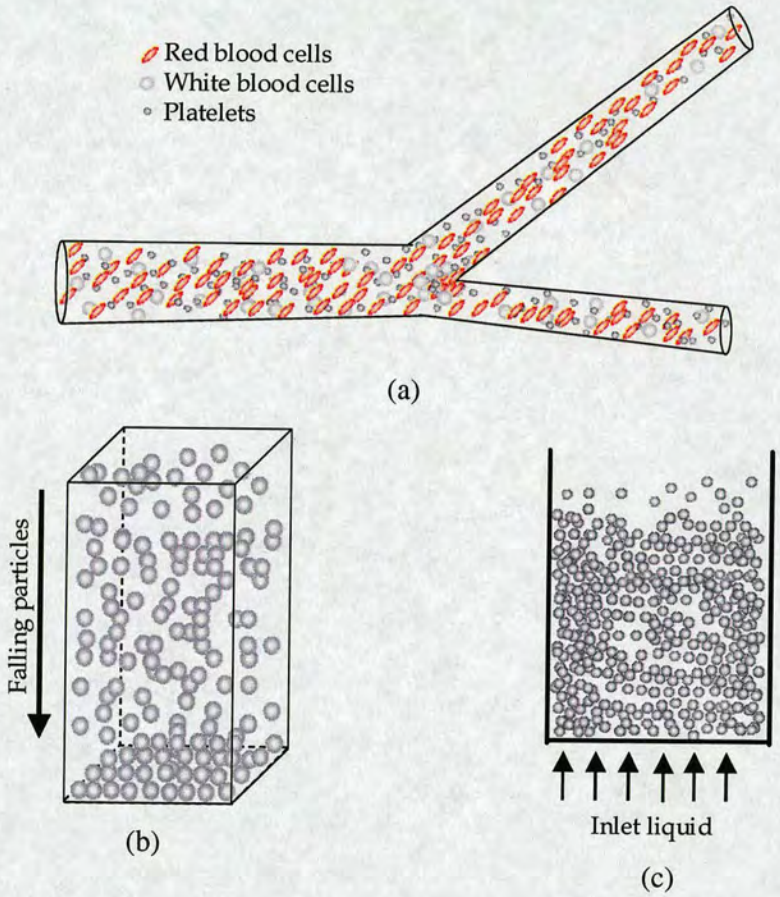

Fig. 2.5 Liquid-solid flow (a) cells/platelets in blood flow, (b) particle sedimentation system and (c) Liquid-fluidised bed system.

Liquid-liquid flows. Liquid-liquid flows are also found in some engineering problems, but are less common than the other three dispersed two-phase flow categories. This type of flow can be found when the two phases are flowing together, e.g. the oil-water flow found in the petroleum industry.

2.3 Dispersed phase flow definition and properties

Several parameters such as particle densities, volume fractions, loadings and/or concentrations are used to characterize the dispersed two-phase flows, Crowe *et al.* (1998) and Kleinstreuer (2003). In this section, some of the most important parameters to describe two-phase flows are presented.

Number density. Often the particle concentration in dispersed two-phase flows is expressed by the number of particles per unit volume, which is defined as:

$$n_p = \frac{N_p}{V} \tag{2.1}$$

where N_p is the number of particles in the volume *V*.

Particle and fluid volume fractions. Volume fraction of both dispersed and continuous phases are two important characteristics in two-phase flows. The volume fraction of the dispersed phase is the volume occupied by the particles per unit volume. Hence this property is expressed by:

$$\alpha_p = \frac{V_p}{V} \tag{2.2}$$

where V_p is the volume of the total particles contain in a volume V. If N_p is the total number of particles as defined in equation 2.1 and all the particles are spherical with the same diameter d_p, V_p can be given by:

$$V_p = N_p v_p \tag{2.3}$$

where $v_p = \frac{\pi}{6} d_p^3$ is the volume of the spherical particle.

The volume fraction of the continuous phase, some times referred to as the void fraction can be expressed as:

$$\alpha_f = \frac{V_f}{V} \tag{2.4}$$

where V_f is the volume of the continuous phase in the volume V. Since, by definition, the sum of the volume fraction of the dispersed phase and the continuous phase is the unity, defined by:

$$\alpha_f + \alpha_p = 1 \tag{2.5}$$

Bulk density. The bulk density, effective density, apparent density or concentration of dispersed phase is defined as the mass of the dispersed phase per unit volume of the mixture and hence is given by:

$$\overline{\rho}_p = \frac{M_p}{V} \tag{2.6}$$

where M_p is the total mass of the dispersed phase (particles) in the volume V. If all particles in the volume V have the same mass, m_p, the bulk density can be defined in terms of the density number by:

$$\overline{\rho}_p = n_p m_p \tag{2.7}$$

The bulk density of the dispersed phase can be also defined in terms of the particle volume fraction as:

$$\overline{\rho}_p = \rho_p \alpha_p \tag{2.8}$$

where ρ_p is the actual or material density of the dispersed phase. The bulk density of the continuous phase can be expressed as:

$$\overline{\rho}_f = \frac{M_f}{V} \tag{2.9}$$

or

$$\overline{\rho}_f = \rho_f \alpha_f \tag{2.10}$$

Thus an expression for the mixture density of the two-phase flow is the sum of the two individual bulk densities:

$$\rho_m = \overline{\rho}_p + \overline{\rho}_f = \alpha_p \rho_p + \alpha_f \rho_f = \alpha_p \rho_p + (1 - \alpha_p)\rho_f \tag{2.11}$$

Mass concentration. In the study of dispersed two-phase flow mass concentration is defined as the ratio of the mass of the dispersed phase to that of the continuous phase:

$$C = \frac{M_p}{M_f} = \frac{\overline{\rho}_p}{\overline{\rho}_f} \tag{2.12}$$

The mass concentration of the dispersed phase is sometimes referred to as the particle mass ratio.

Mass loading. Especially in gas-solid, the local particle loading is frequently defined as the ratio of the mass flux of the dispersed phase to that of the continuous phase:

$$\lambda = \frac{\dot{m}_p}{\dot{m}_f} = \frac{\overline{\rho}_p u_p}{\overline{\rho}_f u_f} \tag{2.13}$$

where u_p and u_f are the velocities of the dispersed and continuous phases respectively. The total mass loading, $\Lambda = \frac{\dot{M}_p}{\dot{M}_f}$ is often approximated as $C = \frac{\bar{\rho}_p}{\bar{\rho}_f}$, Kleinstreuer (2003).

Inter-particle separation distance. The interaction between particles in dispersed two-phase flow depends significantly on the average inter-particle separation distance, Crowe *et al.* (1998). Thus, the inter-particle separation distance is an important parameter in dispersed two-phase flows. The inter-particle separation distance can be determined for regular arrangements of the particles, e.g., consider two particles enclosed in the centre of two cubes with sides, *l*, as show in Figure 2.6.

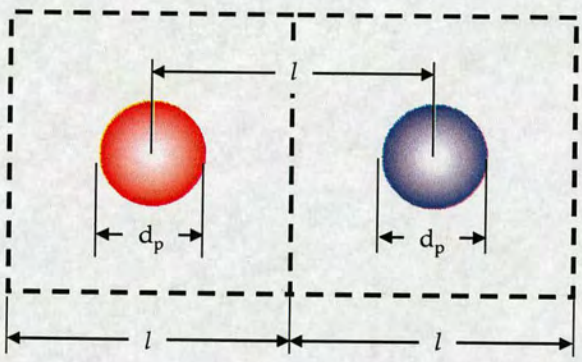

Fig. 2.6 Particle separation distance for a regular particle distribution.

For the specific case describe in Figure 2.6, the volume fraction of the dispersed phase can be defined as:

$$\alpha_p = \frac{\pi d_p^3}{6l^3} \tag{2.14}$$

From equation (2.14) the non-dimensional particle separation distance can be given as function of the volume fraction by:

$$D_o = \frac{l}{d_p} = \left(\frac{\pi}{6\alpha_p}\right)^{\frac{1}{3}} \tag{2.15}$$

The particle separation distance in dispersed two-phase flow can also be expressed in terms of the dispersed mass concentration, C, and the material or actual density ratio of the two phases as:

$$D_o = \frac{l}{d_p} = \left(\frac{\pi\rho_p}{6C\ \rho_f(1-\alpha_p)}\right)^{\frac{1}{3}} \tag{2.16}$$

Phase Coupling. In the equations describing dispersed two-phase flows it is very common to find terms representing one-way coupling, two-way coupling, three-way and four-way coupling, Loth (2007). These terms are used to represent the interactions between the phases in dispersed two-phase flows and they are frequently used to classify the two-phase flow into dilute and dense flows, as shown in Figure 2.7 which is based on the information taken from Loth (2007) who proposed four different coupling regimes:

1. "one-way" coupling: particle-phase motion affected by the continuous phase but not vice-versa,
2. "two-way" coupling: particle-phase also affects the continuous-phase through fluid coupling,
3. "three-way" coupling: flow disturbances caused by particles affect the motion of nearby particles,
4. "four-way" coupling: contact collisions also influence the overall particle motion.

The first three regimes include only fluid dynamic interactions, whereas the fourth regime includes particle collisions. Figure 2.7 indicates that a dispersed two-phase flow may be considered as dilute for particle volume fractions up to $5x10^{-4}$. For volume fraction $\alpha_p > 7.5x10^{-4}$ the flow is considered as dense. One-way coupling

can be considered for particle volume fractions, $\alpha_p < 6x10^{-7}$, which means that the dispersed phase is affected by the continuous phase (fluid-particle) but not vice-versa, the particles follows the flow pathlines. For higher particle volume fractions, $6x10^{-7} < \alpha_p < 3x10^{-5}$, two-way coupling must be taken into account. In this regime the continuous phase affects the particles but the particles can also affect the continuous phase through mass, momentum or energy transfer between the two phases, e.g., the particle's wake causes dissipation (fluid-particle-fluid interactions). In three-way coupling the flow affects the particle but the particle's flow disturbs the motion of neighbouring particles (fluid-particle, particle-fluid and particle-fluid-particle interactions, e.g. hydrodynamic interactions). The three-way coupling is clearly observed at $\alpha_p > 7.5x10^{-4}$ (D_o = 10), but in this work under specific situations particle-fluid-particle interactions have been observed up to $\alpha_p = 3x10^{-5}$ (D_o = 25), Vargas & Easson (2004). In denser regimes, $\alpha_p > 7.5x10^{-4}$ four-way coupling should be included (fluid-particle, particle-fluid, particle-fluid-particle and particle-particle interactions), but particle-particle interactions become dominant at higher particle concentrations, $\alpha_p > 5x10^{-2}$. Direct particle-particle interactions are due to collisions, Sommerfeld (2000) and Loth (2007).

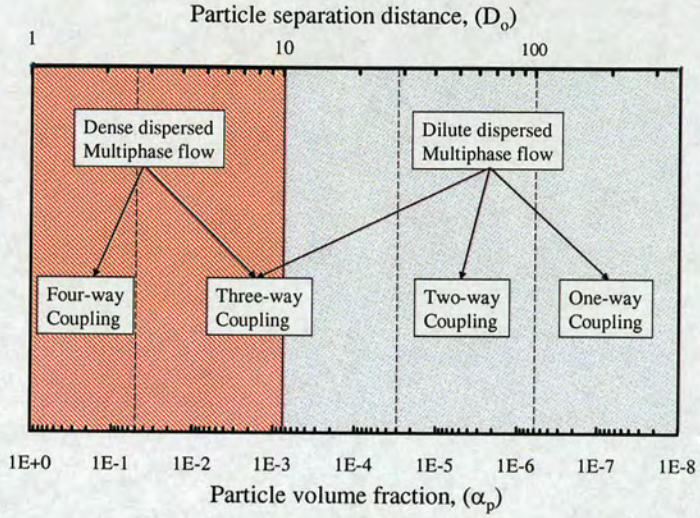

Fig. 2.7 Dispersed two-phase flow regimes as a function of particle volume fraction (α_p) and particle separation distance (D_o), this figure is based on the information taken from Loth (2007).

Particle relaxation time. Particle relaxation time is an important parameter to characterize the dispersed two-phase flows. The particle relaxation time defines the ability of a particle to respond to a local change fluid velocity. This parameter can be estimated from the solution of the simplified equation of motion, in terms of the drag force. For a spherical particle in a gas the equation of motion can be defined as follows:

$$m\frac{dv_p}{dt} = \frac{1}{2}C_D\frac{\pi d_p^2}{4}\rho_f(u_f - u_p)\left|u_f - u_p\right| \tag{2.17}$$

where u_p is the particle velocity and u_f is the continuous phase velocity. By definition the particle Reynolds number in dispersed two-phase flows is

$$Re_p = \frac{\rho_f d_p\left|u_f - u_p\right|}{\mu_f} \tag{2.18}$$

By using the particle Reynolds number definition and dividing by the particle mass the equation (2.17) can be expressed as:

$$\frac{dv_p}{dt} = \frac{18\mu_f}{\rho_p d_p^2}\frac{C_D Re_p}{24}(u_f - u_p) \tag{2.19}$$

The particle relaxation time can be

$$\tau_p = \frac{\rho_p d_p^2}{18\mu_f f_D} \tag{2.20}$$

where f_D is a dimensionless measure of the drag forces acting on the spherical particle, $f_D = \frac{C_D Re_p}{24}$, for Stokes regime this factor approaches unity. Thus the equation (2.19) can be written as:

$$\frac{dv_p}{dt} = \frac{1}{\tau_p}(u_f - u_p) \tag{2.21}$$

The solution of this equation for constant velocity of the continuous phase, u_f, and initial particle velocity, u_p of zero, is:

$$v_p = u_f\left[1 - \exp\left(-\frac{t}{\tau_p}\right)\right] \tag{2.22}$$

The equation above shows that the momentum response time or particle relaxation time is the time required for a particle released from rest to reach 63% ($\frac{e-1}{e}$) of the continuous phase velocity, Figure 2.8 illustrates graphically the particle response time.

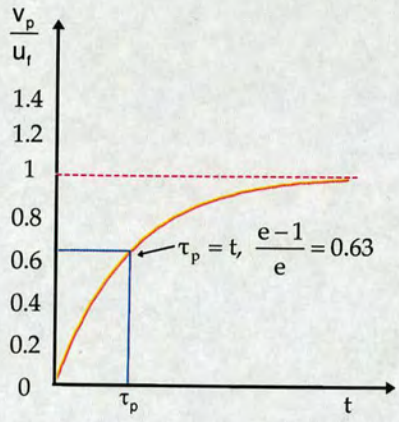

Fig. 2.8 Particle relaxation or particle response time in a multiphase flow.

Stokes number. The particle Stokes number, St_p, is a very important parameter in general fluid-particle flows. The Stokes number is a dimensionless number corresponding to the behaviour of the particles in a fluid flow and can be defined as the ratio of particle response time, τ_p, to some characteristic time, τ_f, of the flow field in the system:

$$St_p = \frac{\tau_p}{\tau_f} \tag{2.23}$$

where the particle response time is given by equation (2.20) and the fluid response time, τ_f, is defined by:

$$\tau_f = \frac{L_{f,c}}{\Delta u_{f,c}} \tag{2.24}$$

The characteristic time of the fluid flow can be very difficult to estimate as it is based on a characteristic length and a characteristic velocity difference of the system studied, but for flows in closed ducts the diameter is typically used as the characteristic length, $L_{f,c}$, and the mean velocity in the duct is used as $\Delta u_{f,c}$. In very

large geometries the diameter of a vortex structure could be used as $L_{f,c}$ and velocity difference across the vortex structure is used as $\Delta u_{f,c}$, Sørensen (2005).

Time between collisions. In dispersed two-phase flows, the time between particle collisions, which can be estimated from the equations for collision frequency is an important parameter. Consider a group of monodispersed spheres with diameter, d_p, and a sphere with the same size travelling through the monodispersed group of spheres with a relative velocity, $u_{p,r}$, with respect to the other spheres as shown in Figure 2.9. In a time Δt, the sphere will intercept all the particles within the virtual tube with diameter $2d_p$ and length $v_{p\text{-}r}\Delta t$. The number of particles in this virtual tube must be, Crowe *et al.*, 1998:

$$N_p = n_p \pi d_p^2 u_{p,r} \Delta t \tag{2.25}$$

where n_p is the number density or particle concentration defined by equation (2.1). The collision frequency, f_{coll}, can be defined as:

$$f_{coll} = \frac{1}{\tau_{coll}} = \frac{N_p}{\Delta t} = n_p \pi d_p^2 u_{p,r} \tag{2.26}$$

So the Stokes number can also be expressed in terms of the particle collisions time as:

$$St_p = \frac{\tau_p}{\tau_{coll}} = \frac{n\pi\rho_p d_p^4 u_{p,r}}{18\mu} \text{ or } \frac{\bar{\rho}_p d_p u_{p,r}}{3\mu} \tag{2.27}$$

where $\bar{\rho}_p$ is the bulk density defined by the equation (2.8).

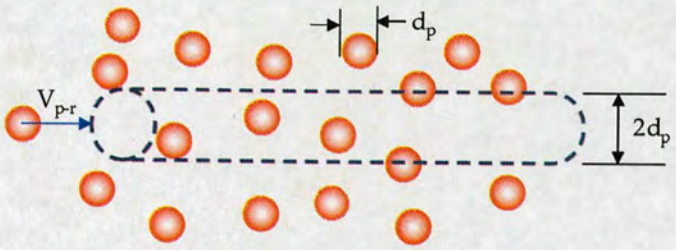

Fig. 2.9 Scheme of particle-particle collisions in a dense two-phase flow.

2.4 Basic equations of moving particles in fluids

A comprehensive study of behaviour of particles in dispersed two-phase flows has not been achieved yet. A great understanding of single particles, especially spherical particles, has been attained, thus equations to describe the movement of isolated particles in fluids have been formulated. On the other hand the behaviour of particles in dispersed two-phase flows has been studied empirically by numerical models and experimental techniques.

2.4.1 Motion of a single spherical particle

This section will discuss the general motion equations of an isolated spherical particle. Typically these equations describe the movement of solid spherical particles, but can be applied to fluid particles or bubbles under certain considerations. Of course, these general equations do not include several features that can be found in dispersed two-phase flows, such as particle-fluid-particle, particle-particle and particle-wall interactions. However, the equation of motion of a single spherical particle introduced in this section will be very useful to understand and illustrate many aspects of dispersed two-phase flows.

The interaction between the fluid and the particle occurs at the particle surface where the interfacial normal and tangential stresses generate a net force on the particle. The normal stress is made up by two components: the stress from body forces -usually gravity- and the normal stress from the fluid motion. The integral of the stress of the body forces over the body surface is the buoyancy force, while the integral of the stress from the fluid motion is the dynamic pressure force, Losenno (2004). The total integral of the shear stress over the particle surface is known as skin friction. The components of the wall shear stress parallel to the fluid velocity form the dynamic drag force F_D over the particle, which greatly depends on the particle surface.

On the other side, all components perpendicular to the flow velocity form the lift force F_L.

Newton's second law of motion is used to describe the movement of a particle in a flow field. For example, for a pure translational movement the equation of motion is given by:

$$m_p \frac{dv_p}{dt} = \sum F \tag{2.28}$$

where the sum of the forces, $\sum F$ is given by the Basset-Boussinesq-Oseen (BBO) equation:

$$m_p \frac{dv_p}{dt} = \sum F = F_g + F_p + F_D + F_{vm} + F_{Basset} \tag{2.29}$$

where F_g is the gravity force, F_p is the pressure force including the buoyancy contribution, F_D is the drag force, F_{vm} is the virtual mass force and F_{Basset} is the basset force.

The first term of the equation (2.29) is related to the weight of the particle; know as the body or gravity force. This force is given by:

$$F_g = m_p g \tag{2.30}$$

where m_p is the particle mass and g is the gravity.

The second term in the equation (2.29) is the pressure force. This force represents the local pressure on the particle surface; this term is some times knows as the external forces. The pressure force term in the equation (2.29) includes the buoyancy term, which represents a force equal to the weight of the fluid displaced by the particle; this term has an opposite direction to the gravity. The pressure term can be expressed as:

$$F_p = V_p(-\nabla p + \nabla \tau) \tag{2.31}$$

where V_p is the particle volume.

The third term in the equation (2.29) is known as the drag force, this term is due to viscous friction between the fluid and the particle surface, and the form drag or pressure drag. In most fluid-particle systems the drag force is the dominant term. The friction part dominates at very low Reynolds number (Re<<1), while at higher Reynolds number the form drag is the dominant term. The drag force can be expressed by:

$$F_D = \frac{1}{2}\rho_f C_D A_p (u_f - u_p)\left|u_f - u_p\right| \tag{2.32}$$

where $A = \frac{\pi d_p^2}{4}$ is the cross section of the spherical particle, C_D is a coefficient that depends on the particle Reynolds number.

The fourth term in the equation (2.29) is define as the virtual mass force or some times called the apparent mass force, which represents the acceleration of the surrounding fluid and can be expressed mathematically as

$$F_{vm} = \frac{\rho_f u_p}{2}\left(\frac{Du_f}{Dt} - \frac{du_p}{dt}\right) \tag{2.33}$$

where u_p is the particle volume, ρf is the fluid density and $\left(\frac{Du_f}{Dt} - \frac{dv_p}{dt}\right)$ is the relative acceleration of the fluid with respect to the particle. $\frac{D}{Dt}$, is the material, Lagrangian, convective, or substantive derivative. It is given by:

$$\frac{D}{Dt} = \frac{\partial}{\partial t} + u_f \cdot \nabla \tag{2.34}$$

where u_f is the fluid velocity. This derivative is very useful in the study of fluid mechanics and when applied to u_f as is the case in the equation (2.33) can be defined as, Wesisstein (2006):

$$\frac{Du_f}{Dt} = \frac{\partial u_f}{\partial t} + (\nabla \times u_f) \times u_f + \nabla(\tfrac{1}{2} u_f^2) \tag{2.35}$$

The last term in equation (2.29) is defined as Basset force, also called the time history term, which accounts for the viscous effects due to the fluid acceleration around the particle. This term can be defined by Crowe *et al.* (1998):

$$F_{basset} = \frac{2}{3} d_p^2 \sqrt{\pi \rho_f \mu_f} \int_0^t \frac{\frac{Du_f}{Dt} - \frac{du_p}{dt}}{\sqrt{t - t'}} dt' + \frac{(u_f - u_p)_0}{\sqrt{t}} \tag{2.36}$$

where t′ is an integrating parameter that represent the total interaction time, $(u_f - u_p)_0$ is the initial velocity difference and once again $\frac{D}{Dt}$ is the material derivative defined by equation (2.34). The BBO equation (2.29) can be expressed as:

$$
\begin{aligned}
m_p \frac{du_p}{dt} &= m_p g \quad \text{Body force} \\
&+ u_p(-\nabla p + \nabla \tau) \quad \text{Pressure force} \\
&+ \frac{1}{2}\rho_f C_D A_p (u_f - u_p)\left|u_f - u_p\right| \quad \text{Drag force} \\
&+ \frac{\rho_f u_p}{2}\left(\frac{Du_f}{Dt} - \frac{du_p}{dt}\right) \quad \text{Virtual mass force} \\
&+ \frac{2}{3} d_p^2 \sqrt{\pi \rho_f \mu_f} \int_0^t \frac{\frac{Du_f}{Dt} - \frac{du_p}{dt}}{\sqrt{t - t'}} dt' + \frac{(u_f - u_p)_0}{\sqrt{t}} \quad \text{Basset force}
\end{aligned}
\tag{2.37}
$$

For most gas-solid flows the ratio of the continuous phase density to the particle density, $\frac{\rho_f}{\rho_p}$ is very small ($\sim 10^{-3}$), the BBO equation (2.37) can be simplified to, Crowe *et al.* (1998):

$$\frac{du_p}{dt} = \frac{1}{\tau_p}(u_f - u_p) + g \tag{2.38}$$

However, the complete BBO equation (2.37) must be used for liquid-solid flows where both densities are comparable, Crowe *et al.* (1998).

2.4.2 Drag coefficient for single spherical particles

As mentioned before in this section, the drag force is the most important force in the study of an isolated moving particle, but it is also a key factor in the study of dynamic particle-fluid-particle interactions. For this reason, a clear understanding of this force is essential.

As shown in equation (2.32) the drag force is expressed in terms of the fluid and particle properties. These properties can be expressed in terms of two non-dimensional parameters, the drag coefficient and the particle Reynolds number. The particle Reynolds number and the drag coefficient can be defined by:

$$Re_p = \frac{\rho_f d_p (u_f - u_p)}{\mu_f} \tag{2.39}$$

$$C_D = \frac{F_d}{\frac{1}{8}\pi\rho_f d_p^2 (u_f - u_p)^2} \tag{2.40}$$

where the term $(u_f - u_p)$ is known in dispersed two-phase flow as the relative or slip velocity between phases.

The particle Reynolds number is the ratio of the inertial to viscous forces and from equation (2.40) it can be seeing that the non-dimensional drag coefficient is a direct function of the particle Reynolds number. So the equation (2.40) can also be expressed as:

$$C_D = \frac{8}{\pi\mu_f (u_f - u_p)} \frac{F_D}{Re_p} \tag{2.41}$$

In 1851 G. G. Stokes found that the drag force for a spherical particle at very low particle Reynolds number ($Re_p << 1$) can be defined as:

$$F_D = 3\pi\mu_f d_p (u_f - u_p) \tag{2.42}$$

Replacing equating (2.42) into equation (2.41) the Stokes drag coefficient can be obtained by:

$$C_D = \frac{24}{Re_p} \tag{2.43}$$

The equation (2.43) is the classical drag coefficient of a sphere for particle Reynolds numbers less than the unity. Because equation (2.43) is limited to very low particle Reynolds numbers, numerous works have been done to extend this equation to higher particle Reynolds numbers. Table 2.1 show five different correlations with a standard deviation less than ±6% from the standard drag curve.

Author(s)	Range	Relationship for C_D	Reference
Stokes (1851)	$Re_p < 1$	$\frac{24}{Re_p}$	Clift *et al.* (1978)
Oseen (1910)	$Re_p < 1$	$\frac{24}{Re_p}\left(1+\frac{3}{16}Re_p\right)$	
Schiller and Neuman (1933)	$Re_p < 800$	$\frac{24}{Re_p}\left(1+0.15Re_p^{0.687}\right)$	
Clift and Gauvin (1970)	$Re_p < 3 \times 10^5$	$\frac{24}{Re_p}\left(1+0.15Re_p^{0.687}\right) + \frac{0.42}{1+4.25\times10^4 Re_p^{-1.16}}$	
Schlichting (1972)	$0.01 < Re_p < 1 \times 10^6$	Standard drag curve	Schlichting (1972)
FLUENT Inc (2005)	Several ranges of Re_p given by Morsi and Alexander (1972)	$a_1 + \frac{a_2}{Re_p} + \frac{a_3}{Re_p^2}$	FLUENT's Manual (2005)

Table 2.2 Relationships of drag coefficients for a single sphere with less than 6% of standard deviation from the typical curve.

Figure 2.10; shows the dependence of drag coefficient of a single spherical particle, based on some empirical relationships. An extensive number of empirical correlations can be found in the monograph of Clift *et al.* (1978). From Figure 2.10

several regimes which are associated with the flow characteristics around the particle are observed.

1. For very small Reynolds numbers ($Re_p < 1$) viscous effects are dominant and no separation is observed. An analytical solution can be obtained, equation (2.43).
2. In the transition region ($1 < Re_p < 1000$) inertial effects become important. For Reynolds numbers above 24 the flow around the particle begins to separate. The initial separation is symmetric, but as the Reynolds number reaches the value around 130, becomes unstable. For this region numerous empirical correlations have been proposed, see table 2.2.
3. For Reynolds numbers above 1000, the drag coefficient remains almost constant up to the critical Reynolds number ($Re_p \sim 2.5x10^5$), since the wake size and structure do not significantly change. This regime is known as the Newton regime with a drag coefficient, $C_d \sim 0.45$.
4. At the critical region ($2.5x10^5 < Re_p < 4x10^5$) a drastic decrease of the drag coefficient is found, caused by the transition from laminar to turbulent boundary layer on the particle surface, which results in a decrease in the particle wake.
5. In the super critical region, $Re_p > 4x10^5$, the drag coefficient increases continuously, but for most practical dispersed flows this region is not relevant.

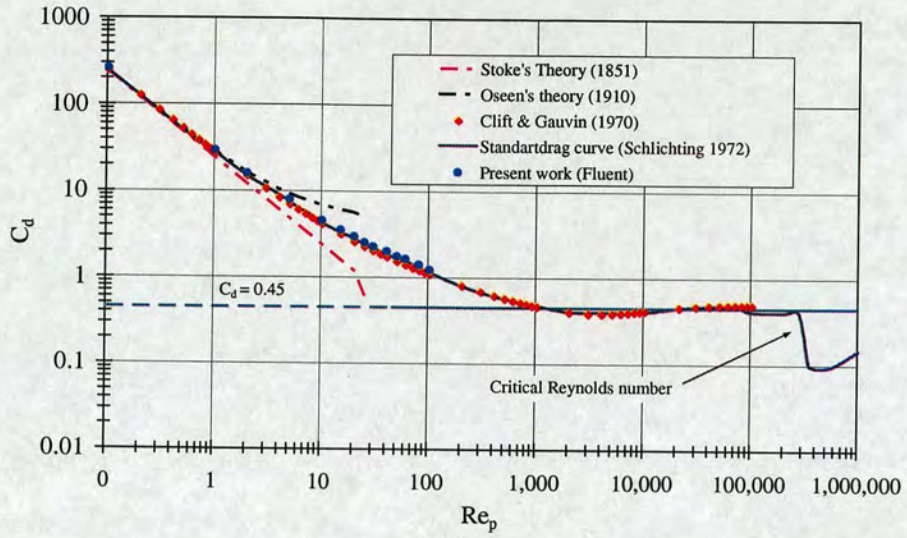

Fig. 2.10 Drag coefficient of a sphere as a function of particle Reynolds number.

2.4.3 Motion of multiple spherical particles

The motion of multiple spherical particles is fundamental in a wide range of engineering and science applications. When a particle moves relative to a viscous flow, it creates a perturbation to this field, which extends to the flow boundaries. Consequently, these perturbations would in theory influence the motion of the flow or any other particle in the flow domain. However, the significant effects of these perturbations are strongly dependant on several variables: (1) particle shape and size; (2) the distance between them, (3) the orientation of the particles relative to the fluid velocity field and each other; (4) their velocity relative to the fluid, among others. For example, particles that are separated by long distances do not interact significantly. If the volume fraction of the dispersed phase is such that the average distance separating the immersed particles is large, the dynamic interaction and collisions can be neglected and one-way coupling can be used in the numerical simulations. For intermediate separation distances the dynamic interactions between the particles are significant, but not the collisions. However for very high

concentrations, both the hydrodynamic interactions and collisions of the particles play an important role in the behaviour of two-phase flows. So, any theory that attempts to describe the dynamics of a system of particles dispersed in a quiescent or moving fluid must deal with the particle-fluid-particle dynamic interactions. Unfortunately, the only exact general solution of the dynamic particle-fluid-particle interactions in a multiple particle system known to date is that for two particles at very low Reynolds number (Re << 1). For example, consider the motion of two particles as shown in Figure 2.11.

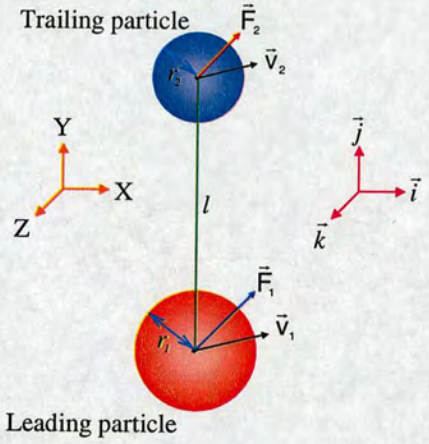

Fig. 2.11 Nomenclature for two interacting spherical particles aligned with the main flow direction ($\theta = 0^o$) for equation (2.44).

If the velocity vectors and the dynamic force vectors are in the same plane, the x-y plane, an analytic solution for the dynamic interactions between the two spheres has been obtained in the Stokes flow regime (Re_p << 1), Happel & Brenner (1973). The total force acting on the leading sphere (1) as a result of the motion of both spheres in the viscous fluid is given by:

$$\frac{\vec{F}_1}{6\pi\mu r_1} = -\frac{\left(\vec{v}_1\cdot\vec{i}\right)-6r_1\left(\vec{v}_2\cdot\vec{i}\right)/(8l)}{1-(36r_1r_2)/(8l)^2}\vec{i}-\frac{\left(\vec{v}_1\cdot\vec{j}\right)-6r_1\left(\vec{v}_2\cdot\vec{j}\right)/(4l)}{1-(36r_1r_2)/(8l)^2}\vec{j} \qquad (2.44)$$

The force acting on the trailing sphere (2) may be obtained from equation (2.44) by interchanging the two subscripts. If the two spherical particles are moving in the same direction, it is apparent that, as for example in the case of sedimentation under gravity, the dynamic force opposing the motion of each particle is reduced as a consequence of the motion of the other particle. Therefore, the two spherical particles would travel faster than that of a single particle in the field flow. In the case of two identical particles, both particles would settle faster and keep the same separation distance. For a complete comprehensive study of the formulation of two moving particles at $Re_p << 1$, the reader is referred to the monographs of Kim & Karrila (1991), Zapryanov & Tabakova (1999) and Michaelides (2006).

However the case is completely different when the inertial forces on the spheres is significant and, hence, the particle Reynolds number is large in this case, the flow is not in the Stokes regime and the forces must be obtained experimentally or numerically. Even for two particles there are no single, simple equations describing the forces on the particle on this region.

2.4.4 Drag coefficient of multiple spherical particles

The standard drag force law for single particle changes when there is more than one particle immersed in the fluid and the separation distance is short enough for dynamic interaction. Most of the drag correlations presented for multiple particle systems have obtained from sedimentation, bubble columns and fluidisation studies, both experimentally and numerically.

Most of the empirical or semi-empirical drag correlations obtained for multiple particle system are based on the hindered settling effect. The Richardson and Zaki correlation is typically used in order to take into account the effect of particle concentration on the drag coefficient, which is defined as follows:

$$f(\alpha_p) = (1-\alpha_p)^{-x} \tag{2.45}$$

where α_p is the solid volume fraction and x is a parameter function of the particle properties and the particle Reynolds number based on the slip velocity, and varies from 2 to 10. Thus, in order to incorporate the additional forces from other particles, and the modifications in flow field, the drag force is multiplied by the correction function, $f(\alpha_p)$, such that:

$$C_{Dm} = C_{Ds} f(\alpha_p)^m \tag{2.46}$$

Where C_{Dm} is the drag coefficient on a particle taking into account the effect of neighbouring particles, and C_{Ds} is the drag coefficient on the same particle when it is falling freely under the fluid and gravity force. The exponent m varies between 1 and 2 depending on the particle Reynolds number, Re_p. Hence, the combined drag law for multiple particles can frequently be found as:

$$C_{Dm} = C_{Ds}(1-\alpha_p)^{-n} \tag{2.47}$$

Therefore, according to the values given for both x and m, the values of n should practically vary from 2 to 20 for rough or smooth particles in a wide range of flow covering both creeping and turbulent flow.

The correlations developed to express the drag coefficient as function of the particle concentration are many and different. Table 2.3 summarises some of the most commonly used and recent expressions.

Author(s)	Relationship for C_{Dm}	Range
Happel (1958)	$C_{Dm} = \frac{3+2(1-\alpha_p)^{5/3}}{3-4.5(1-\alpha_p)^{1/3}+4.5(1-\alpha_p)^{5/3}-3(1-\alpha_p)^2}$	Not specified
Rowe (1961)	$C_{Dm} = \frac{24}{(1-\alpha_p)Re_p}\left[1+0.15(1-\alpha_p)^{0.687}Re_p^{0.687}\right]$	$10 < Re_p < 1000$
Rowe (1987)	$C_{Dm} = D_{Ds}(1-\alpha_p)^{-n},\ n = \frac{2.35(2+0.175Re_p^{3/4})}{(1+0.175Re_p^{3/4})}$	$0.01 < Re_p < 1000$
Di Felice (1994)	$C_{Dm} = \left(0.63+4.8\sqrt{\frac{1}{Re_p}}\right)^2(1-\alpha_p)^{-\left(3.7-0.65\exp\left(\frac{-(1.5-\log Re_p)^2}{2}\right)\right)}$	Not specified
Jie & Kuipers (2003)	$C_{Dm} = C_{Ds}\left[\frac{3=25(1-\alpha_p)^{1/3}}{3-4.5(1-\alpha_p)^{2/3}+4.5(1-\alpha_p)^{2/3}+3(1-\alpha_p)^2}\right]$	Not specified
Dodds & Naser (2004)	$C_{Dm} = \frac{24}{Re_p}\left(1+0.15Re_p^{0.687}+0.000353\left[\log\left(\frac{\pi}{6\alpha_p}\right)^{1/3}\right]^{15.9}+0.16\left[\log(Re_p)\right]^{3.62}\right)$	$1 < Re_p < 50$
Helland *et al.* (2007)	$C_{Dm} = C_{Ds}\left[379(1-\alpha_p)^2-726(1-\alpha_p)+348\right]$	$Re_p \sim 10$

Table 2.3. Empirical correlations of the drag coefficient as function of the particle concentration or particle volume fraction.

2.4.4 Experimental work of multiple spherical particles

Because a sphere is the simplest three dimensional shape of a particle, most of the studies of multiple particle systems have been based on spherical geometry or arbitrary shapes using shape factors based on a sphere, such as sphericity[1] in three dimensional objects or roundness[2] in two-dimensions. Very often, basic estimations

[1] Sphericity is defined as the ratio of the surface of an equivalent-volumetric sphere to the surface area of the non-spherical particle.
[2] Roundness is defined as the ration of the area of an equivalent circle to the area of the non-circular particle.

are made using theoretical or experimental results obtained from spherical particles, e.g., the BBO equation (2.37) has been derived from the assumption of a spherical particle. Figure 2.12, shows a typical microscope image and roundness plot of coal particles used in coal-fire power plants, the mean diameter of the coal particles in the image is around 108 μm. The microscope image and the roundness graph strongly support the study of dynamic particle-fluid-particle interactions based on spherical particles.

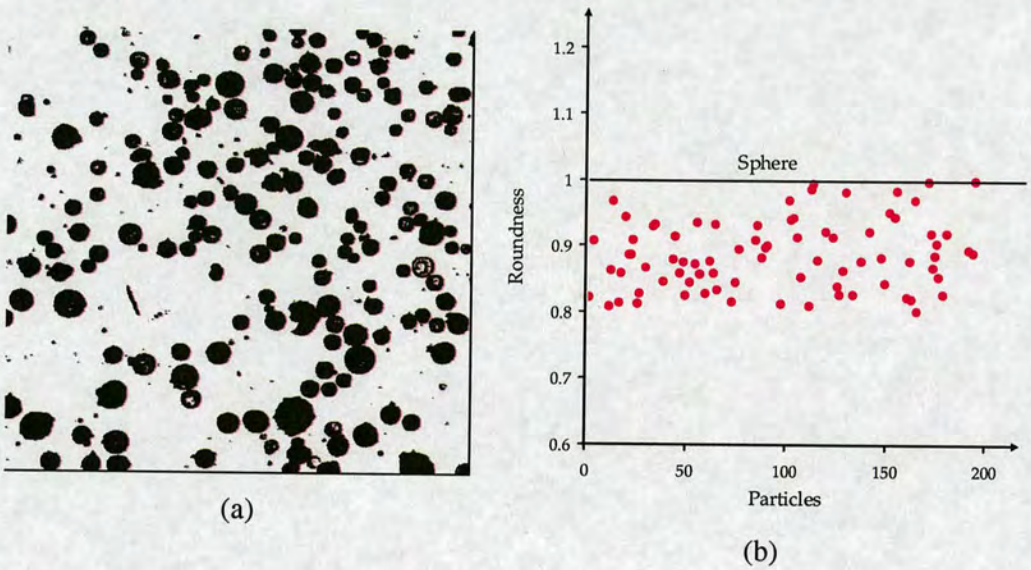

(a) (b)

Fig. 2.12 (a) Microscope image of typical coal particles used in coal-fire power plants and (b) Coal particles roundness.

It is worth mentioning that there are several important cases where the shape of the particles could be not consider as spherical, e.g., red blood cells and elongated bubbles in boiling processes. In these cases, it is common practice to treat the irregular particles in terms of shape factors. In those cases the application of theories obtained from numerical and experimental results using spherical particles can be considered only as a first approximation. The study of drag and lift coefficient of

irregular particles have been proposed by some authors as a function of equivalent diameter[3], Heider & Levenspiel (1989) and Chhabra *et al.* (1999).

Experimental work on the dynamics of multiple particles systems has been done because of the continuing development of laser, optical fibre and high speed cameras technology, such as fibre optic probes, Laser Doppler Anemometry (LDA), Particle Tracking Velocimetry (PTV), Phase Doppler Anemometry (PDA) and Particle Image Velocimetry (PIV), Crowe *et al.* (1998). The majority of experimental studies of multiple particle systems have been done in fluidised beds, free falling particles in containers, bubble columns, pneumatic transport and risers. Most of these works do not deal in depth with local information of individual particles but it is possible to measure the velocity, concentration, position and size of the particles in two-phase flows.

Richardson & Zaki (1954) studied experimentally the sedimentation and liquid-solid fluidisation of spherical particles with diameters greater than 100μm. Their experiments were mainly concerned with the calculation of the sedimentation velocity for a suspension – or fluidisation velocity in a liquid-solid system – as a function of the free falling velocity of a single particle and the concentration of particles, $u_m/u_s = (1 - \alpha_p)^x$, in a wide range of conditions. Rowe (1961) measured the drag on spheres arranged in a regular array. His results showed that the fluid velocity required to support a particle is extremely sensitive to the separation between the spheres. When the spheres are separated in the region of 100 diameters, local changes can occur with a small adjustment in the fluid velocity. Jayaweera *et al.* (1964) experimentally investigated the hydrodynamics of a small number of spheres falling through a viscous liquid for particle Reynolds number from 10^{-4} to 10. They found that clusters comprised of 2-6 spheres fall faster than a single sphere. The settling velocity was found to increase as the average inter-particle distance decreased, in the range of $10d_p$ to $5d_p$. Fortes *et al.* (1987) observed similar findings in columns of rectangular cross-sections at far higher particle Reynolds numbers from 270 up to 1800.

[3] Equivalent diameter of an irregular object is the diameter of a sphere of a equivalent volume.

The technological advances mentioned above also allow the simultaneous measurement of the particle size and velocity of the dispersed phase. This technology can measure the velocity of the continuous phase in the presence of the particles. In the last few decades a considerable amount of time has been devoted to experimental observations of the flow structure, particle velocity and particle concentration in two- and three dimensional two-phase flows. Nicolai *et al.* (1995) used a CCD video camera connected to a fast image processing and acquisition board, located in a personal computer operating with digital imaging software. They measured the particle velocity and particle velocity fluctuation at very low particle Reynolds numbers (~ 10^{-3}) for particle concentrations ranging from 0% to 40%. Jakobsen *et al.* (1996) presented a method using PIV to study pneumatic transport of solid particles. They measured both phases by isolating the measurements of each phase and they also calculated the global and local slip velocity. Delnoij *et al.* (2000) applied the PIV and a single CCD camera technique to study experimentally the two-phase flow in a pseudo-two-dimensional bubble column. Lee *et al* (2004) studied a pneumatic conveying system with a 90° bend. They employed three non-invasive instruments, Electrical Capacitance Tomography (ECT), Particle Image Velocimetry (PIV) and Phase Doppler Anemometry (PDA), to measure solid concentrations and velocity distributions. Losenno (2004) employed LDA, PIV and a single CCD camera to investigate experimentally the dynamics of streams of free falling spherical and irregular particles with mean diameters varying from 60 to 300μm. The particle Reynolds number was between 1 and 70. Particle concentration, particle velocities and velocity fluctuation were reported in this work. Datta *et al* (2007) estimated experimentally the particle velocity and the particle concentration in pneumatic transport using the Electrical Capacitance Tomography (ECT) and the Laser Doppler Anemometry techniques. Available works on dynamic interactions between two and three particles are described in chapter 3 and chapter 4, respectively.

2.4.5 Previous numerical work on multiple spherical particles

In the last two decades Computational Fluid Dynamics (CFD) has provided a very cost-effective way to perform studies investigating particle hydrodynamic behaviour in two-phase flows in most engineering and science disciplines. Generally, there are three main methods used to model two-phase flows. These are the Eulerian-Eulerian (Two-Fluid Model), Lagrangian-Eulerian (Eulerian-Lagrangian) and Direct Numerical Simulation (DNS), see e.g., Crowe *et al.* (1998), Kleinstreuer (2003), Michaelides (2006) and Tsuji (2007).

The Eulerian-Eulerian (E-E) method is called Two-Fluid Model (TFM) because the flow is assumed to consist of two kinds of fluid; one is the real fluid and the other represents the particles. This method is very popular today in the field of two-phase flows, not only in gas-solid flows, but also in gas-liquid and liquid-solid flows. From the mathematical point of view both fluids are modelled by similar equations of conservation and this is the main advantage of this approach. This method was first used for modelling fluidised beds by Gidaspow & Seo (1986). Later, many researchers tried to use this method in two-phase flows, especially in bubble columns, e.g., Zhan *et al.* (2007), Pan *et al.* (1999), Sokolichin & Eigenberger (1994), Greskott *et al.* (1996) and van Baten *et al.* (2005). The kinetic theory of granular flow (KTGF) has been considered using the TFM approach. In the kinetic theory, the constitutive equations in the particulate phase are deduced from equations of particle motion on the microscale. This situation is similar to the constitutive equations in the Navier-Stokes equation that are deduced from the Boltzmann equation of molecular gas. The Kinetic theory in two-phase flows has been applied successfully by several researchers, [Gidaspow (1994), Gidaspow *et al.* (2004), Jiradilok *et al.* (2007), Yu *et al.* (2007)]. Some work has been done in pneumatic transport using Eulerian-Eulerian approach by Lee *et al.* (2004).

In the Lagrangian-Eulerian (L-E) method the particles are tracked in space using Newton's second law, equations of motion. Equation of motion resulting from forces exerted on individual particles is solved to acquire the single particle trajectory. So a

large number of particles should be analyzed before concluding statistical data can be made. Of course the Lagrangian-Eulerian method is more realistic than the Two-Fluid approach but has a major drawback: due to the high number of particles in two-phase flows it is not possible to simulate large systems, large number of particles. In the L-E approach the fluid phase is considered as a continuum by solving the Reynolds time-averaged Navier-Stokes equations (RANS). A number of studies in different two-phase flow engineering and science areas have been performed using Lagrangian-Eulerian approach. These, among others, include the work in the prediction of particle dispersion and distribution in rooms done by Zhao *et al.* (2004), Zhang & Chen (2006), and Zhao *et al.* (2007). Yilmaz & Levy (2001) applied the Lagrangian-Eulerian method to study the formation and dispersion of ropes in pneumatic conveying. Sommerfeld (1992) and Sommerfeld & Huber (1999) used the Lagrangian-Eulerian approach to model particle-wall collision in confined gas-particle flows. Tsuji *et al* (1987) applied L-E to simulate gas-solid two-phase flow in a two-dimensional horizontal channel. Duchanoy & Jongen 2003 and Verdurmen *et al.* (2005) used the L-E approach for collisions and agglomeration of the dispersed phase in food industry.

Direct Numerical Simulations (DNS) have been rapidly adopted in the last decade. In DNS, the flow around each particle is solved based on the complete Navier-Stokes equation. The forces acting on the particles are estimated by integrating the normal and tangential stress over the surface of the particles, which are solutions of the basic equation. Thus the empirical coefficients associated with the drag and lift forces are not necessary. In DNS, the Navier-Stokes equations for the fluid motion and the equations of the particle motion are coupled through the no-slip condition on the particle boundaries, and through the hydrodynamic forces that appear in the equations particle motion. The hydrodynamic forces which arise from the computed motion of the fluid thus are not known in advance. So ideally, the DNS solutions should reproduce all the scales in the flow, from larger eddies to the Kolmogorov microscale eddies without resorting to empirical equations or simplifying assumptions. Some solutions techniques, such as the Finite Difference method (FDM), and the Finite Element method (FEM) are used in connection with the DNS.

Most of the applications of DNS are found where the particle inertial force is relatively small, and for this reason this approach is applied mainly to liquid-particle flows. One of the first studies using the DNS approach to model solid particles was that published by Hu *et al.* (1992), and bubble interaction simulations by means of DNS were first carried out in two- and three-dimensions by Unverdi & Tryggvason (1992a) and (1992b). Three main groups analysing multiphase flows using the DNS approach have been clearly identified: (1) The Daniel D. Joseph group of the University of Minnesota, Glowinski *et al.* (2001), Patankar *et al.* (2001), Choi and Joseph (2001), Pan *et al.* (2002), Joseph (2002), Patankar *et al.* (2002); (2) the Sanjoy Banerjee group in UC Santa Barbara, Pedinotti *et al.* (1992), Pan & Banerjee (1996 and 1997), Kaftori *et al.* (1998) and Badalassi *et al.* (2003) and; (3) the Grétar Tryggvason group at the Worcester Polytechnic Institute, Esmaeeli & Tryggvason (1998) and (1999), Tryggvason *et al.* (2001), Esmaeeli & Tryggvason (2005), Lu *et al.* (2006), Lu & Tryggvason (2006), Lu & Tryggvason (2007). Another researcher active in this area, -DNS in two-phase flows, - is Kajishima [Takiguchi *et al.* (1999), Kajishima *et al.* (2001), Kajishima & Takiguchi (2002) and Kajishima (2004)]. Tezduyar and co-workers using the finite-element and the deformable-space-domain/stabilized space-time (DSD/SST) formulation to fully couple the particle-fluid interactions have been involved in multiphase numerical simulations [Tezduyar *et al.* (1992a and 1992b), Johnson & Tezduyar (1996), Johnson & Tezduyar (1997) and Johnson & Tezduyar (1999)].

The Lattice-Boltzmann Method (LBM) and Direct Simulation Monte Carlo (DSMC) method have been applied recently in multiphase flows. The Lattice-Boltzmann Method has been successfully applied in multiphase flow by several researchers, Ladd (1994), Qi (1999), Qi (2000), Ladd & Verberg (2001), Hill *et al.* (2001a and 2001b), Han *et al.* (2007), Premnath and Abraham (2007), among others. DSMC has been effectively employed in cluster formations by Tanaka *et al.* (1996), Tsuji *et al.* (1998) and Shuyan *et al.* (2005). MC simulations have been successfully used by Castier *et al.* (1998) and Abreu *et al.* (1999) to study particle segregation in gravitational fields, using quasi-hard spheres applying a truncated form of the Lennard-Jones expression.

Variations and combinations of the approaches described above have been implemented in several computer codes, some of which are commercially available. Among these codes are FLUENT/FIDAD, developed by FLUENT Inc.; the CFX developed by AEA Technologies, CFD-2000 developed by Adaptive Research, CFD-2000 by Adaptive Research, PHOENICS by Concentration Heat And Momentum Limited (CHAM) and CFD-ACE+ developed by CFD Research Corporation (CFDRC). But due to excessive CPU time required to include a sufficient number of particles, multiple particle simulations is limited to cases where the particle number is relative small, especially in three dimensions where the full Navier-Stokes equation are solved, e.g. DNS. Currently, a few thousand particles is the maximum.

2.5 Conclusions

This chapter summarised the fundamental concepts, equations, experimental and numerical results attained for the motion of particles in two-phase flows. Present experimental and numerical results give important information on the global particle dynamic interaction in particle-laden flows. However, most of the present works use empirical or semi-empirical formulae and do not deal in depth with local hydrodynamic particle-fluid-particle interactions tree-way coupling-, mainly because of the complexity of these types of flow. Thus, local particle-fluid-particle hydrodynamic interactions in dispersed two-phase flows are required to gain a better understanding of these multiple particle systems.

CHAPTER 3

1 COMPUTER FLUID DYNAMICS SIMULATIONS: TWO FIXED SPHERICAL PARTICLES

This chapter presents the results of the Computational Fluid Dynamics (CFD) Simulations for particle-fluid-particle interaction in terms of drag (C_d) and interaction (C_i) coefficients on two fixed spherical particles placed at different relative positions of each other. The concept of the interaction coefficient (C_i) is based on the general idea of the lift coefficient. The particle positions are defined by the angles between the line connecting the centre of the particles and the main flow direction (θ) and the separation distance (D_o). Flow field structure is also presented in this chapter. The particle Reynolds number in these simulations is Re_p = 15. The results are compared to other available data from the literature.

3.1 Introduction

Two-phase systems are widely known as multiphase flow systems and are found in a wide range of industrial applications, such as the pneumatic transport of solid particles, which is extensively used in the chemical, food, mining, pharmaceutical and coal-fired power industries. In order to improve the efficiency of these applications, it is important to obtain a better understanding of the particle-fluid-particle interactions, where a three-way coupling takes place. Most of the industrial applications of pneumatic transport of particles operate at moderate particle

Reynolds numbers ($20 \leq Re_p \leq 300$), Prahl *et al.* (2007). However, in particle pneumatic systems, elbows and bends are essential components to change the direction of the multiphase flow to its final point within a limited space, but at the same time they are one of the most important factors affecting the flow distribution. Within the elbow the particles and the fluid segregate as a result of inertial forces, the particles move on to the outer wall of the elbow and form a relatively dense phase structure commonly referred to as a "rope", where the particles travel at lower velocity than the rest of the particles outside of this structure, so local low particle Reynolds numbers can be found in these configurations. For different elbow radius to pipe diameter ratios, fluid velocities, particle type, size, pipe roughness, and system configurations, McCluskey *et al.* (1989), Huber & Sommerfeld (1994), Yilmaz & Levy (1998), Schallert & Levy (2000), Yilmaz & Levy (2001), Akilli, *et al.* (2001 and 2005), Bilirgen & Levy (2001) and Yan & Kuan (2006) have reported typical particle Reynolds number in "rope" structures in the range of 9 to 30 in the main flow direction. In the coal-fired power industry, roping and agglomerated particles can continue for long distances after the elbow exit, causing a malfunction in splitter bifurcations and the final delivery; resulting in low efficiency in the burners, high levels of unburned coal and elevated rates of NO_x. These situations motivate the study of particle-fluid-particle interactions at low particle Reynolds numbers.

The study of the flow field around single spheres has been widely investigated both numerically and experimentally at different particle Reynolds numbers by several authors, e.g., Taneda (1956), Masliyah & Epstein (1970), Natarajan & Acrivos (1993); Johnson & Patel (1999); Tomboulides & Orszag (2000), Bagchi & Balachandar (2002), Yu *et al.* (2004). Three different flow regimes have been identified at moderate particle Reynolds numbers ($1 < Re_p < 300$), which is a representative range for industrial applications. In 1956, Taneda in his famous study of the wake behind a sphere at particle Reynolds numbers from 5 to 300 reported that for particle Reynolds number lower than 22 the flow is perfectly laminar, attached to the sphere and there is no visible recirculation behind it, but as the particle Reynolds number approaches to a value of 24, a steady state wake begins to form at the rear of the sphere. However, more recent studies have reported that the steady axisymmetric

recirculation zone occurs at $Re_p = 20$, see Masliyah & Epstein (1970), Johnson & Patel (1999) and Yu *et al.* (2004). At approximately $Re_p = 130$, Taneda (1956) observed that the wake behind the sphere begins to oscillate weakly at the tip of the wake, however the flow outside of the wake is perfectly laminar. Johnson & Patel (1999), Natarajan & Acrivos (1993) and Tomboulides & Orszag (2000) found that the axisymmetry of the wake is lost as the particle Reynolds number reaches a value of 210-212, but the flow stays stable. The beginning of the unsteadiness occurs at particle Reynolds number range of 270 to 300, Taneda (1956), Johnson & Patel (1999), Natarajan & Acrivos (1993) and Tomboulides & Orszag (2000). From these studies and particle Reynolds numbers, $Re_p < 270$, three flow regimes can be clearly identified: (a) unseparated flow for $Re_p < 20$, (b) steady axisymmetric flow with separation for $20 < Re_p < 210$, (c) steady non-axisymmetric flow for $210 < Re_p < 270$. For particle Reynolds numbers, $Re_p > 270$, an unsteady vortex shedding appeared. For a comprehensive report of flow regimes past a single spherical particle the reader is referred to the monographs of Clift *et al.* (1978) and Michaelides (2006).

Unfortunately in multiphase flows, when particle concentration comes up to a certain point the flow field characteristics based on flow past a single particle studies are not appropriate. In these flows the neighbouring particles (particle-fluid-particle interactions) become an important factor in determining the flow characteristics. To gain a better understanding of the particulate multiphase flows, clarification of particle-fluid-particle hydrodynamic interaction at high particle concentration as those found in the "roping" phenomenon is desired. However, in practice the hydrodynamic interactions between particles through the fluid in a region of high concentration is very complex because information about each particle's hydrodynamic interactions are needed. Because of the complexity of the multiphase flows, their experimental investigation is therefore not easy and the most recent non-invasive local techniques (PIV, LDA and HWA) are useless in most cases. Multiphase flow analysis requires dedicated measuring methods to get local and global data, Boyer *et al.* (2002) and Gharib et al. (2002). On the other hand, numerical methods to compute the hydrodynamic forces on each particle requires the

generation of a new mesh at each time step - if a particle is close to a wall or another particle a very fine mesh is needed in order to resolve the flow in this region. The methods used to fully resolve the flow around the particles, such as the direct numerical simulation, are computationally extremely expensive and the number of particles is limited, Lomholt et al., (2002) and Caboussat, (2005). Thus in order to accumulate a fundamental understanding of particle-fluid-particle interactions that take place locally, an alternative approach is the study of a small number of particles, starting with the simplest case of two interacting particles placed relative to each other.

Considering the flow past two particles at very low particle Reynolds numbers (Stokes regime), the first theoretical work has been reported by Smoluchowsky (1911, 1912) and later by Stimson & Jeffrey (1926), Kynch (1958) and Goldman *et al* (1966). A well documented theory of spherical particle's hydrodynamic interactions in the Stokes flow regime ($Re << 1$) can be found in the monographs of Happel & Brenner (1973), Kim & Karrila (1991) and Zapryanov & Tabakova (1999). Early experimental works that considered two particle hydrodynamic interactions were carried out by Evenson *et al.* (1959), Happel & Pfeffer (1960), Rowe & Henwood (1961), Jayaweera & Mason (1964), Taneda (1979), Tsuji *et al.* (1982) and Fortes *et al.* (1987). Numerical studies of two particle hydrodynamic interactions are relatively new, some of the first attempts have being made by Ivanov & Rivkind (1982, 1985) and Tal *et al.* (1983, 1984).

Recently, using experimental and numerical approaches, the study of flow past a small number of particles have been investigated by several researchers at different particle Reynolds numbers. Kim *et al.* (1993) studied numerically the three-dimensional flow over two identical solid and liquid spheres which are held fixed relative to each other. The centres of the particles are connected to a line perpendicular to the flow direction. The study was conducted for three particle Reynolds numbers Re_p = 50, 100 and 150. Their study was focused to the dependency of drag, lift and momentum coefficients as a function of particle separation ($2 \leq D_o \leq 25$). Folkersma *et al.* (2000), using the same configuration as

Kim *et al.* (1993), studied the particle interaction through the drag and lift coefficients for $Re_p = 10$ and 50. Folkersma *et al.* (2000), defined for the first time the forces directed along the line connecting the spheres centres as interaction forces and the coefficient resulting from the two spheres forces as the interaction coefficient. Brydon & Thomson (2001) and Schouveiler (2004) examined numerically the flow past two spheres placed side by side at $Re_p = 300$. They also both observed experimentally the wake interactions between the particles using dye injection. Legendre *et al.* (2003) studied numerically the three-dimensional flow past two identical spherical bubbles moving side by side at several separation distances in a viscous fluid. They imposed a zero-shear-stress condition over the bubbles. They described the hydrodynamic interaction between the two bubbles over a large range of particle Reynolds number ($0.02 \leq Re_p \leq 500$). Tsuji *et al.* (2003) simulated three-dimensional interaction between two fixed spherical particles, placed in tandem and side by side formations for particle Reynolds numbers 30, 100, 200 and 250. More recently, Shao *et al.* (2005) studied numerically and experimentally the interactions of two settling particles with different sizes with a initial separation of 5 particle diameters at $Re_p = 65$ and Prahl *et al.* (2007) presented a numerical study of the variation of the drag and lift coefficients of two fixed solid spherical particles placed at different positions relative to each other. The simulations were carried out for three particle Reynolds numbers: $Re_p = 50$, 100 and 200. Experimental work on hydrodynamic particle interactions has been done by some authors. Zhu (1994) measured the drag force of two interactive particles arranged in tandem for particle Reynolds numbers varying from 20 to 200 and conducted flow visualizations to characterize the flow phenomena. Liang *et al.* (1996) investigated experimentally the drag force for four different particle arrangements for $30 < Re_p < 106$. They also presented some numerical simulations for three particles arranged side by side. Chen & Lu (1999) studied experimentally the drag forces for two particles positioned parallel and perpendicular to the flow for particle Reynolds numbers ranging from 10 to 200. They also reported some measurement for three particles aligned side by side and aligned in a reversed "L" formation (┐). Later, Chen and Wu (2000) investigated experimentally the influences of a second sphere of different size, located at various distances and angles, on the drag force for particle Reynolds numbers in the range of

10 to 200. More recently, Zhang (2005) reported an extensive study of the effect of particles size ratio on the drag force on two particles parallel to the flow for $25 < Re_p < 51$.

From the studies described above important conclusions can be obtained. When two particles are held fixed in a side-by-side configuration, the drag force increases as the particle separation decreases. In addition, at very small particle separations, with the particles almost in contact, some authors have reported that the flow considers the particles as a single body due to the blockage effect, Folkersma *et al.* (2000) and Tsuji *et al.* (2003). As the particle Reynolds number is increased the drag coefficient also decreases, Kim *et al.* (1993) and Chen & Lu (1999). Kim at al. (1993) and Folkersma *et al.* (2000) found that the two particles are repelled by each other when they are close and, weakly attracted to each other at some intermediate separation distances which depend on the particle Reynolds number.

For two particles placed in a tandem formation, i.e., the particles are aligned with the main flow direction, low velocity region is found in front of the trailing particle due to the leading particle and because particle interactions, the leading particle will be subjected to a larger drag force than the trailing particle but even in this situation the drag force on the leading particle is smaller than the drag force on a single particle. As the trailing particle is placed further away, the drag force gradually levels to the value of an isolated particle.

Particles aligned with flow direction are not subjected to any lift force for Reynolds numbers less than 210 and axisymmetry flow, Prahl *et al.* (2007). However, for all other cases the lift force exists and contrary to the drag force, increases as the distance between the two particles decreases.

Most of the studies mentioned before agree that the particles' separation, their relative positions and the particle Reynolds number play an important role in determining the drag and lift forces acting on the interacting particles, which are the

main parameters to compute the particle interactive force between dynamic interacting particles.

In this study, special attention is given to the study of the hydrodynamic particle-fluid-particle interactions between two particles at low particle Reynolds numbers, focusing the attention on the drag and interaction coefficients in order to try to understand the role of the hydrodynamic particle interactions in the roping phenomenon. The separation and the relative position between the particles are the two free parameters involved in this research.

3.2 Numerical method and problem set up

In order to obtain detailed flow fields, pressure distribution, drag and interaction coefficients for three-dimensional flow past two solid identical spherical particles with a diameter, d_p = 100μm, a commercial computational fluid dynamics (CFD) program, FLUENT V6.2.16 is used. The particles are held fixed relative to each other at different positions; separations distances ($1.1 \leq D_o \leq 25$) and angles ($0^o \leq \theta \leq 90^o$) with respect to the main flow direction. In this study the fluid is air at standard conditions ($\rho_a = 1.225 \text{kgm}^3$, $\mu_a = 1.7894 \text{x} 10^{-5} \text{kgm}^{-1}\text{s}^{-1}$) moving with a velocity chosen to give a particle Reynolds number equal to 15. The problem is schematically represented in Figure 3.1. The origin of the coordinate system (0, 0, 0) is located at the centre of the numerical box domain midway between the line connecting the centre of the particles. The two spherical particles are contained in the x-y plane (z = 0). The separation distance (l) between the centres of the particles is normalized by the diameter of the particle (d_p) and it is denoted by D_o. The angle (θ) represents the particles' position with respect to the main flow direction, when aligned with the y-axis ($\theta = 0^o$). The particle located upstream is named as the leading particle (particle 1) and the particle placed downstream is called the trailing particle (particle 2). In order to avoid any wall interactions, the wall boundary conditions of the domain box are located at least 24 particle diameters from each particle. Thus, the geometrical

domain box's sides are set to (x, y, z) = ($49d_p + D_o$ Sin θ, $49d_p + D_o$ Cos θ, $49d_p$), for example, at the maximum particle distance separation between particles ($D_o = 25$) for $\theta = 90^o$, the domain size results in a box of $74d_p$ x $49d_p$ x $25d_p$, which gives a box of 7.4 x 4.9 x 2.5 mm^3.

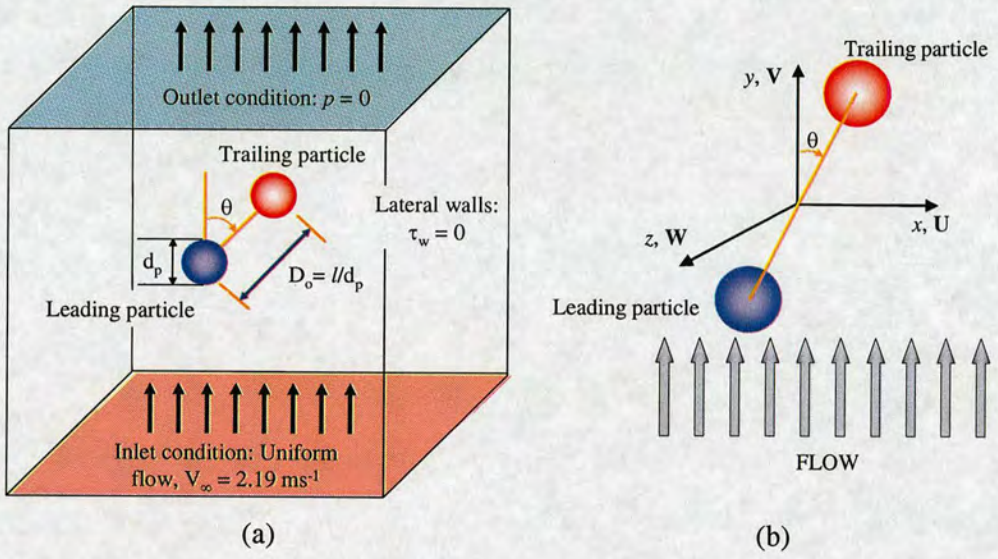

Fig. 3.1 Two fixed spherical particle set up, (a) numerical domain and initial conditions (b) coordinate system origin.

The program FLUENT uses the finite volume method, and the continuity and momentum equations are solved for steady, laminar, axisymmetric, incompressible flow. As the particle Reynolds number is less than 20, unseparated ($1 < Re_p < 20$) flow is studied. For steady, laminar incompressible flow the continuity and momentum equations take the forms:

$$\nabla \cdot \mathbf{U} = 0 \tag{3.1}$$

$$\rho(\mathbf{U}\cdot\nabla)\,\mathbf{U} = -\nabla p + \mu\nabla^2\,\mathbf{U} \tag{3.2}$$

where **U** is the velocity vector and p is the pressure.

The boundary conditions of the system consist of constant uniform flow velocity distribution at the inlet boundary ($U_y = V_\infty = 2.19$ m/s, $U_x = U = 0$ and $U_z = W = 0$), zero-shear-stress at lateral wall boundaries and zero-pressure at the outlet boundary. A non-slip condition is employed over the surface of the leading and surrounding particles.

In order to accurately determine the forces over the spherical particles, FLUENT uses a body fitted coordinate system. The body fitted coordinate system is commonly used for complex geometrics because it better approximates the surfaces. A non-uniform grid system is used in order to minimize the number of cells while maintaining a sufficient degree of accuracy in the solution. Very high grid density close to the particle surfaces was used. The high grid density was created by using a size function in the mesh generation program GAMBIT, which allows you to control the mesh characteristics and potentially reduce number of the cells. The size function has three main parameters: (a) start size, which determines the size adjacent to the spherical particle ($0.01d_p$); (b) growth rate, this parameter determines the ratio of two adjacent mesh-element edge size (1.2) and (c) the size limit, which is the maximum allowable size for the cells ($3d_p$). By using this size function and the Tetrahedral/hybrid (Tet/hybrid) meshing scheme, the entire numerical domain contains around 7×10^5 cells. Figure 3.2(a) shows a slice (cross-subsection) of the numerical domain in the x-y plane for two particles at 45^o and $D_o = 4$. Figure 3.2(b) shows the very high resolution mesh (0.1% of the particle diameter) over one of the two spherical particles.

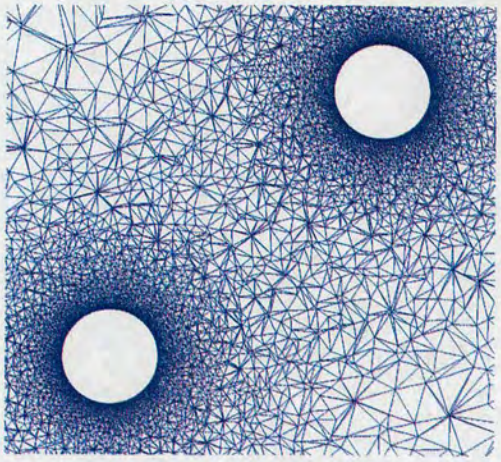

(a)

b)

Fig. 3.2 The grid distribution (a) cross-subsection in the x-y plane and (b) very fine mesh resolution over one of the spherical particles' surface is shown.

Flow governing equations are solved by FLUENT using a three-dimensional (3D) steady flow, implicit segregated method and laminar flow settings. A control-volume-based technique is used to solve the conservation equations for mass and momentum. A second order discretization scheme is used to obtain the flow field around the spherical particles. In this study the pressure-velocity coupling algorithm SIMPLE is used. The calculations are made using the laminar viscous model.

3.3 Results

The results obtained in this study are compared to numerical and experimental data reported in the literature. In §3.3.1 the code validation is treated, in §3.3.2 flow field velocity structure is explained, in §3.3.3 pressure coefficients are presented, in §3.3.4 wall shear stresses are described and in sections §3.3.5 and §3.3.6 drag and interaction coefficients are discussed in detail.

As mentioned before, to study the particle-fluid-particle hydrodynamic interactions in complex multiphase flow systems, numerical simulations of two equal spherical

particles are carried out. Flow field velocity, pressure and wall shear stress contours; streamwise velocity profiles and drag and interaction coefficients are presented in detail in this section to highlight the important role that the particle-fluid-particle hydrodynamic interactions play in the "roping" phenomenon and in general in the two-phase flow at low particle Reynolds numbers. The streamwise velocity profiles are taken at $0.5d_p$ from the surface of the particle and y = 0. The qualitative and quantitative information is presented only for $D_o = 3$ and $\theta = 0^o$, 45^o and 90^o. Complete information for these three cases can be found in the appendix to chapter 3.

Because of flow symmetry in the z plane and in order to illustrate better the flow structure, only the x-y plane is considered. The centre of two fixed spherical particles are contained in the x-y plane at z = 0; hence the strongest interactions occurred within this plane. Figure 3.3 shows an x-y plane of the entire numerical domain with an intersection at z = 0. The dashed lines show the leading (x_L, y_L) and trailing particle (x_T, y_T) coordinates and the continuous lines stand for the origin of system.

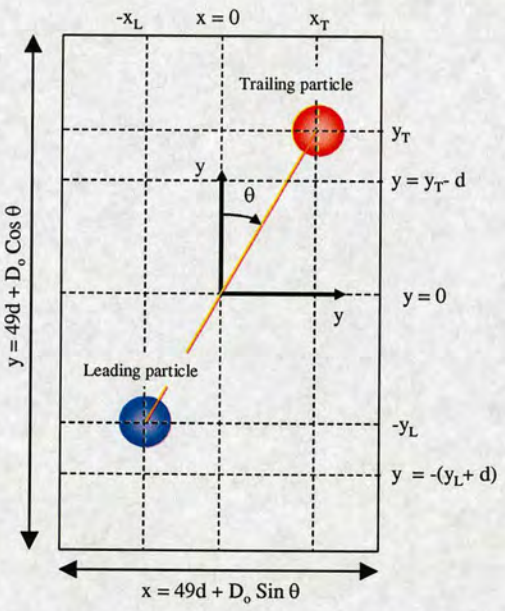

Fig. 3.3 Geometrical (x-y) plane domain for two fixed particles, the intersection of the plane is taken at z = 0.

3.3.1 Code verification

In order to validate the code under our specific geometry and flow conditions the grid dependency and accuracy is verified. First, the grid density independence of the numerical simulation results is verified by several simulations of flow past a single spherical particle with different size functions varying the growth rate parameter (GR). The growth rate in a size function is the factor that determines the density close to the entity; it represents the increase in mesh-element edge length with each succeeding layer of elements; e. g., a growth rate of 1.2 results in a 20% increase in mesh-element edge length with each succeeding layer element. The form drag (C_{dp}), friction drag (C_{df}) and the total drag coefficients (C_d) as a function of grid density for particle Reynolds number, $Re_p = 15$, are given in table 3.1. The form drag coefficient and the friction drag coefficient are defined as

$$C_{dp} = \frac{F_p}{\frac{1}{2}\rho V_\infty^2 \pi \left(\frac{d_p}{2}\right)^2}; \quad C_{df} = \frac{F_f}{\frac{1}{2}\rho V_\infty^2 \pi \left(\frac{d_p}{2}\right)^2} \tag{3.3}$$

where F_p is the form drag force[4] and F_f is the friction drag force[5] over the particle.

Growth Rate	C_{dp}	C_{df}	C_d
1.5	1.275	2.291	3.566
1.3	1.257	2.281	3.538
1.2	1.260	2.276	3.536
1.1	1.249	2.270	3.519
1.05	1.2485	2.2695	3.518

Table 3.1 Drag coefficients over a single particle at $Re_p = 15$, as function of growth rate.

[4] The form drag force is generated by the normal stress (mostly pressure) acting on the surface body
[5] The friction drag force is produced by viscous shear stress acting tangentially to the surface of the body

The C_d variation between GR = 1.05 and GR = 1.2 is less than 1%. GR = 1.2 is employed in this study, because the number of cells is significantly reduced and good relative accuracy is maintained.

Secondly, with the grid density selected (GR = 1.2) the numerical code is verified by comparing the drag coefficient of a single spherical particle for particle Reynolds number ranging from 1 to 100. The results are plotted in the graph shown in Figure 3.4. The difference between the results obtained in this work and those reported by other authors on the drag coefficients for a single sphere are in a very good agreement, with a systematic error of less than 5% in the whole range.

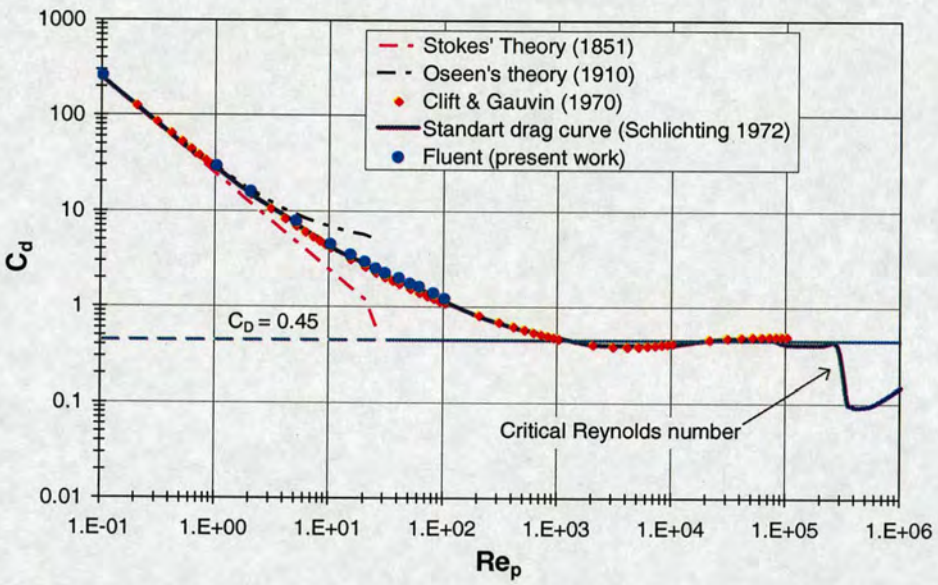

Fig. 3.4 Drag coefficients of a single sphere as a function of Re_p.

3.3.2 Velocity flow field structure

In order to illustrate the flow structure found with two fixed interacting particles flow field velocity contours and streamwise velocity profiles are presented in this section. The general idea is to illustrate how the flow reaching the trailing particle is modified

by the leading particle at low particle Reynolds numbers, measure the modified form and shear drag forces. The streamwise velocity profiles are normalised with the upstream uniform constant velocity ($V_\infty = 2.19ms^{-1}$). In general, the flow structure shows a clear influence of the leading particle over the trailing particle through the particle-fluid-particle interactions, moreover the flow structure highlights the influence of the particle position on the particle-fluid-particle interactions.

Figure 3.5 shows the velocity flow field contours and streamwise velocity profiles for an angle $\theta = 0^o$ and separation $D_o = 2$. Figure 3.5(a) clearly reveals qualitatively the low velocity zone between the two particles. Figure 3.5(b) illustrates quantitatively the same fact. In this case, the velocity reduction at 0.5d upstream of the trailing particle surface with respect to the leading particle is around 90%, but in general for larger separation distances this value decreases until it reaches a value of around 5% for $D_o = 25$. For two particles aligned with the flow ($\theta = 0^o$), the velocity profile of the leading particle at 0.5d shows a minimal difference compared to that of a single particle. Figure 3.6 displays the velocity flow field contours and the streamwise velocity profiles for $\theta = 45^o$ and $D_o = 2$. Figure 3.6(a) shows slightly high velocity between the particles. Figure 3.6(b) gives an idea about the velocity difference in front of the particles at $0.5d_p$, in this case the velocity that reach the trailing particle at $0.5d_p$ close to $\theta = 180^o$ is approximately the same as the leading particle. But due to the interference of the leading particle the velocity profile at the left side of the trailing particle suddenly decays and significantly differs from that of a single particle. Figure 3.7 shows the results for $\theta = 90^o$ and $D_o = 2$. The velocity contours in Figure 3.7(a) show basically the same velocity contours in front of the two particles at 0.5d. High velocity between the particles is observed. As a result of this a clear "nozzle-effect" between the two particles is found. The nozzle effect is responsible for the high local velocity between the particles because flow tries to pass trough the small gap between particles. In order to illustrate quantitatively the relatively high velocity between particles the streamwise velocity profile at $y = 0$ (centre of the particles) is also presented in Figure 3.7(b). The relatively high velocity between the particles is just under the upstream constant velocity ($\sim 0.98V_\infty$).

In general the fluid flow field and the velocity profiles clearly illustrate the hydrodynamic interaction between the two particles, and also show how the leading particle modifies significantly the flow that reaches the trailing one. Without any doubt, particle-fluid-particle hydrodynamic interactions change the pressure and wall shear stress distribution on the particle surfaces. These two factors will be discussed in detail in the next two sections (§3.2.2 and §3.2.3) by means of pressure and wall shear stress[6] coefficients, respectively.

[6] Wall shear stress coefficient is sometimes referred to as skin wall coefficient.

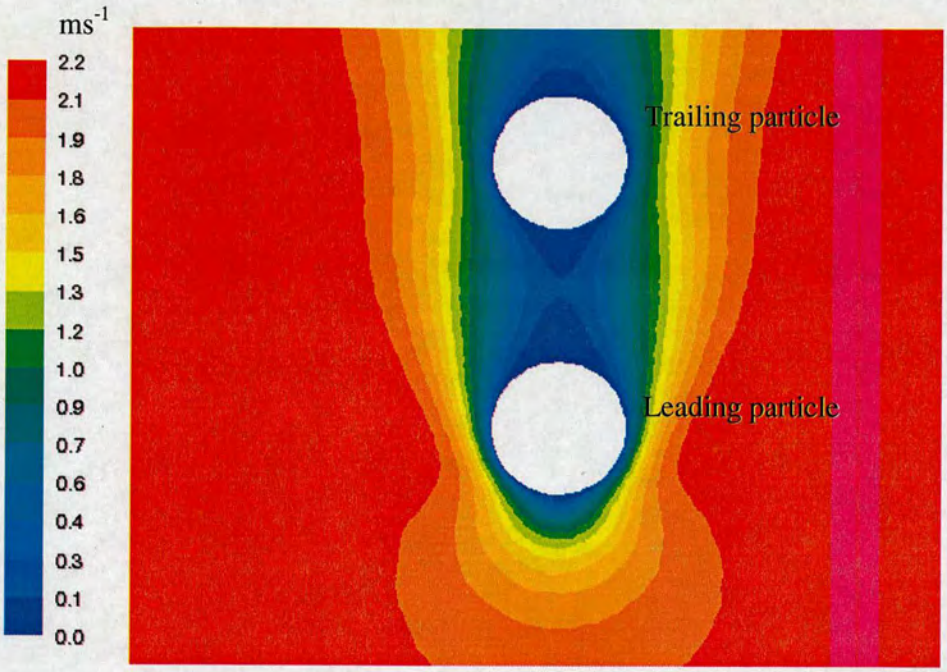

(a)

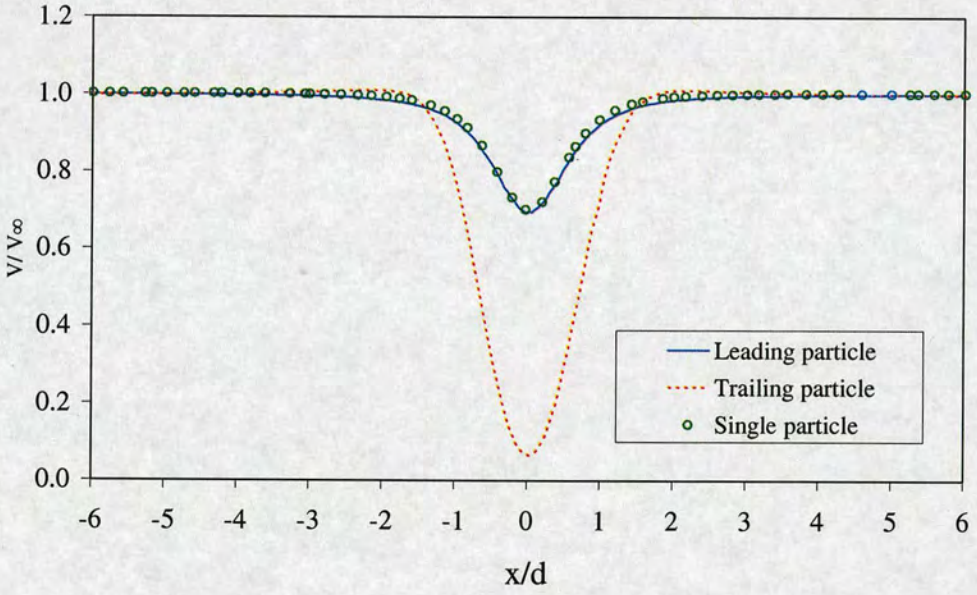

(b)

Fig. 3.5 Two fixed spherical particles separated at $D_o = 2$ and $\theta = 0^o$, (a) velocity flow field contours and (b) streamwise velocity profiles.

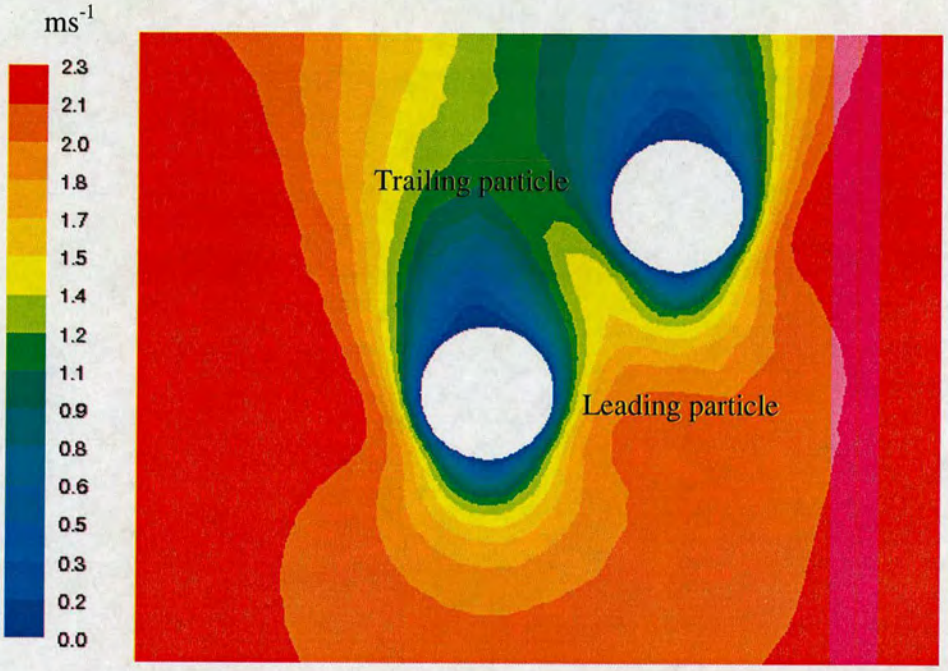

(a)

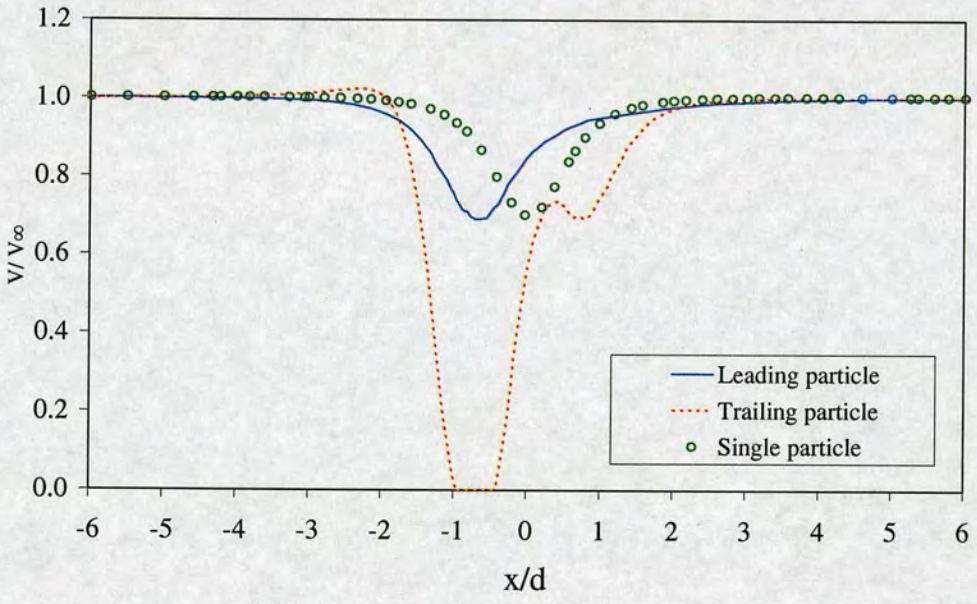

(b)

Fig. 3.6 Two fixed spherical particles separated at D_o = 2 and θ = 45°, (a) velocity flow field contours and (b) velocity profiles.

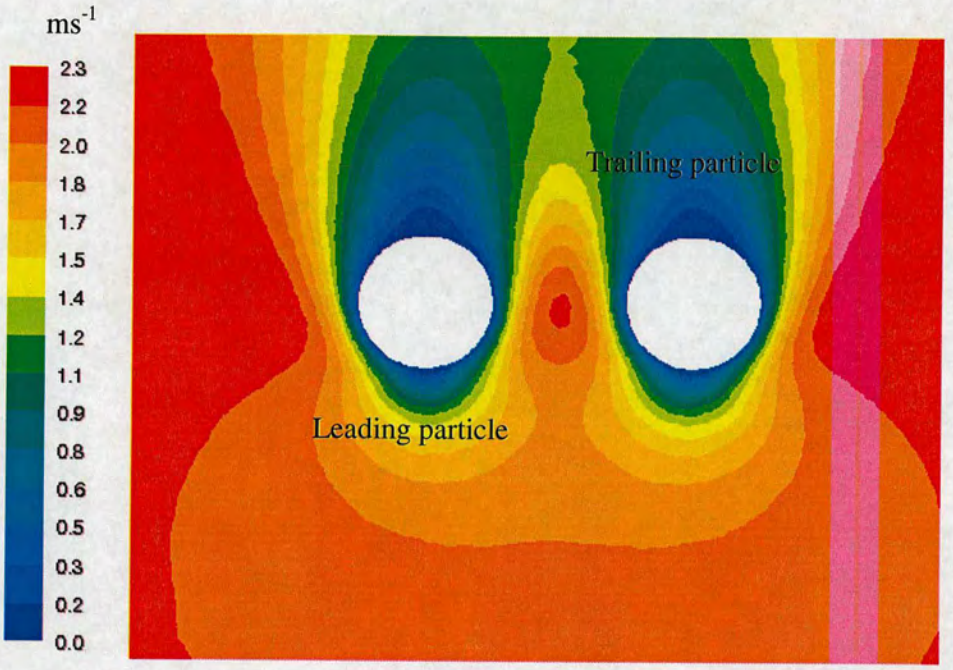

(a)

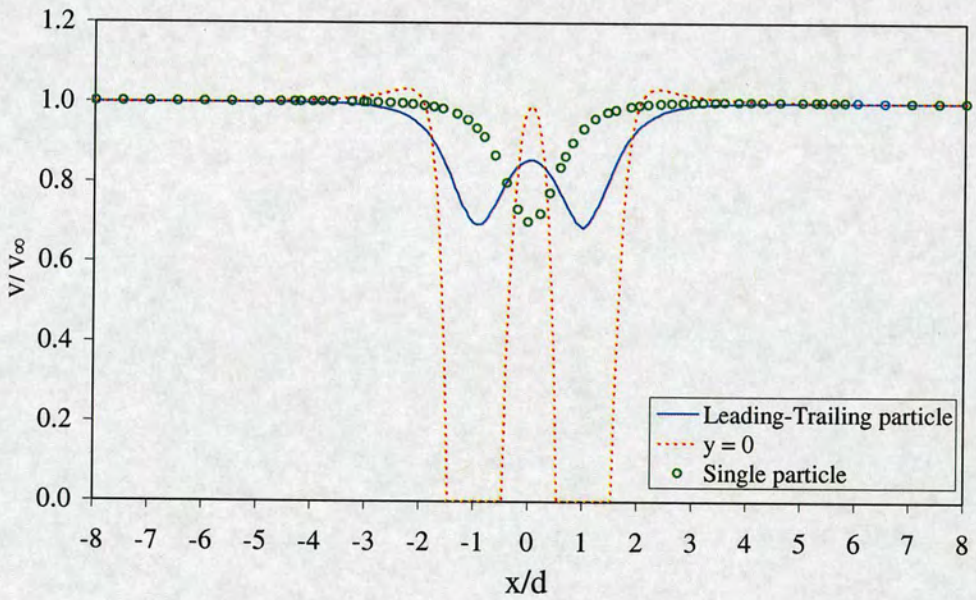

(b)

Fig. 3.7 Two fixed spherical particles separated at D_o = 2 and θ = 90°, (a) velocity flow field contours and (b) velocity profiles.

3.3.3 Pressure coefficients

For low Reynolds numbers pressure and viscous forces are the two dominant forces acting on immersed objects in a fluid flow, and most of the time pressure and viscous forces around particles surface are presented as pressure coefficient (C_p) and wall shear stress coefficient (C_s), respectively. The pressure coefficient, C_p, can be calculated in a dimensionless form by:

$$C_p = \frac{p - p_\infty}{\frac{1}{2}\rho V_\infty^2} \tag{3.4}$$

where the term p represents the pressure at the particle surface, p_∞ is set as the pressure reference far away from the particles ($p_\infty = 0$), ρ is the fluid density and V_∞ is the upstream constant velocity.

Contour plots and profiles of pressure coefficients around the particles for the same cases described in the above section (§ 3.3.2) are represented for the flow velocity field. The pressure profiles are presented as a function of the angle (α) around the particle. The angle (α) is set to zero at the downstream stagnation point as shown in Figure 3.8. The pressure coefficient profile for a single particle is also presented for reference.

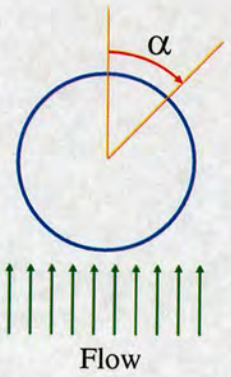

Fig. 3.8 The angle (α) around a particle in the x-y plane.

Figure 3.9 shows the pressure coefficient contours and the pressure coefficient profiles around two particles arranged in tandem ($\theta = 0^o$) for $D_o = 2$. Significant influence of the leading particle on the pressure forces acting on the trailing particle is clearly observed in Figure 3.9. However, the influence of the trailing particle over the leading particle is relative small. For this specific case the pressure coefficients over the leading particle is only around 10% smaller than the pressure coefficients for a single particle, whereas the difference between the maximum pressure coefficient for the trailing particle compared with the pressure coefficient for that of single particle is around 84% smaller. Due to the particle arrangement in this specific case, the higher pressure for the leading particle is found close to $\alpha = 180^o$, but the higher pressure for the trailing particle is found at two different values of α, 148^o and 212^o, respectively. The pressure profiles of the two particles show higher pressure compared to that of the single particle in the ranges of $0^o < \alpha < 118^o$ and $242^o < \alpha < 360^o$.

Figure 3.10 depicts the pressure contour and pressure profiles coefficients when the two particles are at $\theta = 45^o$ and $D_o = 2$. Figure 3.10(a) shows that the two particles experience almost the same pressure close to $\alpha = 180^o$, however as shown in Figure 3.10(b) the leading particle experiences a slightly higher pressure (~ 3%). Our results show that in this particular particle arrangement the stagnation point pressure for the

trailing particle is slightly shifted from $\alpha = 180^{o}$, due to the particle-fluid-particle interaction and is located at $\alpha \sim 176^{o}$. However the stagnation point pressure for the leading particle remains very close to $\alpha = 180^{o}$. Compared to the single particle, the leading particle shows high pressure for $0^{o} < \alpha < 110^{o}$ and $260^{o} < \alpha < 360^{o}$. The trailing particle shows lower pressure between 176^{o} and 260^{o}. Slightly higher pressure is observe in the range $260^{o} < \alpha < 360^{o}$ for the trailing particle.

A basic arrangement when studying interactive particles is the side by side configuration as show in Figure 3.11. In side by side formation the pressure coefficient over the two particles is basically the same, but due to the partial blockage of the flow in the space between the spheres as show in Figure 3.7, the front stagnation point pressure of the two spheres is shifted away from the stagnation point pressure of a single particle a few degrees ($\sim 5^{o}$) to the left side for the leading particle and to the right side for the trailing particle. Thus, the higher pressure over the leading particle is found at $\alpha \sim 175^{o}$, whilst the higher pressure point over the leading sphere is found at an angle $\alpha \sim 185^{o}$. Another important characteristic of this particular arrangement, due to the high velocity between the particles, is the slightly higher pressure found between 60^{o} and 186^{o} for the leading particle compared to that of the trailing particle and the higher pressure for the trailing particle compared to that of the leading particle between the range of 186^{o} and 300^{o}.

In general, due to the hydrodynamic particle-fluid-particle interactions the two particles experienced a smaller pressure force at the upstream stagnation point than the pressure force found over a single particle for small separation distances. But this depends on the relative angle (θ), so the particles exhibit different characteristics, e.g., pressure magnitude and stagnation point pressure positions, as a function of the relative particles' positions.

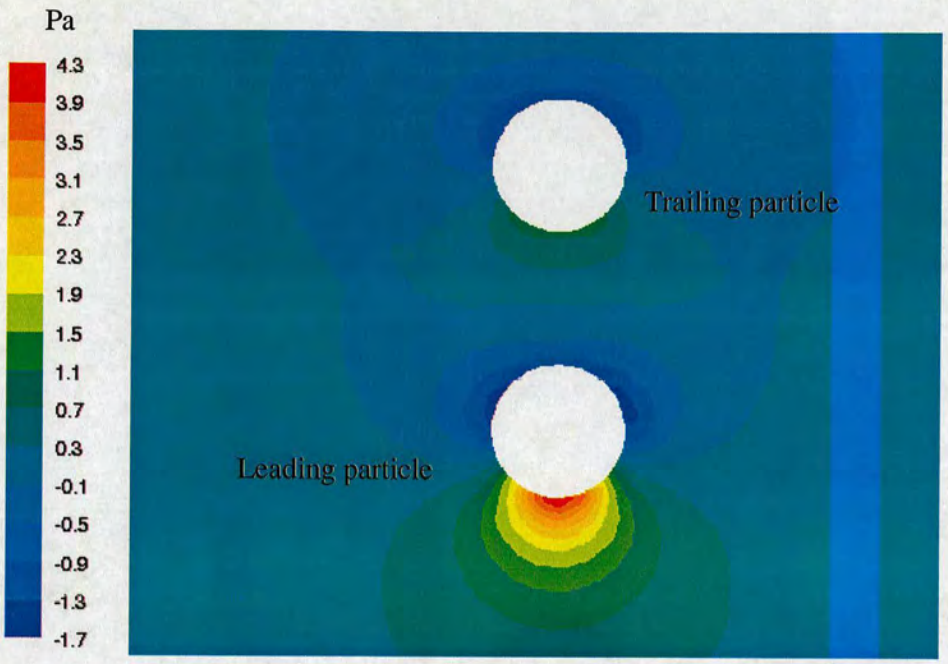

(a)

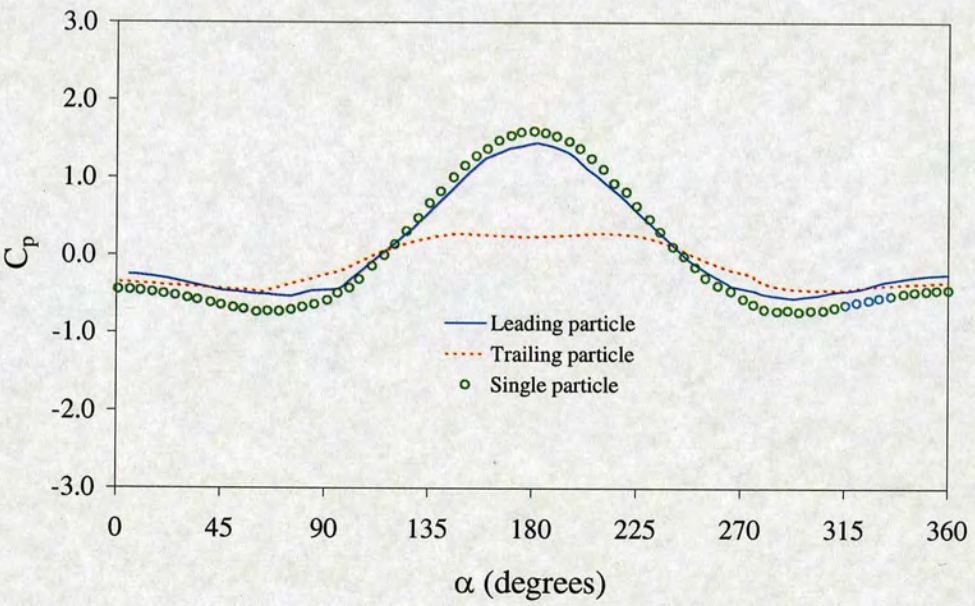

(b)

Fig. 3.9 Two fixed spherical particles at $D_o = 2$, $\theta = 0^o$ and $Re_p = 15$, (a) pressure coefficients contours and (b) profiles.

(a)

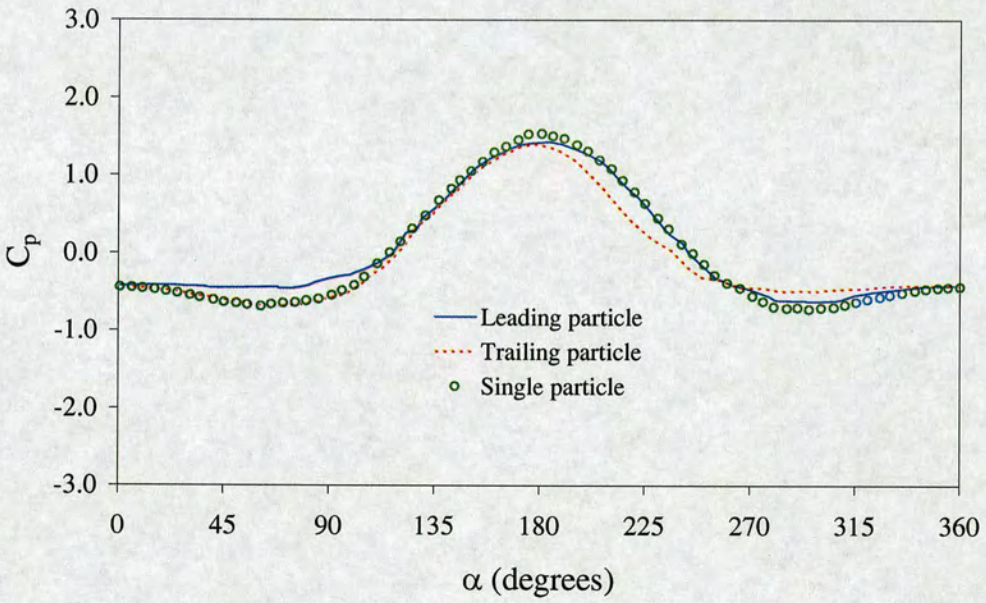

(b)

Fig. 3.10 Two fixed spherical particles at D_o = 2 and θ = 45° (a) pressure coefficients contours and (b) profiles.

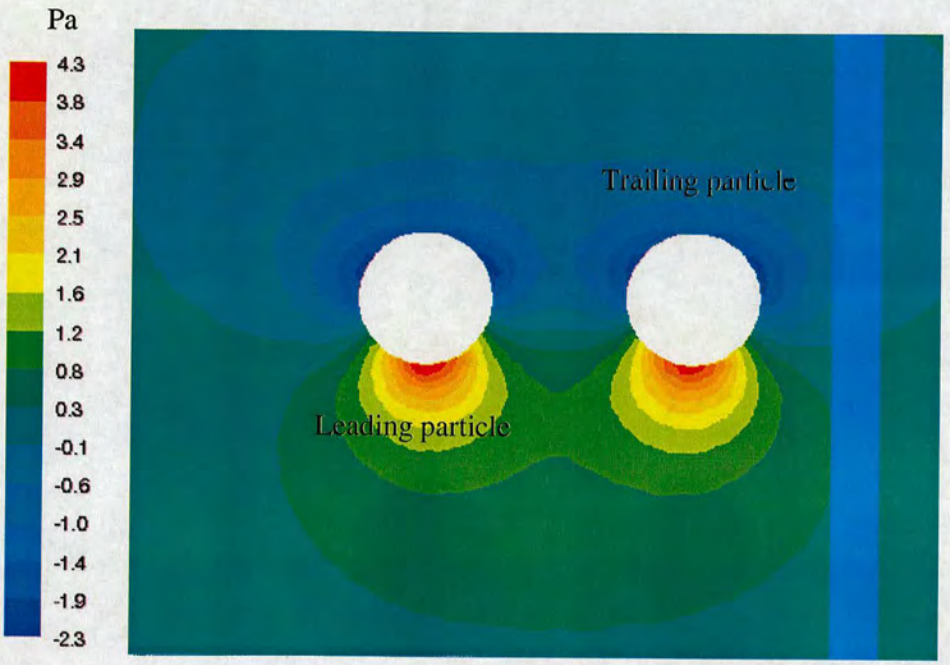

(a)

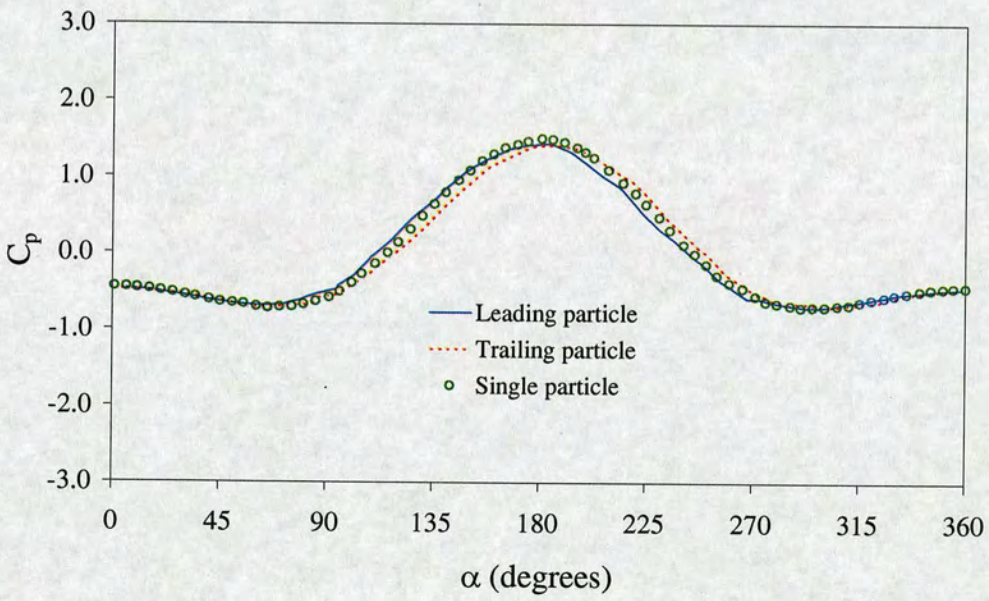

(b)

Fig. 3.11 Two fixed spherical particles at D_o = 2 and θ = 90° (a) pressure coefficients contours and (b) profiles.

3.3.4 Wall shear stress coefficients

Similarly to the velocity flow characteristics and pressure coefficients presented in the above sections (§3.2.1 and §3.2.2), wall shear stress forces are presented in figures 3.12, 3.13 and 3.14, in terms of wall shear stress coefficients, C_s. Viscous force along with the pressure force are the forces acting over an object when this object is immersed in a fluid flow under specific characteristics, e.g., laminar, steady flow. The wall shear stress coefficients are due to viscous shear forces produced at the particle surface. Moreover, for low Reynolds numbers, which is our case of study, the viscous shear force is larger than the pressure force. The skin friction or wall shear stress coefficient, C_s, can be expressed in a dimensionless form by:

$$C_s = \frac{\tau_w}{\frac{1}{2}\rho V_\infty^2} \tag{3.5}$$

where the term τ_w stands for the shear wall stress at the particle surface, ρ is the fluid density, V_∞ is the upstream constant velocity.

Figure 3.12 depicts the wall shear stress coefficients contours and profiles for $\theta = 0^o$ and $D_o = 2$. Figure 3.12(a) shows that the wall shear stress coefficient for the leading particle is significantly higher than the wall shear stress coefficient of the trailing particle, but also from Figure 3.12(b) it can be observed that the wall shear stress distribution over the particles is significantly different from one to the other due to the particle-fluid-particle interaction. When the leading and trailing spheres' profiles are compared to each other, higher wall shear stress coefficients between $70^o < \alpha < 290^o$ for the leading particle are found and slightly higher wall shear stress coefficients for the trailing particle in the ranges $0^o < \alpha < 70^o$ and $290^o < \alpha < 360^o$ are observed.

Compared with the single particle wall shear stress coefficient, the trailing particle's wall shear stress coefficient is around 37% smaller than that of the leading particle,

whilst the wall shear stress coefficient of the leading particle is just 3% under the wall shear stress coefficient of a single particle. The maximum values of the wall shear stress coefficients for the two particles are located at $\alpha = 120^{o}$ and $\alpha = 240^{o}$ for the leading particle and for the trailing particle are at $\alpha = 98^{o}$ and $\alpha = 260^{o}$. The minimum value of the wall shear stress (at $\alpha = 180^{o}$) for the trailing particle compared with that one of a single particle is practically the same. However, the minimum value of the wall shear stress coefficient (at $\alpha = 180^{o}$) for the leading particle shows a slight difference compared with that one of the single particle.

Figure 3.13 shows the wall shear stress friction coefficient of two spherical particles placed at $\theta = 45^{o}$ and $D_o = 2$. Figure 3.13(a) illustrates the wall shear stress coefficient contours, this picture depicts graphically how the wall shear stress forces are distributed over the two particle surface, some differences can be observed form figure 3.13(a), high wall shear stress at opposite sides is observed. The downstream stagnation point wall shear stress is shifted from $\alpha = 0^{o}$, for the leading particle is found at $\alpha \sim 257^{o}$ (shifted to left), whilst for the trailing one is located at $\alpha \sim 5^{o}$ (shifted to right). Figure 3.13(b), clearly show this differences, e.g., the highest wall shear stress coefficient is found at $\alpha \sim 232^{o}$ and $\alpha = 116^{o}$ for the leading and trailing particle respectively. Both the leading and trailing wall shear stress coefficient profiles are slightly higher than the single particle in some regions, the wall shear stress from the leading particle is slightly higher in some regions $0^{o} < \alpha < 75^{o}$ and $180^{o} < \alpha < 232^{o}$, the wall shear stress from the trailing particle is slightly higher between $\alpha = 170^{o}$ and $\alpha = 220^{o}$.

Wall shear stress coefficients for two particles placed side by side at $D_o = 2.0$ are presented in Figure 3.14. Figure 3.14(a) displays wall shear stress coefficient contours over the particle and 14(b) depicts the wall shear stress coefficient profiles around the particles. The leading and trailing particles show basically the same wall shear stress characteristics between them which are very similar to those found for a single particle, however, slight differences can be found. First, the upstream stagnation point, as pointed out in figure 3.11(b) for pressure coefficients, is shifted

from that of single particle. The upstream stagnation point is at $\alpha = 178^{o}$ and $\alpha = 182^{o}$ for the leading and trailing particles, respectively. Secondly, the shear stress at the single particle surface is still a bit higher (~ 5.5%) than the shear stress over the leading and trailing particles. Finally, a higher wall shear stress at the leading particle surface can be found in two different regions ($25^{o} < \alpha < 130^{o}$) and ($180^{o} < \alpha < 220^{o}$), whilst high wall shear stress can be found for the trailing particle between ($130^{o} < \alpha < 180^{o}$) and ($220^{o} < \alpha < 335^{o}$).

In general, the stagnation points of the wall shear stress coefficients are located at different positions depending on the particle arrangement. The wall shear stress profiles show that at $\alpha = 180^{o}$, the magnitude of the wall shear stress differs from zero for all cases shown here. For all cases the maximum values of the wall shear stress coefficients of the two interacting particles are slightly lower than that of the single particle.

From the information obtained from velocity flow field structure, velocity profiles, pressure coefficients and wall shear stress coefficients profiles, it appears that pressure and viscous forces are influenced by the particles relative position and as a result of this; the particle-fluid-particle hydrodynamic interactions play an important role in relatively dense two-phase flows.

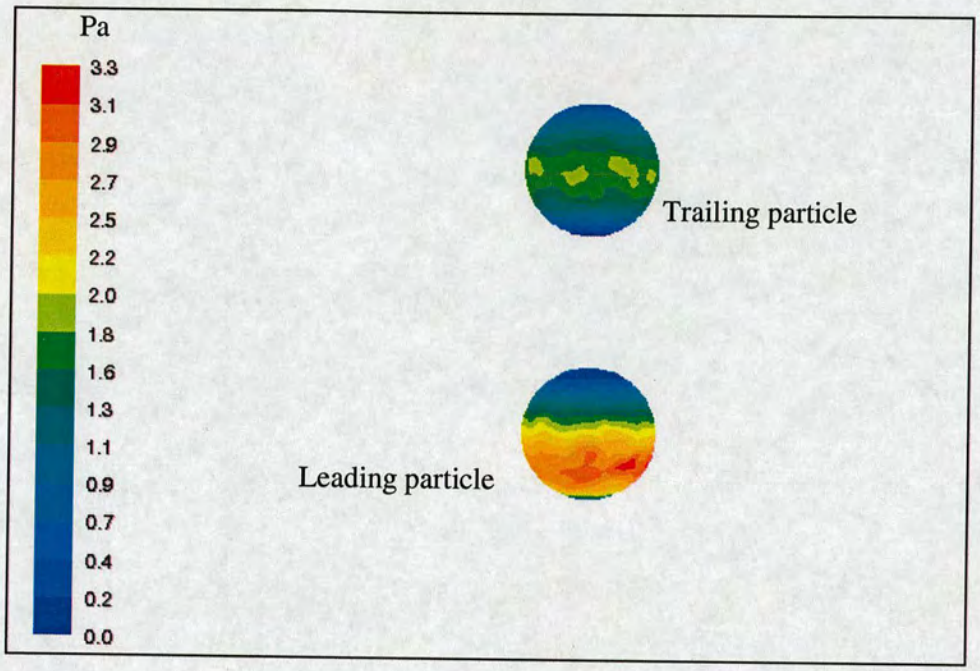

(a)

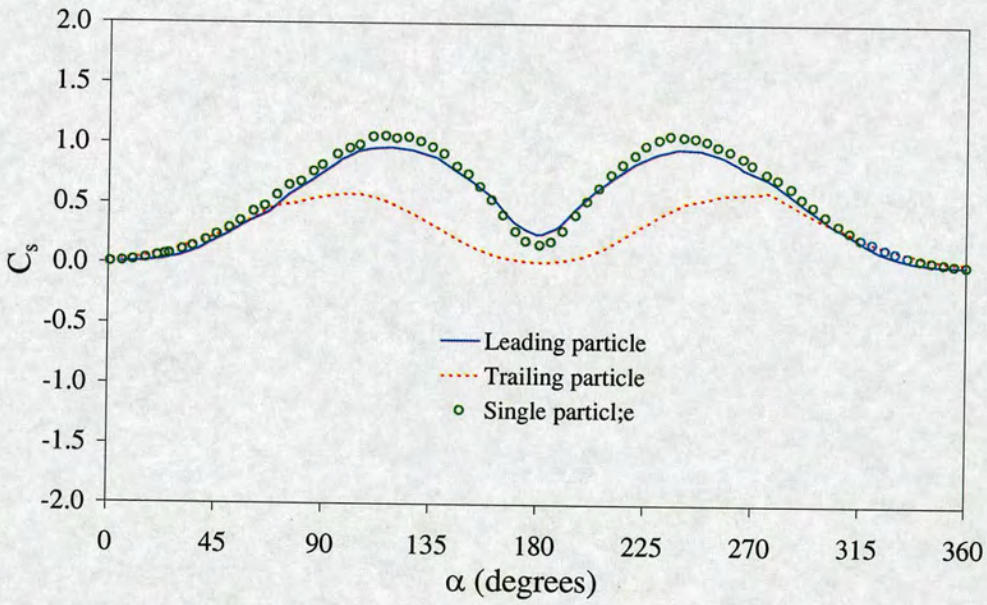

(b)

Fig. 3.12 Two fixed spherical particles at $D_o = 2$ and $\theta = 0^o$ (a) skin coefficients contours and (b) profiles.

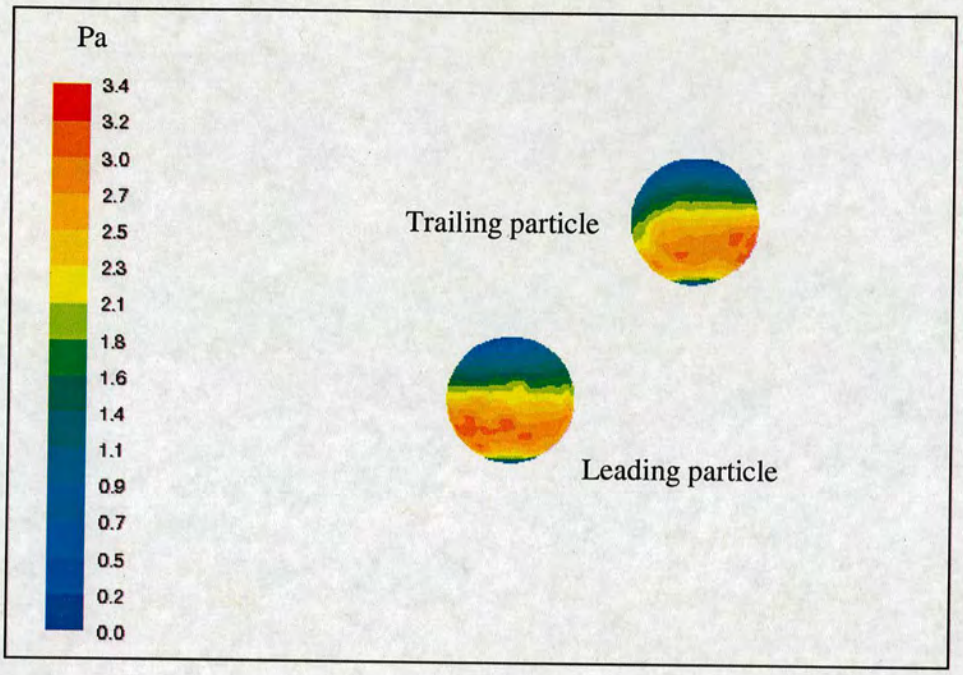

(a)

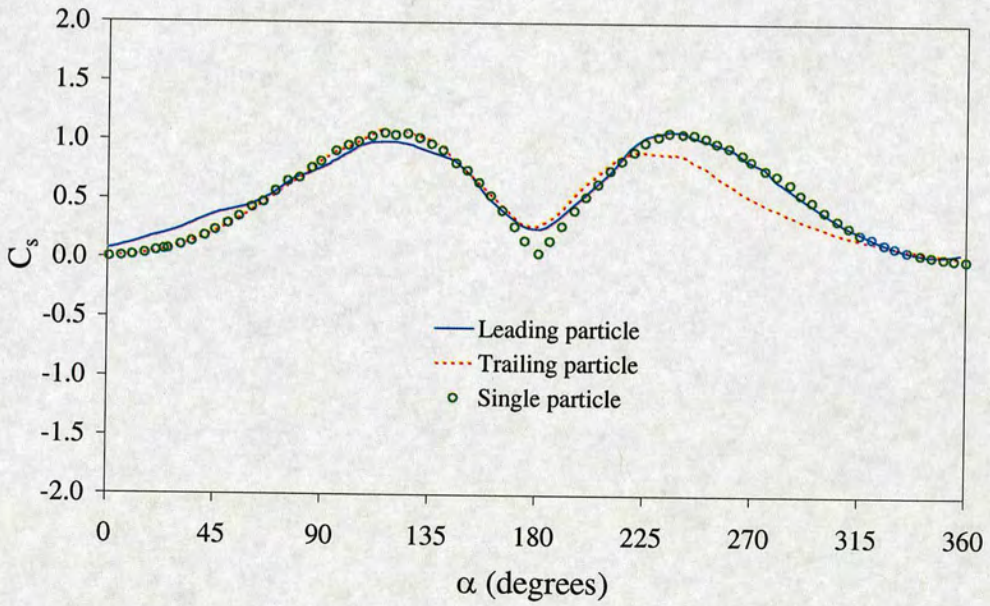

(b)

Fig. 3.13 Two fixed spherical particles at D_o = 2 and θ = 45° (a) wall shear stress coefficients contours and (b) profiles.

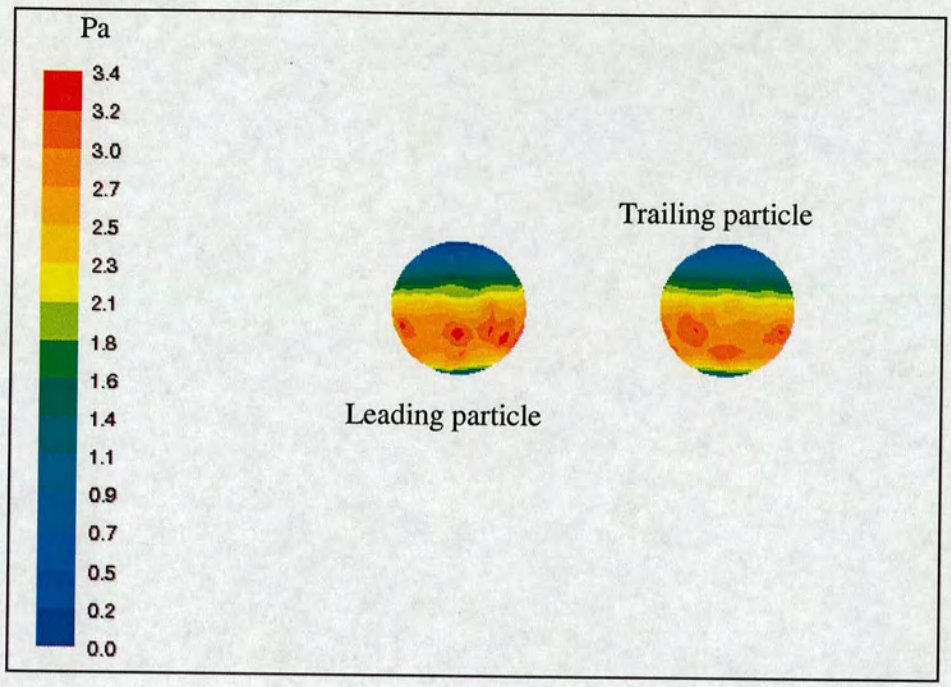

(a)

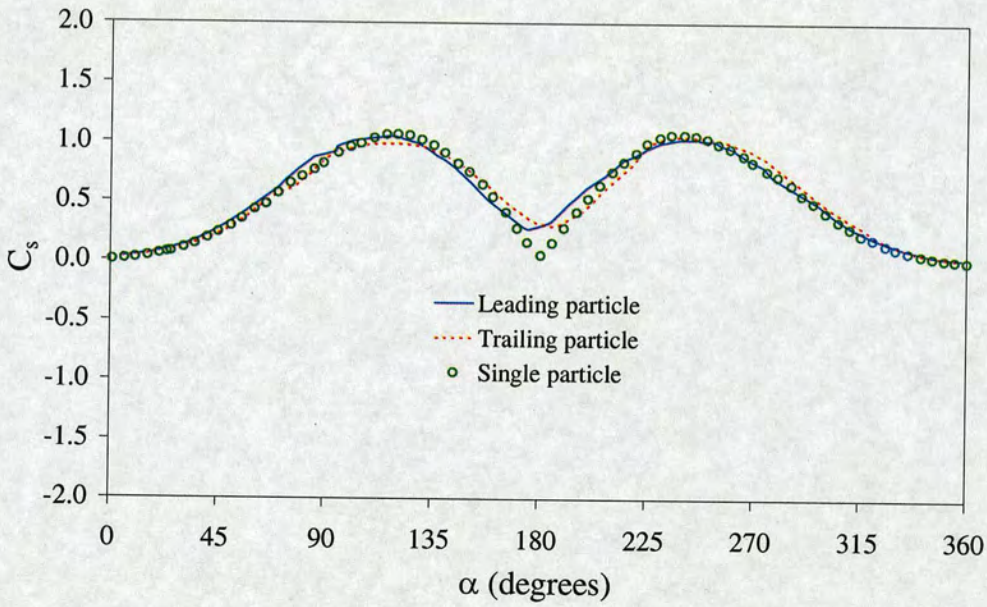

(b)

Fig. 3.14 Two fixed spherical particles at $D_o = 2$ and $\theta = 90^o$ (a) wall shear stress contours and (b) profiles.

3.4.5 Drag coefficients

The total drag force over an object immersed in a fluid flow is defined as the sum of the form drag force and the friction drag force as defined by equation (3.3). Drag coefficients for two particles aligned streamwise and side by side have been reported both numerically and experimentally by some authors for particle Reynolds numbers, Re_p, varying from 30 to 300, Tsuji *et al.* (1982), Zhu *et al.* (1994), Liang *et al.* (1996), Chen & Lu (1999), Folkersma *et al.* (2000), Chen & Wu (2000), Kim *et al.* (1993), Tsuji *et al.* (2003) and Prahl *et al.* (2007). However, in some important industrial applications of multiphase flows, lower particle Reynolds numbers are found, e.g., in the case of coal-fire power plants, coal particles are pneumatically transported from the mill through ducts consisting of numerous bends and straight sections, so centrifugal forces in the bends are believed to lead to the formation of a stratified gas-solid flow. This is the so called "roping" phenomenon[7]. Particles within the rope have been detected at lower velocity than the rest of the particles indicating an interaction between the particles. Particle Reynolds number, Re_p, for the roping phenomenon has been reported by several authors in the range of 10 to 30, which is only one third to one half of the rest of the flow, McCluskey *et al.* (1989), Huber & Sommerfeld (1994), Yilmaz & Levy (1998, 2001); Akilli *et al.* (2005) and Yan & Kuan, (2006). Hence, hydrodynamic particle-fluid-particle interactions at low particle Reynolds numbers are of practical significance in industrial applications.

In order to investigate the drag force on two fixed interacting particles as a function of particle separation distance (D_o) and angle (θ), the drag coefficient has been calculated. The total drag coefficient, C_d, is given by:

$$C_d = \frac{F_d}{\frac{1}{2}\rho V_\infty^2 \pi \left(\frac{d_p}{2}\right)^2} \tag{3.6}$$

[7] A rope is a high density ribbon of particles which is created when a uniform air-coal flow segregates at a pipe bend into two regimes: one has a low coal to air ratio whereas the second regime, termed the rope, has a high coal to air ratio (McCluskey *et al.* 1989).

where F_d stands for the total drag force, ρ is the fluid density, V_∞ is the constant upstream velocity and d_p is the particle diameter.

Drag coefficients were calculated from leading and trailing particles at large range of angles and separations. Figure 3.15 and 3.16 shows a large mapping of drag ratio data for both leading and trailing particles, respectively.

Figure 3.15 illustrates the leading particle drag ratio variation for separation distances from $D_o = 1.1$ up to $D_o = 25$ and angles between 0^o and 90^o. As an overall trend, except for $\theta = 75^o$ and $\theta = 90^o$ which show a higher drag coefficient between 1.5 and 3 particle diameter separation, lower values of drag coefficients are found for small separation distances, but increase rapidly as the separation distance increases until reaching similar values to those of a single particle. It is also observed that as the angle between the particles decreases the drag coefficient on the leading particle decreases. However, the drag coefficient variation of the leading particle as a function of the particle angle position (θ) is small ($0.85 \leq C_d/C_{ds} \leq 1.01$). Chen & Wu (2000) and Prahl *et al.* (2007) for higher particle Reynolds numbers reported maximum values of 1.2 and 1.1, respectively. These values were evaluated for higher particle Reynolds numbers ($50 \leq Re_p \leq 200$). Equal drag coefficients for leading and trailing particles in a side-by-side arrangement are found.

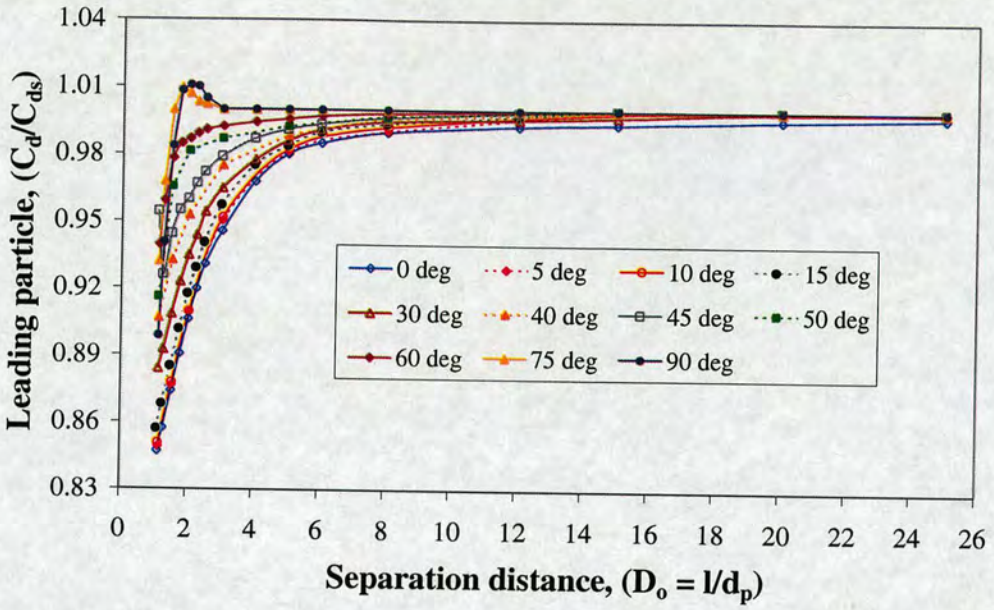

Fig. 3.15 Drag ratio as a function of the relative particle position (D_o,θ) for the leading particle at $Re_p = 15$.

Figure 3.16 shows the drag ratio for the trailing particle, which shows a similar trend to the leading particle, but the variation with the particle position (θ) is greater than those in the trailing particle. The variation between the maximum and minimum value is larger ($0.46 \leq C_d/C_{ds} \leq 1.01$). As a result of these differences, it is evident that the leading particle's influence over the trailing particle is significantly larger than the influence of the trailing over the leading particle. This phenomenon is mainly because the fluid is disturbed by the leading particle and does not recover to its uniform state before encountering the trailing particle as show by the velocity profiles in Figures 3.5 and 3.7. A complete set of velocity profiles can be found in the appendix to chapter three for separation distances between $D_o = 1.1$ and $D_o = 25$ and $\theta = 0^o$, 45^o and 90^o.

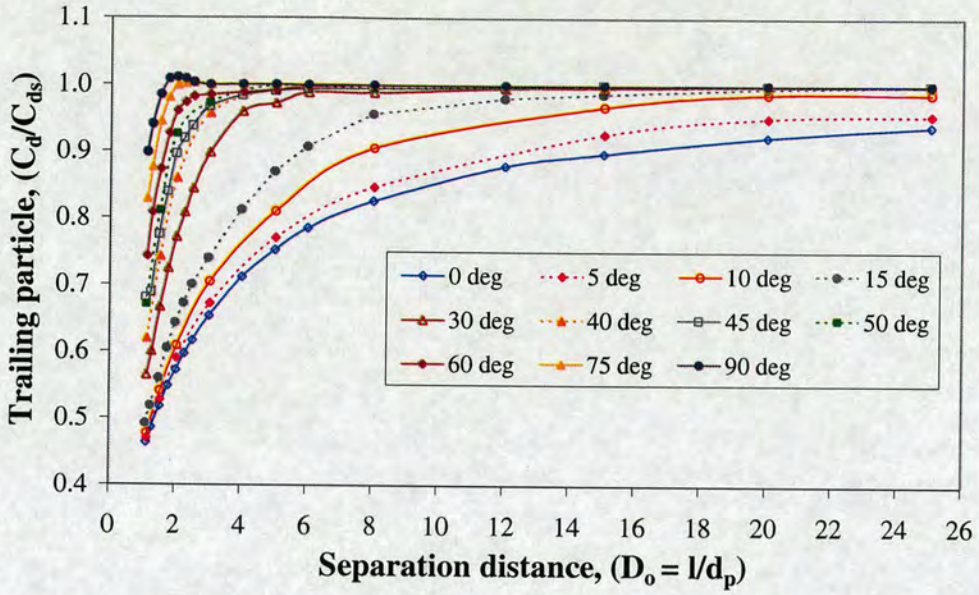

Fig. 3.16 Drag ratio coefficients as a function of the relative particle position (D_o,θ) for the trailing particle.

Comparison with available numerical and experimental data have been made for the two most common arrangements, two particles placed in tandem formation (θ = 0°) and two particles placed side-by-side (θ = 90°). Figure 3.17 shows the non-dimensional drag coefficient comparison for the leading and trailing particle in tandem formation for particle separation distances up to D_o = 8. Figure 3.17(a) illustrates the non-dimensional drag coefficient of the leading particle (θ = 0°). Data comparison agrees with that reported by Chen &Wu (2000), Tsuji *et al.* (2003) and Prahl *et al.* (2007), especially those reported by Tsuji *et al.* (2003). The data reported here compared with those reported by Zhu et al. (1994) present a good agreement for D_o > 2.On the other hand, Figure 3.17(b) depicts the comparison of drag coefficients for the trailing particle (θ = 0°) with those reported by other authors, such as Zhu *et al.* (1994), Chen Lu (1999), Chen &Wu (2000), Tsuji *et al.* (2003) and Prahl *et al.* (2007). From figure 3.17(b) it can be observed that the present results follow the same trend as the data reported by the other authors.

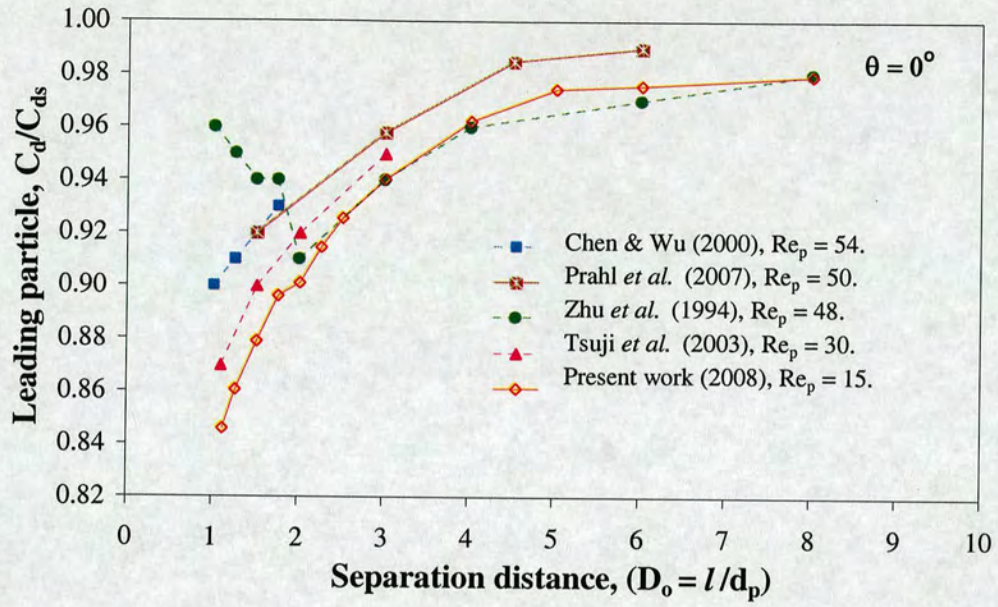

(a)

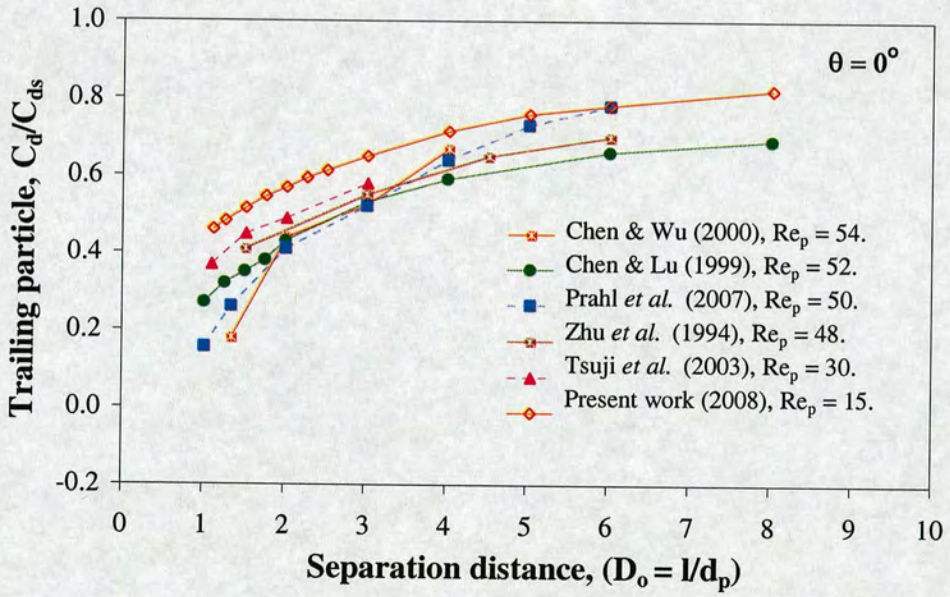

(b)

Fig. 3.17 Comparison of drag coefficients for (a) leading particle and (b) Trailing particle aligned with the flow (θ = 0°).

In general, from Figure 3.17 two different patterns can be observed: the drag coefficients from leading particle increase as the particle Reynolds number increases, whereas for the trailing particle the drag coefficients decrease as the particle Reynolds number increases. Since this study is carried out at the lowest particle Reynolds number ($Re_p = 15$), as expected, the data from this work is found lying on the bottom for the leading particle and on the top for the trailing particle, so as seen in Figure 3.17, the present results follow the trend of the results reported in the literature for similar particle Reynolds numbers.

Considering two particles placed side-by-side ($\theta = 90^o$), comparison of drag coefficients is presented in Figure 3.18. Results show good agreement with present data and those reported by Chen & Lu (1994), Kim *et al.* (1993), Liang *et al.* (1996) and Tsuji *et al.* (2003). The drag coefficients show three different trends compared to that of a single particle, depending on the particle Reynolds number. First, most of the data agree that for particle separation distances, $D_o > 4.0$, the drag coefficient tends to that of a single particle. Second, for separation distances between $D_o = 4$ and $D_o = 1.5$ the magnitude of the drag coefficient is always greater than that of the single particle. Last, for $D_o < 2.0$ the data from this study show a fall in the drag coefficient magnitude, this trend has been also reported for smaller separation distances, $D_o < 1.5$ at larger particle Reynolds numbers, $Re_p = 37$ and 50 by Liang *et al.* (1996) and for $Re_p = 30$ by Tsuji *et al.* (2003).

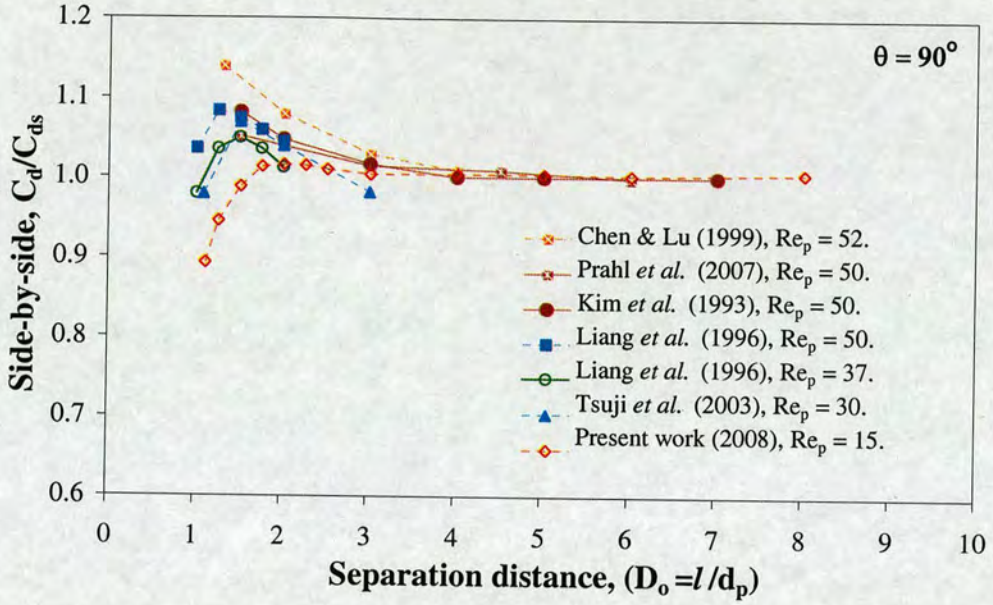

Fig. 3.18 Comparison of drag coefficients for two particles in a side-by-side arrangement ($\theta = 90^o$).

As stated by Tsuji *et al.* (2003) for low particle Reynolds numbers, $Re_p < 30$, the pressure drag occupies a small part of the total drag, so shear drag is the main component. Figure 3.19 shows the wall shear stress and pressure coefficients distribution at $Re_p = 15$, $D_o = 1.1$ for $\theta = 90^o$. For very small particle separations ($D_o < 2.0$), the flow treats the two particles as one big object instead of two individual particles. The high pressure region that occurs in front of each particle is united to form a large zone of high pressure. Similarly there is a low pressure region behind the two particles. These conditions increase the streamwise pressure gradient and decrease the drag wall shear stress (WSS). The wall shear stress reduction is due to the very low velocity ($v \rightarrow 0$) between the two particles, so a large area of the particles presents very small values of WSS as clearly shown in Figure 3A.26(c). Form drag (pressure) at low particle Reynolds numbers occupies a small part of the total drag, thus, this is considered as a possible explanation for the drag coefficient reduction for small separation distances, $D_o < 2$.

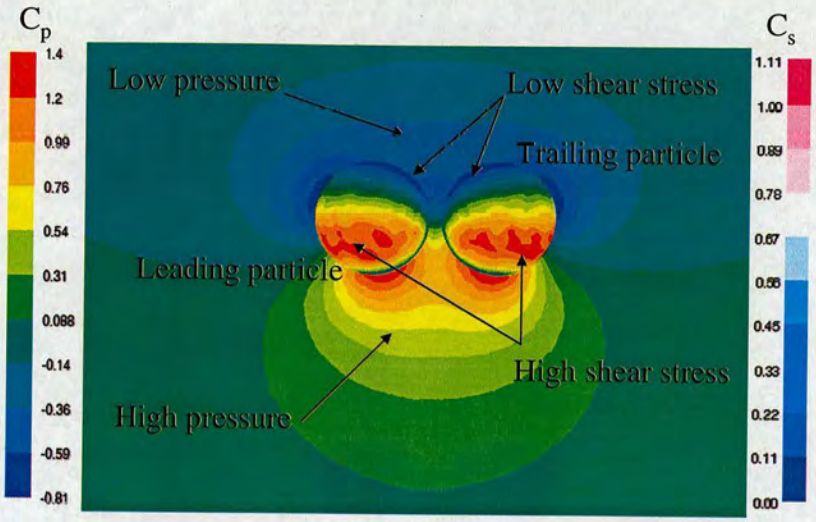

Fig. 3.19 Pressure and wall shear stress coefficients for two fixed particles at $D_o = 1.1$, $\theta = 0^o$ and $Re_p = 15$.

3.3.6 Interaction coefficients

The concept of hydrodynamic particle interactions in viscous fluids for very low velocity flows (Stokes' flow regime, $Re_p >> 1$) was firstly introduced by Smoluchowski (1911, 1912). Recently, Kim *et al.* (1993) and Folkersma *et al.* (2000) introduced the concept of the particle interaction coefficient as the lift force divided by $(\frac{1}{2}\rho V_\infty^2 \pi(d_p/2)^2)$ for two particles placed side-by-side. They defined the interaction coefficient as the forces acting parallel to the line connecting the centre of the two spheres. Based on this concept, a general definition for two interacting particles can be expressed in the form, Vargas & Easson (2004):

$$C_i = \frac{8F_i}{\rho V_\infty^2 \pi d_p^2} \tag{3.7}$$

where F_i denotes the total interaction force, ρ is the fluid density, V_∞ is the upstream constant uniform velocity and d_p is the particle's diameter.

Applying the concept of interaction coefficient employed by Kim *et al.* (1993) and Folkersma *et al.* (2000), the interaction force can be expressed as a function of the particles position (θ) and the total drag forces in the main plane (x-y) by the next equation:

$$F_i = \left(F_{2(1)}^{2-b;x} - F_{1(2)}^{2-b;x}\right)\sin(\theta) + \left(F_{2(1)}^{2-b;y} - F_{1(2)}^{2-b;y}\right)\mathrm{Cos}(\theta) \qquad (3.8)$$

where $F_{1(2)}^{2-b;x}$ denotes the total drag force in the x-axis direction over the leading particle, $F_{2(1)}^{2-b;x}$ stands for the total drag force in the x-axis direction at the trailing particle surface, whilst $F_{1(2)}^{2-b;y}$ and $F_{2(1)}^{2-b;y}$ represent the total drag force in the y-axis direction for leading and trailing particle, respectively. The total drag force is considered positive when it is directed toward the positive axis direction. The interaction force, F_i, can be positive or negative, if $F_i < 0$ the interaction coefficient is negative and the two particles attract each other. On the other hand, if $F_i > 0$ the interaction coefficient is positive, and this means that the two particles repel each other. The deduction of equation (3.8) can be found in the appendix to chapter 3.

Figure 3.20 shows the attraction and repulsion that occurs due to the hydrodynamic interactions between two fixed particles. Attraction occurs either when the forces over the two particles are acting in same direction, Figure 3.20(a), so the particles could approach each other or when the force over the leading particle is greater than the force over the trailing particle, Figure 3.20(b), thus the leading particle must travel faster and approach the trailing particle. In contrast to attraction, repulsion occurs when the forces over the two particles are working in opposite directions, Figure 3.20(c) -as a result the two particles repel each other- or the force over the trailing particle is greater than that of the leading particle, so the trailing particle moves faster than the leading one and they never approach each other, Figure 3.20(d).

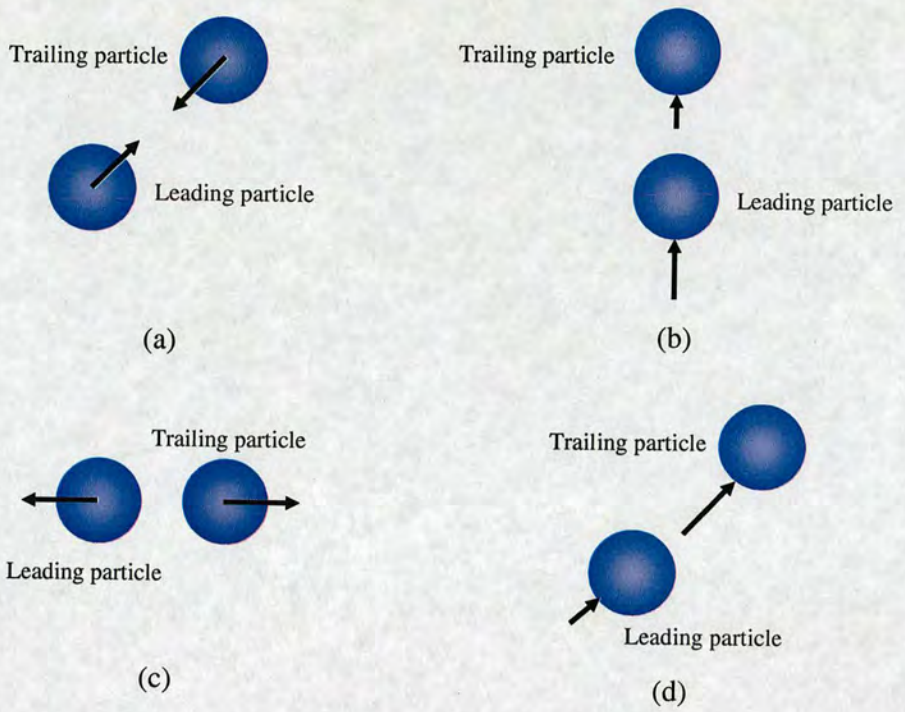

Fig. 3.20 Two approaching particles (a) forces in the same direction, (b) higher force on the leading particle; two separating particles (c) forces in opposite direction and (d) larger force on the trailing particle.

This analysis can be applied when the particles are travelling with the flow as in particle pneumatic transport. Different analysis is applied for two free falling particles and is out of the reach of this work, but a brief description is given below. The physics for falling particles is basically the same. The two falling particles phenomenon has been described by several authors, Fortes *et al.* (1987), Johnson & Tezduyar (1996), Hu *et al.* (2001) and Shao *et al.* (2005), among others. For example, it is known that, when two particles are falling in a stagnant Newtonian fluid they will interact undergoing repeated drafting, kissing and tumbling (DKT). In this case, the leading particle falls slower than the trailing particle due to its large drag force, whilst the trailing will fall faster due to its smaller drag force, because of the leading particle wake with low pressure. Attraction phenomenon for two particles in tandem arrangement has been reported up to $D_o = 6$ by Shao *et al.* (2005) and for $D_o \sim 5$ at $\theta \sim 13^o$ by Johnson & Tezduyar (1996). Because the leading particle creates a pressure drop in its wake which makes the trailing particle move faster, the trailing

particle is drafted into the wake of the leading particle. The interaction in this period is called "drafting". Eventually, the trailing particle will contact the leading particle, so-called "kissing" contact. Kissing particles form a long body that is unstable in Newtonian fluids. The kissing particles aligned with the mainstream will rotate to the broadside-on orientation, so the pair particle tumbles to a side by side configuration.

Figure 3.21 shows the variation of interaction coefficients, C_i, of two fixed solid spherical particles placed at different positions relative to each other. In order to highlight the angle position (θ) and the separation distance (D_o) dependency, the C_i has been plotted as a function of angle positions and separation distances, Figure 3.21(a) and 3.21(b), respectively. A positive value of C_i means that repulsion forces exist, whilst negative values stand for attractive forces. Two general trends for the particle interaction coefficients are observed from figure 3.21(a). For $\theta > 45^o$ only positive interaction coefficients are observed, whilst for $\theta < 45^o$ all interaction coefficients are negative. Second, the interaction coefficients for $30^o < \theta < 90^o$ change rapidly and reach a null value at $D_o < 8$, whilst for angles between 0^o and 15^o the variation on C_i is gradual and do not reach the null value even for $D_o = 25$. Figure 21(b) shows that for particle separation distances greater than $D_o > 8$ the coefficient is significant only for angles $\theta \leq 15$.

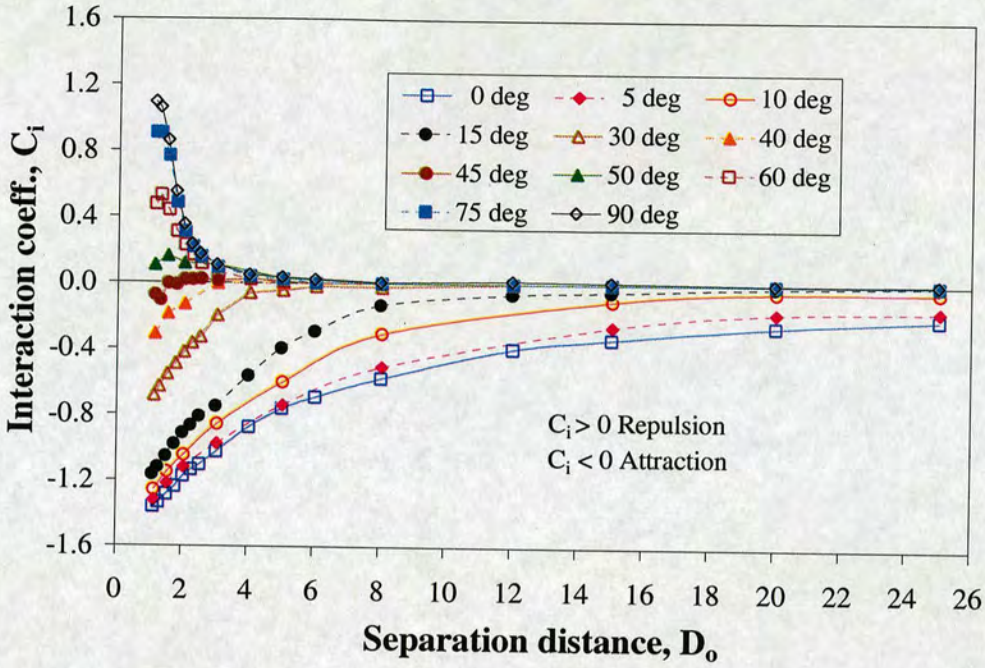

(a)

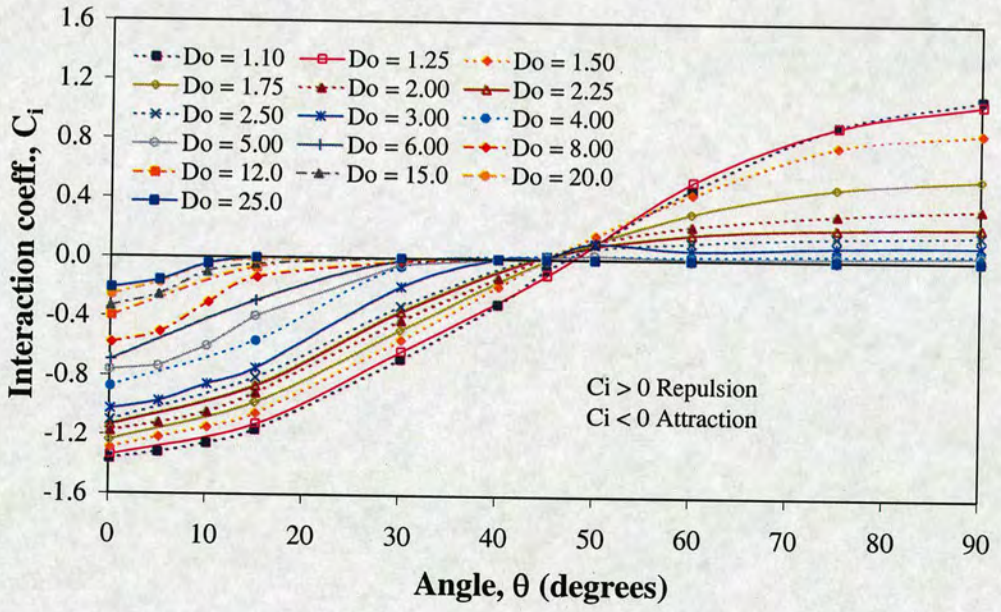

(b)

Fig. 3.21 Interaction coefficients C_i between two solid spheres at $Re_p = 15$, (a) as a function of the angle (θ) and (b) as a function of the separation D_o.

Figure 3.22 depicts the interaction coefficients comparison for two particles placed side-by-side, $\theta = 90^{o}$. The present results agree with other published results especially with those reported by Legendre *et al.* (2003) and Folkersma *et al.* (2000). They reported interaction coefficients at particle Reynolds numbers similar to this study ($20 \geq Re \geq 10$). Kim *et al.* (1993) and Folkersma *et al.* (2000) reported small negative interaction coefficients for intermediate separation distances ($8 < D_o < 21$) at particle Reynolds number, $Re_p = 50$, but this trend is not observed for lower particle Reynolds number, in fact, Legendre *et al.* (2000) reported that the interaction coefficient is always positive for two spherical bubbles placed in side-by-side arrangement when the particle Reynolds number is lower than a critical value ($Re_p \approx 28$), which is in agreement with the present results.

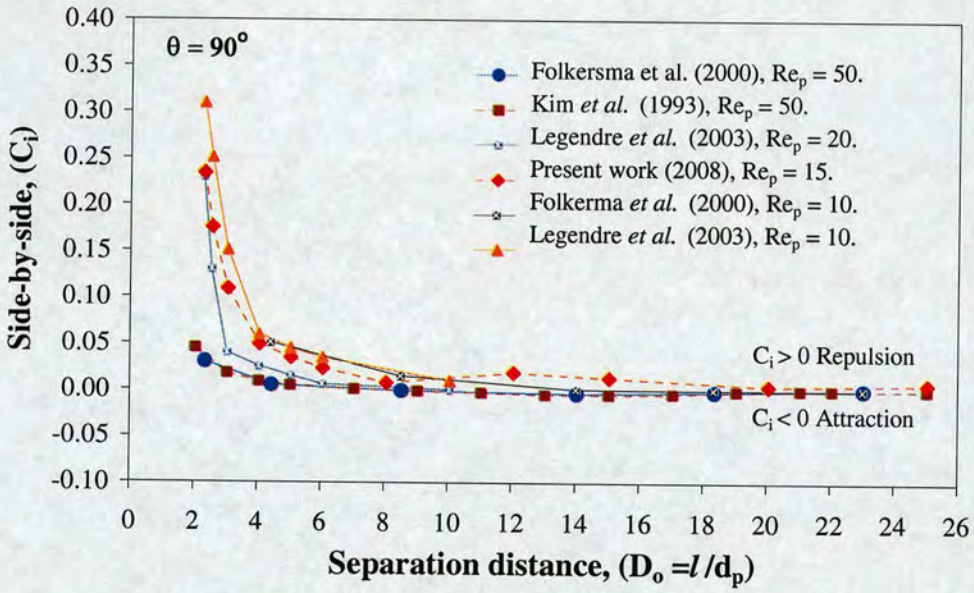

Fig. 3.22 Comparison of interaction coefficients, C_i, with available data for two particles placed side by side ($\theta = 90^{o}$) as a function D_o for $Re_p < 50$.

It is observed from Figure 3.21 that the interaction coefficients change sign as a function of relative position between the two particles and eventually tend to zero. Thus zones of attraction and repulsion between a pair of particles can be obtained. The boundaries of the interactive zones were computed using 1% of the maximum interactive coefficient ($C_i = -1.4$) found at $\theta = 0^{o}$ and $D_o = 1.1$. Thus the minimum

value of C_i in the interactive zones is 0.014. Figure 3.23 shows a map of the attraction and repulsion zones for two fixed particles for particles Reynolds number, $Re_p = 15$. If two particles are placed at relative small particle separation distances ($D_o < 6$) and their relative position with respect to the main flow is between 45° and 90°, the particles will experience only repulsive force ($0.014 < C_i < 1.1$). The repulsive zone is relative small compared with the attractive zone and is enclose in the dense flow regime ($D_o \leq 10$) where the particle volume fraction is of the order of 0.24%. On the other hand, when a second particle is placed downstream of the leading particle between 0° and 45° the two particles will undergo only attractive force ($-1.4 < C_i < -0.014$). The influence of the neighbouring particle at large separation distance in line formation is very small, e.g., if the particles' drag coefficient is compare with that of a single particle, the drag coefficient for particle separation distances greater than ten particle diameters is less than 1% and 17% for the leading and trailing particle, respectively. Because the boundaries of the interactive zones were calculated using 1% of the maximum value of the interactive coefficient, the interaction coefficient within the dense area ($D_o < 10$), but not included in interactive zones is less than 0.014. For example, if a particle is located at $\theta = 45°$ and $D_o = 8$ as show in Figure 3.23, the interaction coefficient is equal to 0.013, which represents less than 1% of the maximum value.

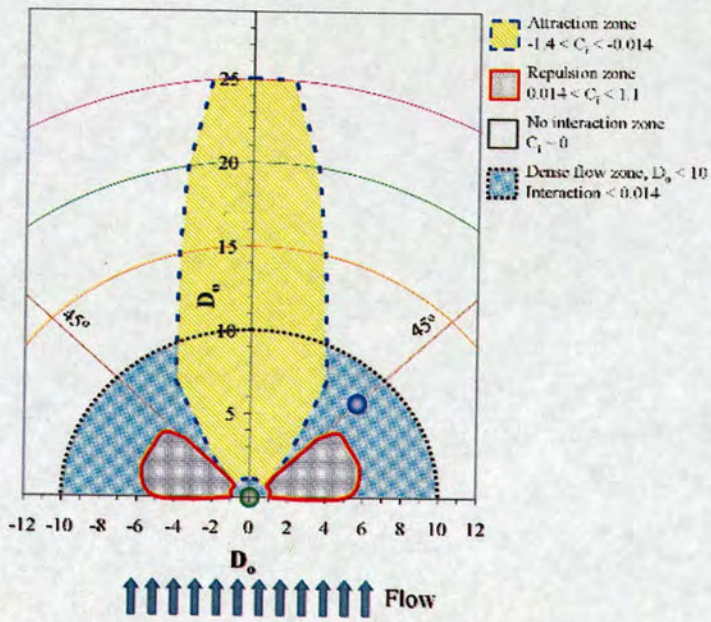

Fig. 3.23 Draw map of attraction-repulsion zones for two fixed solid spherical particles placed relative to each other at $Re_p = 15$.

3.4 Conclusions

The hydrodynamic interaction between two fixed spherical particles placed at different positions relative to each other, at particle Reynolds number of 15, has been investigated using CFD. This study has mainly focused on the drag (C_d) and interaction (C_i) coefficients. Both the separation and the angle relative to the main flow direction of the two spherical particles are found to influence the drag and the interaction coefficient that the particles are subject to. A large area of particle interaction was found downstream of the leading particles and corresponds to the attraction coefficient, for small values of θ. The strongest effect on drag force for a pair of particles immersed in a fluid flow, compared with that of a single particle case, is observed when the particles are aligned with the fluid flow. The drag reduction for two particles in tandem arrangement is as high as 15% for the leading particle and 54% for the trailing particle, when they are very close. When the two particles are placed side-by-side and the separation distance is small, the two

particles experience the same drag reduction, which is around 10% compared to the drag of a single particle.

In contrast to the drag coefficient, the highest attraction and repulsion coefficients are found at small separation distances. The former is found in a tandem formation and the latter is found in a side-by-side arrangement. If the volume fraction is of the order of 10^{-3}, both the attraction and repulsion forces due to hydrodynamic interaction play an important role in the two-phase flow study, so this work highlights the importance of the need to introduce the particle-fluid-particle hydrodynamic interactions (three-way coupling) even for low particle Reynolds numbers within the two-phase flows model framework. The interactive forces obtained from two particles will be used to obtain a pair potential to simulate multiple particles applying a Monte Carlo method in chapter 5.

CHAPTER 4

4 COMPUTER FLUID DYNAMICS SIMULATIONS: THREE FIXED SPHERICAL PARTICLES

In the previous chapter simulations of the interactions between two fixed spherical particles were compared with experimental and numerical data available in the literature. In this chapter the interactions between three fixed spherical particles are considered since multibody interactions will be the most important forces neglected in the Monte Carlo simulations. This will give a measure of the limits of the two-body approximation.

Two main configurations of three particles are used: three collinear particles and three particles placed at the corners of an equilateral triangle, for both cases a wide range of particle separations have been studied ($1.1 \leq D_o \leq 10$). The main objective of this chapter is to illustrate the hydrodynamic effect on the forces in a two-particle hydrodynamic interactions system by the presence of a third particle and justify the use of two particle hydrodynamic interactions in multi-particle interaction simulations in chapter 5, using a Monte Carlo method. For three-particle systems at higher flow regimes than Stokes flow, almost no numerical or experimental results are currently available, so most of the results presented here are only compared with those obtained from two particle simulations by application of the two particle additivity approximation, which can be carried out by using only the two spheres mimicking a three-particle system, placing one of the particles in two relative different positions.

4.1 Introduction

Multiparticle hydrodynamic interactions play an important role in determining the properties of dispersed two-phase flow systems, especially at high particle volume fraction. Many-particle hydrodynamic interactions are traditionally studied via one or two-particle system. Beyond two particle hydrodynamic interactions, published results are rather limited, including in the Stokes regime. The method of reflections, started by Smoluchowski (1911) is applied to the solution of two and three interacting particle systems in the Stokes flow regime ($Re << 1$). Kynch (1958) studied three-particle configurations in the Stokes flows regime using the method of reflections. Some decades later, Kim (1987) and Clercx & Schram (1992) applied additional theorems and methods to determine the component of the grand mobility matrix in their study, a system of three interacting spherical particles in the Stokes flow regime. Kim (1987) studied a three-particle problem: three identical spherical particles located at the corners of an equilateral triangle, falling perpendicular to the plane of the triangle. Clercx & Schram (1992) applied a method allowing the study of three particles with arbitrary configurations. They computed the sedimentation velocities, including the three-particle interactions, for particle volume fractions up to 0.13. Happel & Pfeffer (1960) analysed experimentally three falling collinear particles for very low Reynolds numbers ($0.3 \leq Re \leq 0.7$). They observed that when the distance between the three particles is the same, the formation is unstable because the middle sphere is influence by interaction effects from the other two spheres. These interaction effects cause that the middle sphere moves closer to the leading sphere, which produce a particle pair. These two particles will travel at higher velocity than the trailing particle. At certain time the distance between the middle particle and the trailing particle will be greater than the distance between the leading and middle particle because of the greater velocity of the particle pair.

For higher Reynolds numbers, Jayaweera *et al.* (1964) studied experimentally clusters of three to six equal size spheres in the range of particle Reynolds numbers between 0.06 and 7. They found that multiparticle clusters fall faster than a single particle. This velocity enhancement is greater the more compact the cluster. Wang &

Liu (1992) reported a study of hydrodynamics and heat transfer of three fixed collinear spherical particles with equal diameter for two different separation distances (D_o = 2 and 4) at particle Reynolds number, Re_p = 718. Lower drag coefficient for the middle particle was reported for the two separation distances. Johnson & Tezduyar (1996) simulated three falling spheres unevenly spaced along the horizontal line, at particle Reynolds number, Re_p = 100. The spheres for this case rearranged into a neutrally-stable and stable states. First, the middle sphere moves to be equidistant from the other two spheres to form the neutrally-stable state (three particles evenly spaced). After this point, the middle sphere moves out of the line and eventually the three spheres form an equilateral triangle parallel to the flow, the stable state. Liang *et al.* (1996) described the drag coefficients for three collinear particles at Re_p = 54, 78, 92 and 106. They found that the leading particle has the highest drag ratio: the middle and trailing particles have much lower drag ratios because of the wake effect. At small separation distances, the middle particle has the largest drag reduction, however as the separation distance increases to a value from 2 to 3 particle diameters, the drag of the middle particle becomes larger than that of the trailing particle, but the difference between them is not significant. Chen & Lu (1999) considered three particles side-by-side configuration (the middle particle was considered as the test particle) and three particles in a reversed "L" configuration (ך) for three different particle Reynolds numbers, Re_p = 52, 82 and 102. The third particle was placed at D_o = 1.33 from the test sphere (trailing sphere). The drag coefficient on the test sphere in the side-by-side formation was increased whilst in reversed "L" arrangement the drag magnitude was substantially closer to that of a single particle under the influence of the third particle. Lomholt (2000) presented a numerical and experimental study of three rising particles in tandem arrangement at particle Reynolds number, $Re_p < 10$. He described two drafting-kissing-tumbling (DTK) events. The first involved the leading and middle particles and the second the trailing and middle particles, the second DTK event formed a particle pair and travels at higher velocity than the leading particle and therefore the pair formed by the middle and trailing particles overtakes the leading particle leaving it behind.

4.2 Numerical method and problem set up

Three-dimensional flow past three fixed solid spherical particles, d_p = 100μm, is studied using a commercial CFD program, FLUENT V6.2.16. The particles are held fixed relative to each other at different separation distances ($1.1 \leq D_o \leq 10$) and angles ($0^o \leq \theta \leq 90^o$) with respect to the main flow direction. Two different arrangements are used in order to study the influence of a third particle in the hydrodynamic interactions on a two-particle system: three particles in line and three particles place in the corners of an equilateral triangle, as shown in Figure 4.1. In both cases, the particles are placed at even separation. As in the two-particle CFD simulations, the fluid is air at standard conditions ($\rho = 1.225\,kgm^3$, $\mu = 1.7894 \times 10^{-5}\,kgm^{-1}s^{-1}$) moving with a velocity chosen to give a particle Reynolds number, Re_p = 15. In both configurations, for ease in describing the particles, they are identified as particle 1, particle 2 and particle 3. Similar to the two-particle system simulations, the three particles are contained in the x-y plane at z = 0. The separation distance (l) between the centres of the particles is non-dimensionalized by the diameter of the particle (d_p) and it is denoted by D_o. The angle (θ) represents orientation with respect to the main flow direction, which is aligned with the y-axis. In three collinear particles, $\theta = 0^o$, when the particles are aligned with the main flow direction, whilst in triangular configuration the orientation angle (θ) is equal to zero, when particle 1 and particle 3 are aligned with the main flow direction as shown in Figure 4.1.

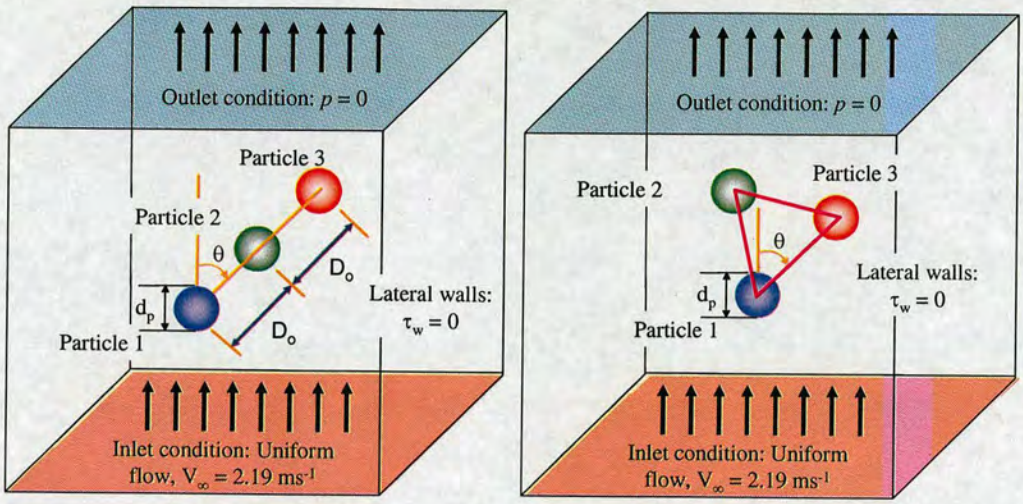

Fig. 4.1 Problem setup (a) three particles in line formation and (b) three particles in an equilateral triangle configuration.

The same meshing method, boundary and numerical conditions as in two-particle interactions are used. High grid density near to the particles' surface, constant uniform velocity in the y direction, $\mathbf{U_y} = \mathbf{V_\infty} = 2.19$ ms^{-1}, $\mathbf{U_x} = \mathbf{U} = 0$ and $\mathbf{U_z} = \mathbf{W} = 0$, zero wall shear stress at the lateral wall boundaries, zero pressure at the outlet boundary and non-slip condition over the surface of the particles are applied. The Navier-Stokes equations are solved assuming steady laminar flow and an implicit segregated method is used. The control-volume technique is employed to solve the conservation equations for mass and momentum. A second order discretization scheme is applied to obtain the flow field around the particles. The pressure-velocity coupling algorithm SIMPLE is used. Figure 4.2 shows a cross subsection of grid domain in the x-y plane for three particle in line at $D_o = 2$ and $\theta = 0^o$ and three particles in a triangular configuration for $D_o = 2$ and $\theta = 0^o$. In order to compare the three-particle system with the two-particle system, the same particle Reynolds number is used, $Re_p = 15$.

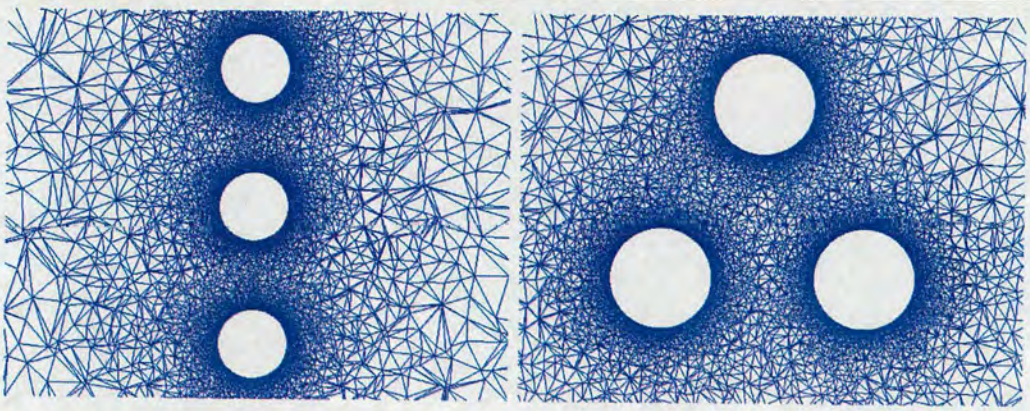

(a) b)

Fig. 4.2 The grid distribution for three particles at $D_o = 2$ for (a) three particle in line at $\theta = 0^o$ and (b) three particles in triangular arrangement at $\theta = 90^o$.

4.3 Results

The results obtained in this chapter are compared with numerical data reported in chapter three. In this chapter, the two-particle system is represented by 2-b whilst 3-b stands for the three-particle system.

Flow field visualizations and streamwise velocity, drag forces and interaction coefficients profiles are used to understand the three particle hydrodynamic interactions and how they differ from the two-particle system. The streamwise velocity profiles are taken at 0.5 particle diameters from the surface of the particles. Streamwise velocity profiles at $y = 0$ are also obtained when required. As in the two-particle system, the centres of the particles in the three-particle system is contained at $z = 0$; the main hydrodynamic interactions occurred in the x-y plane. The flow field velocity, pressure and wall shear stress are analysed in sections 4.3.1, 4.3.2, and 4.3.3, respectively. Flow field visualization, velocity profiles and, pressure and wall shear stress coefficients are discussed in detail for two specific cases: (1) three collinear particles and (2) three particles placed at the vertices of an equilateral triangle. For both cases the separation between the particles is two particle diameters ($D_o = 2$). In the case of three collinear particles, the particles are aligned with the

flow ($\theta = 0^o$) and for the case of triangular arrangement, two of the particles are placed side-by-side and the line connecting their centres are perpendicular to the main flow direction ($\theta = 90^o$).

4.3.1 Velocity flow filed structure for three interacting particles

Field velocity contours and streamwise velocity profiles are presented in this section. The main idea of this is to highlight the third particle influence on the flow structure and compare the difference with the flow structure in a two-particle system. These differences, if any, will change the drag and lift forces acting on the spheres (F_d, F_L). The streamwise velocity profiles are normalised with the upstream constant uniform velocity, $V_\infty = 2.19$ ms^{-1}. As reference, the velocity profiles obtained from the two-particle system are also plotted.

Figure 4.3 illustrates the velocity flow field and the velocity profiles of three spherical particles in line at $\theta = 0^o$ and $D_o = 2$. The velocity contours in Figure 4.3(a) show low velocity zones between the particles and the velocity profiles in Figure 4.3(b) illustrates the same fact. For this specific situation, the velocity reduction in front of the particle 2 compared with particle 1 is around 91%, very similar to the difference found in the two-particle system (90%). For this case, slightly higher velocity (1%) is found in front of the particle 3 compared to that of particle 2, this condition is observed for particle separation distances between $D_o = 1.1$ and $D_o = 2.25$. For larger separation distances ($D_o > 2.25$) the velocity in front of particle 2 is higher than the velocity in front of the particle 3, the same condition was also reported by Liang *et al.* (1996) for higher particle Reynolds numbers ($54 \leq Re_p \leq 106$). Lower velocity (3%) in front of particle 1 is observed compared to that of the leading particle in a two particle interactions.

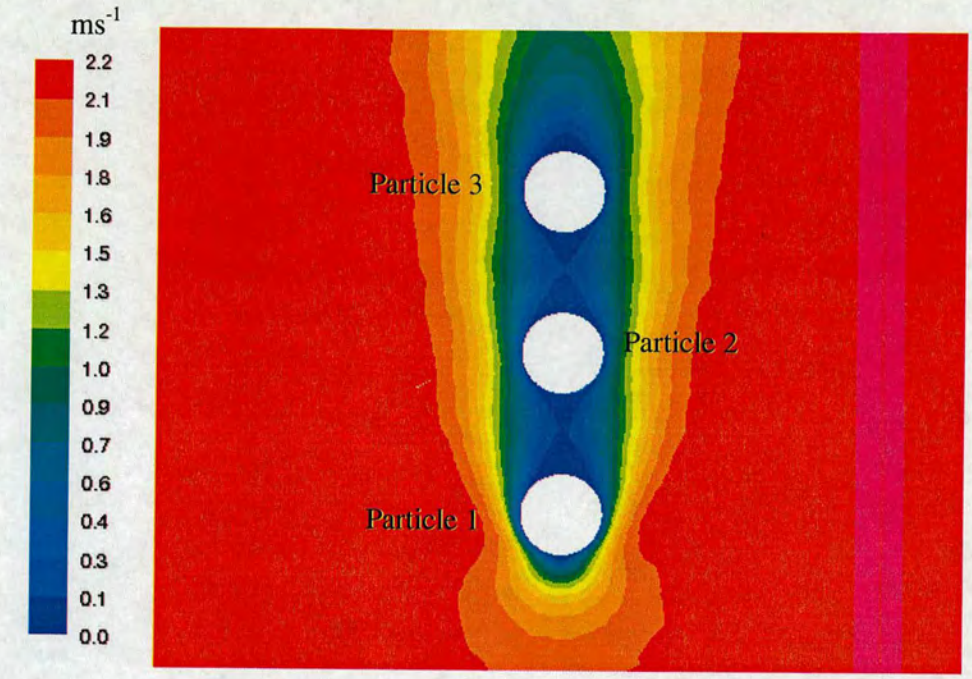

(a)

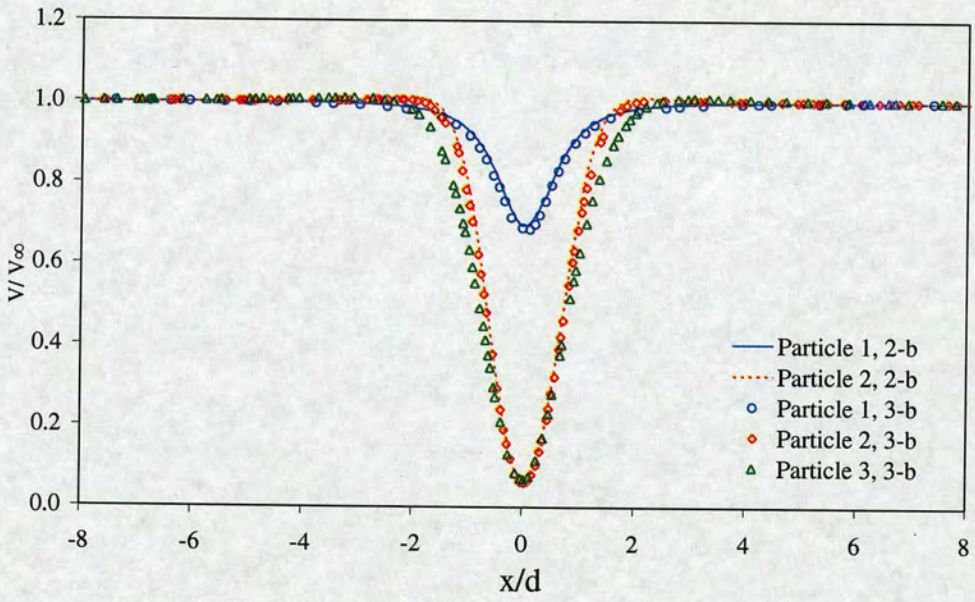

(b)

Fig. 4.3 Three fixed spherical particles at $D_o = 2$ and $\theta = 0^o$ (a) velocity flow field contours and (b) streamwise velocity profiles.

Figure 4.4 displays the velocity flow field contours and the streamwise velocity profiles for three particles placed at the vertices of an equilateral triangle with sides equal to two particle diameters, in this case the line connecting the centres of the particles one and three is perpendicular to the main flow direction. High velocity flow between these particles is observed, similar to the velocity found in two-particle system at the same conditions. However due to the presence of a third particle (particle 3) some differences can be found, as shown in Figure 4.4(b). Lower velocity is observed in a three-particle configuration than in a two-particle arrangement. For this particular case, the difference in velocity between two and three interacting particles at halfway between the particles ($x = 0$) is in the order of 6% for the velocity profile in front of particles and only 1% for the velocity profile at $y = 0$.

In general, the field velocity illustrates the hydrodynamic interaction between the particles and shows how a third particle modifies the flow. Some differences compared with two particle interaction system on the flow field velocity are observed. The flow field velocity plays an important role in the pressure and wall shear stress distribution over the particles' surface. These two parameters: pressure and wall shear stress are presented in sections 4.3.2 and 4.3.3, respectively.

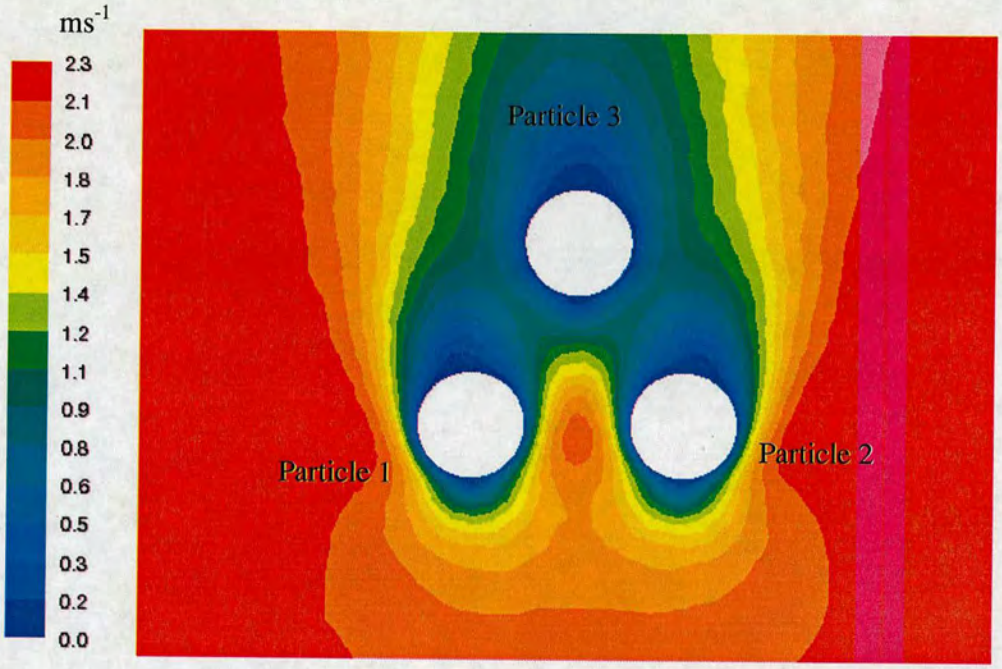

(a)

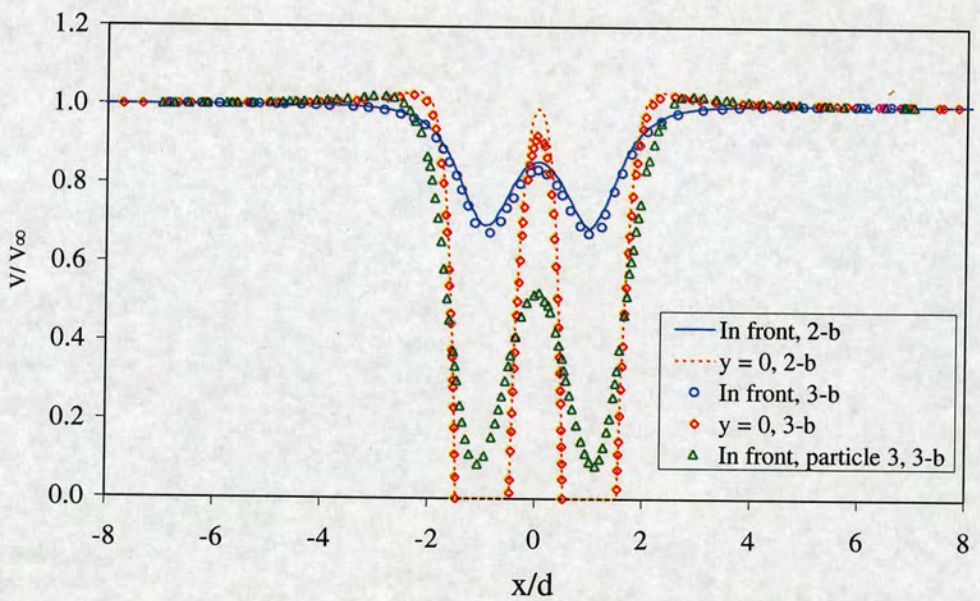

(b)

Fig. 4.4 Three fixed spherical particles placed at $D_o = 2$, particles 1 and 2 are at $\theta = 90^o$ (a) velocity flow field contours and (b) velocity profiles.

4.3.2 Pressure coefficients for three fixed interacting particles

The pressure distribution acting on interacting particles plays an important role in the interaction forces, as discussed in chapter 3. Figures 4.5 and 4.6 show contour plots and profiles of pressure coefficients. The same geometries used to describe the velocity field in the previous section are used. The pressure coefficient profiles from two-particle system are used as reference.

Figure 4.5 shows the pressure coefficient contours and profiles around three particles arranged in a line formation for $D_o = 2$. The presence of particle 1 significantly modifies the pressure forces on downstream particles (particles 2 and 3). There is high pressure over particle 1 and low pressure on particles 2 and 3. Clear particle interaction is found in the three-particle system. The influence of particles 2 and 3 (trailing particles) over particle 1 (leading particle) is relatively small. For the case shown in Figure 4.5, the pressure coefficient over particle 1 at the upstream stagnation point is around 11% greater than that of particle 1 in a two-particle system. The pressure at the stagnation point of particle 1 for a three-particle system is very close to the pressure found in a single particle system. The pressure coefficient difference at the upstream stagnation point between particle 1 and an isolated particle is less than 2.5%. The pressure coefficient on particle 2 is smaller than of the pressure on particle 3 but this trend changes for larger separation distances, $D_o > 2$. The pressure coefficient on particle 3 is basically the same as the pressure coefficient on the trailing particle for two-particle system. This is probably because the main interaction over particle 2 and 3 is due to particle 1.

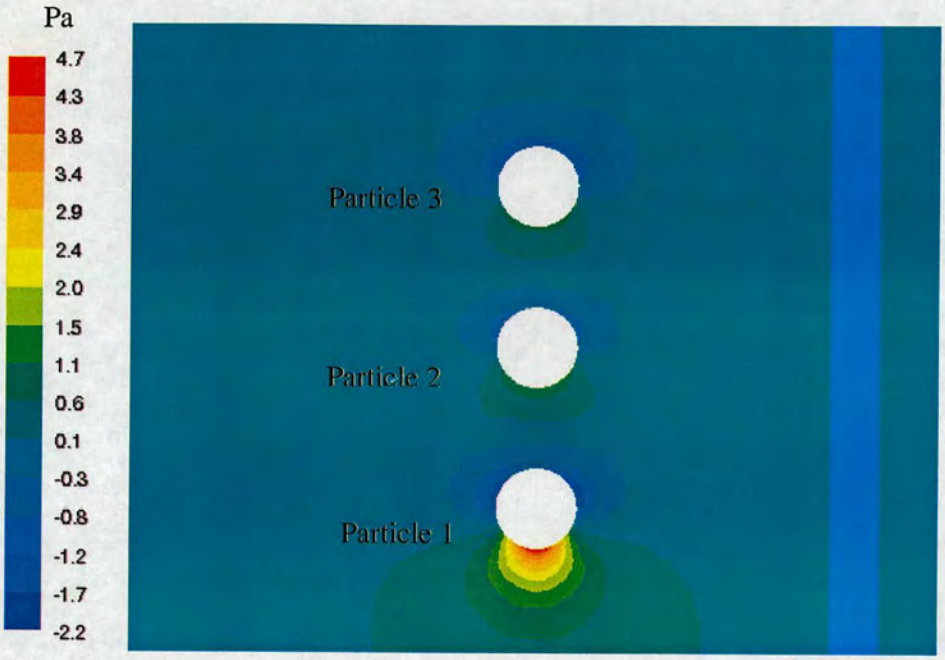

(a)

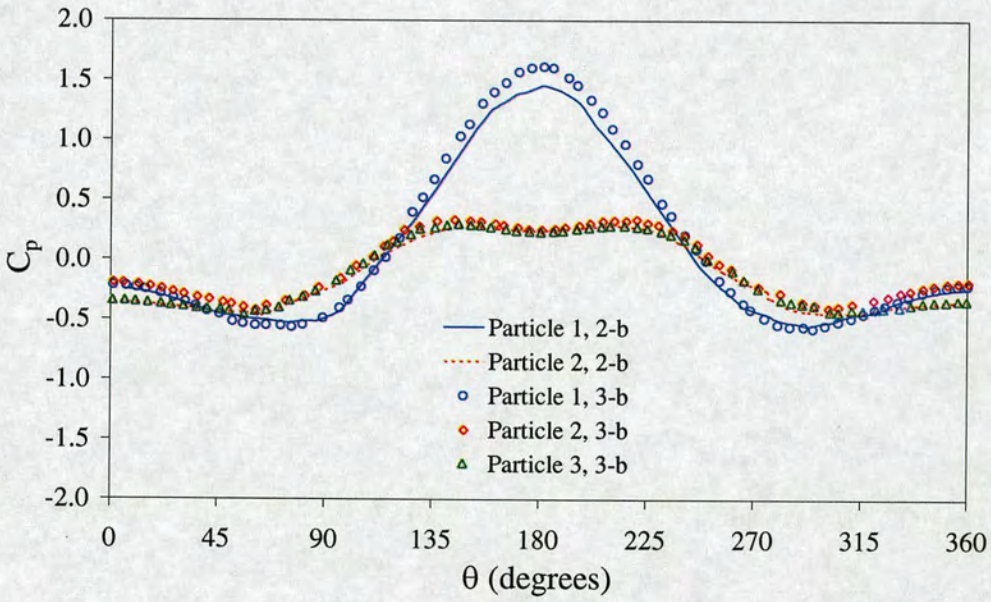

(b)

Fig. 4.5 Three fixed particles at D_o = 2 and θ = 0°. (a) Pressure coefficients contours and (b) pressure coefficients profiles.

Figure 4.6, shows the contour and profiles of the pressure coefficients for three-particle system, arrange in a triangular geometry. The line connecting the centres of Particle 1 and particle 2 is perpendicular to the main flow direction. The sides of the equilateral triangle is $D_o = 2$. Figure 4.6(a) shows high pressure on particles 1 and 2. Low pressure is found over particle 3. Quantitative values of pressure distribution coefficients are compared with the pressure coefficients from the two–particle system at $\theta = 90^o$. As shown in Figure 4.6(b) particles 1 and 2 show same trend as particle 1 and particle 2 in two-particle systems interactions (2-b). Higher values of pressure are found on particle 1 from three-particle system between $\theta = 0^o$ and $\theta = 240^o$ compared to particle 1 from two-particle system interaction. When the pressure profile of particle 2 from three-particle system is compared with pressure profile of particle 2 from the two-particle system, high pressure values are observed between $\theta = 120^o$ and $\theta = 360^o$ for particle 2 in the three-particle system. Very low pressure values are noted over particle 3 in the range of $95^o \leq \theta \leq 265^o$, but in the ranges of $0^o \leq \theta \leq 95^o$ and $265^o \leq \theta \leq 360^o$ slightly higher values of pressure over particle 3 is observed.

In all cases studied here, similar qualitative trends are showed for the pressure coefficient profiles on particle 1 and particle 2 in the presence of a third compared with those obtained from a two-particle system, but small quantitative differences are found between the two systems. In a three-particle system higher pressure is experienced on particles 1 and 2 than in two-particle system as shown in Figure 4.5 and 4.6.

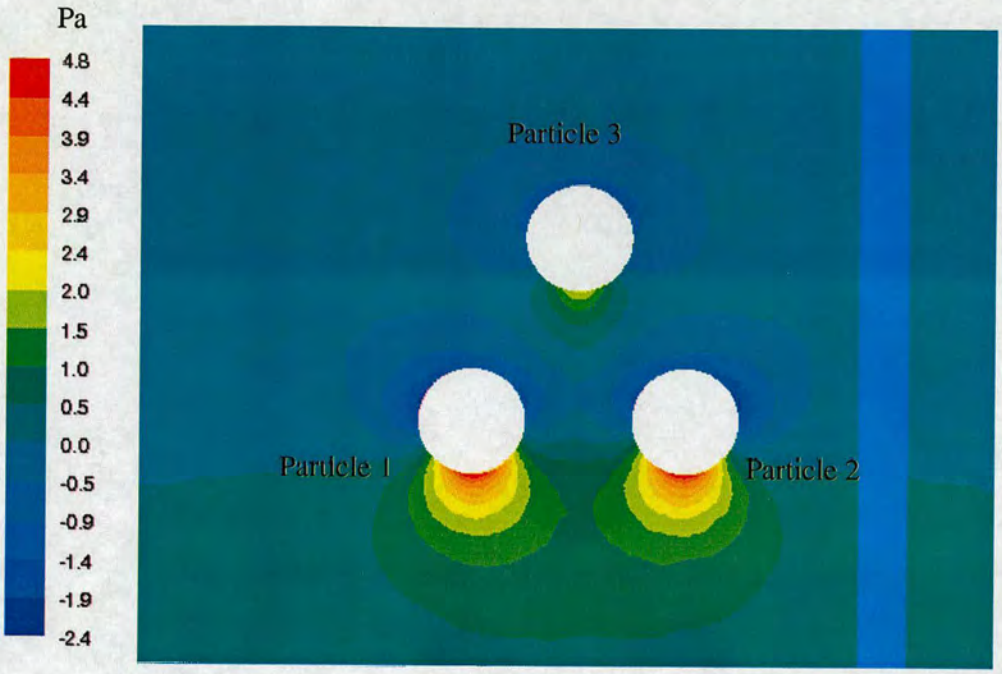

(a)

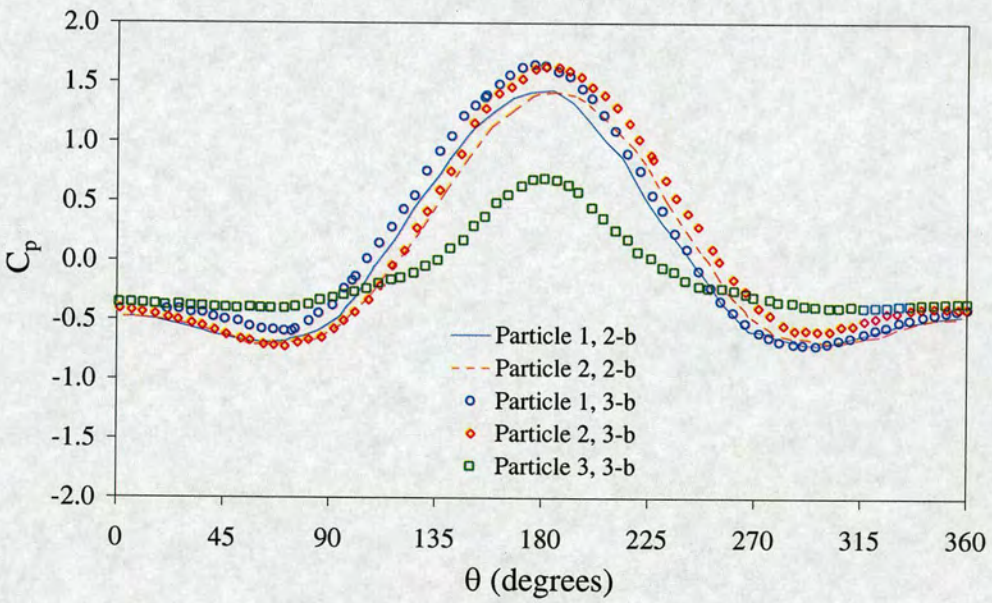

(b)

Fig. 4.6 Three fixed spherical particles arrange in an equilateral triangle separated at $D_o = 2$ and $\theta = 90^o$: (a) contours and (b) profiles.

4.3.3 Wall shear stress coefficients for three interacting particles

Wall shear stress (WSS) force is an important component of the total force acting on a body immersed in a fluid flow. Thus, similarly to velocity field and pressure coefficients, presented in previous sections 4.3.1 and 4.3.2, contours and profiles of wall shear stress coefficients are presented in figures 4.7 and 4.8 for three particles in line formation and triangular configuration at the same particle separation distance and angle.

Figure 4.7 depicts the wall shear stress coefficient contours and profiles for three particles aligned with main flow direction ($\theta = 0^o$), separated at $D_o = 2$. Figure 4.7(a) shows the wall shear stress coefficient contours, considerably higher values are observed for particle 1 compare with the values of particles 2 and 3. Plots of wall shear stress coefficients are shown in Figure 4.7(b); this figure shows qualitatively difference between particle 1 and particles 2 and 3. Great difference is observed between particle 1 and particle 3, the maximum wall shear stress coefficient difference between these two particles is around 45%, for this specific case. A very small difference on wall shear stress coefficients is found between particle 2 from two-particle system and particles 2 and 3 from three-particle system. Particle 1 from three-particle system shows a similar wall shear stress coefficients pattern to that of particle 1 from two-particle system, but significant difference is observed close to the stagnation point, between $\theta = 165^o$ and $\theta = 195^o$, the maximum difference is around 18% found at $\theta = 180^o$.

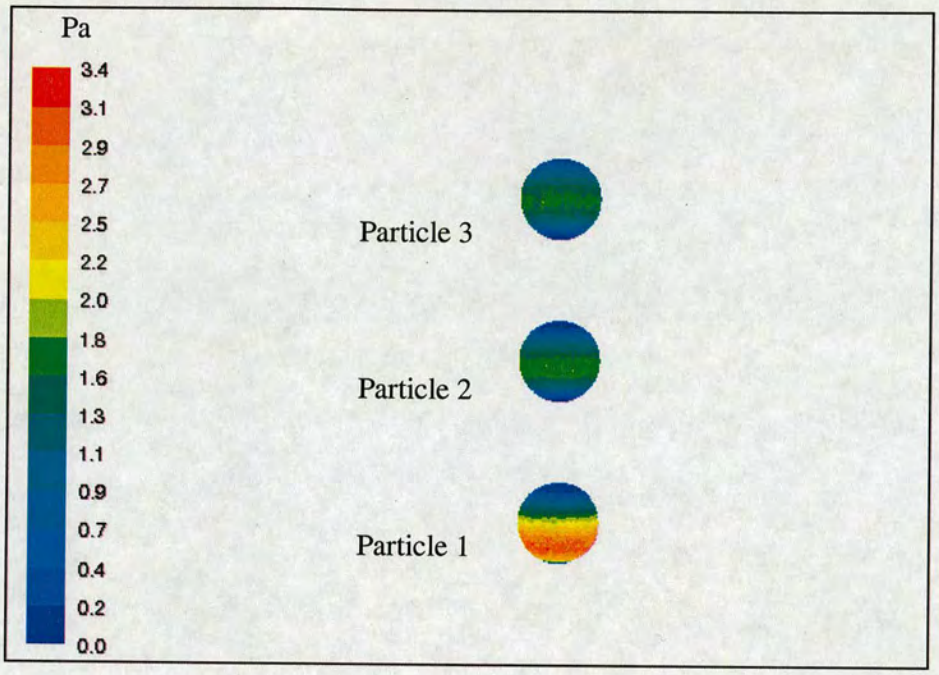

(a)

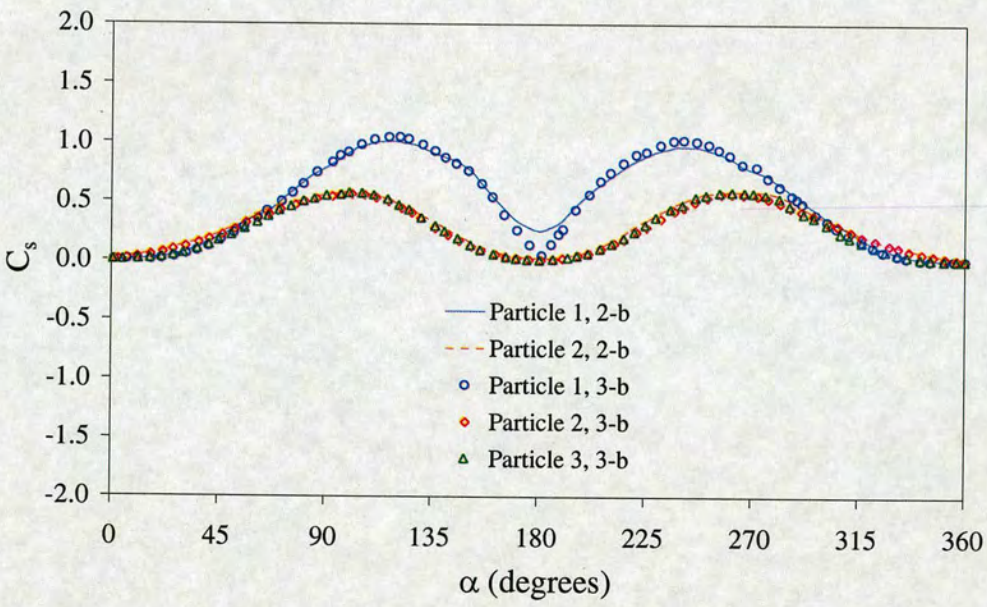

(b)

Fig. 4.7 Wall shear stress coefficients for three fixed spherical particles in line formation ($\theta = 0^o$), separated at $D_o = 2$: (a) contours and (b) profiles.

Figure 4.8 shows the wall shear stress coefficient of three spherical particles placed in the corners of an equilateral triangle with sides length of $D_o = 2$. For this case, the line connecting the centres of particle 1 and particle 2 is normal to the main flow direction. Figure 4.8(a) illustrates graphically the wall shear stress coefficient over the three interacting particles; high wall shear stress is shown on particles 1 and 2, with lower values over particle 3. The wall shear stress coefficient profiles on particle 1 and particle 2 show similar trends to those found in two-particle system, except close to the upstream stagnation point ($\alpha = 180^o$), where lower values are found for particle 1 and 2 compared with those values observed for two-particles system. The maximum difference between these values is around 17%. Close to the rear stagnation point, higher values of wall shear stress between $\alpha = 0^o$ and $\alpha = 45^o$ for particle 1 are found and higher values of wall shear stress coefficients in the range of $\alpha = 315^o$ and $\alpha = 360^o$ for particle 2 are also noted.

In general, for all cases studied in this work the wall shear stress for three-particle system show differences to those found in two-particle system in some extent. Most of the results from a three particle hydrodynamic interactions exhibited higher mean values of wall shear stress coefficients than the values obtained from a two-particle system. Thus, higher interacting forces between three particles could be expected.

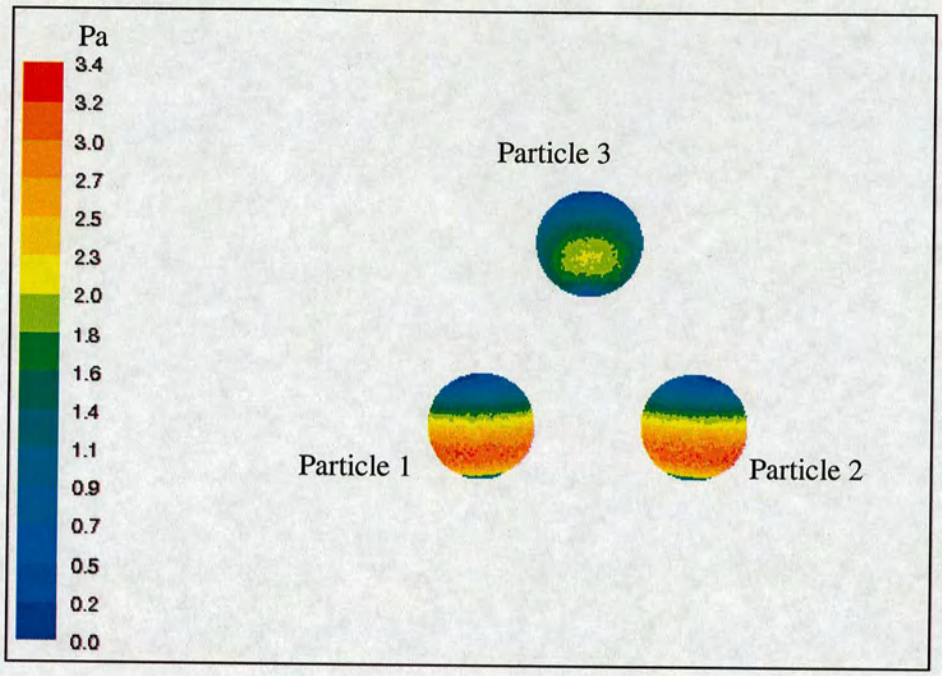

(a)

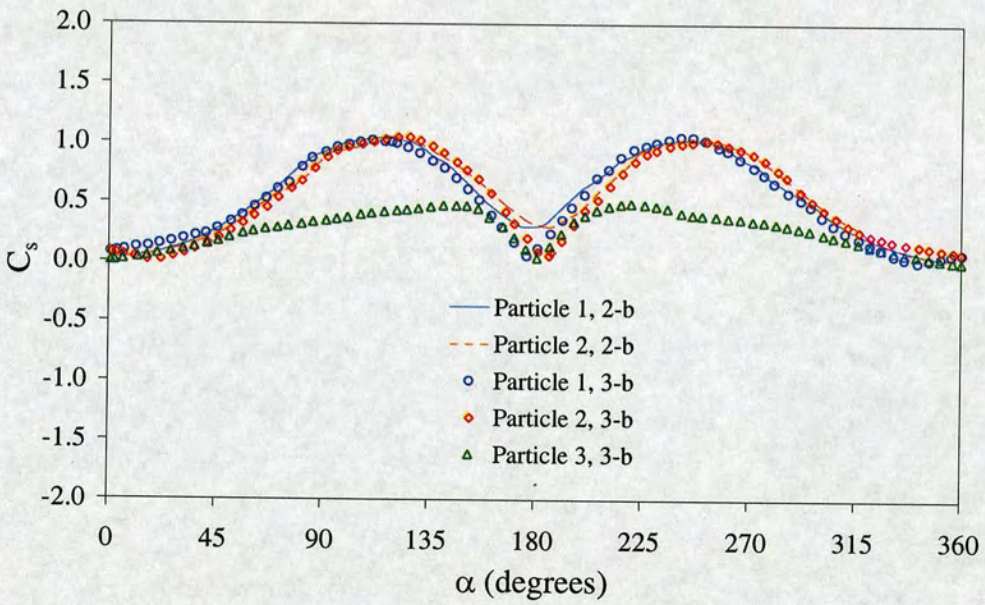

(b)

Fig. 4.8 Wall shear stress coefficients for three fixed spherical particles in triangular formation at $D_o = 2$ and $\theta = 45^o$: (a) contours and (b) profiles.

4.3.5 Drag and lift forces: three-particle system vs. two-particle system

At this point, it is possible to state that different forces over the particles can be obtained from a three-particle system compared to those found in a two-particle system, because the velocity field generated by the presence of a third particle is transmitted through the fluid and influences the forces on the other two particles. How much does a third particle contribute to the hydrodynamic interaction on a pair of particles? A suitable approach to try to answer this question is comparing the drag and lift force from the two systems. The drag and lift forces are used to evaluate the interactive force between particles. An approximation to a three-particle system from the two-particle system is needed. Thus, to mimic a three-particle system from two-particle system, one of the two particles is placed at two different positions. Figure 4.9 show the two-particle system in a "virtual" equilateral triangular formation, similar methodology is applied to form a "virtual" three-particle system in line formation from two-particle system, see appendix 4. The drag and lift forces are evaluated over the reference particle (particle 1 in Figure 4.9), under the influence of these two different positions and they are compared with the three-particle system. The methodology to evaluate the forces over the reference particle, from the mimic three-particle system is described in detail in the appendix to chapter 4.

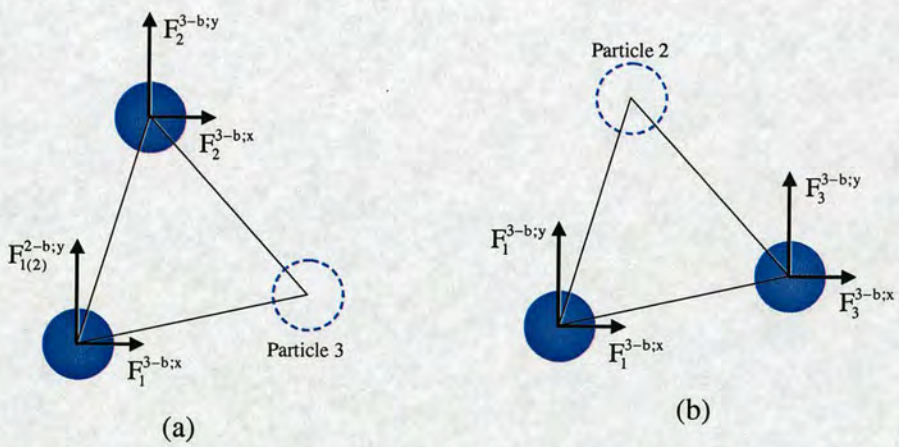

Fig. 4.9 Two interacting particle system in a "virtual" equilateral triangular formation, (a) particles 1 and 2 and, (b) particles 1 and 3.

The equations employed to calculate the drag and lift forces over the reference particle from the two-particle system are obtained in the appendix to chapter 4.

Drag force (y direction):

$$F_{1(23)}^{3-b;y} = F_{1(2)}^{2-b;y} + F_{1(3)}^{2-b;y} - F_{s}^{1-b;y} \tag{4.1}$$

Lift force (x direction):

$$F_{1(23)}^{3-b;x} = F_{1(2)}^{2-b;x} + F_{1(3)}^{2-b;x} - F_{s}^{1-b;x} \tag{4.2}$$

where

$F_{1(23)}^{3-b;y}$ = drag force over particle 1 due to particle 2 and 3 in a mimic three-particle system.

$F_{1(23)}^{3-b;x}$ = lift force over particle 1 due to particle 2 and 3 in a mimic three-particle system.

$F_{1(2)}^{2-b;y}$ = drag force over particle 1 due to particle 2 in a two-particle system.

$F_{1(2)}^{2-b;x}$ = lift force over particle 1 due to particle 2 in a two-particle system.

$F_{1(3)}^{2-b;y}$ = drag force over particle 1 due to particle 3 in a two-particle system.

$F_{1(3)}^{2-b;x}$ = lift force over particle 1 due to particle 3 in a two-particle system.

$F^{1-b;y}$ = drag force over a single particle.

$F^{1-b;x}$ = lift force over a single particle.

In order to compare the forces, both drag and lift force are normalized by the dynamic pressure and the sphere cross-section area as shown in chapter 3, equation 3.6. The drag coefficient (C_d) is normalized by the drag coefficient of a single particle (C_{ds}) at the same particle Reynolds number, whereas the lift coefficient (C_L) is left unchanged.

Figure 4.10 depicts the drag ratio ($C_{d1(23)}/C_{ds}$) and the lift coefficients obtained from the mimic three-particle system and the actual three-particle system in line formation ($\theta = 0^o$) as a function of the particle separation distance (D_o). In the figure, the drag and lift forced were obtained over particle 1 (blue circle) due to the hydrodynamic influence force from particle 2 and 3. Figure 4.10(a) shows the drag forces, the greatest difference occurs at small particle separation distance, the maximum difference is less than 12%. Minimal variation is observed for large particle separation distances ($D_o > 2$), for $D_o = 8$ this variation is of the order of 2%. The lift coefficient variation could not be evaluated; the force in the x direction for this configuration is too small as show in Figure 4.10(b). However, this condition rapidly changes as the angle (θ) increases.

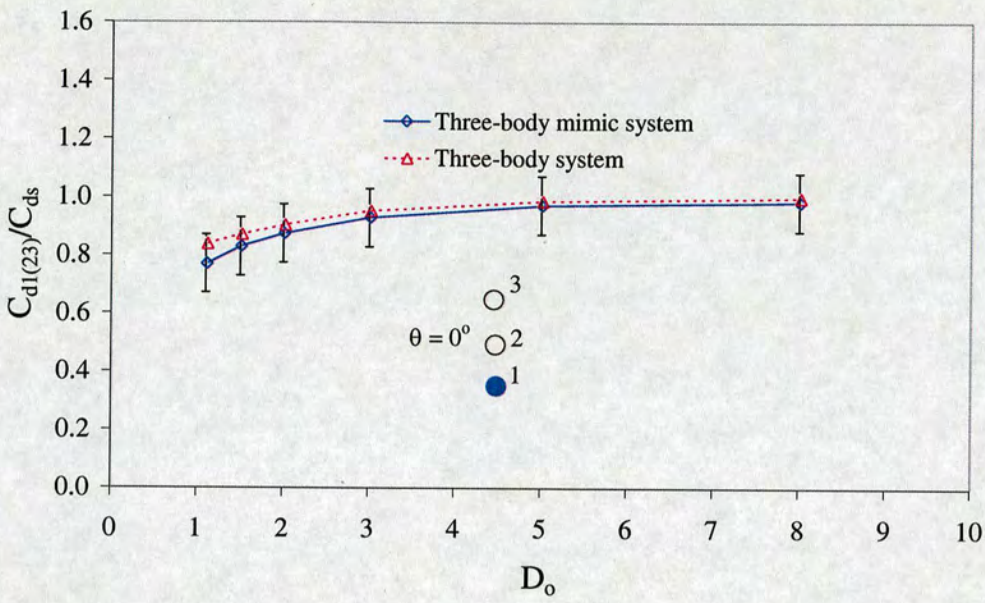

(a)

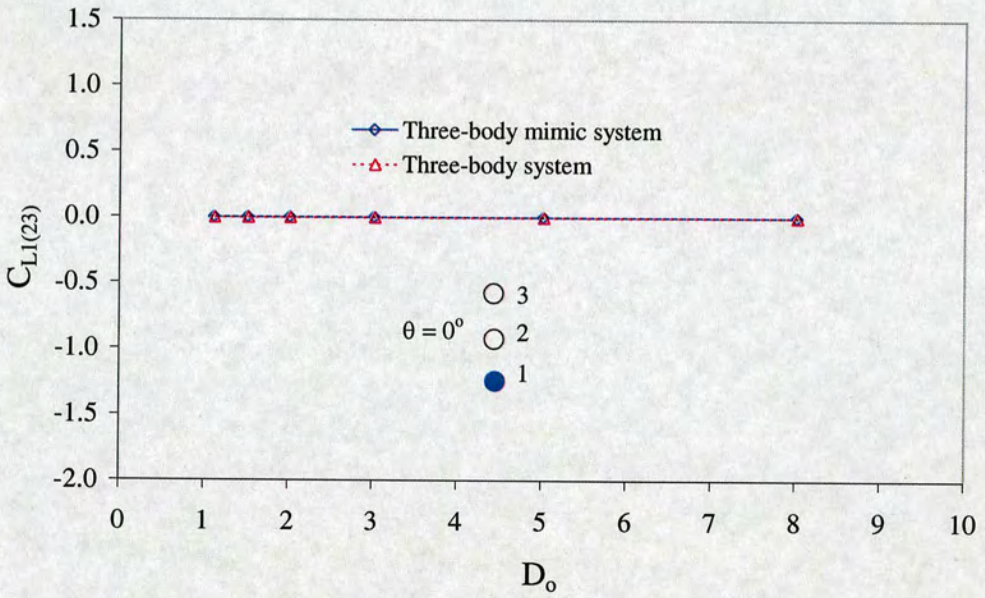

(b)

Fig. 4.10 The (a) drag ratio and (b) lift coefficient for two-particle and three interacting particle system in line formation at $\theta = 0^o$.

Figures 4.11, 4.12 and 4.13 illustrate the drag ratio and lift coefficients obtained from two and three interacting particles system with particles in line at $\theta = 30^{o}$, 60^{o} and 90^{o} as a function of particle separation distance (D_o). The same trend in the drag ratio for the three different angles ($\theta = 30^{o}$, 60^{o}, 90^{o}) as in Figure 4.10 is found, maximum difference in drag force between the two systems is observed at small separation distances, between 10% and 3% for $D_o < 2$ and smaller difference is experienced at $2.0 < D_o < 8.0$, see Figures 4.11(a), 4.12(a) and 4.13(a). Although, lift forces at these angle positions become significant, the difference between the two systems is well under 2% for the whole range of particle separation distances ($1.1 \leq D_o \leq 8$) as shown in Figures 4.11(b), 4.12(b) and 4.13(b). In general, it is observed that the angle position (θ) in the in line formation has a minimal influence in the lift forces. In the other hand, moderate variation is found in the drag forces, with large difference (~10%) at short particle separation distances ($D_o < 2$) and less than 3% difference at larger particle separations.

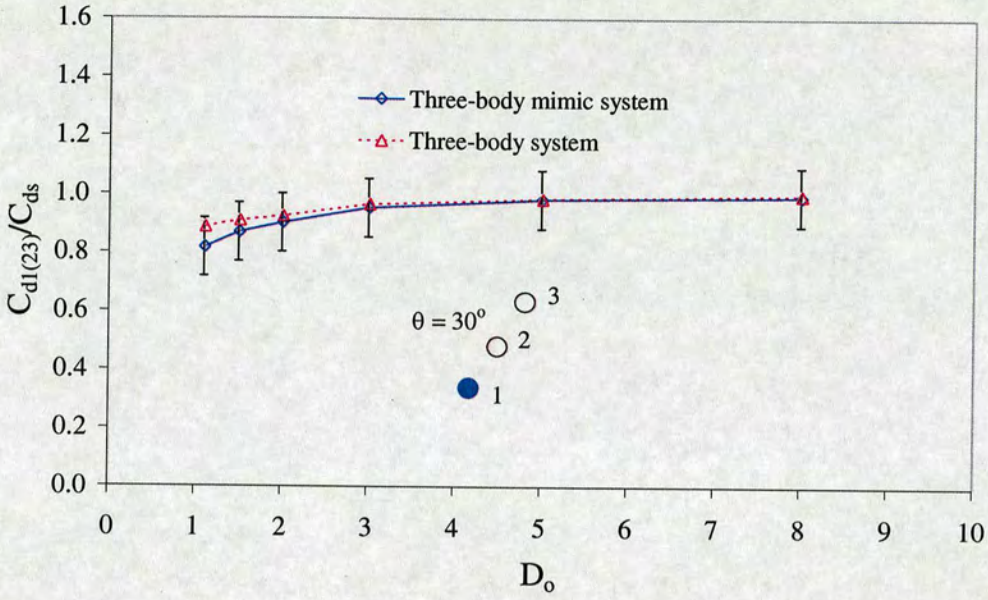

(a)

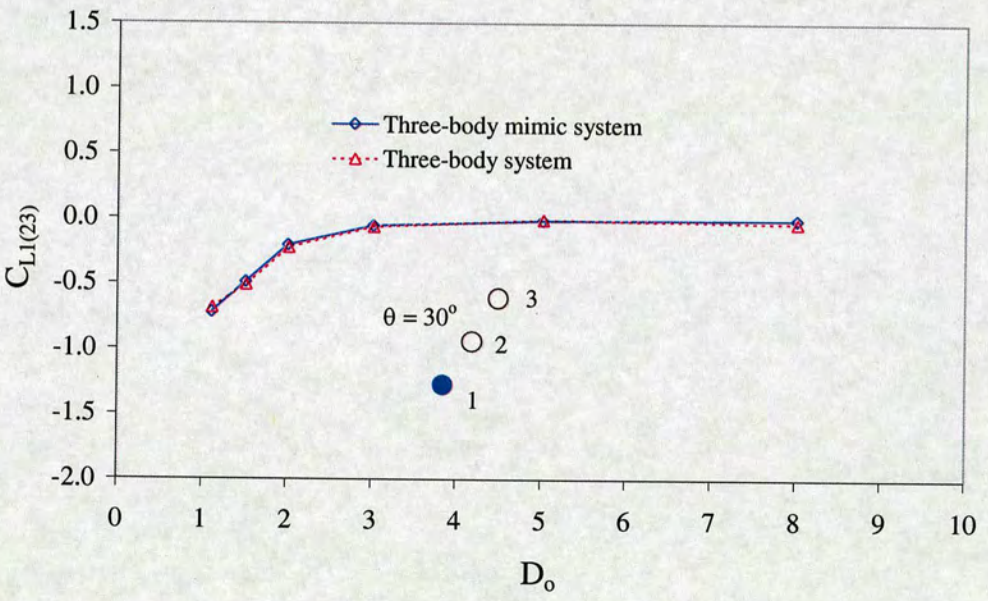

(b)

Fig. 4.11 The (a) drag ratio and (b) lift coefficient for two-particle and three interacting particle system in line formation at θ = 30°.

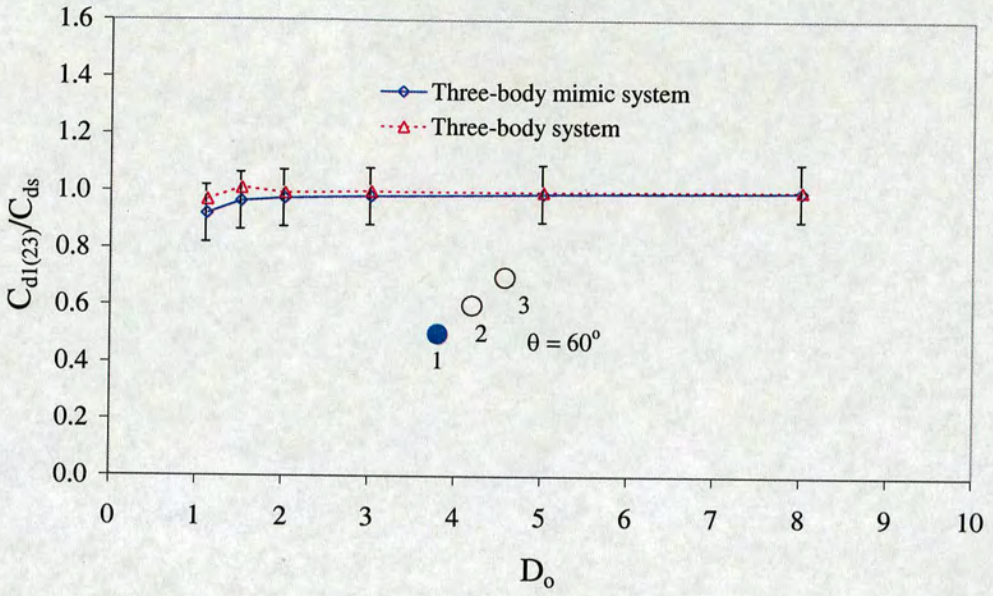

(a)

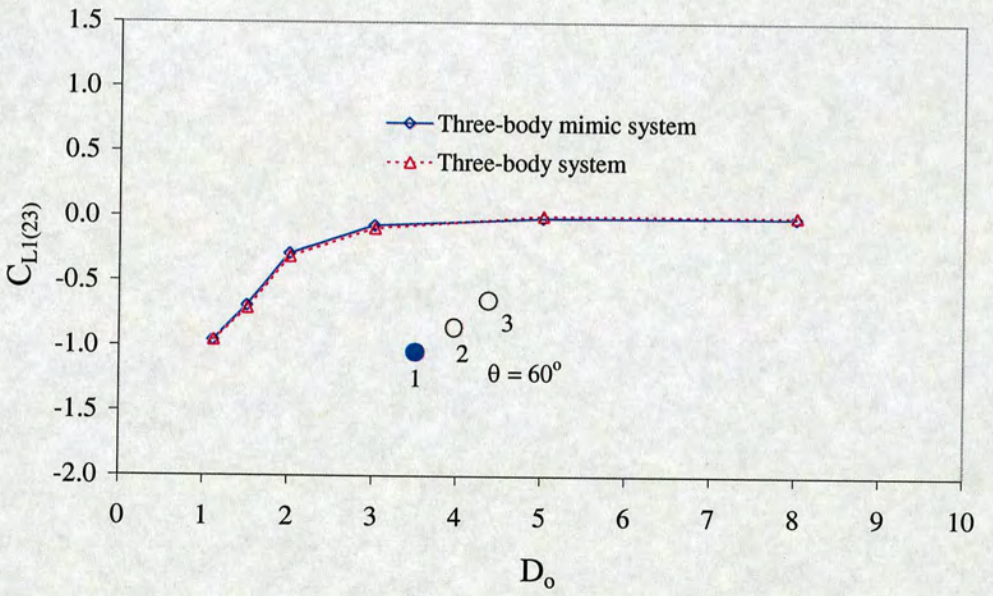

(b)

Fig. 4.12 The (a) drag ratio and (b) lift coefficient for two-particle and three interacting particle system in line formation at θ = 60°.

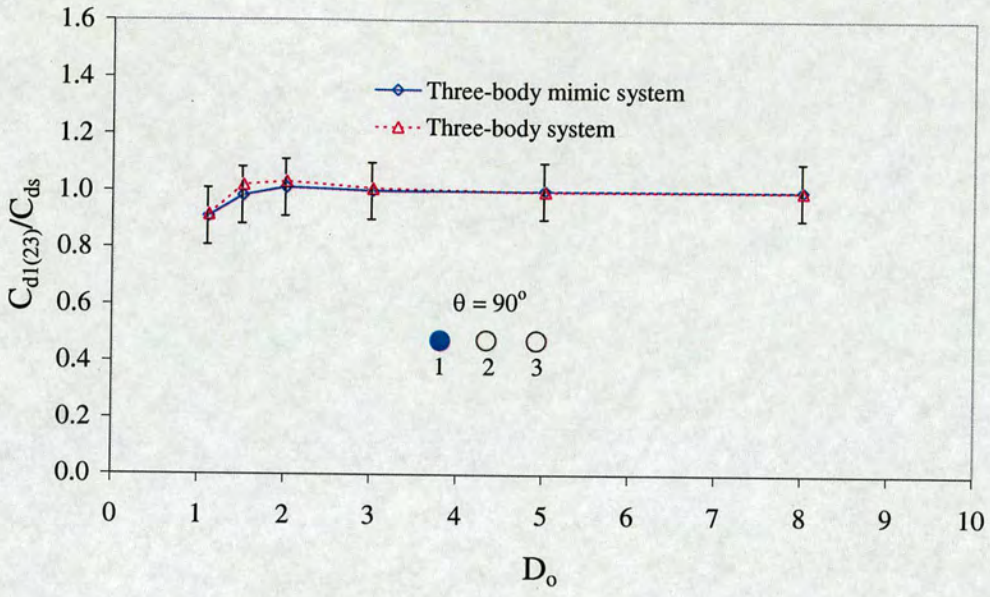

(a)

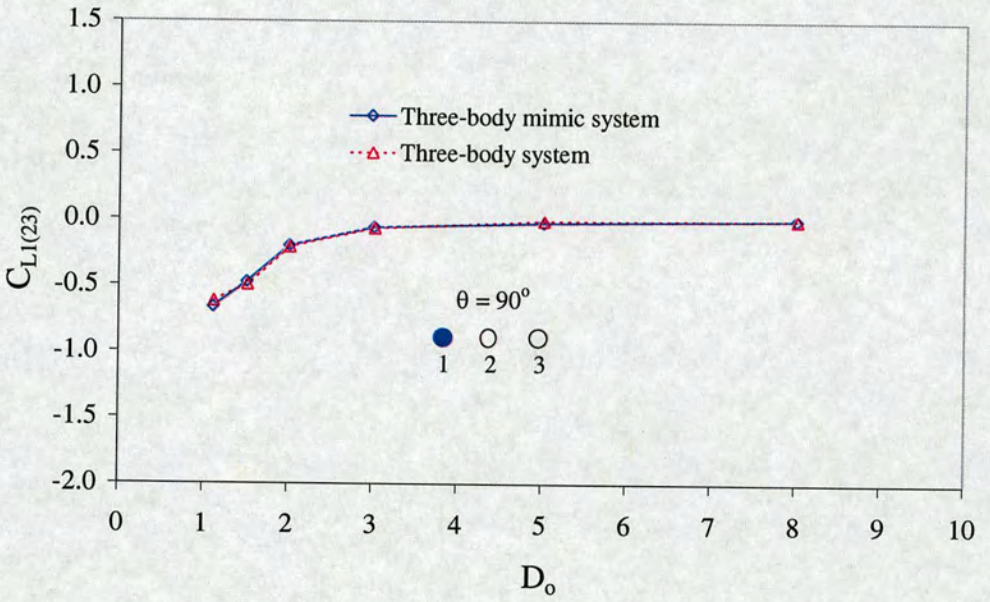

(b)

Fig. 4.13 The (a) drag ratio and (b) lift coefficient for two-particle and three interacting particle system in line formation at θ = 90°.

In order to verify the drag and lift forces sensitivity to the geometry formation, an equilateral triangle configuration was used. Figures 4.13, 4.14 and 4.15 depict the forces over a particle in the three interacting particles mimic system and in the actual equilateral triangle formation at different angle orientations as a function of the particle separation distance ($\theta = 0^o$ and 90^o).

Figure 4.13 shows the drag and lift forces over particle 1 (blue particle) at $\theta = 0^o$, which means that particle 1 and particle 3 are aligned with the main flow direction, whilst particle 2 is located mid-way besides particle 1 and 3. The drag force follows the same trend for both systems with a maximum difference of 3% in the whole distance range ($1.1 \leq D_o \leq 8$). Similar tendency is observed in the lift force with an excellent correlation between the two systems, except for $D_o = 1.1$ where the difference is around 14%.

Figure 4.14 illustrates the forces on particle 1 for an equilateral triangle arrangement at $\theta = 90^o$, for this case particle 1 and particle 3 are perpendicular to the main flow direction and particle 2 is locate downstream of particle 1 and 3. Figure 4.14(a) shows the drag ratio, in this case the larger difference between the two systems exist at small particle separation distances with a maximum value of 11% at $D_o = 1.1$. Of course the minimum difference is found at $D_o = 8$ with less than 1% in variation. On the other side, Figure 4.14(b) exhibits an excellent agreement between the two systems for the lift force between $D_o = 2$ and $D_o = 8$. However for smaller particle separation distances ($D_o < 2$), considerable discrepancy is found, which is probably is caused because the flow treats the three particles as a single big body. The high pressure region that occurs in front of particle 1 and particle 3 is united to form a large zone of high pressure. So does the low pressure region behind these two particles. These conditions increased the streamwise pressure gradient and decreased the drag wall shear stress (WSS). Form drag (pressure) at low particle Reynolds number occupies a small part of the total drag, Tsuji *et al.* (2003). Thus, this is considered as a possible explanation for the drag coefficient reduction for particle separation distances less than two particle diameters.

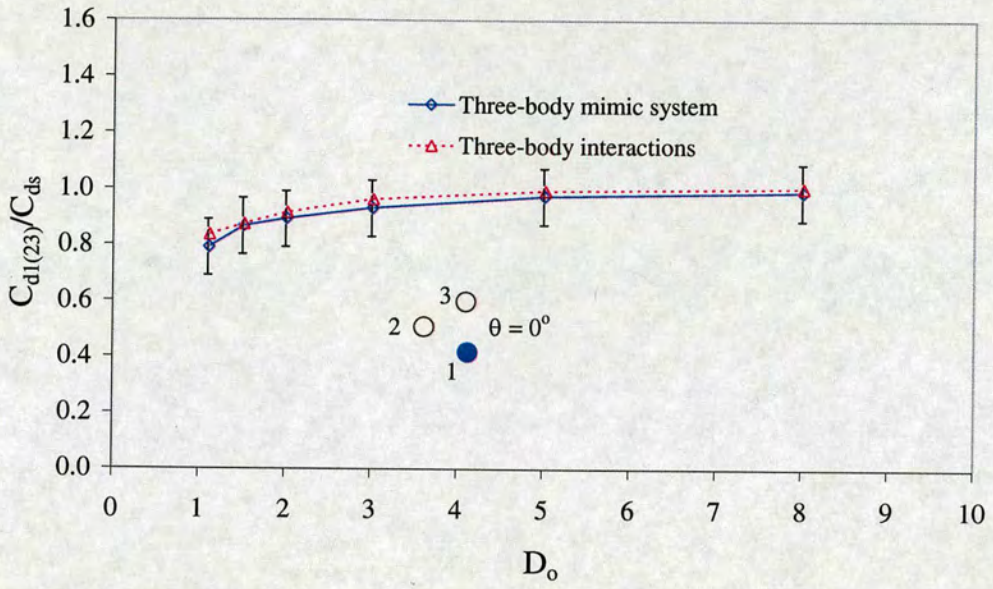

(a)

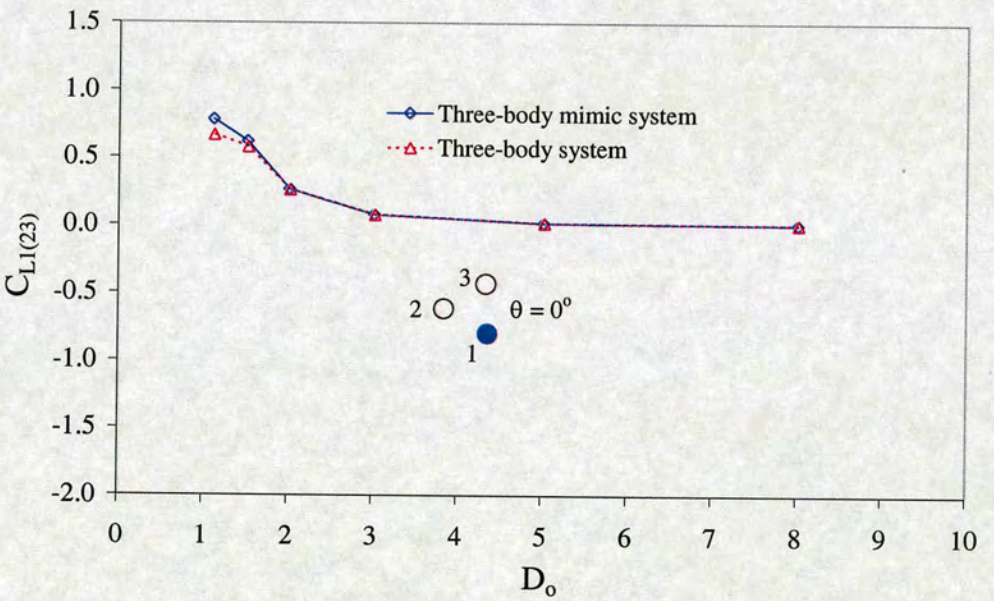

(b)

Fig. 4.14 The (a) drag ratio and (b) lift coefficient for two and three interacting particle system in equilateral triangle formation at θ = 0°.

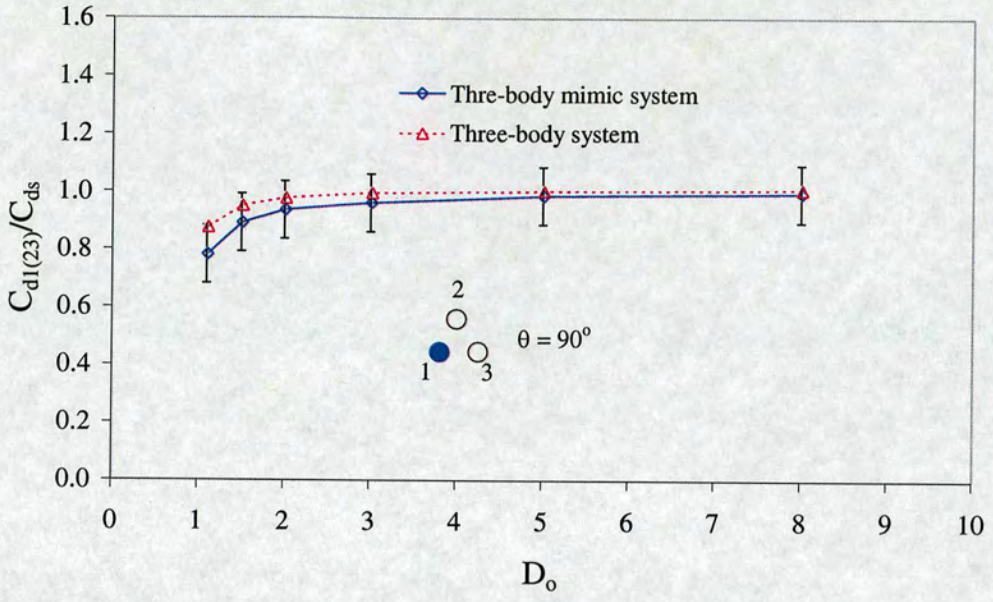

(a)

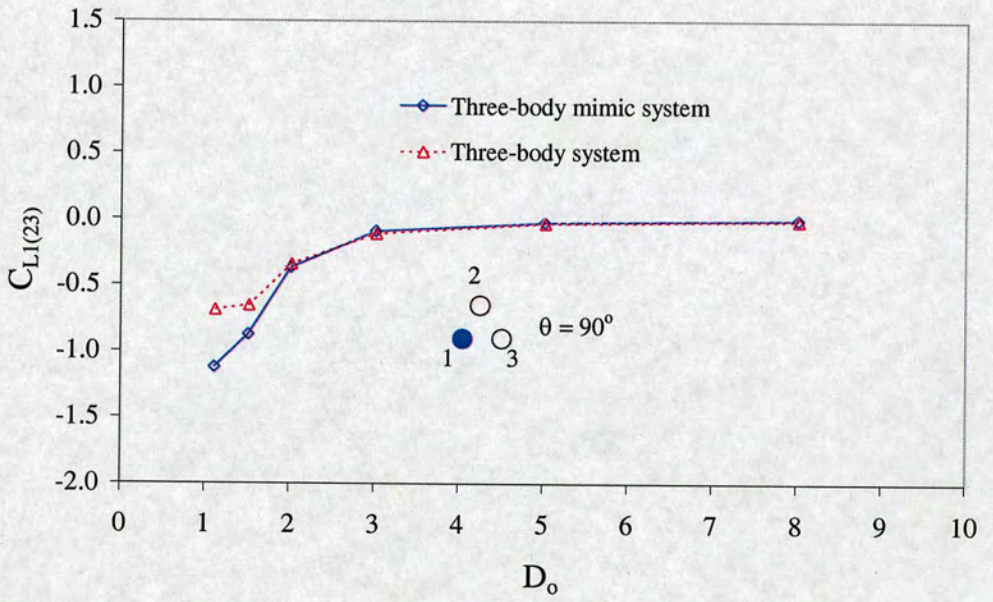

(b)

Fig. 4.15 The (a) drag ratio and (b) lift coefficient for two and three interacting particle system in equilateral triangle formation at θ = 90°.

Figure 4.15 shows the drag and lift forces over particle 2 in an equilateral triangle formation, the equilateral triangle orientated at the same angle as the above figure. A different pattern is observed in this case, minimal variation at small particle separation distances ($D_o < 3$), a relative slight difference for larger particle separation distances ($D_o > 3$), but no more than 4%. A possible explanation for this trend is the nozzle effect phenomenon. Results from two particles placed side-by side showed that the nozzle effect start appearing between $D_o = 2$ and $D_o = 3$, completely established between four and six particle diameter separations and start disappearing between $D_o = 7$ and $D_o = 8$, for this reason smaller variation is observed at $D_o = 8$. See appendix to chapter 3 for an evolution of the nozzle effect base on the velocity profiles. On the other hand, because of the symmetry flow on particle 2, virtually zero lift force is observed over this particle for three-particle mimic system and for the actual three-particle system, Figure 4.15(b).

According to the data display from Figure 4.9 through Figure 4.15, particle configuration and orientation seems to play a reasonable moderate influence in the patterns of the drag and lift forces from the two systems.

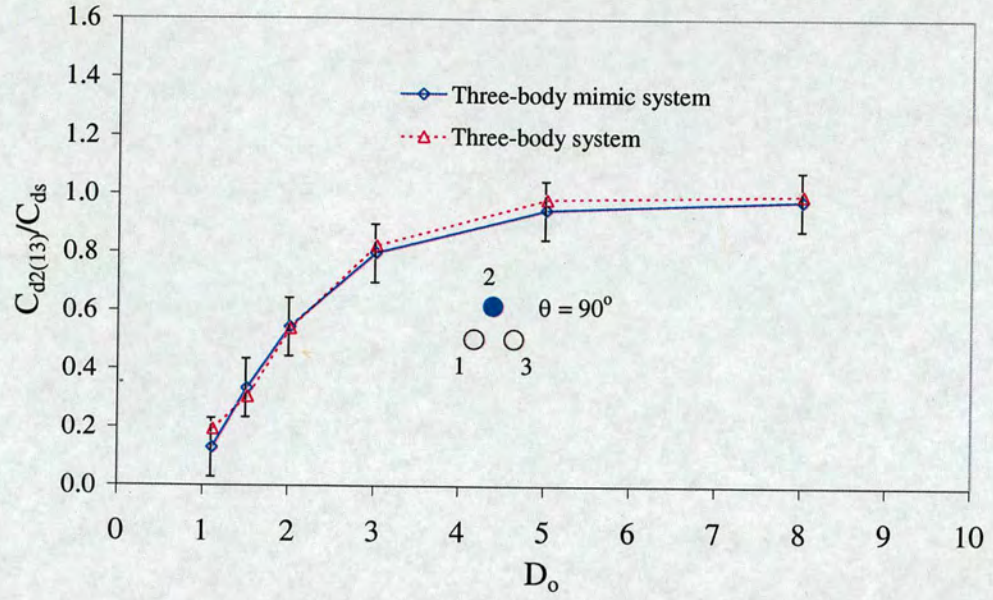

(a)

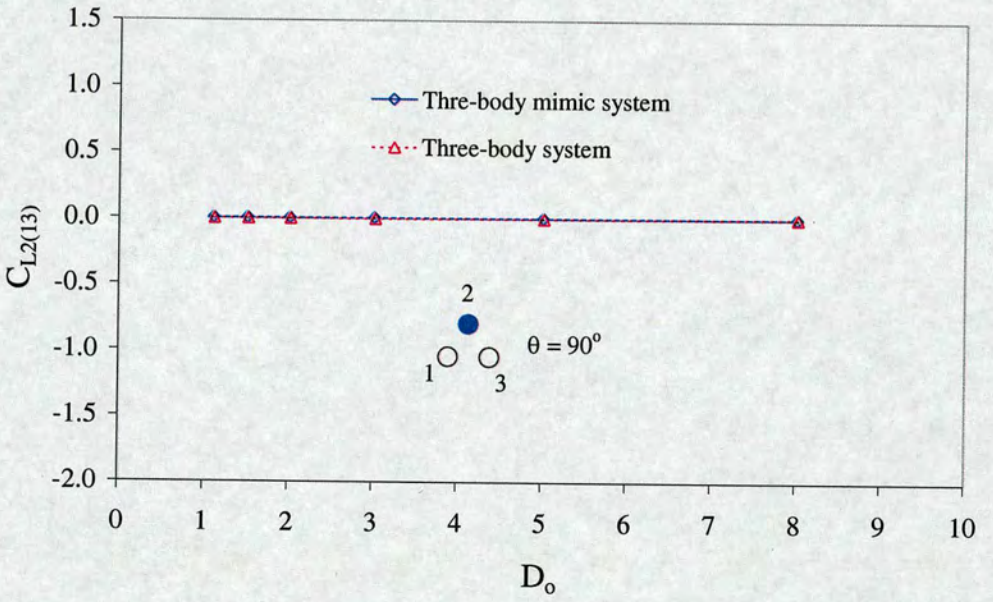

(b)

Fig. 4.16 The (a) drag ratio and (b) lift coefficient for two and three interacting particle system in equilateral triangle formation at θ = 90°.

4.4 Conclusions

Numerical simulations on a system of three fixed interacting particles have been carried out using a commercial CFD program, FLUENT V6. The study has primarily concentrated on observing qualitatively and quantitatively the hydrodynamic influence of three particle interactions over two particle interactions arrangement. Qualitative information of the three interacting particle system has been shown through flow velocity field, pressure coefficient and wall shear stress coefficient contours, whilst the quantitative difference has been made out through velocity, pressure and wall shear stress profiles.

In order to find the force difference between two and three-particle system, a quantitative comparison in section 4.3.5 of the drag and lift forces had been done. An easy way to calculate the forces on a particle in a mimic three hydrodynamic interacting particles has been proposed, the method is quite flexible and could be adapted to different multiple particle geometries very easily, see appendix to chapter 4 for a complete description of this method. As reported by Figure 4.10 through Figure 4.15, it is clear that the forces on particles from three mimic particle system always bring in an excellent qualitative trends compare with the forces from the actual three-particle system, but slight differences arise for small particle separation distances ($D_o < 3$), which is less than 10% in most of the cases studied here. Since a relative small difference in drag and lift force between the two systems is found the interacting forces obtained from the two-particle system could be used in multiple particle Monte Carlo simulations without much loss of accuracy. Some additive interacting forces approximations based on a pair particle system have been applied successfully in other research areas using the Monte Carlo method, e. g., Chun (1999), Philips (1995) and Camp (2003, 2006).

CHAPTER 5

5. MONTE CARLO SIMULATIONS: MULTIPLE PARTICLES

Along with the problem setup, a brief description of the Monte Carlo method is given in this chapter. The methodology used to obtain the pairwise potential energy function $U(r,\theta)$ from CFD simulations of two fixed spherical particles is also presented. The pairwise potential energy function is used to simulate many particles interactions using the canonical (NVT) ensemble Monte Carlo method. Multiparticle Monte Carlo simulations at different granular temperature (T_g) and different particle volume fractions (α_p) are carried out. Qualitative information about the final particle structure of the system in equilibrium is given by snapshots and the radial distribution function $g(r)$ is used to explore the particle structure quantitatively. The calculated equilibrium is verified by examining the potential energy using the binning diagnostic tool. The results are qualitatively compared with some relevant experimental data reported in the literature and finally some conclusions from the canonical (NVT) ensemble Monte Carlo simulations are obtained.

5.1 Introduction

Nowadays, two-phase modelling is experiencing rapid development thanks to worldwide research activity in physics, mathematics, computer science and engineering. Thus simulation is widely used to analyze very complex systems, such as two-phase flows. Many modelling methods and strategies have been used to

simulate two-phase flows: some of these have reproduced the behaviour of a small number of particles very well, from a few hundreds in 3D to a few thousands in 2D, for instance using the DNS (direct numerical simulation) method Hu *et al.* (1992), Hu (1996), Johnson & Tezduyar (1996) and Choi & Joseph (2001). For a comprehensive list on multiparticle simulations the reader is referred to section 2.4.5 in chapter 2. Apart from DNS simulations, the existing approaches to modelling two-phase flows can be classified into two main categories: the Two-Fluid Model (TFM) and the Discrete Approach (DA). The later includes, the Euler-Lagrange (E-L) method, lattice-gas automata method (LGA), Lattice Boltzmann Method (LBM), Monte Carlo (MC) simulations, Discrete Element Method (DEM) and Discrete Particle Simulation (DPS).

Most of today's numerical simulations on multiple particle interactions do not include the hydrodynamic interaction force due to particle-fluid-particle interaction, which comes directly from drag and lift forces (equation 3.8). The majority of these studies only include the drag force over the particles, but in a multiparticle system, the presence of other particles shows that the interacting force between particles could play an important role in particle interaction in two-phase flows. Kim *et al.* (1993), Folkersma *et al.* (2000), Vargas & Easson (2005) and a recent paper published by Prahl *et al.* in 2007, stated the need for new models to take into account the lift and drag force within the particle hydrodynamic interactions in two-phase numerical models.

In order to gauge the importance of the hydrodynamic force due to particle-fluid-particle interactions, especially at relative high particle concentration ($\alpha_p > 1\%$) and low particle Reynolds number ($Re_p = 15$) a basic study is required. Whilst DNS simulations provide detailed solutions for small number of particles, they are not scalable to large systems due to computer requirements. In chapter 3 extensive CFD simulations for two fixed spherical particles placed at different positions relative to each other have been carried out to obtain an interaction force as a function of the particles' relative position. This interaction force can be used to model a multiparticle system.

In principle, the study of a multiparticle system with an interaction force (attraction/repulsion) between two particles is identical to a molecular system, thus under this similarity two options become evident: Molecular Dynamics (MD) simulation and Monte Carlo (MC) simulations. The choice between these two methods is largely determined by the phenomenon under investigation and the information required. MD simulations give configurational distribution and dynamical information of the system, but in order to obtain this information of a collection of particles, the forces acting on each particle are required, which obviously can be obtained by integrating Newton's equations of motion. On the other hand, MC simulations can only give information about the configuration distribution of the system (i.e., the statistical distribution of final particle positions). No dynamical information is possible. The Monte Carlo method follows a statistical approach and only the adoption of an inter-particle potential to represent the interaction between the particles of system is required. An inter-particle potential can be obtained directly by integrating the interaction forces between two fixed spheres. As one of the objectives of this work is to measure the importance of the hydrodynamic interaction force in the stability of the ropes and clusters in coal transport after bends, the MC method is a suitable tool.

The Monte Carlo simulation method using random numbers has been applied to give approximate solutions to many problems. The method was firstly introduced by Newman, Ulam and Metropolis, Metropolis & Ulam (1949), Metropolis (1987) and Eckhardt (1987) to study neutron diffusion and since then the MC method has been used satisfactorily to model a large variety of problems, from pi (π) estimation, Wolfram Mathematica, (2007) to many other fields, including chemistry, biology, physics, engineering, and economics, Matsumoto & Saito (1970-1, 1970-2), Bird (1978), Satoh *et al.* (1996), Camp (2003, 2006), Hecquet *et al.* (2007).

5.2 Problem set up and numerical method

A series of MC simulations are carried out in a cuboidal box, whose size depends on the particle volume fraction ($\alpha_p = \pi/6D_o^3$). In all cases the largest dimension of the box is aligned with the flow direction, which is from the bottom to the top as show in figure 5.1. Figure 5.1(a) shows an initial particle structure configuration system containing 128 face centred cubic unit (FCC) cells (N_p = 512,) at D_o = 3 ($\alpha_p = 1.93\%$). Each face centred cubic cell unit contains four identical spherical particles as shown in Figure 5.1(b).

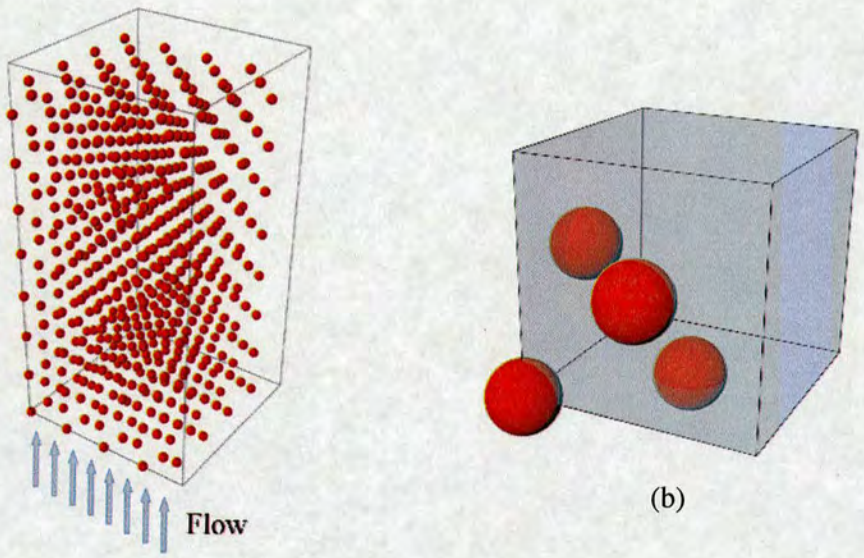

Fig. 5.1 Problem setup (a) cuboidal box with 128 unit cells (512 spherical particles) at D_o = 3 and (b) a typical face centred cubic unit.

A series of MC simulations are carried out in a cuboidal box by using the canonical ensemble (NVT). In the canonical ensemble, the number of particles (N_p), the volume (V) and the temperature (T) of the system are constant. In most of the cases, the number of particles of the system in this study is kept between 500 and 1000, with particle volume fractions typically found in roping phenomena ($0.24\% \leq \alpha_p \leq 1.93$). In order to observe the particle clustering and roping, the additive pairwise

potential $U(D_o,\theta)$ is applied. The volume fractions employed in the simulations are in agreement with typical concentrations at which roping phenomenon are observed in coal transport. Some simulations at lower volume fractions are also carried out ($0.015\% \leq \alpha_p \leq 0.1\%$). The Monte Carlo code used in this work was developed by Dr. Philip J. Camp (2007a) from the University of Edinburgh. The basic algorithms of the code are very general, and can be found in the standard molecular simulation literature, Allen & Tildesley (1987) and Frenkel & B. Smit (2002). Figure 5.2 shows a general algorithm for the Monte Carlo method used in this work.

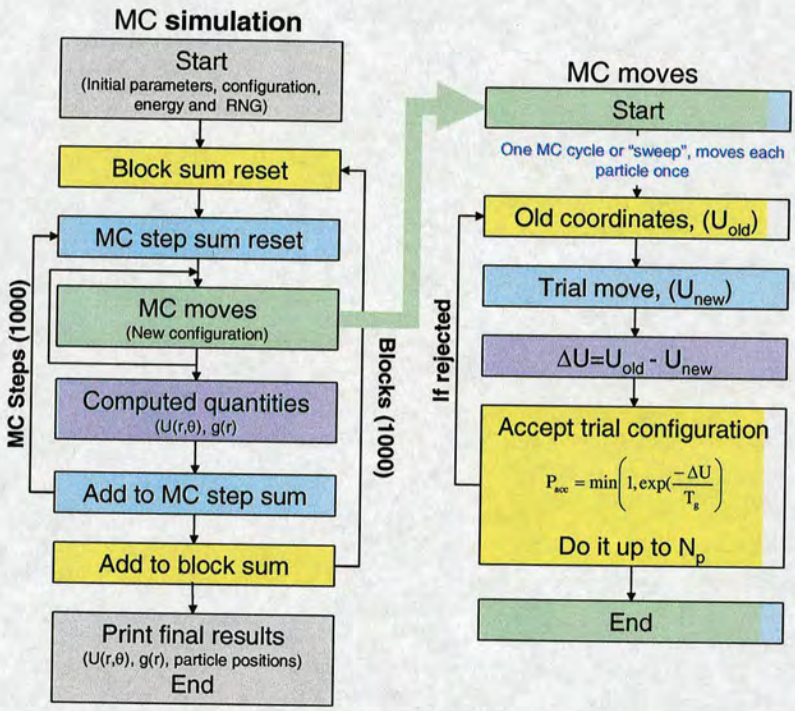

Fig. 5.2 General MC algorithm and acceptance/rejection diagram, after Kofke (2006).

Monte Carlo simulations require random or pseudo-random number generators (RNGs) with uniform distribution (0.0, 1). The MC code for this study uses a portable RNG designed by Marsaglia and collaborators; see Marsaglia *et al.* (1990) Marsaglia and Zaman (1993) and Marsaglia & Tsang (2004). This RNG employs two different integer seeds ij and kl, where $0 \leq ij \leq 31328$ and $0 \leq kl \leq 30081$.

Permutations of this seeds give 900 million sequences of pseudo-random values, each of length 10^{30}, and each of which is independent of the other.

Periodic boundary conditions (PBC) are applied to the system, Allen & Tildesley (1987). Figure 5.3 shows schematically the periodic boundary conditions in two-dimensions. In 3D the original cuboidal simulations box is replicated throughout space, thus the original simulation box and the replicated boxes form a bigger (infinite) system. During the simulation, when a particle in the original box is moved, its particle image in the surrounding replicated boxes is moved in exactly the same way. Some times the particles leave the original box, but one of its images enters the box through the opposite side. There are no walls at the boundary of the original box, thus there are no wall particle interactions. But the number of particles in the original system is conserved (constant N_p), and so in the virtual boxes. Due to the replicated boxes, an infinite number of particle images exist, but our attention is base only on the particles contained in the original box.

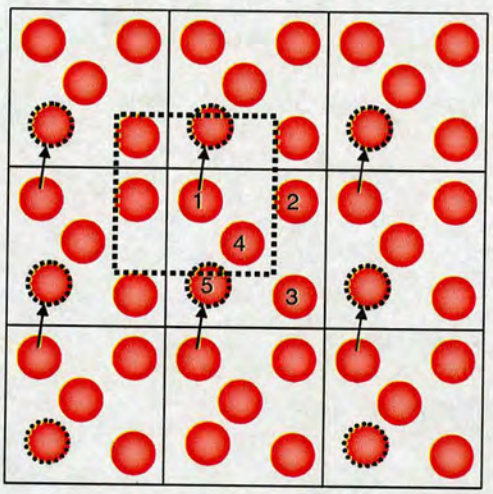

Fig. 5.3 Periodic boundary conditions and minimum image convention.

One of the most important parts of an MC simulation is the choice of potential energy function. In this work it is assumed that the potential energy is pairwise additive, ignoring three body interactions. E. g. consider particle 1 in Figure 5.3, first, the interactions between particle 1 and all the particles in the simulation box are

computed. In addition, the interactions between particle 1 and all the particle images in the replica box should be included, thus an infinite number of interactions exist and it is impractical to evaluate all of them. In order to deal with this unpractical situation, the minimum image convention (MIC) is applied. Therefore only those particles close to particle 1 are considered and the interactions with far distant particles can be ignored. For example, taking particle 1 as a centre, a box can be constructed with the same size and shape as the original box, see Figure 5.3 (dashed line square). Thus, only the interactions between particle 1 and all the other particles whose centre lie within this minimum convection box are considered. Consequently, there are only ($N_p - 1$) particles interactions involving particle 1.

Typically, MC simulations are carried out in steps called Monte Carlo steps (N_{step}), but for convenience in this work the MC code is organized in blocks (N_{block}), each block contains a specific number of Monte Carlo steps, $N_{step} = 1000$. Most of the simulations in this work are carried out until $N_{block} = 1000$. Every MC step includes several MC cycles; which depends on the number of particles in the system. During each MC cycle, a displacement attempt for each particle is made. The particle to be displaced is chosen randomly. In this work, the new trial particle coordinates are obtained randomly up to a maximum value of dr_{max}, which involves generating random numbers on the interval from -1 to 1 as shown in equation (5.1) for the three coordinates:

$$\begin{aligned} x_{new} &= x_{old} + \text{rand}(-1.0,1.0)\frac{dr_{max}}{L_x} \\ y_{new} &= y_{old} + \text{rand}(-1.0,1.0)\frac{dr_{max}}{L_y} \\ z_{new} &= z_{old} + \text{rand}(-1.0,1.0)\frac{dr_{max}}{L_z} \end{aligned} \tag{5.1}$$

The change in potential energy resulting from the trial displacement is the energy of the system with the particle at the new trail position (U_{new}) minus the energy of the system with the particle at its old position (U_{old}):

$$\Delta U = U_{new} - U_{old} \tag{5.2}$$

The change in potential energy is evaluated and the acceptance rule, based on the Metropolis criterion, is applied. If the move is accepted, the coordinates and the total potential energy of the system $(U \rightarrow U + \Delta U)$ are updated.

The Metropolis criterion can be summarised by the probability of acceptance of an attempted conformation:

$$P_{acc} = \min\left(1, \exp\left(\frac{-\Delta U}{T_g}\right)\right) \tag{5.3}$$

where T_g is the granular temperature in kg m^2 s^{-2}, defined as function of the mass of the particles and the rms velocity fluctuation, see equation (5.10).

If $\Delta U < 0$, $P_{acc} = 1$ and the move is accepted.
If $\Delta U > 0$, a random number is generated, rand(0.0, 1.0).
If rand $\leq \exp(-\Delta U / T_g)$, the move is accepted. If rand $\geq \exp(-\Delta U / T_g)$, the move is rejected and the old configuration is retained.

The acceptance rate is controlled by the maximum displacement (dr_{max}), because the displacements result in a potential energy change (ΔU). Very large displacements are unlikely to be accepted, but while small displacements are more likely to be accepted, progress towards equilibrium is very slow. For many systems a good rule of thumb is to adjust dr_{max} to give 50% of acceptance rate, this rule is applied in the code used in this study. Since it is hard to tell *a-priori* what the optimal value of the dr_{max} will be; this value is often adjusted once the MC simulations are underway.

An important question to ask when you are running MC simulations is "when is the system in equilibrium?" Useful diagnostic tools for MC simulation equilibration

detection have been reported in the literature, such as binning, autocorrelation and hot and cold starts. Binning accumulates separate averages over blocks of certain number of MC steps, and monitors for convergence of block averages. Autocorrelations, evaluate a correlation function $\langle \varphi(\tau)\varphi(0) \rangle$ for some observable φ. Hot and cold starts, check that the simulations starting from different configurations, e.g. random configurations and ordered configurations, converge to the same equilibrium, Berg (2006) and Camp (2007). The binning diagnostic tool is used in this work to verify the convergence of the MC simulations.

5.3 The potential energy function

Once a reliable energy potential function (U) is obtained, Monte Carlo simulations are straightforward. In chapter 3 a series of hydrodynamic interaction forces between two particles as function of angle (θ) and separations distance (D_o) were obtained. These data are used to obtain an analytic form of the potential energy as function of these two variables, U(r θ). In order to employ the common nomenclature used in MC simulations, in this chapter r is used instead of l, as the particle separation distance, thus r is defined as $D_o d_p$. A three step procedure is used to obtain an analytic fit to the potential energy function. First, in 5.3.1 the interaction forces are fitted applying a Legendre polynomial expansion. Second, as described in the same subsection, the fitted Legendre expansion coefficients are correlated using a superposition of two Gaussian functions. Third, in subsection 5.3.2, the force field is integrated to obtain the pair potential function.

5.3.1 Force fitting

From chapter 3, it seems that particle interactions in two-phase flows at low particle Reynolds numbers are strongly affected by the hydrodynamic interaction force between particles. In order to observe these effects numerically, interacting particles

are simulated using the Monte Carlo method, but to carry out MC simulations an analytic form of the hydrodynamic interaction forces is needed. The hydrodynamic interaction forces can be obtained from the force field $F_i(r, \theta)$, where r is defined as the separation distance between the particles ($r = l$) and θ is the angle between the two particles with respect to the main flow direction, see Figure 3.1. For convenience $F_i(r,\theta)$ is evaluated in Newtons [kg m s^{-2}] and it is expanded in the basis set of Legendre polynomials as follows, Camp (2006a):

$$F_i(r,\theta) = \sum_n C_n(r) P_n(x) \tag{5.4}$$

where P_n is the Legendre polynomial of order n, $x = \text{Cos}\ \theta$. By symmetry only the even values of n are used. Very good fits are obtained by including even Legendre polynomials terms up to n = 6.

Table 5.1 shows the Legendre polynomials used to correlate the hydrodynamic interactive forces, whilst Table 5.2 shows the values of the six expanded coefficients $C_n(r)$ for D_o $\left(= r/d_p\right)$ from 1.1 up to 25 for particle Reynolds number of 15 and particle diameter of 1 x 10^{-4} m.

N	$\mathbf{C_n(r)P_n(x),\ x = \text{Cos}\ \theta}$
0	C_0
2	$C_2\left[\frac{1}{2}\left(3x^2-1\right)\right]$
4	$C_4\left[\frac{1}{8}\left(35x^4-30x^2+3\right)\right]$
6	$C_6\left[\frac{1}{16}\left(231x^6-315x^4+105x^2-5\right)\right]$

Table 5.1 First six even Legendre polynomials used to fit the hydrodynamic forces between two spherical particles.

D_o	C_o $1x10^{10}$	C_2 $1x\ 10^{10}$	C_4 $1x10^{10}$	C_6 $1x10^{10}$
1.10	65.20	-360.44	3.61	-16.72
1.25	66.45	-357.15	-6.43	-7.11
1.50	57.97	-300.71	-29.58	-16.63
1.75	29.22	-235.79	-61.51	-15.53
2.00	12.82	-184.54	-74.69	-24.31
2.25	3.45	-152.44	-85.57	-27.96
2.50	-1.22	-128.47	-85.90	-39.91
3.00	-6.11	-95.85	-79.28	-55.07
4.00	-4.93	-55.91	-69.31	-64.29
5.00	-7.57	-43.30	-56.81	-66.34
6.00	-5.17	-26.02	-47.00	-63.47
8.00	-6.40	-20.34	-30.59	-55.46
12.00	-2.76	-8.24	-22.85	-42.24
15.00	-2.71	-5.93	-10.88	-27.22
20.00	-1.94	-3.48	-7.24	-22.30
25.00	-1.37	-2.55	-5.17	-15.38

Table 5.2 Expanded coefficients for the first six even Legendre polynomials for D_o up to 25 and $Re_p = 15$.

Once the $C_n(r)$ are obtained, it is straightforward to compute the hydrodynamic interactive forces from equation (5.4) as function of the particle separation distance (r) and the angle position (θ) to be compared with the hydrodynamic interactive forces obtained from CFD simulations. Figure 5.4 shows, the Legendre correlations, including terms up to n = 6. A good correlation is observed between the FLUENT data and the analytic relationship. The maximum difference up to $D_o = 8$ is less than 12% in the worst cases, for example, in $D_o = 6$ at $\theta = 0^o$ the maximum difference between the data from FLUENT and the correlation is less than 10%. Though, for greater particle separations $D_o > 10$ bigger differences are found, around 20%. However, the interest of this work is for particle separation distances less than 10

particle diameters, the correlations obtained using the Legendre polynomials are considered as satisfactory for this study.

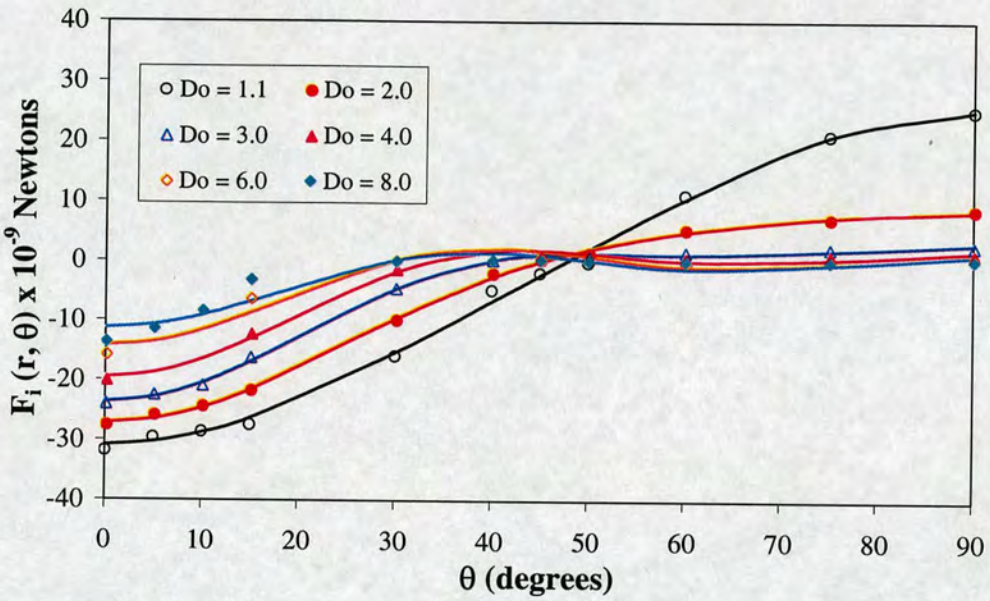

Fig. 5.4 CFD data (symbols) and fitting data (lines) comparison.

In order to obtain a relationship for the potential energy, the next step is to find an analytic correlation for the Legendre expansion coefficients, $C_n(r)$ from table 5.2. The variation of the Legendre coefficients as function of the particle separation distance between the particles is found to be very well correlated by a superposition of two Gaussian distribution in the form, Camp (2006a):

$$C_n(r) = g_1 \exp\left[-\left(\frac{r - d_p}{h_1}\right)^2\right] + g_2 \exp\left[-\left(\frac{r - d_p}{h_2}\right)^2\right] \qquad (5.5)$$

where r $(= D_o d_p)$ is the separation distance between the two particles, d_p stands for the particle diameter, g_1, g_2, h_1 and h_2 constants to be determined. Table 5.3 show the values for g_1, g_2, h_1 and h_2. The values for g_1 and g_2 are given in units of

$1x10^{-9}$ Newtons and the values for h_1 and h_2 are given in terms of particle diameters ($d_p = 1 \times 10^{-4}$).

N	g_1	h_1	g_2	h_2
	1×10^{-9}	1×10^{-4}	1×10^{-9}	1×10^{-4}
0	7.78144	0.890645	-0.6684	15.3592
2	-24.5916	0.909302	-12.1709	3.92072
4	-8.50118	7.26746	9.18018	0.651117
6	-6.85526	16.6977	5.86892	1.78035

Table 5.3 Table 5.3 Values for g_1, g_2, h_1 and h_2 for equation 5.5.

A comparison of the computed values of g_1, g_2, h_1 and h_2 using equation (5.5) with the values from Table 5.3 is shown in Figure 5.5, excellent correlation is found between the Legendre expansion coefficients and equation (5.5). The solid lines represent the values obtained by equation (5.5) and the symbols represent the values from Table 5.3.

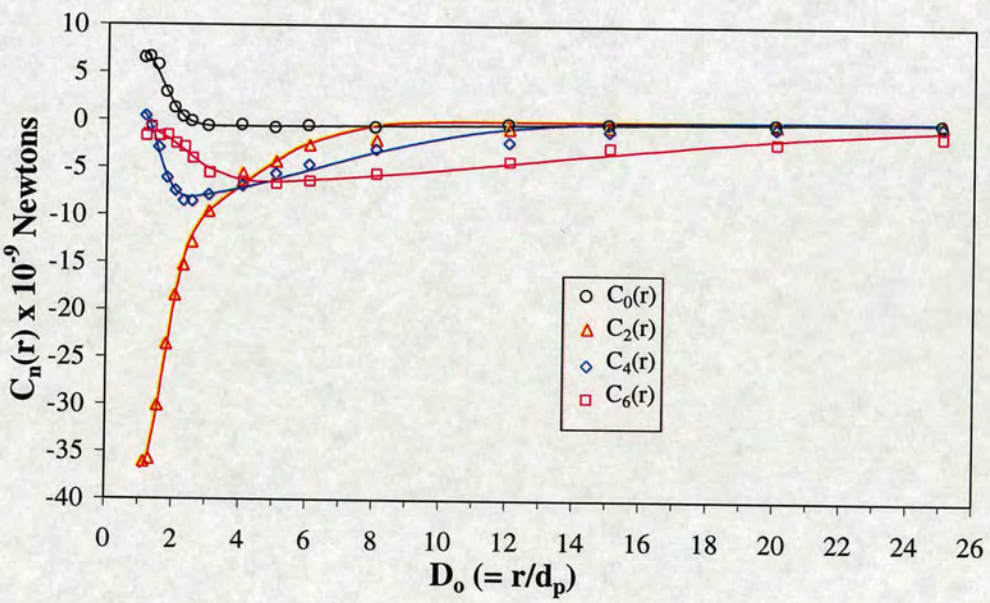

Fig. 5.5 Fit correlations for Legendre expansion coefficients $C_n(r)$.

5.3.2 The Pair potential

Pair potential energy functions are commonly used to study many-particle systems applying Monte Carlo methods or Molecular Dynamics Simulations. The most common and simple potential energy function used in Monte Carlo or Molecular Dynamics methods to simulate a pair of neutral atoms or molecules subject to attractive and repulsive forces is the Lennard-Jones pair potential. The force function can be computed from the pair potential or vice versa. The force function is the negative of the gradient of the pair potential. However, because the hydrodynamic pair particle interaction in a Newtonian fluid behaves in a different way, it was necessary to obtain an appropriate pair potential function.

In this study, if the interactive force between the two spherical particles is considered conservative, the pair potential energy $U(r,\theta)$ is obtained from equations (5.4) and (5.5) as an expansion of Legendre polynomials as following (Camp, 2006):

$$U(r,\theta) = \sum_{n} U_n(r) P_n(\mathrm{Cos}\theta) \tag{5.6}$$

where

$$U_n(r) = \int_{r}^{\infty} C_n(r')dr' = \frac{\pi}{2}\left[g_1 h_1 \mathrm{erfc}\left(\frac{r-d_p}{h_1}\right) + g_2 h_2 \mathrm{erfc}\left(\frac{r-d_p}{h_2}\right)\right] \tag{5.7}$$

Given the forces from equations (5.4) and (5.5), the coefficients $U_n(r)$ are obtained. Figure 5.6 shows the four Legendre polynomial expansion coefficients as functions of the dimensionless particle separation.

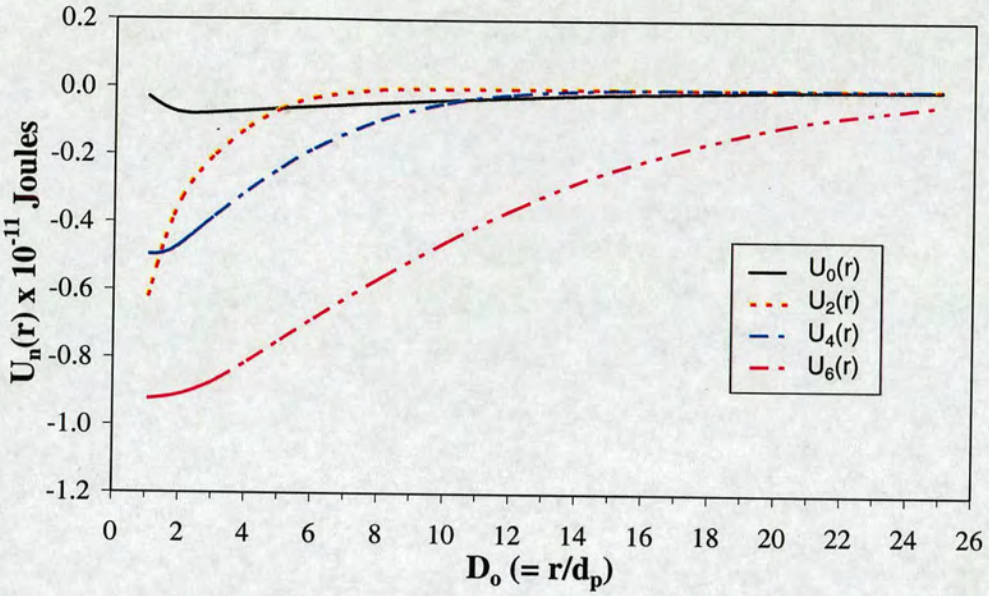

Fig. 5.6 Legendre polynomial expansion coefficients $U_n(r)$.

By using equations (5.6) and (5.7) the pair potential energy can be calculated as a function of the particles' separation at different angles. Figure 5.7 shows the pair potential energy for a wide range of angles ($0^o \leq \theta \leq 90^o$) as function of the particle separation distance ($1.0 \leq D_o \leq 25$). From Figure 5.7 it is observed that the minimum potential energy [$U_{min} = U(r,\theta)_{min} = -2.07 \times 10^{-11}$ Joules] is found for two particles aligned with the main flow direction ($\theta = 0^o$) at the minimum separation distance, $D_o = 1$.

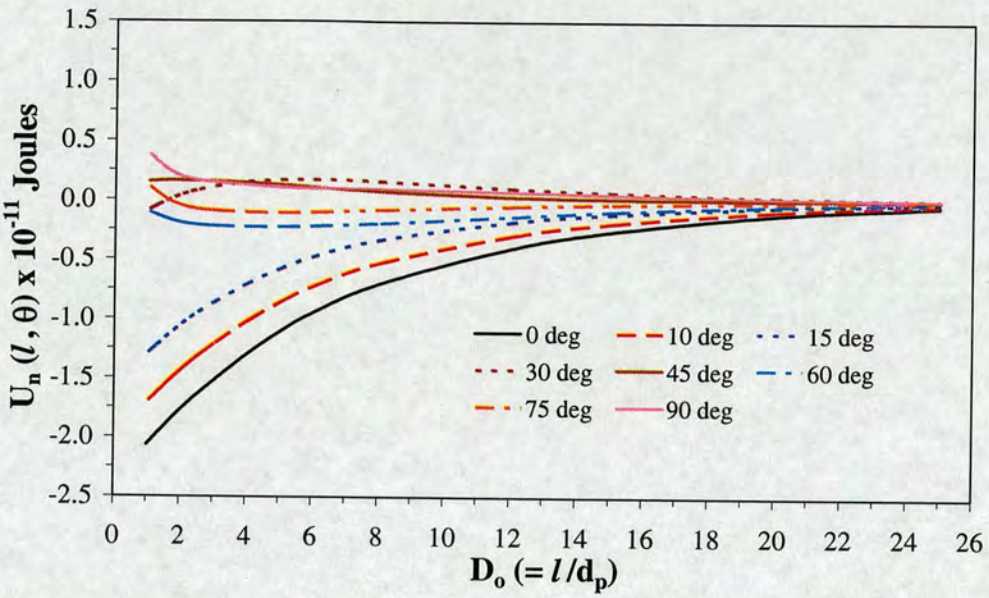

Fig. 5.7 Pair potential energy for several angle positions as function of the separation distance.

5.4 Results

The particle concentrations found in ropes after pipe bends in pneumatic transport varies from 12 kg m^{-3} to around 30 kg m^{-3} at the bend exit, which corresponds to particle volume fractions of $\alpha_p = 0.008$ (0.8%) and $\alpha_p = 0.02$ (2%), which clearly corresponds to a dense two-phase flow. Figure 5.8 shows the interaction coefficients for the typical particle separation found in the roping phenomenon. The attractive forces in the dense regime dominate over the repulsive forces as show in Figure 5.8. For D_o = 3, which is the maximum particle concentration reported in roping phenomenon, the repulsive force represents less than 10% of the attractive force. Most of the Monte Carlo simulations in this work are carried out at particle volume fractions typical of roping phenomenon, but some MC simulations were also run at higher volume fractions to compare with data available in the literature.

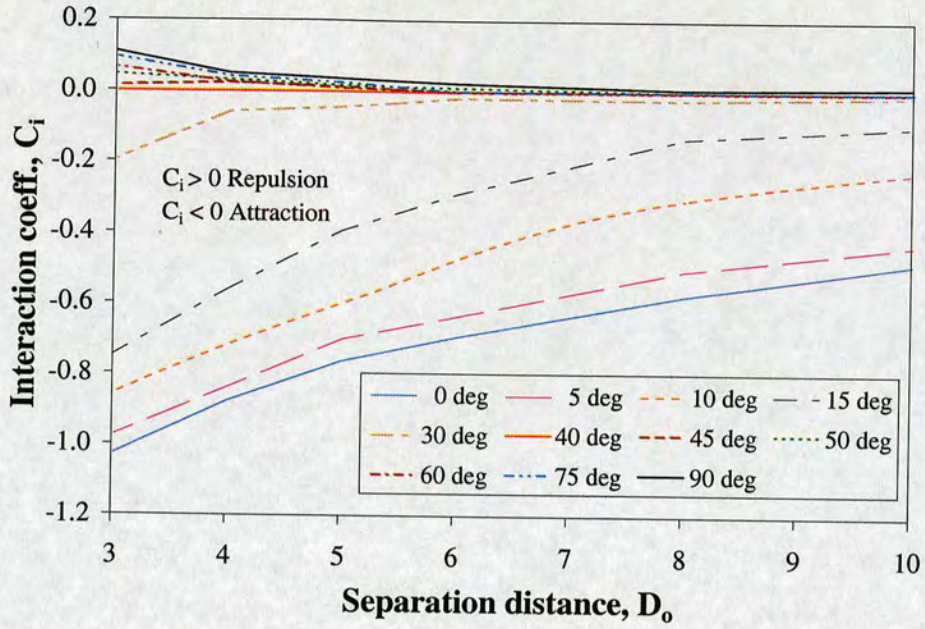

Fig. 5.8 Two fixed spherical particles interaction coefficients (C_i) in the dense flow regime ($3.0 \leq D_o \leq 10$).

Therefore once the pair potential function is obtained and the range of particle volume fraction range is chosen; the only missing parameter needed to carry out the MC simulations is the so called granular temperatures (T_g), which in this case will be obtained from experimental work in the literature applying the kinetic theory of granular flows.

The kinetic theory of granular flow (KTGF) is an extension of the classical kinetic theory of dense gases. It uses a method based on statistical mechanics to describe the mean and fluctuating velocity of particles found in continuous granular media. In kinetic theory of granular flows, the particle velocity, u_p, is subdivided into local mean velocity, u_{mean}, and random fluctuating velocity, u', described by the next equation:

$$u_p = u_{mean} + u' \tag{5.8}$$

By analogy with the thermodynamic property of a dense gas and assuming that the distribution of individual particle velocities follows a Maxwell-Boltzmann distribution, the kinetic energy (KE) can be defined as:

$$KE = \frac{3}{2}kT = \frac{1}{2}mu_{rms}^2 \tag{5.9}$$

where k is the Boltzmann constant equal to 1.38066×10^{-23} J K^{-1}, T is a temperature, m is the mass of the particle and u_{rms} $\left(=\sqrt{\overline{u'^2}}\right)$ is the root mean square of the random velocity fluctuations. According to Gidaspow *et al.* (2004) and Yu *et al.* (2007) in the kinetic theory of granular flows k is equal to unity and T is a pseudo-temperature called granular temperature, T_g, which can be defined as:

$$T_g = \frac{1}{3}mu_{rms}^2 \tag{5.10}$$

Reference values of granular temperature (T_g) used in this work are based on the experimental work of free falling particles from Losenno (2004). She studied the interactions between spherical particles in a free falling stream with particle size and particle Reynolds number very similar to those used in the CFD simulations in chapter 3.

Table 5.4 shows some relevant values from Losenno (2004). The corresponding values of T_g computed from Losenno's data are shown in column 4, which varies from 0.6 up to 4.3 J. Large variations are observed in the T_g values because of the wide range of particle diameters ($115 \leq d_p \leq 165$) and values of the root mean square of the random velocity fluctuations ($0.11 \leq u_{rms} \leq 0.27$ ms^{-1}). The corresponding reduced temperature T^* is defined in terms of the absolute value of the minimum pair potential energy, $U(r,\theta)$, between two particles by

$$T^* = \frac{T_g}{|U_{min}|} \tag{5.11}$$

The minimum pair potential energy as show in Figure 5.7 is obtained at $D_o = 1.0$, when the particles are perfectly aligned with the main flow direction ($\theta = 0^o$). At this angle the potential is given by the sum of the expansion coefficients, $U_n(r)$ at $r = d_p$, since all of the values of $P_n(\theta)$ at $\theta = 0^o$ in equation (5.6) are equal to unity. The values of $U_n(r)$ from Figure 5.6 are:

$U_0(r) = -2.956 \times 10^{-13}$ J
$U_2(r) = -6.211 \times 10^{-12}$ J
$U_4(r) = -4.946 \times 10^{-12}$ J
$U_6(r) = -9.218 \times 10^{-12}$ J

Hence, the absolute value of the minimum pair potential energy is the sum of the expansion coefficients, $|U_{min}| = 2.067 \times 10^{-11}$J. The minimum value of granular temperature ($T_e = 1.3 \times 10^e$ J, Table 5.4) is around 65% of the absolute value of the minimum pair potential energy. On the other hand, the maximum value of the granular temperature ($T_g = 9.0 \times 10^{-11}$ J , Table 5.4) is more than 4 times greater than the absolute value of the minimum pair potential energy. Given the uncertainties in the reference values of the experimental granular temperature from Losenno's work, the Monte Carlo simulations in this work are carried out over a reduced temperature (T^*) ranging from 0.5 up to 6. This range includes the minimum and maximum values of the experimental granular temperature from Losenno's work.

d_p (x 10^{-6} m)	Re_p	u_{rms} (ms^{-1})	T_g ($kg\ m^2 s^{-2}$)	T^*
	Mass flow rate ($\dot{m}$) = 0.3 g s^{-1}			
115	8	0.23	3.5×10^{-11}	1.70
137	11	0.11	1.3×10^{-11}	0.63
165	14	0.18	6.0×10^{-11}	2.90
	Mass flow rate ($\dot{m}$) = 0.5 g s^{-1}			
115	8	0.20	2.5×10^{-11}	1.20
137	9	0.21	5.0×10^{-11}	2.42
165	10	0.22	8.0×10^{-11}	3.87
	Mass flow rate ($\dot{m}$) = 1.0 g s^{-1}			
115	10	0.27	4.8×10^{-11}	2.33
137	9	0.23	6.0×10^{-11}	2.90
165	9	0.22	9.0×10^{-11}	4.35

Table 5.4 Table 5.4 Granular temperatures at different particle Reynolds numbers and mass flow rates, Losenno (2004).

5.4.1 Particle structure

In this section, the "equilibrium" particle structure obtained from MC simulations is considered. In a particulate flow, the granular or pseudo-temperature is directly related to the particle velocity fluctuations, Zhang & Reese (2003). Thus, the influence of the granular temperature in the system is observed in final configurations.

Snapshots obtained from MC simulations conducted at high particle volume concentration (α_p = 2%, D_o = 3.0) with 512 particles at $0.5 \leq T^* \leq 6.0$ are shown in Figure 5.9 – 5.12. Snapshots at lower concentrations $(4 \leq D_o \leq 10)$ with 512 and 1000 particles are presented in the appendix to this chapter.

Figure 5.9(a) shows the case of $T^* = 0.5$: in this figure ten compact clusters (ropes) with no dispersion are clearly observed. This phenomenon is due to the strong hydrodynamic interactive forces at small separations and the low pseudo-thermal energy of the particles. In the case of $T^* = 1.0$, which is shown in Figure 5.9(b), all particles are still aggregated but the number of particle ropes is smaller than for $T^* = 0.5$, the compactness of these clusters seems to be lower, which indicates that the multiparticle structures obtained at lower temperature ($T^* = 0.5$), are beginning to break down due to velocity fluctuations. At higher temperature $T^* = 2.0$ as shown in Figure 5.9(c) gives a very different structure than that shown at $T^* = 1.0$. A single particle rope with some disperse particles is observed. This phenomenon is probably induced by the strong particle interaction at this volume fraction in the main flow direction. Figure 5.9(d) shows the case of $T^* = 2.5$, a single particle rope with a few disperse particles is still observed, in this case round 85% of the particles are clustered in the rope. The multiple ropes observed at low velocity fluctuations ($0.5 \leq T^* \leq 1.0$) are aggregated into a single rope structure at intermediate temperatures, this phenomenon is clearly observed for $2.0 \leq T^* \leq 3.0$. For this particular case, the actual particle dispersion is started $T^* > 3.0$ as shown in Figures 5.9. At $T^* = 3.5$ most of the particles are dispersed; as depicted in Figure 5.9(f), an obvious particle dispersion is observed for $T^* \geq 4.0$ as illustrated in Figure 5.9(g) and Figure 5.9(h).

Similar patterns are observed at lower particle volume fractions $(4 \leq D_o \leq 10)$ for particles numbers of 512 and 1000. The particle structures may possibly be summarised as several clusters (ropes) at low granular temperatures ($0.5 \leq T^* \leq 1.0$), some pseudo particle dispersion occurred and the number of particle ropes is reduced into one or two ($1.0 \leq T^* \leq 3.0$) and finally at higher temperature, $T^* \geq 4.0$ in all cases studied here an obvious particle dispersion is readily observed.

Small differences can be detected as function of the initial particle density, e. g., the actual particle dispersion at lower particle volume fractions starts at lower temperature as shown in Figure 5.9 and in the figures in appendix to this chapter. For

example, at $\alpha_p = 2\%$ the particle dispersion starts at $T^* = 3.0$, the particle dispersion for the cases of $\alpha_p = 0.8\%$, 0.2% and 0.1% starts at lower temperature, $T^* = 2.5$, and in the case of $\alpha_p = 0.05\%$ ($D_o = 10$) the actual particle dispersion starts at $T^* = 2.0$. However, for all cases studied here ($0.05\% \leq \alpha_p \leq 2.0\%$ and $500 \leq N_p \leq 1000$) complete particle dispersion is observed at $T^* \geq 4.0$.

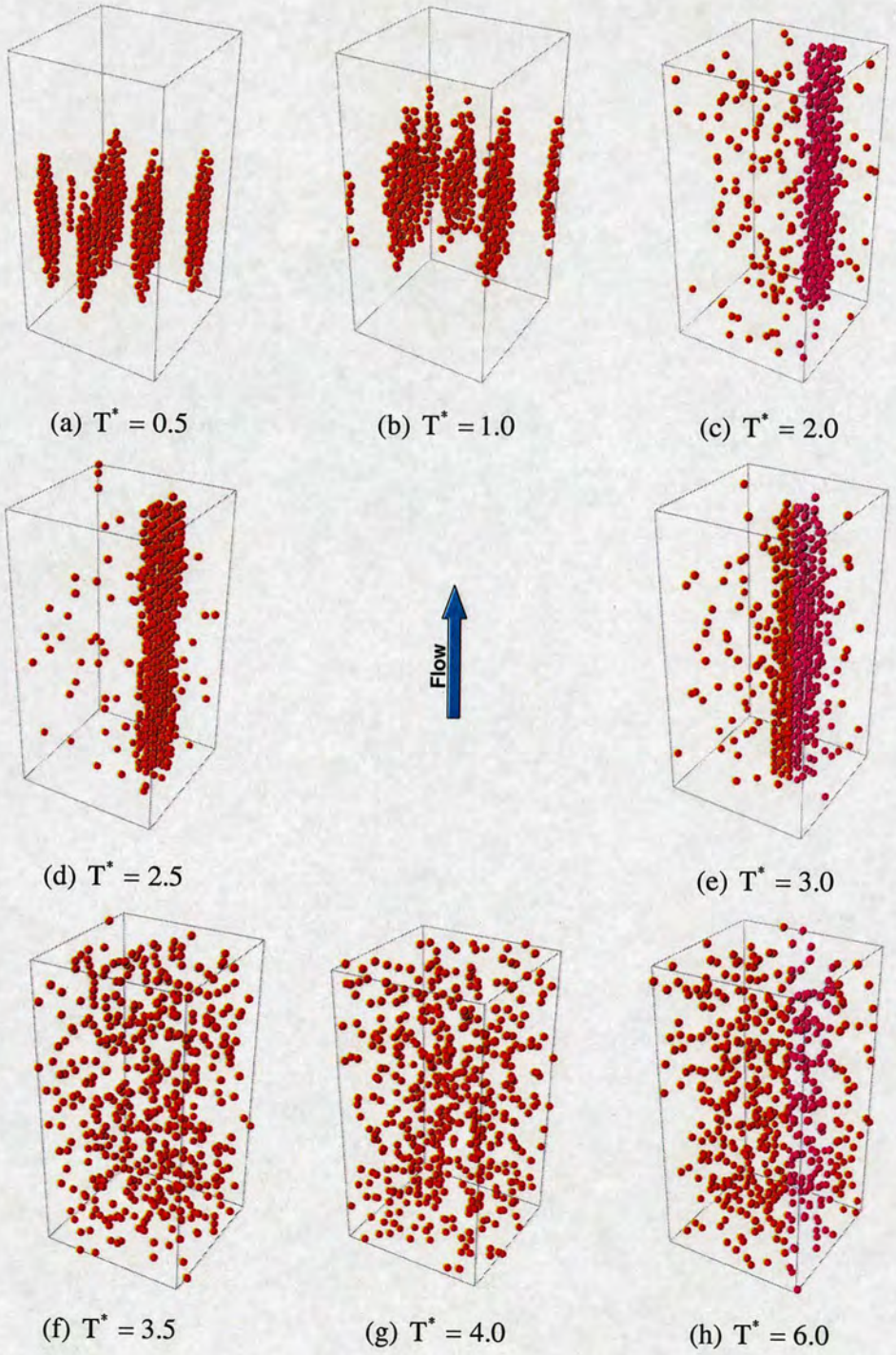

Fig. 5.9 Snapshots from canonical Monte Carlo simulations (NVT) of 512 particles at $\alpha_p = 2\%$ in the isotherms T^* between 0.5 and 6.0.

5.4.2 Radial distribution function

The snapshots shown in the above figures give an excellent qualitative description of the final particle structure in the system, but sometimes quantitative information about the particle structure is useful for a better understanding of the system. The most common function used in MC simulation is the so-called radial distribution function (RDF), g(r) which according to Allen & Tildesley (1987) can be defined as:

$$g(r) = \frac{1}{N_p}\left\langle \sum_i \sum_{j \neq i} \delta(r - r_{ij}) \right\rangle \tag{5.12}$$

where N_p is the number of particles, δ denotes the Dirac delta function, the brackets denote the averaging over the ensemble of the particles, the sums run over different pair of particles in the system and r_{ij} is the distance between particles i and j.

The easiest way to express the delta function from equation 5.12 is in terms of the number of particles in a bin as follows:

$$g(r) = \frac{1}{N_p}\frac{N_b(r)}{N_{id}(r)} \tag{5.13}$$

where $N_b(r)$ is the average number of particles in a shell (bin) of width dr at distance r and $N_{id}(r)$ is the average number of particles in the same interval (r, r + dr) in an uniform particle distribution system at same particle density, $N_{id}(r)$ can be defined by:

$$N_{id}(r) = \frac{4\pi\rho}{3}\left[(r + dr)^3 - r^3\right] \tag{5.14}$$

where ρ is the number density of particles in a uniform dispersion. The radial distribution function is equal to zero at small particle separations, r. For example, in this work g(r) = 0 at $r \leq d_p$: this is because overlap of particles is forbidden. At very

large values of r ($r \rightarrow \infty$) the radial distribution function tends to unity, which represents a uniform particle distribution, i.e. no clusters or ropes of particles exist.

The radial distribution function in this work is calculated from the structure of the system in equilibrium The width of the bin (dr) used to compute the RDF's in this study is 0.2. The RDF's at high volume fraction, $\alpha_p = 2\%$ are illustrated in Figure 5.10. Figure 5.11 and Figure 5.12 depict the radial distribution function for lower volume fractions, $\alpha_p = 0.8\%$ and $\alpha_p = 0.2\%$ respectively. Identical trends of g(r) are found in all cases study here.

Figure 5.10 shows the radial distribution function from the snapshots shown in Figure 5.9. In general, the radial distribution function shows common characteristics for low values of T^*. For example, at $T^* = 0.5$, 1.0 and 2.0, $g(r) = 0$ at $D_o < 1$, a sharp peak of g(r) is found at $D_o \sim 1$. At $D_o > 1$, g(r) decreases gradually until it reaches a value of g(r) close unity at $D_o = 5$. Some specific features can be observed in the radial distribution function, e. g., as the T^* is increased, the maximum value of the g(r) decreases. The shape of g(r) graphs is representative of the cluster (rope) formation and the position, sharpness and the amplitude of the peak provide a measure of the cluster degree. For $T^* = 4$ the radial distribution function rises from $g(r) = 0$ to the asymptotic value of $g(r) = 1$. This type of graph is characteristic of particle dispersion.

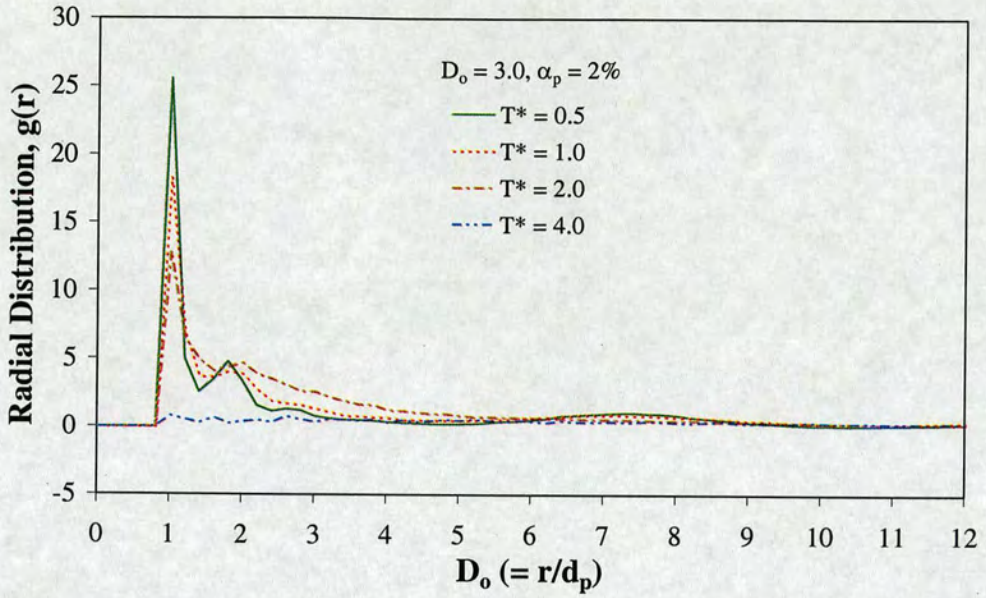

Fig. 5.10 Radial distribution function for 512 particles at initial volume fraction of $\alpha_p = 2\%$ after 2×10^3 MC cycles.

Figure 5.11 shows the radial distribution function for volume fraction, $\alpha_p = 0.8\%$ and temperatures between 0.5 and 4.0. Similar trends are observed in the graphs obtained from a higher volume fraction ($\alpha_p = 2\%$). Well-defined ropes of particles are formed at $T^* = 0.5$. At higher temperatures only one particle rope is observed ($T^* = 2.0$) as shown in figure 5.1A. At $T^* = 4.0$ the particle rope is completely dispersed as show by the blue line which rises from g(r) = 0 to g(r) ~ 1 and fluctuates around that value.

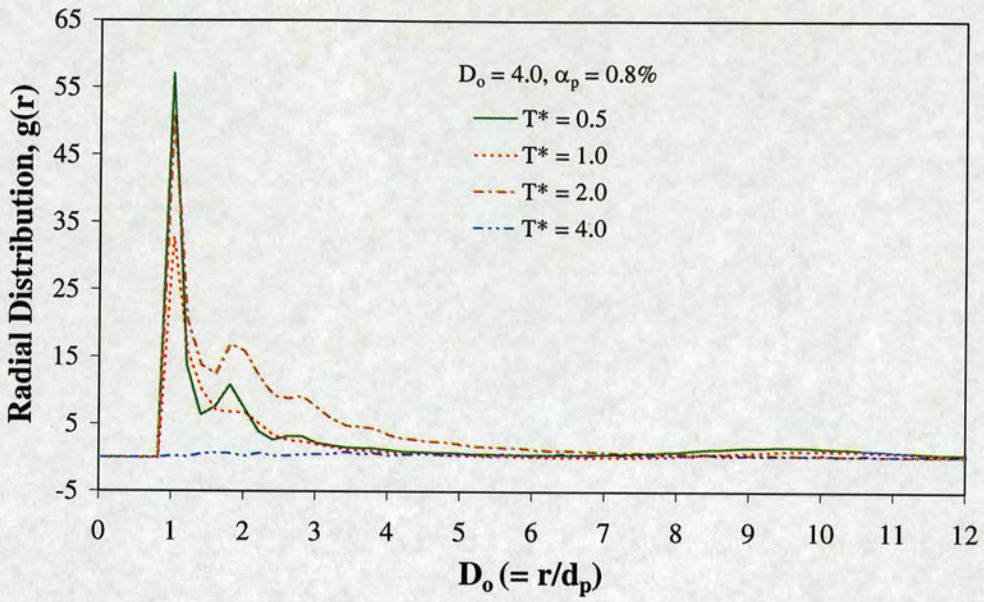

Fig. 5.11 Radial distribution function, g(r) for 512 particles at initial volume fraction of α_p = 0.8% after 2 x 10^3 MC cycles.

Figure 5.12 shows the radial distribution function for α_p = 0.2%. These graphs show the same tendency as those observed for α_p = 2% and α_p = 0.8%, i.e. g(r) values increase from zero to a maximum value at $r/d_p \sim$ 1 at low and intermediate temperatures ($0.5 \leq T^* \leq 2.0$), but for T^* = 4.0 most of the particles are dispersed as show by the curve fluctuating around unity. The snapshots for these four cases are shown in Figure 5.2A in the appendix to this chapter.

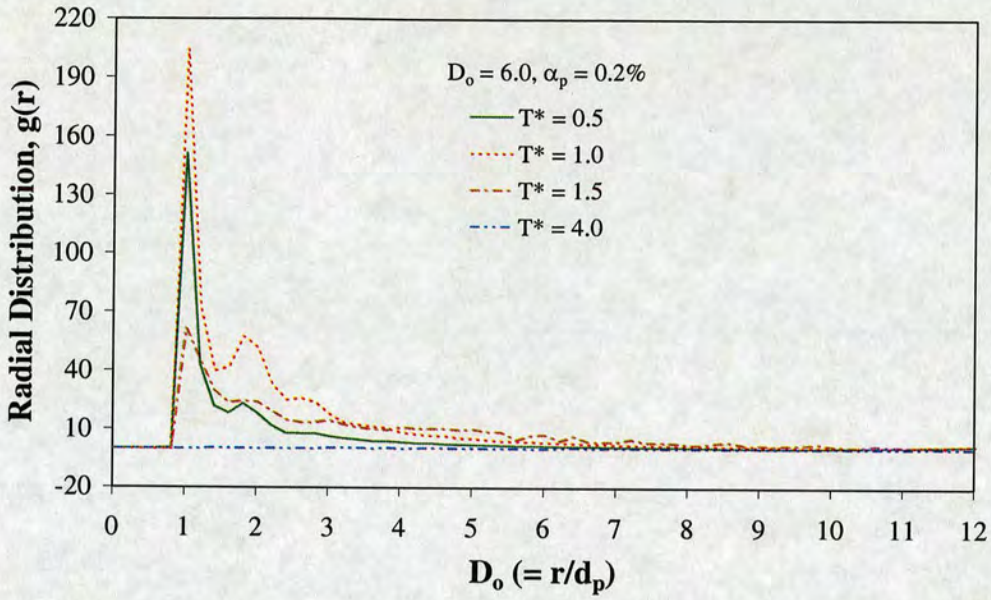

Fig. 5.12 Pair distribution function, g(r) for 512 particles at initial volume fraction of α_p = 0.2% after 2 x 10^3 MC cycles.

MC simulations with 10^3 spherical particles show the same tendency in the g(r) values. Snapshots of MC simulations with 10^3 particles are shown in the appendix to this chapter, which qualitatively illustrates the same phenomenon observed with 512 particles: particle clustering at low temperatures and particle dispersion at $T^* > 4.0$.

Back-calculation of the root mean square velocity fluctuations (u_{rms}) can be done using equation 5.10 and 5.11. For example, for coal particles with a characteristic density of 1600 kgm^{-3} and mean particle diameter of 100 μm the corresponding RMS particle velocity fluctuations at T^* where the particle dispersion was observed for most of the volume fractions studied here, $T^* = 4$ is around 0.6 ms^{-1}, which represents approximately 3% of the typical conveying velocity in coal transport in power plants (U = 20 ms^{-1}).

Sommerfeld & Kussin (2004) reported RMS particle velocity fluctuations between 1.0 and 1.7 ms^{-1} parallel to the main flow direction in a horizontal conveying pipe for particle size of 100 μm, mass loading of up to 2 and conveying velocity of 20 ms^{-1}.

They also reported particle slip velocities in the range of 1.0 and 2.0 ms^{-1} for particle diameters between 60 and 150 μm for various pipe roughnesses. The particle Reynolds number, based on the slip velocity is around 10. They found that for high pipe roughness (7μm) the particle concentration becomes almost constant across the channel, they conclude that this phenomenon was created by the modification of the particle velocity and particle velocity fluctuation due to the wall roughness. Huber & Sommerfeld (1994) reported that the ropes formed due to the elbow (horizontal to vertical) in the pipe system dispersed between 1.5 and 2.5 pipe diameters downstream of the bend. The axial particle root mean square velocity was $u_{rms} > 1.0$ ms^{-1}. These high values of u_{rms} were obtained with spherical glass beads ($\rho_p = 2500$ kg m^{-3}) with mean diameters of about 42 μm in a stainless steel pipe with a mean roughness height of 30 μm and superficial air velocities of 14 and 21 ms^{-1}. Both studies, reported particle self-dispersion for RMS particle velocity fluctuations greater than 1.0 m^{s-1}, but RMS particle velocity fluctuation found in this work at T* = 4.0, where particle dispersion is observed for most of the volume fractions studied here, is at least 40% smaller than those reported by Sommerfeld & Kussin (2004) and Huber and Sommerfeld (1994). Thus, these results suggest that even for RMS particle velocity fluctuation less than 1.0 ms^{-1}, self-particle dispersion could be possible.

5.4.3 Potential energy and the equilibration of the system

MC simulations can start from a lattice, or from a disordered configuration at different particle volume fractions and temperatures, consequently it is essential to run the simulation for a certain number of iterations so the system can reach the energy equilibrium at the end of the simulation, Allen & Tildesley (1987). By definition the equilibration of the system is reached when its properties, such as the energy, remain constant (or at least fluctuate around a constant mean value) over time. Thus, one way to monitor the equilibrium of the system is recording the potential energy, $U(r,\theta)$. In this work, the system equilibration is estimated from the

potential energy. The potential energy is recorded in MC blocks; each MC block contains 10^3 Monte Carlo steps (or MC Cycles).

In general, it is difficult to establish a priori the number of iterations in a numerical simulation experiment, in order to guarantee the equilibrium of the system and MC simulations are no exception. In MC simulations a rule of thumb typical number of MC blocks is between 500 and 1000, Allen & Tildesley (1987) and Camp (2007).

In this study extra MC blocks have been set in some cases (2000 MC blocks) in order to assure that the system is in equilibrium, but in most cases 10^3 MC blocks were enough to obtain very good potential energy equilibrium in the system.

Figure 5.13 shows the equilibration period of the potential energy for MC simulations at α_p = 2% and T^* = 0.5. For low reduced temperatures, T* =0.5, the system equilibration is reached at very small number of MC blocks as shown in the Figure 5.13 by the record of the potential energy as function of the MC blocks. An autocorrelation function of the recorded potential energy as function of the MC blocks is also computed to describe the average persistence on time of the potential energy fluctuations. The autocorrelation function, $A_{xx}(\tau)$, is defined as:

$$A_{xx}(\tau) = \frac{A_x(\tau)}{\sigma_x^2} \qquad 5.15$$

where $A_x(\tau)$ is define by:

$$A_x(\tau) = \frac{1}{N-\tau}\sum_{i=1}^{N-\tau}\left(x_i - \bar{x}\right)\left(x_{i=\tau} - \bar{x}\right) \qquad 5.16$$

and σ_x^2 is the covariance defined as:

$$\sigma_x^2 = \frac{1}{N}\sum_{i=1}^{N}\left(x_i - \bar{x}\right)^2 \qquad 5.17$$

The value of $A_x(\tau)$ at $\tau = 0$ is equal to the covariance σ_x^2, thus the autocorrelation function $A_{xx}(0) = 1$. For a time series, the form of the autocorrelation function for $\tau > 0$ is such that it generally decreases rapidly to its first zero crossing, after which it may become negative and start to oscillate about zero.

An inset of the autocorrelation function from potential energy is also shown in Figure 5.13, the curve shows an excellent equilibration of the system at very early stage of the simulation (MC block < 100), but as rule all the simulations were extended at least until 1000 MC blocks (each MC block contains 10^3 MC steps).

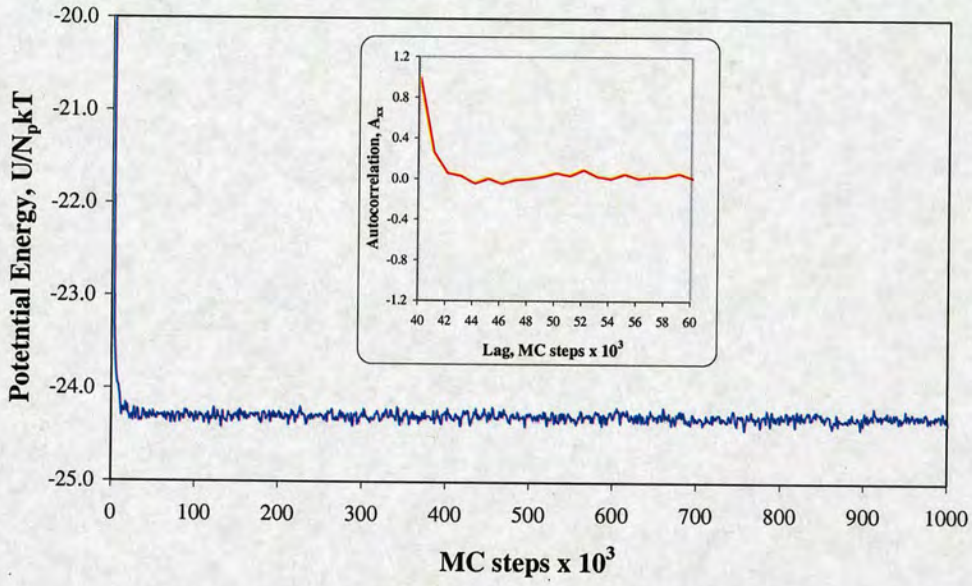

Fig. 5.13 The potential energy system from Monte Carlo simulations at particle volume fraction, $\alpha_p = 2\%$ and $T^* = 0.5$.

Figure 5.14 shows the Monte Carlo simulations at $\alpha_p = 2\%$ and $T^* = 4.0$. This figure shows a pseudo-equilibration for MC blocks less than 200, but as the simulation continues a big change in the potential energy is observed between 200 and 400 MC blocks, which is possibly cause by the change from cluster structure to particle dispersion. In this case more MC blocks are applied in order to try to detect more changes in the potential energy system. However, no significant change is observed,

thus good equilibration is achieved from 400 MC blocks onwards as shown in the autocorrelation in inset of the same figure. In cases like this, in order to guarantee a good potential energy autocorrelation the MC simulation is run until 2000 MC blocks where no systematic drift is observed and the potential energy starts to oscillate around a steady value. The potential energy data shown in Figures 5.13 and 5.14 corresponds to the snapshots shown in figures 5.9(a) and 5.18(g) respectively.

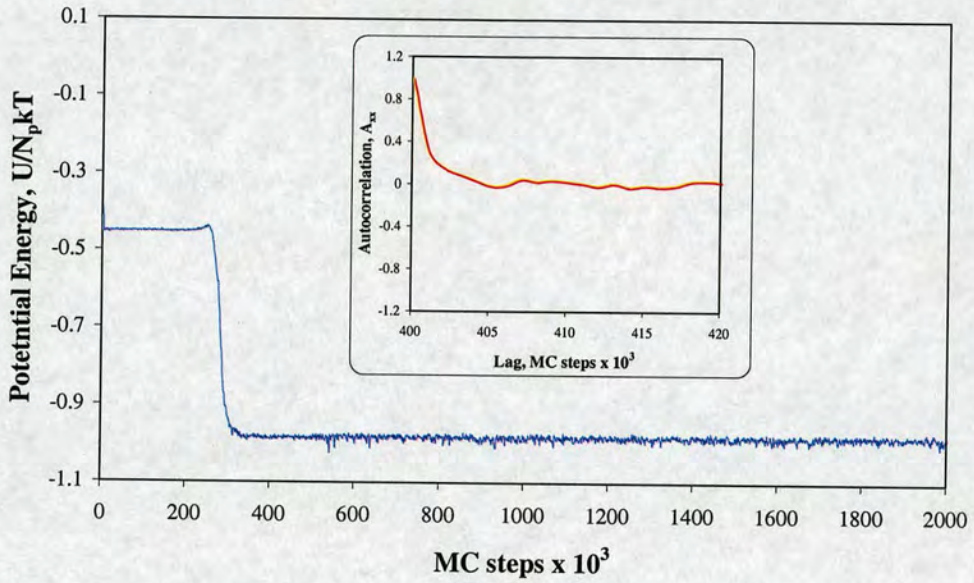

Fig. 5.14 The potential energy of the system from Monte Carlo simulations at particle volume fraction, $\alpha_p = 2\%$ and $T^* = 4.0$.

5.4.4 Particle structures: comparison with experimental data

The MC final structures are compared with experimental results available in the literature. Deficiency of experimental studies of two-phase flows at high particle volume fractions and low particle Reynolds numbers is evident because of their complexity, but some basic experimental works have been reported in the literature. Losenno (2004) studied experimentally the particle interactions in a two-phase stream flow of free falling spherical and irregular particles. The study was based on

particle Reynolds number ($1 \leq Re_p \leq 70$) with initial (at the exit of the particle source, hopper) volume fraction varying between 1.6×10^{-5} and 8×10^{-4}. The experiments were carried out by applying PIV and LDA experimental techniques with mean particles diameters in the range of 75μm to 300μm. Good images were reported in Losenno's work. Thus, excellent qualitatively comparison with the particle structures obtained in this work has been made. Unfortunately, to my knowledge, no relevant quantitative information has been reported in the literature to compare with.

Table 5.5 shows the parameters from Losenno (2004) and for one case in present work. Figure 5.15 compares the experimental results from Losenno (2004) with MC simulations from the present work. A good qualitative similarity in the particle structure is observed, a single rope at very high concentration with linear trains of particles close to it.

	Losenno (2004)	**Present work**
d_p (μm)	137	100
Re_p	11	15
ρ_p (kg m^{-3})	2500	-
α_p (%)	0.015	0.015
U_{rms} (ms^{-1})	0.11	0.17
T^*	0.65	0.6
N_p	-	512

Table 5.5 Parameters for Figure 5.14: quality comparison between experimental data and MC simulations.

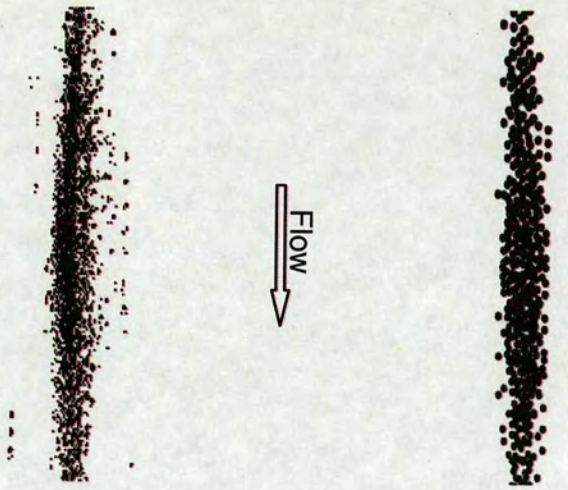

Fig. 5.15 Particle structure at initial α_p = 0.015% (a) experimental work from Losenno (2007) and (b) MC simulations at T* ~ 0.6.

Additionally, Table 5.6 shows the parameters for another case from Losenno (2004) and this work. The comparison is depicted in Figure 5.16. The experimental and numerical results show high particle concentration at the centre line of the particle structure with some scattering particles around the cluster. In both cases the images from Losenno (2004) were taken at the developed or self-similar region located at 0.90 m from the exit of the particle source.

	Losenno (2004)	**Present work**
d_p (μm)	137	100
Re_p	10	15
ρ_p (kg m^{-3})	2500	-
α_p (%)	> 1.0	2.0
U_{rms} (ms^{-1})	0.11	
T^*	2.35	2.30
N_p		512

Table 5.6 Parameters for Figure 5.15: quality comparison between experimental data and MC simulations.

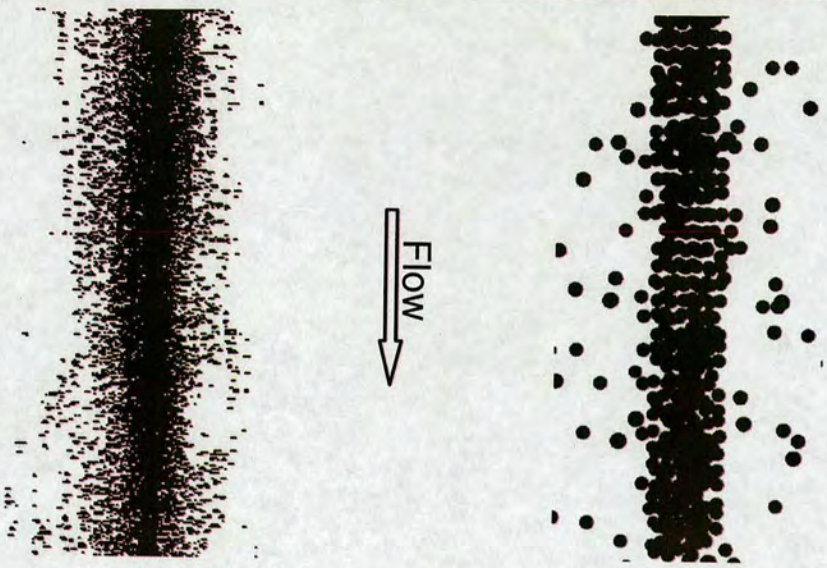

Fig. 5.16 Particle structure at α_p ~ 2% (a) experimental results from Losenno (2007) and (b) Monte Carlo simulations at T^* ~ 2.3.

5.5 Conclusions

A series of Monte Carlo simulations in a cuboidal box containing 512 or 1000 particles have been carried out using a pairwise energy potential obtained from hydrodynamic interactive forces of CFD simulations of two fixed spherical particles at particle Reynolds number typical of the roping phenomenon (Re_p = 15). The angular part of the hydrodynamic interactive forces was described by a series of Legendre polynomials. Very good fits are obtained by including Legendre polynomials terms up to n = 6. The radial dependence of the potentials was modelled by fitting the Legendre coefficients, $C_n(r)$, to a superposition of two Gaussian distributions. Finally, the pairwise potential energy, $U(r,\theta)$ was obtained by integration of the forces as an expansion of Legendre polynomials as $U(r,\theta) = \sum_n U_n(r)P_n(\cos\theta)$.

The particle velocity is defined as $u_p = u_{mean} + u'$ and according to the kinetic theory of granular flows (KTG), thus the granular temperature or pseudo temperature T_g can be defined as $\frac{1}{3} m u_{rms}^2$.

The results from MC simulations for 512 and 1000 particles show similar particle structure distributions as function of the dimensionless or reduced temperature, T^*. Several clusters (ropes) are observed at low $T^* < 1$, at intermediate values $1 < T^* < 3$, only one or two ropes are observed, in most of the cases at $T^* = 3$ the beginning of particle dispersion is noted, but only from $T^* \geq 4$ a clear particle dispersion is obtained most cases studied here. The clustering or roping for $T^* \geq 4$ is mainly attributable to the dominant attractive forces in the dense particle regime and the low particle velocity fluctuation, which is directly related to in the reduced temperature. In general, without other particle interactions (e.g. particle collisions) than the hydrodynamic interactions, it could be stated that at low particle velocity fluctuations, particle clustering or roping can be found. T* = 4.0 corresponds to a RMS particle velocity fluctuation of 0.6 ms^{-1} for a typical pneumatic conveying velocity of 20 ms^{-1} and mean particle diameter of 100 μm, this value represent only 3% of the conveying velocity.

The radial distribution function g(r) from the final particle structure is used to show quantitatively the particle distribution. At low $T^* < 3$, g(r) rises dramatically from zero ($r < d_p$) to a maximum value close to $r = d_p$ and at larger values of r, the values g(r) steadily decrease to g(r) = 1. The strong peak is a typical characteristic of cluster formation. For higher values of $T^* \geq 4$, g(r) increased from zero ($r < d_p$) to g(r) = 1, where it oscillates around this value.

No relevant quantitative experimental data was found in literature to compare with, for this reason only qualitative comparisons can be made. Quite similar particle structures are found when compared with a stream of free falling particles at comparable dynamic parameters, particle volume fraction and particle sizes as shown in Figure 5.15 and Figure 5.16.

CHAPTER 6

6 CONCLUSIONS AND FUTURE WORK

A summary and the final conclusions of the two and three particle Computational Fluid Dynamic simulations and many-particle Monte Carlo simulations are given and finally, in the last section, some suggestions for future work in two-phase flow particle hydrodynamic interactions are proposed.

6.1 Conclusions

In this work the importance of the hydrodynamic particle interaction forces (F_i) in two-phase flows at low particle Reynolds number ($Re_p = 15$) has been studied. These are the conditions under which roping phenomena are typically observed in the pneumatic transport systems of coal-fired power plants. First, a series of CFD simulations were made with two fixed, spherical particles with diameters of 100 μm placed at different relative positions. Second, CFD simulations were carried out with three fixed spherical particles. Last, many-particle Monte Carlo (MC) simulations were performed using the hydrodynamic interaction forces found from the two particle CFD simulations. A commercial CFD program (FLUENT) was used for the two and three particle simulations, while the Monte Carlo simulations were carried out with a MC code developed by Dr. Camp from the School of Chemistry in the University of Edinburgh (Camp, 2007a).

The main objective of the two fixed spherical particles CFD simulation was to obtain the force field in order to measure the importance of the particle-fluid-particle hydrodynamic interactions at low particle Reynolds number typical of roping phenomenon. Simulations were carried out at several particle positions, relative to the undisturbed fluid velocity. These simulations were analysed by means of velocity profiles, pressure coefficients, wall shear stress coefficients, drag coefficients and interaction coefficients.

Three body interactions were neglected in the multiparticle MC simulations, so a study of three-particle system was required to estimate the errors introduced by this approximation. Two different arrangements were used in the study of the three-body system: three collinear spherical particles and three equidistant spherical particles. The hydrodynamic forces in a three-particle system were studied by means of velocity profiles, pressure coefficients, wall shear stress coefficients and, drag and lift forces. The main objective of the CFD three fixed particles simulations was to illustrate the hydrodynamic effect on the forces of a two-particle system and justify the use of a pair potential force field in many-particle simulations.

Multiparticle MC simulations were carried out in a cuboidal box with 512 or 1000 particles at different reduced temperatures (T^*) and particle volume fractions (α_p) typical of roping phenomenon. The main aim of the MC simulations was to calculate the particle distribution due only to the particle-fluid-particle interaction force and the pseudo-temperature, which is directly related to the particle velocity fluctuation through the granular kinetic theory. The multiparticle interactions in MC simulations were modelled by using a pairwise potential energy $U(r,\theta)$ obtained from the two fixed particle interaction forces.

By means of numerical CFD particle simulations, it is been verified that particle-fluid-particle dynamic interactions in two-phase flows, especially at large particle concentrations are of great significance in the interaction between particles. Monte Carlo simulations demonstrate that both the particle concentration and the granular

temperature play an important role in the particle clustering and particle dispersion in two-phase flows.

From multiparticle Monte Carlo results could be stated that particle roping or clustering phenomenon at low particle velocity fluctuations (low pseudo-temperature, T^*) is mainly because of at this volume fraction ($\alpha p \leq 2\%$) the interactive-attractive force are predominant over the repulsive one. However, when particle velocity fluctuations are increased at certain level ($T^* = 4$), the particles are completely dispersed.

It is hoped that the results presented in this study can lead to a better understanding of the particle interactions in multiphase flows, particularly in the study of roping phenomenon found after bends in a coal-fired power plant's pneumatic transport system. The broad achievements of this study are summarised in the following order: results from CFD simulations of two fixed spherical particles; simulations of three fixed spherical particles and many-particle Monte Carlo simulations.

6.1.1 Two fixed spherical particle CFD simulations

1. **Flow field.** In general the fluid flow field analysis included the calculation of contours and profiles of: velocity, pressure and wall shear stress. These parameters showed that the flow field patterns are directly influenced by the relative positions of the two particles. As a result of this, different hydrodynamic forces due to the fluid flow act on the upstream (leading) and downstream (trailing) particle. Qualitative and quantitative analyses of flow velocity, pressure and wall shear stress are given in chapter 3.

2. **Drag forces.** The highest drag force reduction for the two-particle system, compared to that of a single particle, appears when the two particles are aligned with the main flow direction ($\theta = 0^o$). The maximum drag reduction for two particles at $\theta = 0^o$ and $D_o = 1.1$ was as high as 15% for the leading

particle and 54% for the trailing particle. When the two particles are placed side-by-side ($\theta = 90^o$) both particles experienced the same drag reduction. The maximum drag reduction for this particle arrangement was only 10% relative to that of a single particle, found at $D_o = 1.1$. In general, lower values of drag coefficients for the two particles compared to that of a single particle are found, except for $1.5 < D_o < 3.0$ for $\theta = 75^o$ and 90^o, where slightly higher values (less than 1%) are reported for both particles, see Figures 3.15 and 3.16. The drag coefficients for $\theta = 0^o$ and $\theta = 90^o$ shown a very good agreement with results reported in the literature.

3. **Interaction coefficients.** Lift forces were not analysed separately, because they are implicitly included in the hydrodynamic interactive force (F_i), which is based on the concept of lift force proposed by Kim *et al.* (1993) and Folkersma *et al.* (2000) when they studied the interaction between two particles placed side-by-side. Due to the different flow patterns that occur around the particles, attractive and repulsive forces between the particles arise. Pressure forces at low particle Reynolds number are only a small part of the total force over the particle, so viscous shear force is the main component. The difference between these two forces varies from 38% up to 55% for the leading particle and from 38% up to 68% for the trailing particle.

In this study, only attractive forces were found for $\theta < 45^o$, whilst for angles greater than 45^o, only repulsive forces were observed. In general, strong particle interactions are found at small particle separation distances; as the particle separation is increased the interactions decrease until they vanish. At very small angles, weak interaction forces remain even at $D_o = 25$. The maximum values for both repulsive and attractive interacting forces were found at $D_o = 1.1$. The maximum attractive force was found at $\theta = 0^o$, whilst the maximum repulsive force was found at $\theta = 90^o$. The maximum repulsive force is around 80% of the maximum attractive force and the influence zone

for repulsive forces is quite small compared with the influence zone of attractive forces, as shown in Figure 3.23. For $\theta = 45^{\circ}$ both attractive and repulsive forces are observed but their maximum value for this case is very small (< 10%) compared with the maximum values for the other cases.

6.1.2 Three fixed spherical particles CFD simulations

1. **Flow field.** The analysis of the flow field structure in a three fixed interacting particle system shows how a third particle modifies the flow. Only small differences are found when the results are compared with two fixed interacting particles, and, as the particle separation increases, these differences tend to zero. For example, at the smallest particle separation distance ($D_o = 1.1$) the maximum difference between velocity, pressure coefficient and wall shear stress coefficient for particle 1 (leading particle) is less than 10%.

2. **Drag and lift forces.** A suitable method to compare the hydrodynamic influence over the drag and lift force due to a third particle with those found in the two-particle system is proposed.

   The maximum difference in drag and lift forces in most of the cases studied here were less than 10% for particle separation distances smaller than three particle diameters. Greater discrepancies (~14%) were found in the lift force for $D_o < 2.0$ in the specific case when two particles are place in line with flow direction and a third particle was placed beside them. A possible explanation for this larger difference is that at very short particle separations the particles start to influence the flow as a single, large body.

   Since a relatively small difference is found between the two systems, the two particle interaction forces could be used in a multiparticle Monte

Carlo simulations with certain confidence as a pairwise additive force system for the cases studied here.

6.1.3 Multiparticle Monte Carlo simulations

Based on the two fixed particle hydrodynamic interactive force additivity, a pairwise potential energy was used to model a multiparticle system with the Monte Carlo method.

The analysis of the final particle distribution as a function of the volume fraction (α_p) and reduced temperature (T^*) show that for low reduced temperature ($0.5 \leq T^* \leq 1.0$) several clusters or ropes of particles are formed. At higher reduced temperature ($1.0 \leq T^* \leq 3.0$) the number of clusters are reduced to only one or two, a complete particle dispersion is observed at $T^* > 4$. Slight differences are observed as a function of the particle separation for volume fractions studies here. For example, at initial α_p = 2% (D_o = 3.0) the particle dispersion starts at T^* = 3.0, the particle dispersion for the cases where the initial volume fractions are 0.8% (D_o = 4.0), 0.2% (D_o = 6.0) and 0.1% (D_o = 8.0) starts at lower temperature, $T^* \sim 2.5$, and finally for the case where α_p = 0.05% (D_o = 10) the particle dispersion starts at the lowest reduced temperature: T^* = 2.0.

Given that the reduced temperature is directly related to the particle velocity fluctuation, for a typical conveying velocity of 20 ms^{-1} and pulverised coal with a mean diameter of 100μm in power plants, the reduced temperature of 4.0 at which most of the cases studied here are disperse corresponds to a RMS velocity fluctuation of 0.6 ms^{-1}, which is only 3% of the conveying velocity.

As a final conclusion, it seems that the new methodology used in this work to model hydrodynamic multiparticle interactions, which applies an additive pairwise potential function obtained from CFD simulations of two fixed particles, could be a useful

alternative tool for this kind of problem. This work shows the importance of the hydrodynamic attractive/repulsive forces between particles and the particle velocity fluctuations in the hydrodynamic roping (clustering) formation/dispersion phenomenon in a multiparticle system at low particle Reynolds number ($Re_p = 15$).

6.2 Recommendations for future work

As with many studies of particle interactions in two-phase flows, this work has perhaps suggested more questions about the nature of particle hydrodynamic interaction forces than it has answered. However the results of this investigation have provided some important findings, which need further investigation. Hence, some recommendations for future research in this subject are posed in the following three paragraphs.

Although most of the results found in this study have been compared with results reported in the literature for similar conditions, with very good qualitative agreement found, experimental work at typical particle volume fraction ($2\% \leq \alpha p \leq 0.24\%$) and low particle Reynolds number ($Re_p \sim 15$) of roping phenomenon is needed for quantitative comparisons with, the CFD and MC simulations reported here.

Though only small differences arise between the dynamic forces in two and three fixed particle system, it will be important to include the three particle interactions at very short particle separations to observe their influence on the dynamics of a multiparticle system.

With regard of the phenomenon of roping, almost no information is available about the granular temperature, which is required for the multiparticle Monte Carlo simulations. This data is badly needed, since, as this study show, granular temperature is one of the key parameters for cluster formation/dispersion. Further study, both numerically and experimentally on this topic at the roping regime is necessary.

REFERENCES

Abreu, C. R. A., Macias-Salinas, R., Tavares, F. W. and Castier, M., (1999). A Monte Carlo simulation of the packing and segregation of spheres in cylinders, Brazilian Journal of Chemical Engineering, [online], vol. 16, issue 4, pp. 395-405. Available from: http://www.doaj.org.

Adrianov, N., (2003). Analytical and numerical investigation of two-phase flow, PhD Thesis, Fafakultät für Mathematik, Universität, Magdeburg, Germany.

Akilli, H., Levy, E., Sahin, B., (2005). Investigation of gas–solid flow structure after a 90° vertical-to-horizontal elbow for low conveying gas velocities, Journal of Advanced Powder Technology, vol. 16, issue 3, pp. 261-274.

Akilli, H., Levy, K., Sahin, B., (2001). Gas-solid flow behaviour in a horizontal pipe after a 90° vertical-to-horizontal elbow, Powder Technology, vol. 16, issue 1, pp. 43-52.

Aliseda, A., Cartellier, A., Hainaux, F., Lasheras, J., (2002). Effect of preferential concentration on the settling velocity of heavy particles in homogeneous isotropic turbulence, Journal of Fluid Mechanics, vol. 468, pp. 77-105.

Allen, M. P. and Tildesley, D. J., (1987). Computer simulation of liquids, Oxford University Press Inc. New York.

Azzopardi, B. J., Cloke, M., Thomson, A. W. and Wilson J. A., (2001). Potential cost and efficiency saving through improved multiphase application in UK fossil-fired power generation, Report No. Coal R206, DTI/Pub URN 01/583,School of Chemical, Environmental and Mining Engineering, University of Nottingham, Crown Copyright, pp. 1-118. Available [on line] at: http://www.berr.gov.uk/files/file18626.pdf.

Badalassi, V. E., Ceniceros, H. D. and Banerjee, S. (2003). Computation of multiphase systems with phase field models, Journal of Computational Physics, vol. 190, issue 2, pp. 371-397.

Bagchi, P., and Balachandar, S., (2002). Effect of free rotation on the motion of a solid sphere in linear shear flow at moderate Re, Physics of Fluids, vol. 14, issue 8, pp. 2719-2737.

Barnes, R. N.; Selves, T.P. and Woodhead, S. R., (1995). The sensing of unbalanced pulverised fuel feed rates at the exit of riffle boxes in coal fired power station fuel distribution systems. Proceedings of the 20th, International Conference on Coal Utilisation and Fuel Systems, Florida, USA.

Berg, B. A., (2006). Tutorial lecture on Markov chain Monte Carlo simulations and their statistical analysis, GBA Theoretical Chemistry Lecture Series, [on line] Boston, 11/29/2006. Available from: http://www.hep.scs.fsu.edu/~berg/research/boston/lecture1.pdf.

Bilirgen, H. and Levy, E., (2001). Mixing and dispersion of particle ropes in lean phase pneumatic conveying, Powder Technology, vol. 119, issue 2-3, pp. 204-212.

Bilirgen, H., Levy, E. and Yilmaz, A. (1998). Prediction of pneumatic conveying flow phenomena using commercial CFD software, Powder technology, vol. 95, issue 1, pp. 37-41.

Bird, G. A., (1978). Monte Carlo simulation of gas flows, Annual Reviews of fluid Mechanics, vol. 10, pp. 11-31.

Birlingen, H. and Levi, E., (2001). Mixing and dispersion of particle ropes in lean phase pneumatic conveying, Powder Technology, vol. 119, pp. 134-152.

Biswas, S., Esmaeli, A. and Tryggvason, G., (2005). Comparison of results from DNS of bubbly flows with a two-fluid model for two-dimensional laminar flows, International Journal of Multiphase Flow, vol. 31, pp. 1036-1048

Boryczko, K., Dzwinel, W. and Yuen, D. A., (2003). Dynamical clustering of red blood cells in capillary vessels, journal of Molecular Modelling, vol. 9, pp. 16-33.

Boyer, C., Duquenne, A-M. and Wild, G., (2002). Measuring techniques in gas-liquid and gas-liquid-solid reactors, Chemical Engineering Science, vol.57, pp. 3185-3215.

Brydon, A. D. and Thomson, M. C., (2001). Flow interactions between two spheres at moderate Reynolds numbers, 14th Australian Fluid Mechanics Conference, Adelaide, Australia, 10-14 December.

Bunner, B., Tryggvason, G., (2002b). Dynamics of homogeneous bubbly flows. Part 2. Velocity fluctuations, Journal of Fluid Mechanics, vol. 466, pp. 53–84.

Bunner, B., Tryggvason, G., (2003). Effect of bubble deformation on the properties of bubbly flows, Journal of Fluid Mechanics, vol. 495, pp. 77–118.

Caboussat, A., (2005). Numerical simulation of the two-phase free surface flows, Archives of Computational Methods in Engineering, State of the art review, vol. 12, Issue2, pp. 165-224.

Camp, P. J., (2003). Structure and phase behavior of a two-dimensional system with core-softened and long-range repulsive interactions, The American Physical Society: Physical Review E, Vol.68, pp. 061506(1)-061506(8).

Camp, P. J., (2006). Structure and dynamics in a monolayer of core-softened particles, Journal of Molecular Liquids, vol. 127, pp. 10–13.

Camp, P. J., (2006a). Fitting coefficients and Monte Carlo simulations, Internal Communication, philip.camp@ed.ac.uk.

Camp, P. J., (2007). Lectures on Monte Carlo Simulations, School of Chemistry, University of Edinburgh, Internal Communication, philip.camp@ed.ac.uk.

Camp, P. J., (2007a). Monte Carlo homemade code, School of Chemistry, University of Edinburgh, Internal Communication, philip.camp@ed.ac.uk.

Castier, M., Delgado, O. and Tavares, F., (1998). Monte Carlo simulation of particle segregation, Powder Technology, vol. 97, pp. 200-207.

Chen, R. C. and Lu, Y. N., (1999). The flow characteristics of an interactive particle at low Reynolds numbers, International Journal of Multiphase flow, vol. 25, pp. 1645-1655.

Chen, R. C. and Wu, J. L., (2000). The flow characteristics between two interactive particles, Chemical Engineering Science, vol. 55, pp. 1143-1158.

Chhabra, R. P., Agarwal, L. and Sinha, N. K., (1999). Drag on non-spherical particles: an evaluation of available methods, Powder Technology, vol. 101, pp. 288-295.

Choi, H. and Joseph, D., (2001). Fluidisation by lift of 300 circular particles in plane Poiseuille flow by direct numerical simulation, Journal of Fluid Mechanics, vol. 438, pp. 101-128.

Chun, M-S, (1999). Computer simulation study on the concentration distribution of spherical colloids within confined spaces of well-defined pore, Macromolecular Theory Simulations, vol. 8, pp. 418-427.

Clercx, H. J. H. and Schram, P. P. J. M., (1992). Three particle hydrodynamic interactions in suspensions, Journal of chemical physics, vol. 96, issue 4, pp. 3137-3151.

Clift, R., J.R. Grace, and M.E. Weber, (1978). Bubbles, Drops and Particles, pp 380, Academic, New York.

Crowe, C., (2000). On models for turbulence modulation in fluid-particle flows, International Journal of Multiphase Flow, vol. 26, pp. 719-727.

Crowe, C., Sommerfeld, M., Tsuji, Y., (1998). Multiphase flows with droplets and particles, CRC Press, Boca Raton, Florida (USA).

Datta, U., Dyakowski, T. and Mylvaganam, S. (2007). Estimation of particulate velocity components in pneumatic transport using pixel based correlation with dual plane ECT, Chemical Engineering Journal, vol.130, issues 2-3, pp.87-99.

Delnoij, E., Kuipers, J. A. M., van Swaaij, W. P. M. and Westerweel, J. (2000). Measurement of gas–liquid two-phase flow in bubble columns using ensemble correlation PIV, Chemical Engineering Science, vol. 55, issue 17, pp. 3385-33951

Di Felice, R., (1994). The voidage function for fluid particle interaction systems, International Journal of Multiphase Flow, vol. 20, issue 1, pp. 153-159.

Duchanoy, C. and Jongen T., (2003). Efficient simulation of liquid–solid flows with high solids fraction in complex geometries, Computers and Fluids, vol. 32, issue 10, pp.1453-1471.

Eckhardt, R. (1987). Stan Ulam, John Von Neumann, and the Monte Carlo Method, Los Alamos Science, Special issue, vol. 15 , pp. 131-141.

Elghobashi and Truesdell, (1993). On the two-way interaction between homogeneous turbulence and dispersed solid particles. Part I: Turbulence modification, Physics of Fluids A, vol. 5, issue7, pp. 1790-1801.

Ellenberger, J., van Baten, J, M., and Krishna, R., (2005). Exploiting the Bjerknes force in bubble column reactors, Chemical Engineering Science, vol. 60, issue 22, pp. 5962-5970.

Epstein, N., (2003). Applications of liquid-solid fluidisation, International Journal of Chemical Reactor Engineering, vol.1, review R1, pp. 1-18.

Esmaeli, A. and Tryggvason, G., (1998). Direct numerical simulations of bubbly flows, Part 1. Low Reynolds number arrays, Journal of. Fluid Mechanics, vol. 377, pp. 313–345.

Esmaeeli, A., Tryggvason, G., (1999). Direct numerical simulations of bubbly flows. Part 2. Moderate Reynolds number arrays, Journal of Fluid Mechanics, vol. 385, pp. 325–358.

Esmaeeli, A., Tryggvason, G., (2005). A direct numerical simulation study of the buoyant rise of bubbles at O(100) Reynolds number, Physics of Fluids, vol. 17, pp. 093303 (1-19).

Evenson, G. F., Hall, E. W. and Ward, S. G., (1959). Interaction between two equal-size equal-settling spheres moving through a viscous liquid, British Journal of Applied Physics, vol. 10, pp. 43-47.

Feng, J., Hu H. and Joseph, D. D., (1994). Direct simulation of initial value problems for the motion of solid bodies in a Newtonian fluid. Part 2. Couette and Poiseuille flows, Journal of Fluid Mechanics. vol. 277, pp. 271–301.

FLUENT Inc (2005). FLUENT 6.2 User's Guide, http://www.see.ed.ac.uk/~fluent_6216/ fluent/help/index.htm.

Fokeer, S., Kingman, S., Lowndes, I. and Reynolds, A., (2004). Characterisation of the cross sectional particle concentration distribution in horizontal dilute flow conveying –a review, Chemical Engineering and Processing, vol. 43, pp. 677-691.

Folkersma, R., Stein, H., and van de Vosse, F., (2000). Hydrodynamics interactions between two identical spheres held fixed side by side against a uniform stream

directed perpendicular to the line connecting the spheres' centre, International Journal of Multiphase flow, vol. 26, pp. 877-887.

Fortes, A. F., Joseph, D. D. and Lundgren, T. S., (1987). Nonlinear mechanics of fluidisation of beds of spherical particles. Journal of Fluid Mechanics.vo.177, pp. 467–483.

Frenkel, D. and Smit, B., (2002). Understanding molecular simulation: From algorithms to applications, 2nd ed., Academic Press, San Diego (USA).

Gharib, M., Pereira, F., Dabiri, D., Hove, J-R. and Modarress, D., (2002). Quantitative flow visualization: toward a comprehensive flow diagnostic tool, Annual Meeting of the society for Integrative and Comparative Biology, pp. 42: 964-970, 2-6 January, Anaheim, California, USA.

Gidaspow, D., (1994). Multiphase flow and fluidisation: continuum and kinetic theory descriptions, Academic Press, New York.

Gidaspow, D., Jung, J. and Singh, R. K., (2004). Hydrodynamics of fluidisation using kinetic theory: an emerging paradigm 2002 Flour-Daniel lecture, Powder Technology, vol. 148, pp. 123–141.

Gidaspow, D., Seo,Y.C., (1986). Hydrodynamics of fluidisation: supercomputer generated vs. experimental bubbles, Journal of Powder & Bulk Solids, Technology, vol. 10, issue 3, pp. 19–23.

Giddings, D., Aroussi, A., Pickering, S. J. and Mozaffari, E., (2004). A ¼ scale test facility for PF transport in power station pipelines, Fuel, vol. 83, issue 16, pp.21952204.

Glowinski, R., Pan, T., Hesla, T, Joseph, D. and Périaux, J., (2001). A Fictitious Domain Approach to the Direct Numerical Simulation of Incompressible Viscous Flow past Moving Rigid Bodies: Application to Particulate Flow, Journal of Computational Physics, vol. 169, issue 2, pp.363-426

Glowinski, R., Pan, T.-W., Hesla T.I. and Joseph, D.D., (1999). A distributed Lagrange multiplier/fictitious domain method for particulate flows, International. Journal Multiphase Flow, vol. 25, pp. 755–794.

Gore and Crowe, (1989). Effect of particle size on modulating turbulent intensity, International Journal of Multiphase Flow, vol. 15, issue 2, pp. 279-285.

Grevskott, S., Sannæs, H. B., Duduković, M. P., Hjarbo, K. W. and Svendsen, H. F., (1996). Liquid circulation, bubble size distributions, and solids movement in two- and three-phase bubble columns, Chemical Engineering Science, vol. 51, issue 10, pp. 1703-1713.

Han, K., Feng, Y-T. and Owen, D-R-J., (2007). Coupled Lattice Boltzmann and discrete element modelling of fluid–particle interaction problems, Computers & Structures, vol. 85, issues 11-14, pp. 1080-1088

Happel, J. and Brenner, H. (1973). Low Reynolds number hydrodynamics. Noordhoff International Publishing, Leiden, The Netherlands.

Happel, J. and Pfeffer, R., (1960). The motion of the two spheres following each other in a viscous fluid, A. I. Ch. E. Journal, vol. 6, pp. 129-133.

Hecquet, D., Ruskin, H. J. and Crane, M. (2007). Optimization and parallelization strategies for Monte Carlo simulation of HIV infection, Computers in Biology and Medicine, vol. 37, pp. 691-699.

Heider and Levenspiel, (1989). Drag coefficient and terminal velocity of spherical and non-spherical particles, Powder Technology, vol. 58, pp. 63–70.

Hetsroni, (1989). Particles-turbulence interaction, International Journal of Multiphase Flow vol. 15, issue 5, pp. 735-746.

Hill, R. J., Koch, D. L. & Ladd, A. J. C., (2001a). The first effects of fluid inertia on flows in ordered and random arrays of spheres, Journal of Fluid Mechanics, vol. 448, pp. 213-241.

Hill, R. J., Koch, D. L. and Ladd, A. J. C., (2001b). Moderate-Reynolds-number flows in ordered and random arrays of spheres, Journal of Fluid Mechanics, 448, pp. 243-278.

Hu, H. H., Patankar, N. A. and Zhu M. Y., (2001) Direct numerical simulations of fluid–solid systems using the arbitrary Lagrangian–Eulerian technique, Journal of Computational Physics, vol. 169, pp. 427–462.

Hu, H., (1996). Direct simulation of flows of solid-liquid mixtures, International Journal of. Multiphase Flow, vol. 22, issue 2, pp.335-352.

Hu, H.H., Joseph, D.D., Crochet, M.J., (1992). Direct simulation of fluid particle motions. Theoretical Computational Fluid Dynamics, vol. 3, issue 5, pp. 285-306.

Huber, N. and Sommerfeld, M., (1994). Characterization of the cross-sectional particle concentration distribution in pneumatic conveying systems, Powder Technology, vol. 79, pp. 191-210.

Huber, N. and Sommerfeld, M., (1998). Modelling and numerical calculation of dilute-phase pneumatic conveying in pipe systems, Powder Technology, vol. 99, pp. 90-101.

Ishii, M., (1975). Thermo-fluid Dynamic Theory of Two-phase Flow, Eyrolles, Paris

Ivanov, K. P. and Rivkind, V. Ya., (1982). Steady flow of a viscous incompressible fluid past two particles at moderate Reynolds numbers, Journal of fluid dynamics, vol. 17, issue 1, pp. 138-142.

Ivanov, K. P. and Rivkind, V. Ya., (1985). Steady flow of a viscous incompressible fluid around two particles of different dimensions, Journal of fluid dynamics, vol. 20, issue 1, pp. 158-160.

Jakobsen, M. l., Easson, W. J., Greated, C. A. & Glass, D. H., (1994). Pneumatic particle conveyance in pipe bend: simultaneous two-phase PIV measurements of the slip velocity between the air and the particle-phase, Proc. Of the 7th International Symposium on Applications of Laser Techniques to Fluid Mechanics, Lisbon, Portugal, July 11 – 14.

Jakobsen, ML, Easson, WJ, Greated, CA, Glass, DH, (1996). Particle image velocimetry: simultaneous two-phase flow measurements, Measurement Science and Technology, IOP, vol.7, issue9, pp. 1270-1280.

Jayaweera, O. L. F. and Mason, B. J., (1964). The behaviour of clusters of spheres falling in a viscous fluid. Part1. Experiment. Journal of Fluid mechanics, vol. 20, pp. 121-128.

Jiradilok, V., Gidaspow, D. and Breault, R. W., (2007). Computation of gas and solid dispersion coefficients in turbulent risers and bubbling beds. Chemical Engineering Science, doi: 10.1016/ j.ces.2007.01.084

Johnson, A. and Tezduyar, T., (1995). Numerical simulation of fluid-particle interactions, Proceedings of International Conference on Finite Elements in Fluids, October, Venezia, Italy.

Johnson, A. and Tezduyar, T., (1996). Simulation of multiple spheres falling in a liquid-filled tube, Journal of Computer Methods in Applied Mechanics and Engineering, vol. 134, pp. 351-373.

Johnson, A. and Tezduyar, T., (1997). 3D simulation of fluid-particle interactions with the number of particles reaching 100, Journal of Computer Methods in Applied Mechanics and Engineering, vol. 145, pp. 301-321.

Johnson, T. A. and Patel, V. C. (1999). Flow past a sphere up to a Reynolds number of 300, Journal of Fluid Mechanics, vol. 378, pp. 19-70.

Joseph, D., (2002). Interrogations of direct numerical simulation of solid–liquid flow. Available at http://www.efluids.com/efluids/books/joseph.htm.

Kaftori, D., Hetsroni, G. and Banerjee, S. (1998) The effect of particles on wall turbulence, International Journal of multiphase Flow, vol. 24, issue 3, pp. 359-386.

Kaftori, D., Hetsroni, G., Banerjee, S., (1998). The effect of particles on wall turbulence. Int. J. Multiphase Flow 24, 359–386.

Kajishima, T. (2004). Influence of particle rotation on the interaction between particle clusters and particle-induced turbulence, International Journal of Heat and Fluid Flow, vol. 25, issue 5, pp. 721-728.

Kajishima, T. and Takiguchi, S. (2002). Interaction between particle clusters and particle-induced turbulence, International Journal of Heat and Fluid Flow, vol. 23, issue 5, pp. 639-646.

Kajishima, T., Takiguchi, S., Hamasaki, H. and Miyake, Y., (2001). Turbulence structure of particle-laden flow in a vertical plane channel due to vortex shedding, JSME International Journal Fluids and Thermal Engineering, Series B, vol. 44, issue 4, pp. 526–535.

Kim, I., Elghobashi, S., and Sirignano, W., (1993). Tree-dimensional flow over two spheres placed side by side, Journal of Fluid Mechanics, vol. 246, pp. 465-488

Kim, S. and Karrila S. J., (1991): Microhydrodynamics: Principles and selected applications. Butterworth-Heinemann, Boston, USA

Kim, S., (1987). Stokes flow past three spheres: an analytic solution. Physics of Fluids, vol. 30, pp. 2309-2314.

Kleinstreuer, C., (2003). Two-phase flow: theory and applications, Taylor & Francis, Inc., New York, NY

Kofke, D., (2006). Lectures on Molecular Simulation, SUNY Buffalo, http://www.eng.buffalo.edu/~kofke/ce530/index.html, page visited on May 2006.

Kussin, J. and Sommerfeld, M., (2002). Experimental studies on particle behaviour and turbulence modification in horizontal channel flow with different wall roughness, Experiments in Fluids, vol. 33, pp. 143–159.

Kuusela, E., (2005). Steady-state sedimentation of non-Brownian particles with finite Reynolds numbers, PhD Dissertation of Laboratory of Physics, Helsinki University of Technology.

Kynch, G. J., (1958). The slow motion of two or more spheres through a viscous fluid, Journal of Fluid Mechanics, vol. 5, pp. 193-208

Ladd A. and Verberg, R., (2001). Lattice-Boltzmann simulations of particle–fluid suspensions, Journal of Statistical Physics, vol. 104, issue 5-6, pp. 1191–1251.

Ladd, A., (1994). Numerical simulations of particulate suspensions via a discretized Boltzmann equation. Part 1. Theoretical Foundation, Journal of Fluid Mechanics, vol. 271, pp. 285–309

Lain, S. and Sommerfeld, M., (2003). Turbulence modulation in dispersed two-phase flow laden with solids from a lagrangian perspective, International Journal of Heat and Fluid Flow, vol. 24, pp. 616-625.

Lantermann, U. and Hänel, D., (2007). Particle Monte Carlo and lattice-Boltzmann methods for simulations of gas–particle flows, Computers & Fluids, vol. 36, issue 2, pp. 407-422.

Lázaro and Lasheras (1989), Particle dispersion in turbulent plane free shear layer, Physics of Fluids A, vol. 1, issue6, pp. 1035-1044.

Lee, L-Y., Quek, T-Y, Deng, R., Ray, M-B. and Wang, C-H, (2004). Pneumatic transport of granular materials through a 90° bends, Chemical Engineering Science, vol. 59, issue 21, pp. 4637-4651.

Legendre, D., Magnaudet, J. and Mougin, G., (2003). Hydrodynamic interactions between two spherical bubbles rising side by side in a viscous liquid, Journal of Fluid Mechanics, vol. 497, pp. 133-166.

Levy, A. and Mason, D., (1998). The effect of a bend on the particle cross-section concentration and segregation in pneumatic conveying systems, Powder Technology, vol. 98, pp. 95-103.

Liang, S.-C., Hong, T., & Fan, L.-S., (1996). Effects of particle arrangements on the drag force of a particle in the intermediate flow regime, International Journal of Multiphase flow, vol. 22, pp. 285-306.

Ljus, C., Johansson, B., Almstedt, A., (2002). Turbulence modification by particles in a horizontal pipe flow, International Journal of Multiphase Flow, vol. 28, pp. 1075-1090.

Lomholt, S. Stenum, B. and Maxey, M. R., (2002). Experimental verification of the force coupling method for particulate flows, International Journal of Multiphase Flow, vol. 28, issue 2, pp.225-246.

Lomholt, S., (2000). Numerical investigations of macroscopic particle dynamics in microflows, Ph.D. Thesis, Risø National Laboratory, Roskilde, Denmark.

Losenno, C, Easson, W. J., (2001). Free-falling of irregular particles, International Conference on Multi-Phase Flow, ASME, New Orleans, no 522.

Losenno, C., (2004). An investigation of stream of irregular particles in free fall, PhD, Thesis, University of Edinburgh, Edinburgh, Scotland.

Loth, E., (2007). Computational fluid dynamics of bubbles, drops and particles, University of Illinois at Urbana-Champaign, Draft for Cambridge University Press, available at: http://www.ae.uiuc.edu/~loth/CUP/Loth.

Lu, J. and Tryggvason, G., (2006). Numerical study of turbulent bubbly downflows in a vertical channel, Physics of Fluids, vol.18, pp.103302 (1-10).

Lu, J. and Tryggvason, G., (2007). Effect of bubble size in turbulent bubbly downflow in a vertical channel, Chemical Engineering Science, vol. 62, issue 11, pp. 3008-3018.

Lu, J., Biswas, S., Tryggvason, G., (2006). A DNS study of laminar bubbly flows in a vertical channel, International Journal of Multiphase Flow, vol. 32, pp. 643–660.

Malmgren, A., Oluwande, G. and Riley, G., RWE Innogy plc., (2003). Multiphase flow in coal-fired power plants. Report No. COAL R252 DTI/PUB URN 03/1635. First published Crown copyright.

Marsaglia, G. and Tsang, W. W., (2004). The 64-bit universal RNG, Statistics and Probability Letters, vol. 66, pp. 183-187.

Marsaglia, G. and Zaman, A., (1993). Monkey test for random number generators, Computers and Mathematics with Applications, vol. 26, issue 9, pp. 1-10.

Marsaglia, G., Narasimhan, B. and Zaman, A., (1990). A random number generator for PC's, Computer Physics Communications, vol. 60, pp.345-349.

Masliyah, J. H. and Epstein, N. (1970). Numerical study of steady flow past spheroids, Journal of Fluid Mechanics, vol. 44, pp. 493-512.

Matsumoto, S. and Saito, S. (1970-1). On the mechanism of suspension of particles in horizontal pneumatic conveying: Monte Carlo simulation based on irregular bouncing model, Journal of Chemical Engineering of Japan, vol. 3, issue 1, pp. 83-92.

Matsumoto, S. and Saito, S. (1970-2). Monte Carlo simulation of horizontal pneumatic conveying based on the rough wall model, Journal of Chemical engineering of Japan, vol. 3, issue 2, pp. 223-230.

Maury, B., (1999). Direct simulations of 2d fluid-particle flows in biperiodic domains, Journal of Computational Physics, vol. 156, issue 2, pp. 325-351.

Maury, B., (2003). Fluid-particle shear flows, ESAIM: Mathematical Modelling and Numerical Analysis, vol. 37, issue 4, pp. 699-708.

McCluskey, D. R, Easson, W. J., Greated, C. A., Glass, D. H., (1989). Use of particle image velocimetry to study roping in pneumatic conveyance, Particle and Particle Systems Characterisation, vol.6, issue 3, pp.129-132.

McCluskey, D. R., (1992). An optical investigation of air-particle flows, PhD, Thesis, University of Edinburgh, Edinburgh, Scotland.

Metropolis, N. (1987). The beginning of the Monte Carlo method, Los Alamos Science, special issue, vol. 15, pp. 125-130.

Metropolis, N. and Ulam, S. (1949). The Monte Carlo method, Journal of American Statistical Association, vol. 44, pp. 335–341.

Metropolis, N., Rosenbluth, A. W., Rosenbluth, M. N., Teller, A. H. and Teller, E. (1953). Equation of state calculations by fast computing machines, Journal of Chemical Physics, vol. 21, pp. 1087-1092.

Michaelides, E., (2006). Particles, bubbles & drops: Their motion, heat and mass transfer, World Scientific Publishing Company Incorporated, Hackensack, New Jersey (USA).

Natarajan, R. and Acrivos, A., (1993). The instability of the steady flow past spheres and disks, Journal of Fluid Mechanics, vol. 254, pp. 323-344.

Nicolai, H., Herzhaft, B., Hinch, E.J., Oger, L. and Guazzelli, E., (1995). Particle velocity fluctuations and hydrodynamic self-diffusion of sedimenting non-Brownian spheres. Physics of Fluids, vol. **7**, pp. 12–23.

Pan, T, Joseph, D., Bai, R., Glowinski, R., and Sarin, V., (2002). Fluidisation of 1204 spheres: simulation and experiment, Journal of Fluid Mechanics, vol. 451, pp. 169-191.

Pan, Y. and Banerjee, S., (1996). Numerical simulation of particle interactions with wall turbulence, Physics of Fluids, vol. 8, issue 10, pp. 2733-2755.

Pan, Y., Banerjee, S., (1997). Numerical investigation of the effects of large particles on wall turbulence. Physics of Fluids vol. 9, pp. 3786–3807.

Pan, Y., Dudukovic, M. P. and Chang, M., (1999). Dynamic simulation of bubbly flow in bubble columns, Chemical Engineering Science., vol. 54, issue (13-14), pp. 2481-2489.

Pan, Y., Tanaka, T. and Tsuji, Y., (2002). Turbulence modulation by dispersed solid particles in rotating channel flows, International Journal of Multiphase flow, vol. 28, pp. 527-552.

Patankar, N. A., Ko, T., Choi, H. G. and Joseph, D. D, (2001). A correlation for the lift-off of many particles in plane Poiseuille flows of Newtonian fluids, Journal of Fluid Mechanics, vol. 445, pp. 55-76.

Patankar, N., Joseph, D., Wang, J., Barree, R., Conway, M. and Asadi, M., (2002). Power law correlations for sediment transport in pressure driven channel flows. International Journal of Multiphase Flow, vol. 28, issue 8, pp. 1269–1292.

Pedinotti, S. Mariotti, G. and Banerjee, S. (1992). Direct numerical simulation of particle behaviour in the wall region of turbulent flows in horizontal channels, International Journal of Multiphase Flow, vol. 18, issue 6, pp. 927-941

Phillips, R. J., (1995). Calculation of multiple sphere linearized Poisson-Boltzmann interactions near cylindrical fibres and planar surfaces, Journal of Colloidal and Interface Science, vol. 175, pp. 386-399.

Prahl, L., Hölzer, A., Arlov, D., Revstedt, J., Sommerfeld, M., Fuchs, L., (2007) On the interaction between two fixed spherical particles, International Journal of Multiphase Flow, vol. 33, issue 7, pp.707-725.

Premnath, K-N. and Abraham, J., (2007). Three-dimensional multi-relaxation time (MRT) lattice-Boltzmann models for multiphase flow, Journal of Computational Physics, vol. 224, issue 2, pp. 539-559.

Qi, D., (1999). Lattice-Boltzmann Simulations of Particles in non-zero-Reynolds-number flows, Journal of Fluid Mechanics, vol. 385, pp. 41-62.

Qi, D., (2000). Latttice-Boltzmann simulations of fluidisation of rectangular particles, International Journal of Multiphase flow, vol.26, issue 3, pp. 421-433.

Qi, D., (2001). Simulations of fluidisation of cylindrical multiparticles in a three-dimensional space, International Journal of Multiphase Flow, vol. 27, issue 1, pp. 107-118.

Rani, S., Winkler, C. and Vanka, S., (2004). Numerical simulation of turbulence modulation by dense particles in a fully developed pipe flow, Powder Technology, vol. 141, pp. 80-99.

Rautiainen, A., Stewart, G., Poikolainen, V. and Sarkomaa, P., (1999). An experimental study of vertical pneumatic conveying, Powder Technology, vol. 104, issue 2, pp. 139-150.

Richardson, J. F., and Zaki, W. N., (1954). Sedimentation and fluidisation, Part I, Transaction of the Institution of Chemical Engineers, pp. 32, 35–53.

Rowe, P. N. and Henwood, G. A., (1961). Drag forces in a hydraulic model of a fluidise bed –part 1, Transactions of the Institution of Chemical Engineers, vol.39, pp. 43-54.

Rowe, P. N., (1961). Drag forces in a hydraulic model of a fluidised bed, Part II, Transaction of the Institution of Chemical Engineers, vol. 39, pp. 175-180.

Rowe, P. N., (1987). A convenient empirical equation for estimation of Richard–Zaki exponent, Chemical Engineering Science 42, pp. 2795-2796.

Sato *et al.*, (2000). Effect of inter-particle spacing on turbulence modulation by Lagrangian PIV, International Journal of Heat and Fluid Flow, vol. 21, issue 5, pp. 554-561.

Satoh, A., Chantrell, R. W., Kamiyama, S-I. and Coverdale, G. (1996). Three dimensional Monte Carlo simulations of thick chainlike clusters composed of ferromagnetic fine particles, Journal of Colloid and Interface science, vol. 181, issue 2, pp. 422-428.

Schallert, R. and Levy, E., (2000). Effect of a combination of two elbows on particle roping in pneumatic conveying, Powder Technology, vol. 107, issue. 3, pp. 226-233.

Schlichting, H., (1972). Teoría de la capa límite. Ed. URMO. Madrid, España.

Schouveiler, L., Brydon, A., Leweke, T. and Thompson, M. C., (2004). Interaction of the wakes of two spheres placed side by side, European Journal of Mechanics B/Fluids, vol. 23, pp. 137-145.

Shao, X.-M., Liu, Y. and Yu, Z.-S., (2005). Interaction between two sedimenting particles with different sizes, Journal of Applied Mathematics and Mechanics-China, vol. 26, issue 3, pp. 407-414.

Shuyan, W., Huanpeng, L., Huilin, L., Wentie, L, Jiamin, D. and Wei, L., (2005). Flow behaviour of clusters in a riser simulated by direct simulation Monte Carlo method, Chemical Engineering Journal, vol. 106, issue 3, pp. 197–211.

Smoluchowski, M., (1912). On the practical applicability of Stoke's law, Proc. 5th International Congress of Mathematics, vol. 2 (Cambridge: Cambridge University Press) p. 192

Smoluchowsky, M., (1911). On the mutual action of spheres which move in a viscous liquid. Bull Acad. Science Cracovie A1: 28–39

Sokolichin, A. and Eigenberger, G., (1994). Gas—liquid flow in bubble columns and loop reactors: Part I. Detailed modelling and numerical simulation, Chemical Engineering Science, vol. 49, issue 24, part 2, pp. 5735-5746.

Sommefeld, M., (2000). Theoretical and experimental modelling of particulate flows, Lecture series 2000-06, von Karman Institute for Fluid Dynamics, Institut für Verfahrenstechnik, Fachbereich Ingenieurwissenschaften, Martin-Luther-Universität Halle-Wittenberg, D-06099 Halle (Saale), Germany

Sommerfeld, M. and Huber, N., (1999). Experimental analysis and modelling of particle–wall collisions, International Journal of Multiphase Flow, vol. 25, pp. 1457–1489.

Sommerfeld, M., (1992). Modelling of particle–wall collisions in confined gas–particle flows. International Journal Multiphase Flows, vol. 18, pp. 905–926.

Sommerfeld, M.and Kussin, J., (2004). Wall roughness effects on pneumatic conveying of spherical particles in a narrow horizontal channel, Powder Technology, vol. 142, pp. 180–192.

Sørensen, H., (2005). Experimental investigation of non-spherical particle aerodynamics, PhD Thesis, Institute of Energy Technology, Aalborg University, Denmark.

Stimson, M. and Jeffery, G. B., (1926). The motion of two spheres in a viscous fluid, Proceedings of the Royal Society of London A, vol. 111, pp.110-116.

Takiguchi, S., Kajishima, T. and Miyake, Y., (1999). Numerical scheme to resolve the interaction between solid-particles and fluid-turbulence, JSME International Journal, series B, Fluids and Thermal Engineering, 42, issue 3, pp. 411–418

Tal, R., Lee, D.N. and Sirignano, W.A., (1984). Heat and momentum transfer around a pair of spheres in viscous flow, International Journal of Heat and Mass Transfer, vol. 27, pp. 1953–1962.

Tanaka, M., Maeda, Y. and Hagiwara, Y., (2002). Turbulence modification in homogeneous turbulent shear flow laden with small heavy particles, International Journal of Heat Transfer and Fluid Flow, vol. 23, issue 5, pp. 615-626.

Tanaka, T., Yonemura, S., Kiribayashi, K. and Tsuji, Y., (1996). Cluster formation and particle induced instability in gas-solid flows predicted by the DSMC method, JSME International Journal, Series B, vol. 2, pp. 239-245.

Taneda, S., (1956). Experimental investigation of the wave behind a sphere at low Reynolds number, Journal of Physics Society of Japan, vol. 11, pp. 1104-1108.

Tang *et al.*, (1992). Self-organising particle dispersion mechanism in a plane wake, Physics of Fluids A, vol. 4, issue 10, pp. 2244-2251.

Tashiro, H., Watanabe, E., Shimano, H., Funatsu, K. and Tomita, Y., (2001). Effect of mixing gas-fine particle suspension flow with small amount of coarse ones in a

horizontal pipe, International journal of Multiphase Flow, vol.27, issue 11, pp. 2001-2013.

Tezduyar, T. E., Behr, M. and Liou, J., (1992a). A new strategy for finite element computations involving moving boundaries and interfaces—The deforming-spatial-domain/space-time procedure: II. Computation of free-surface flows, two-liquid flows, and flows with drifting cylinders, Computer Methods in Applied Mechanics and Engineering, vol 94, issue 3, pp. 353-371.

Tezduyar, T. E., Behr, M. and Liou, J., (1992a). A new strategy for finite element computations involving moving boundaries and interfaces—The deforming-spatial-domain/space-time procedure: I. The concept and the preliminary numerical tests, Computer Methods in Applied Mechanics and Engineering, vol 94, issue 3, pp. 339-351.

Thelen, T. and Ramirez, W. F., (1999). Modelling of solid-liquid fluidisation in the stokes flow regime using two-phase flow theory, A. I. Ch. E. Journal, vol. 45, issue 4, pp. 708-723.

Tomboulides, A.G. and Orszag, S.A., (2000). Numerical investigation of transitional and weak turbulent flow past a sphere, Journal of Fluid Mechanics, vol. 416, pp. 45-73.

Tryggvason, B. Bunner, A. Esmaeeli, D. Juric, N. Al-Rawahi, W. Tauber, J. Han, S. Nas and Y.-J. Jan, (2001). A front tracking method for the computations of multiphase flow, Journal of Computational Physics. Vol.169, pp. 708–759

Tsuji, T., Narutomi, R., Yokomine, T., Ebara, S. and Shimizu, A., (2003). Unsteady Three-dimensional simulation of interactions between for and two spheres, International Journal of Multiphase Flow, vol. 29, pp. 1431-1450.

Tsuji, Y., (2007). Multi-scale modelling of dense phase gas-particle flow, Chemical Engineering Science, vol. 62, issue 13, pp. 3410-3418.

Tsuji, Y., Morikawa, Y. and Shiomi, H., (1984). LDV measurements of an air-solid two-phase flow in a vertical pipe, Journal of Fluid Mechanics, vol. 139, pp. 417-434.

Tsuji, Y., Morikawa, Y., Tanaka, T., Nakatsukasa, N. and Nakatani, M., (1987). Numerical simulation of gas-solid two-phase flow in a two-dimensional

horizontal channel, International Journal of Multiphase Flow, vol. 13, issue 5, pp. 671-683.

Tsuji, Y., Morikawa, Y., Terashima, K., (1982). Fluid-dynamic interaction between two spheres, International Journal of Multiphase Flow, vol. 8, issue1, pp. 71-82.

Tsuji, Y., Tanaka, T. and Yonemura, Y., (1998). Cluster patterns in circulating fluidised beds predicted by numerical simulation (discrete particle model versus two-fluid model), Powder Technology, vol. 95, issue 3, pp. 254-264

Unverdi, S.O., Tryggvason, G., (1992a). Computations of multi-fluid flows, Physica D, vol. 60, pp. 70-83.

Unverdi, S.O., Tryggvason, G., (1992b). A front-tracking method for viscous, incompressible multi-fluid flows. Journal of Computational Physics, vol. 100, pp. 25-37.

Vargas, S. and Easson, W. J., (2004). Forces between two spheres at low Reynolds number, 3Rd International symposium on Two-Phase Flow Modelling and Experimentation, Pisa, Italy.

Verdurmen, R. E. M., Verschueren, M., Gunsing, M., Straatsma, H., Blei, S. and Sommerfeld, M., (2005). Simulation of agglomeration in spray dryers: the EDECAD project, Le Lait: Dairy Science and Technology Journal, vol. 85, pp. 343-351.

Wang, B-X. and Liu, T., (1992). Research on hydrodynamics and heat transfer for fluid flow around heating spheres in tandem, International Journal of Heat and amass Transfer, vol. 35, issue 2, pp. 307-317.

Weinstein, E. W., Convective Derivative, From Math World--A Wolfram Web Resource. http://mathworld.wolfram.com/ConvectiveDerivative.html), page consulted in 2006.

Wolfram Matematica, (2007). Monte Carlo estimate for Pi, The Wolfram Demonstrations Project http://demonstrations.wolfram.com/MonteCarloEstimate ForPi/, page consulted in 2007.

Yan, W. and Kuan, B. (2006), Experimental investigation of dilute turbulent particular flow inside a curved 90o bend, Chemical Engineering Science, Vol. 61, pp. 3593-3601.

Yilmaz, A. and Levy, E., (1998). Roping phenomena in pulverized coal conveying lines, Powder Technology, vol. 95, issue 1, pp. 43-48.

Yilmaz, A. and Levy, E., (2001). Formation and dispersion of roes in pneumatic conveying, Powder Technology, vol. 114, issue 1, pp. 168-185.

Yonemura, S., Tanaka, T and Tsuji, Y., (1995). Cluster formation in dispersed gas-solid flows: effects of physical properties of particles, Proceedings of the 2nd International Conference on Multiphase Flow, pp. PT4-25-PT430, April 3-7, Kyoto, Japan.

Yu, L., Lu, J., Zhang, X. and Zhang S., (2007). Numerical simulation of the bubbling fluidised bed coal gasification by the kinetic theory of granular flow (KTGF), Fuel, vol. 86, issues 5-6, pp. 722-734.

Yu, L., Lu, J., Zhang, X. and Zhang, S., (2007). Numerical simulation of the bubbling fluidised bed coal gasification by the kinetic theory of granular flow (KTGF), Fuel, vol. 86, pp. 722-734.

Yu, Z., Pan-Thien, N. and Tanner, R. I., (2004) Dynamic simulation of sphere motion in a vertical tube, Journal of Fluid Mechanics, vol. 518, pp. 61–93.

Zapryanov, Z. and Tabakoba, S., (1999). Dynamic of bubbles, drops and rigid particles, Kluwer Academic Publisher, The Netherlands.

Zhan, J., Zhang, J. P. And Fan, L.-S., (2005). Effect of particle size ratio on the drag force of an interactive particle, Trans. IChemE, part A, Chemical Engineering Research and Design, Vol. 83, issue 4, pp. 339-343.

Zhang, D., Deen, N. G. and Kuipers, J. A. M., (2006). Numerical simulation of the dynamic flow behaviour in a bubble column: A study of closures for turbulence and interface forces, Chemical Engineering Science, vol. 61, issue 23, pp.7593-7608.

Zhang, Y and Reese, J. M., (2003). The drag force in two-fluid models of gas–solid flows, Chemical Engineering Science, vol. 58, issue 8, pp. 1641-1644.

Zhang, Z. and Chen, Q., (2006). Experimental measurements and numerical simulation of fine particle transport and distribution in ventilated rooms, Atmospheric Environment, vol. 40, issue 18, pp. 3396–3408.

Zhao B, Yan, C., Yang, X. and Liu, S., (2008). Particle dispersion and deposition in ventilated rooms: Testing and evaluation of different Eulerian and Lagrangian models. Building and Environment, vol. 43, issue 4, pp.388-397.

Zhao, B., Zhang, Y., Li, X., Yang, X. and Huang, D. T., (2004). Comparison of indoor aerosol particle concentration and deposition in different ventilated rooms by numerical method, Building and Environment, vol. 39, issue 1, pp. 1–8.

Zhu, C., Liang, S.-C. & Fan, L.-S., (1994). Particle wake effects on the drag force of an interactive particle, International Journal of Multiphase Flow, vol. 20, issue. 1, pp.117-129.

APPENDIX TO CHAPTER 3

A3 HYDRODYNAMIC INTERACTING FORCE CONCEPT, VELOCITY, PRESSURE AND WALL SHEAR STRESS PROFILES

In the first section (§A3.1) of this appendix a description of the concept of the interacting force (F_i) and the equation used in section §3.2.4 to evaluate the interaction force along the line connecting the two particle centres is given. In the second section (§A3.2) a series of velocity profiles, pressure and wall shear stress coefficients profiles for two fixed interacting particles in the particle separation range of $1.1 \leq D_o \leq 25$, at three different position angles $\theta = 0^o$, $\theta = 45^o$ and $\theta = 90^o$ are reported in order to support the final conclusions in chapter3.

A3.1 The concept of interacting force between two fixed particles

The concept applied to calculate the interaction force between two fixed spherical particles placed at different positions is given in this section. Kim *et al.* (1993) and Folkersma *et al.* (2000) defined the interacting force as the force parallel to the line connecting the centres of the spheres in their study of two interacting particles placed side-by-side. For this specific case, the interacting force between the two particles corresponds to the lift force, the force perpendicular to the main flow direction. However, when the particles are placed at different positions with respect to the main flow direction a general concept of interaction force between the two particles is needed. Applying the idea of Kim *et al.* (1993) and Folkersma *et al.* (2000), a general

equation for two fixed interacting spherical particles as a function of the angle position (θ) is obtained. Figure A3.1 shows the forces over the two interacting particles in two coordinate systems, one when the main flow direction is parallel to the y-axis and the other when the line connecting the particle centres is aligned with the x-axis (a rotated system). Thus, the component in the x′ direction (rotated system) on each particle contributes directly to the hydrodynamic interaction force between the two particles.

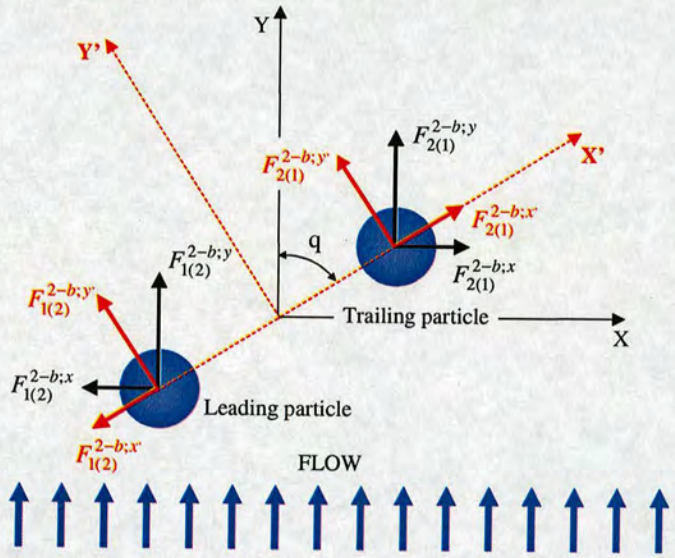

Fig. 3A.1 Forces over two interacting particles in the x-y and x′ – y′ planes.

Fundamental geometry analysis is applied to Figure A3.1 to readily obtain a mathematical expression for the force in the rotate system x′ and y′: $F_{1(2)}^{2-b;x'}$ and $F_{1(2)}^{2-b;y'}$ are a function of the angle position (θ) and the forces on the original system (no rotated system). The forces on the rotated system are given for leading particle (particle 1) in equation A3.1:

$$\begin{aligned} F_{1(2)}^{2-b;x'} &= F_{1(2)}^{2-b;x}\mathrm{Sin}(\theta) + F_{1(2)}^{2-b;y}\mathrm{Cos}(\theta) \\ F_{1(2)}^{2-b;y'} &= -F_{1(2)}^{2-b;x}\mathrm{Cos}(\theta) + F_{1(2)}^{2-b;y}\mathrm{Sin}(\theta) \end{aligned} \qquad \text{(A3.1)}$$

Similar expressions are obtained for particle 2 (trailing particle) under the influence of particle 1:

$$\begin{aligned} F_{2(1)}^{2-b;x'} &= F_{2(1)}^{2-b;x}\mathrm{Sin}(\theta) + F_{2(1)}^{2-b;y}\mathrm{Cos}(\theta) \\ F_{2(1)}^{2-b;y'} &= -F_{2(1)}^{2-b;x}\mathrm{Cos}(\theta) + F_{2(1)}^{2-b;y}\mathrm{Sin}(\theta) \end{aligned} \qquad \text{(A3.2)}$$

Base on the hydrodynamic interaction force definition (force parallel to the line connecting the particle centres), the only component that contributes to the total interaction force between the particles is the force in the x′ direction. The total interacting force in this work is defined as the difference between the force over the leading particle, $F_{1(2)}^{2-b;x'}$ and the force over the trailing particle, $F_{2(1)}^{2-b;x'}$. Thus, the final expression for the interacting force between two fixed spherical particles placed at different positions relative to each other could be defined as:

$$F_i = F_{1(2)}^{2-b;x'} - F_{2(1)}^{2-b;x'}$$

or

$$F_i = \left(F_{2(1)}^{2-b;x} - F_{1(2)}^{2-b;x}\right)\sin(\theta) + \left(F_{2(1)}^{2-b;y} - F_{1(2)}^{2-b;y}\right)\mathrm{Cos}(\theta) \qquad \text{(A3.3)}$$

A3.2 Velocity profiles, pressure coefficients, skin coefficients profiles

In order to observe the evolution of the velocity field, the pressure and the wall shear stress around the two interacting particles and support the final conclusions in chapter 3, a series of plots of velocities profiles, pressure coefficients, wall shear stress coefficients are given. Three different angles positions ($\theta = 0^o$, 45^o and 90^o) as function of the separation distances ($1.1 \leq D_o \leq 25$) are shown. The streamwise velocity profiles at some sections are plotted; in front of the particles at 0.5d from the particle surface and, at the centre the particles for side-by-side formation. The pressure and wall wall shear stress coefficients are plotted as a function of the angle (α) around the particle as defined in Figure 3.8.

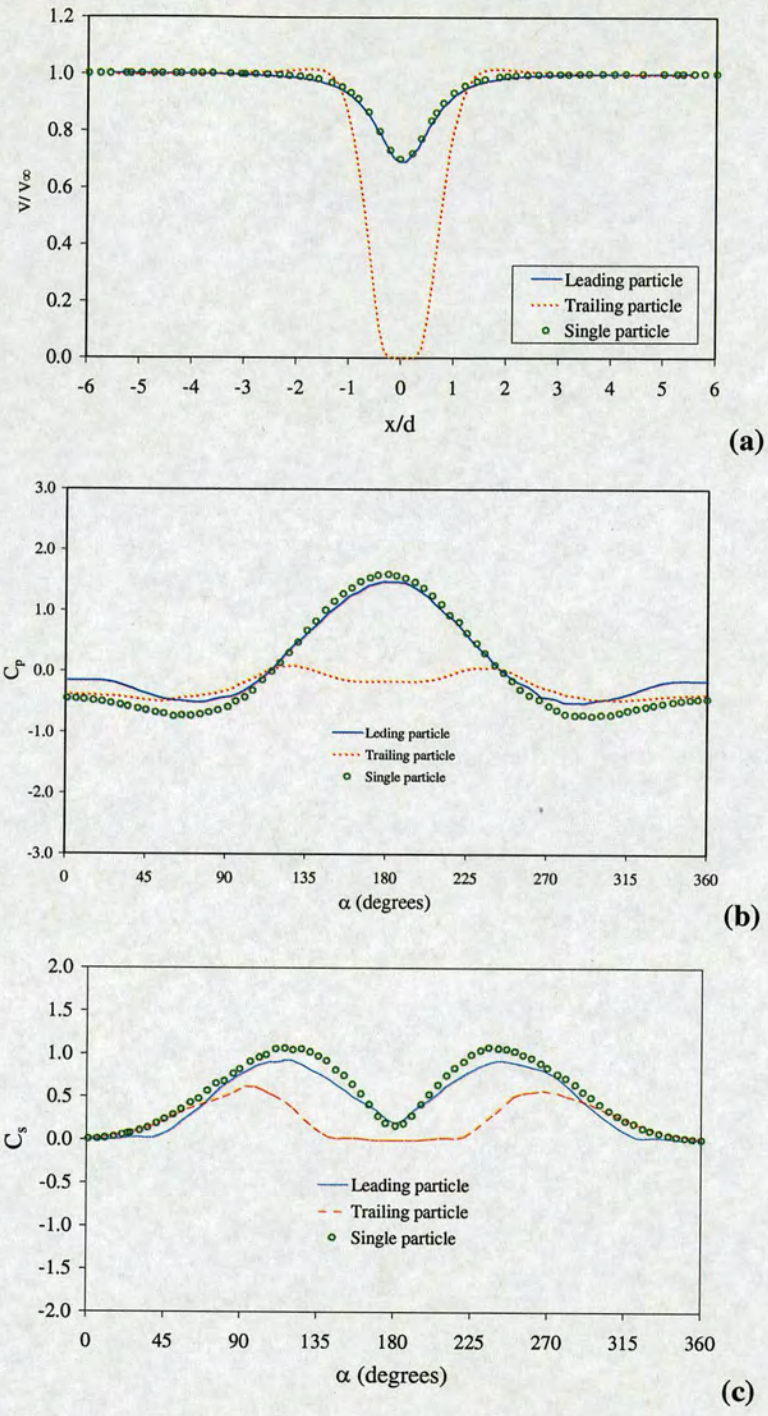

Fig. 3A.2 (a) Streamwise velocity profiles, (b) pressure coefficients and (c) wall shear stress coefficients for a single spherical particle and two fixed spherical particles at $D_o = 1.10$, $\theta = 0^o$ and $Re_p = 15$.

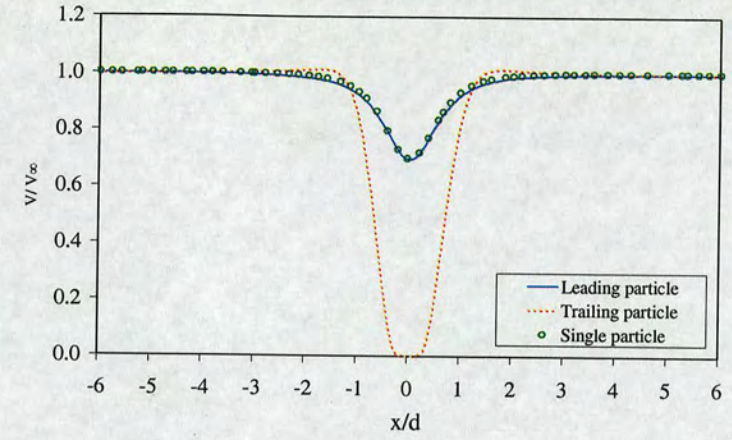

(a)

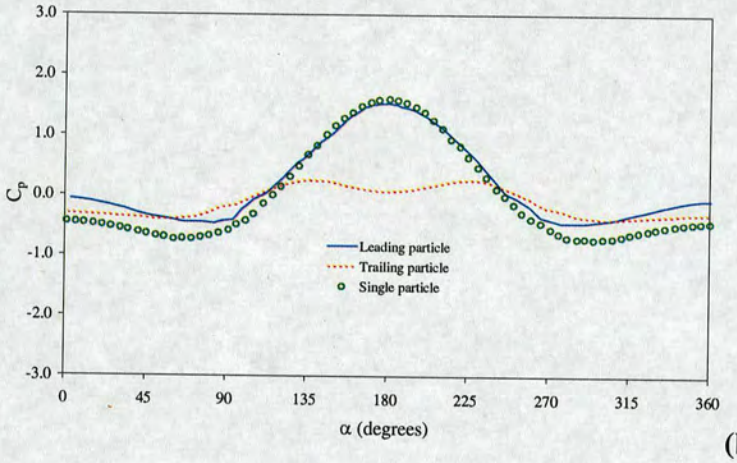

(b)

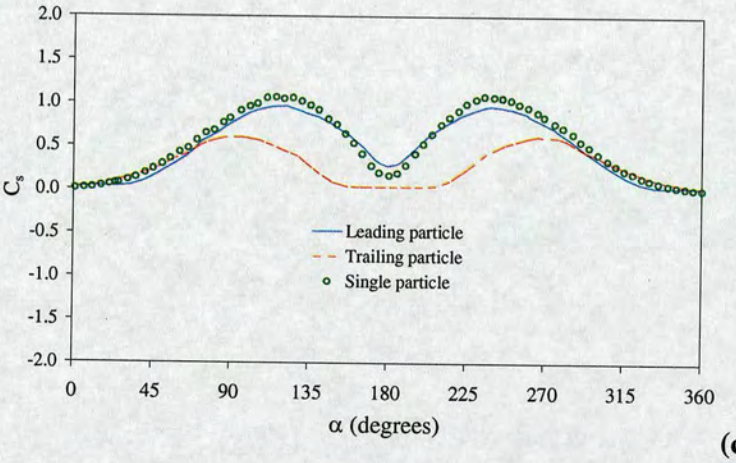

(c)

Fig. 3A.3 (a) Streamwise velocity profiles, (b) pressure coefficients and (c) wall shear stress coefficients for a single spherical particle and two fixed spherical particles $D_o = 1.50$, $\theta = 0^o$ and $Re_p = 15$.

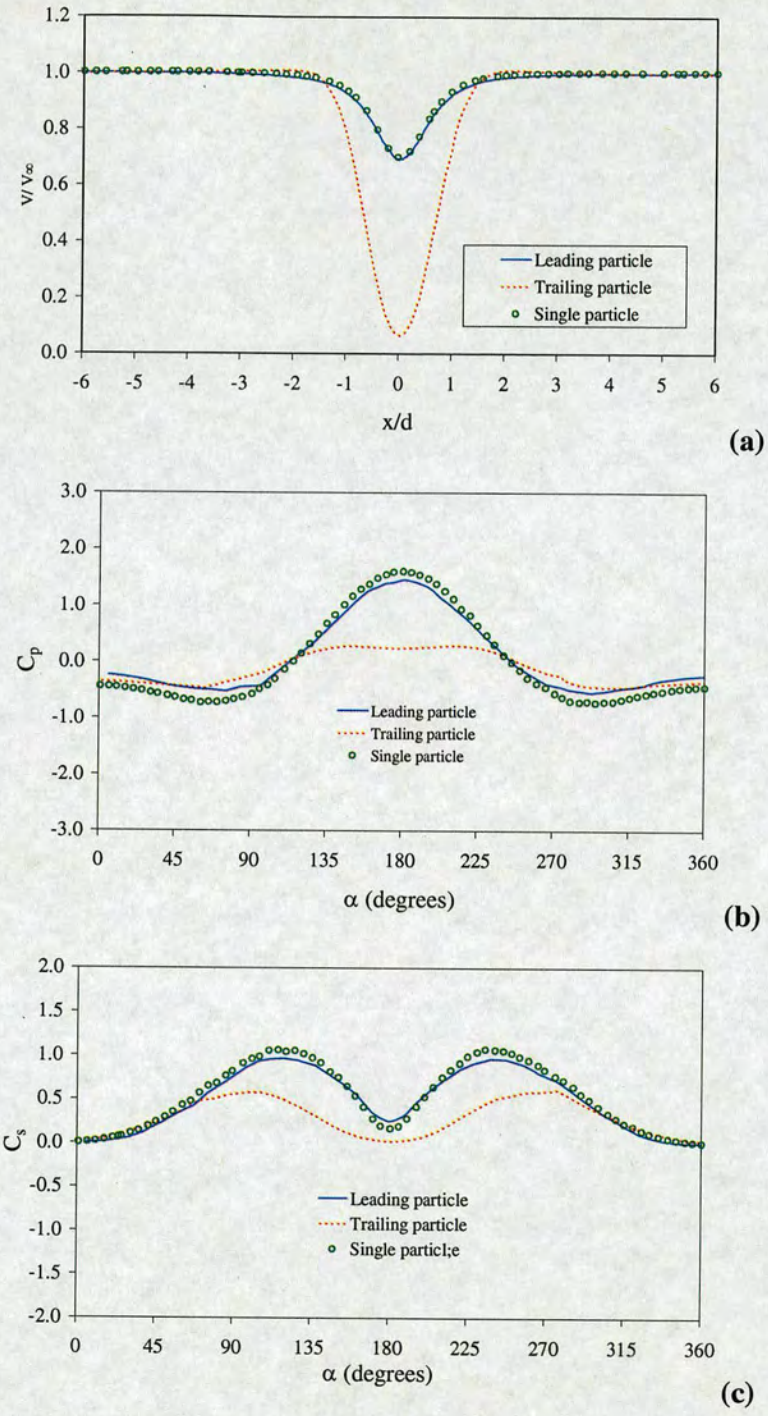

Fig. 3A.4 (a) Streamwise velocity profiles, (b) Pressure coefficients and (c) wall shear stress coefficients for a single spherical particle and two fixed spherical particles at $D_o = 2.0$, $\theta = 0^o$ and $Re_p = 15$.

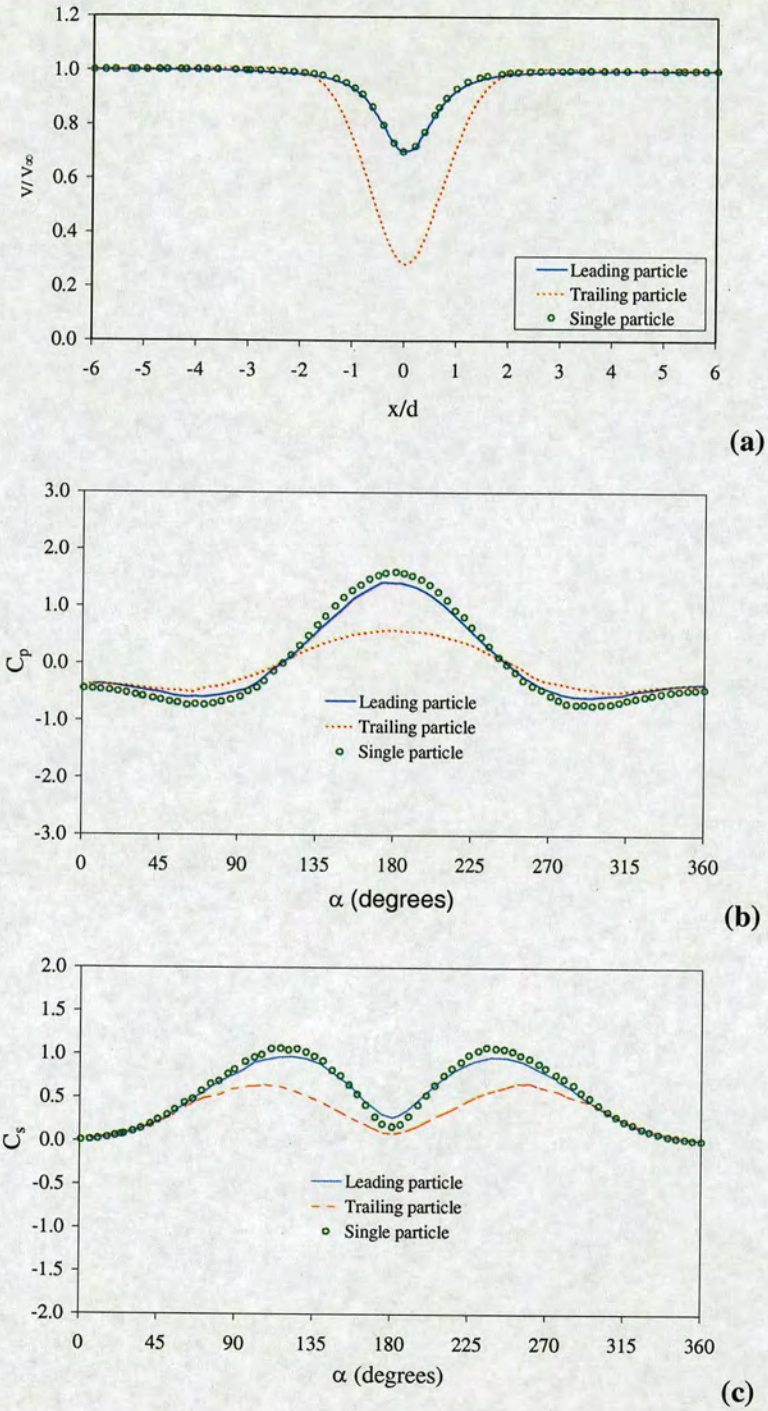

Fig. 3A.5 (a) Streamwise velocity profiles, (b) pressure coefficients and (c) wall shear stress coefficients for a single spherical particle and two fixed spherical particles at $D_o = 3$, $\theta = 0^o$ and $Re_p = 15$.

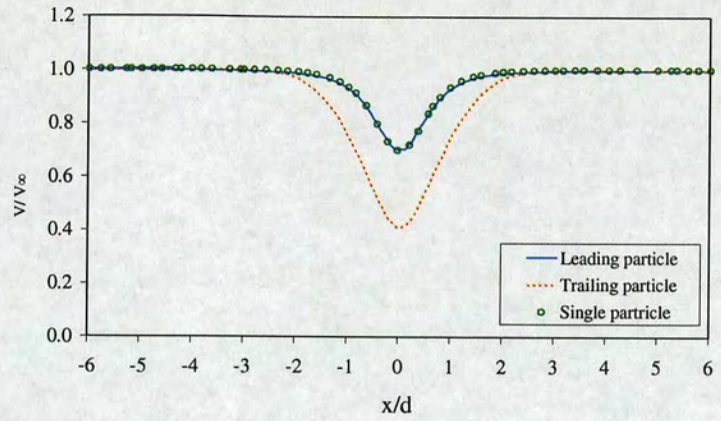

(a)

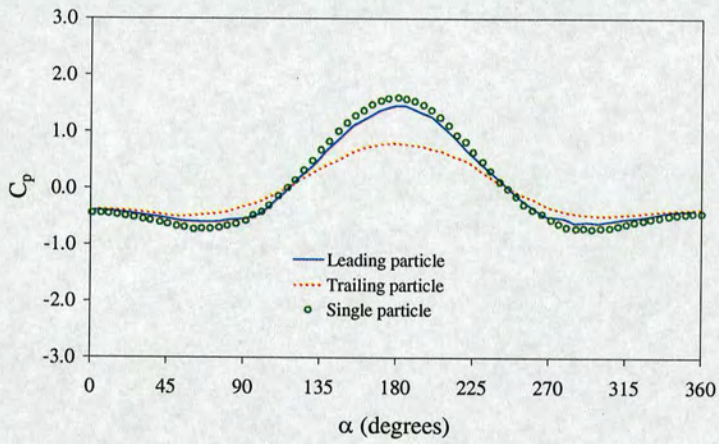

(b)

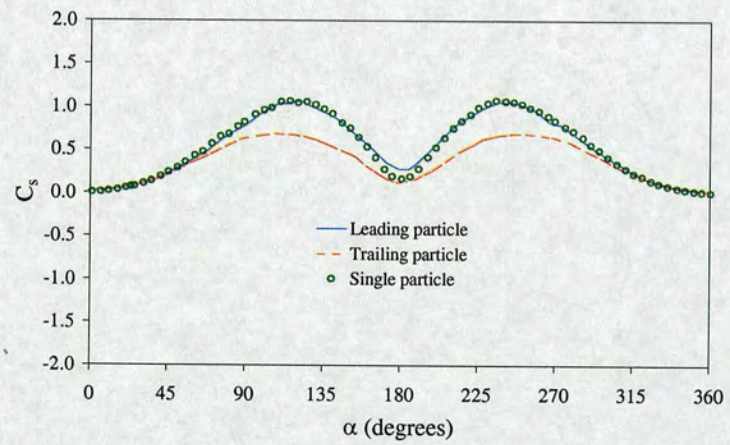

(c)

Fig. 3A.6 (a) Streamwise velocity profiles, (b) pressure coefficients and (c) wall shear stress coefficients for a single spherical particle and two fixed spherical particles at $D_o = 4.0$, $\theta = 0^o$ and $Re_p = 15$.

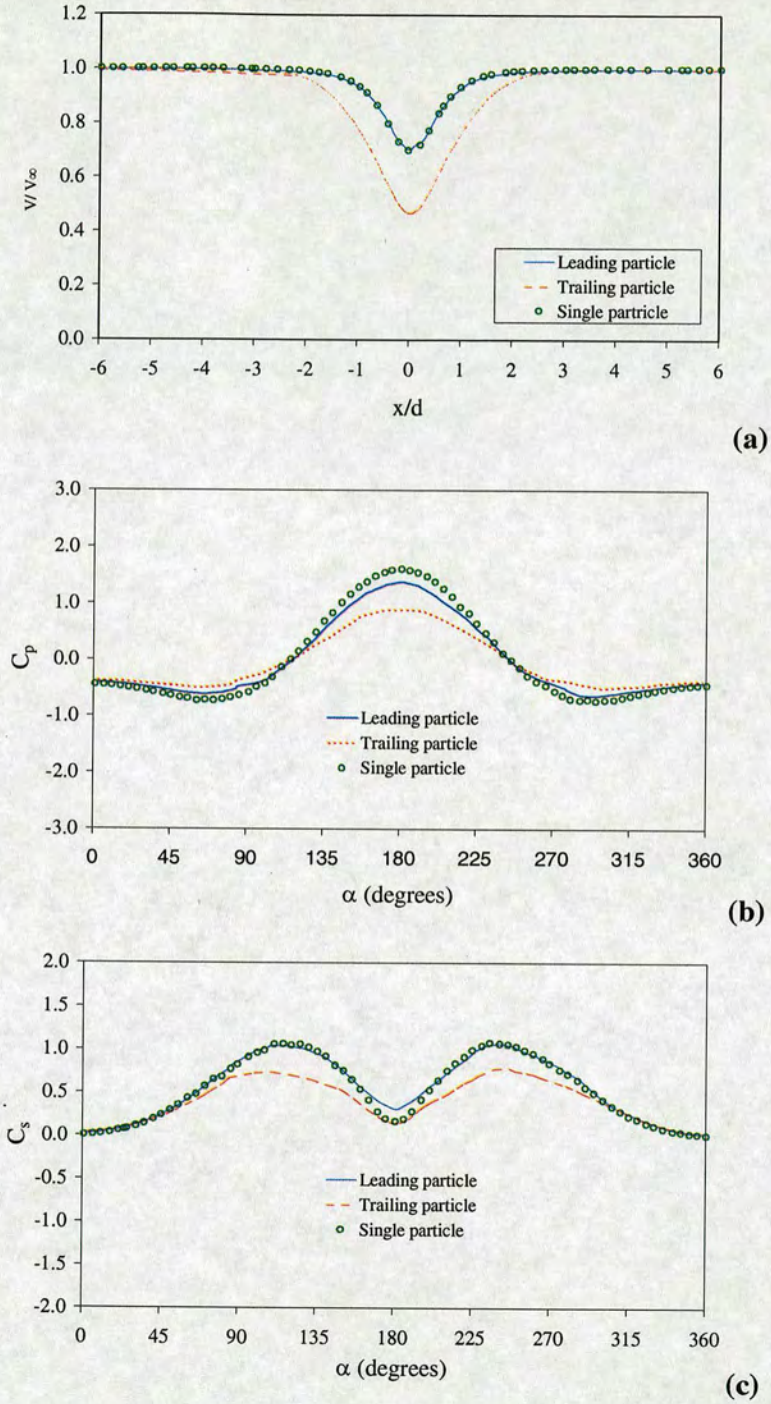

Fig. 3A.7 (a) Streamwise velocity profiles, (b) pressure coefficients and (c) wall shear stress coefficients for a single spherical particle and two fixed spherical particles at $D_o = 5.0$, $\theta = 0^o$ and $Re_p = 15$.

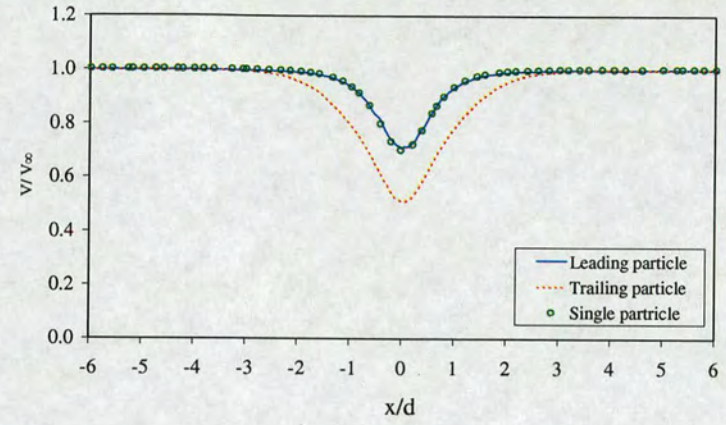

(a)

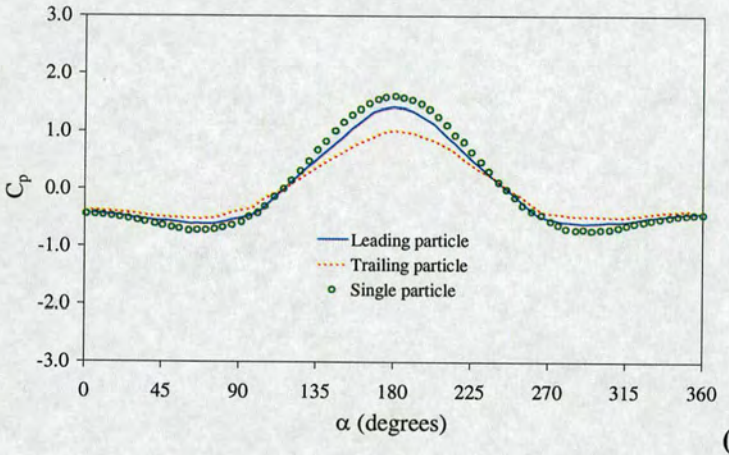

(b)

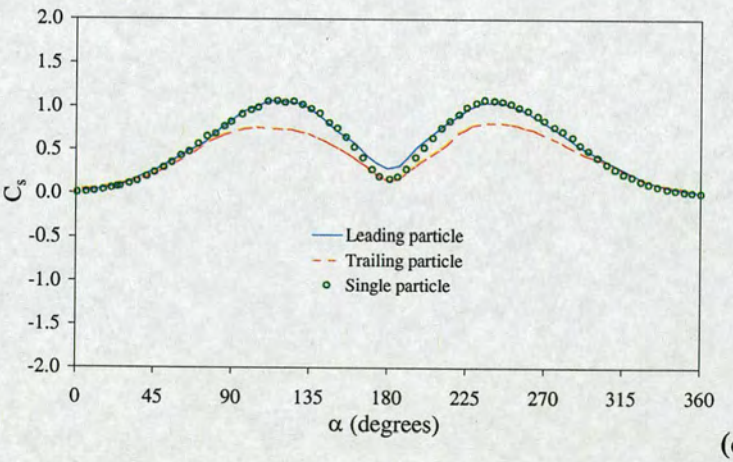

(c)

Fig. 3A.8 (a) Streamwise velocity profiles, (b) pressure coefficients and (c) wall shear stress coefficients for a single spherical particle and two fixed spherical particles at $D_o = 6.0$, $\theta = 0^o$ and $Re_p = 15$.

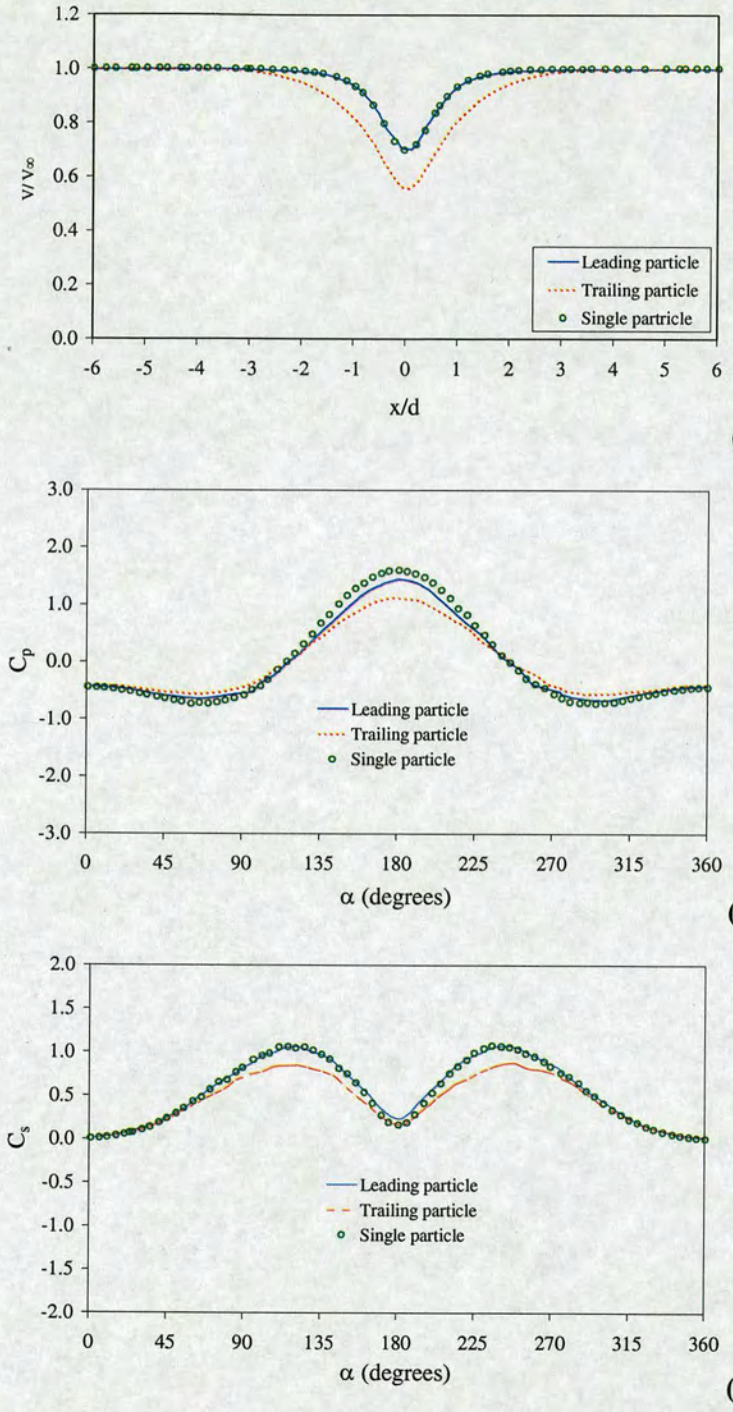

Fig. 3A.9 (a) Streamwise velocity profiles, (b) pressure coefficients and (c) wall shear stress coefficients for a single spherical particle and two fixed spherical particles at $D_o = 8.0$, $\theta = 0^o$ and $Re_p = 15$.

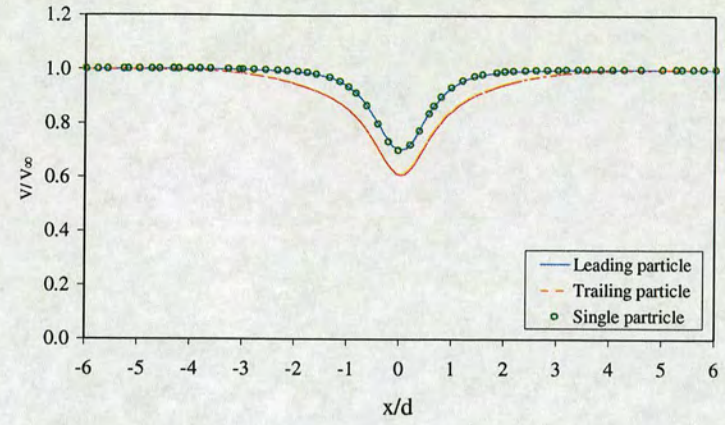

(a)

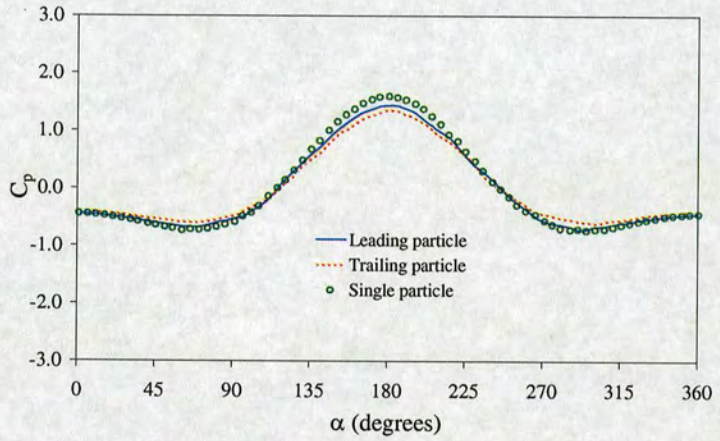

(b)

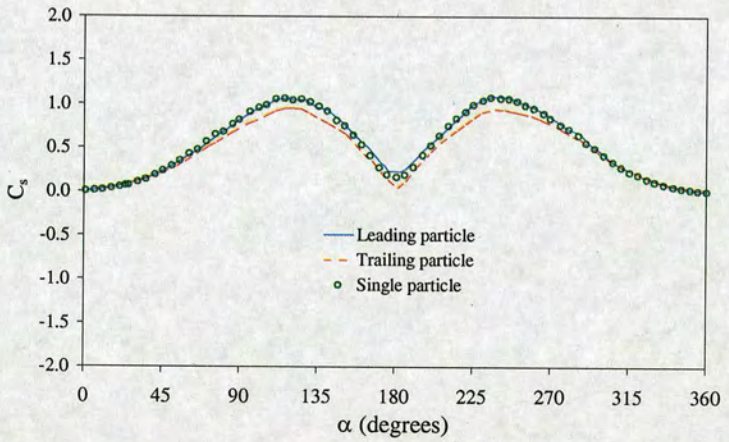

(c)

Fig. 3A.10 (a) Streamwise velocity profiles, (b) pressure coefficients and (c) wall shear stress coefficients for a single spherical particle and two fixed spherical particles at $D_o = 12.0$, $\theta = 0^o$ and $Re_p = 15$.

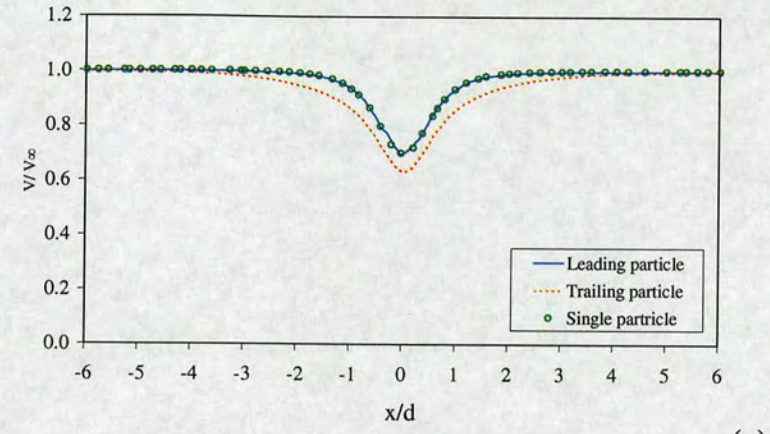

(a)

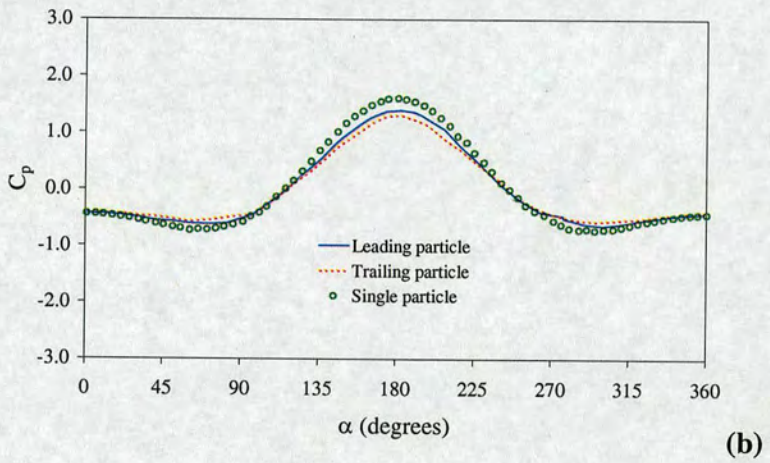

(b)

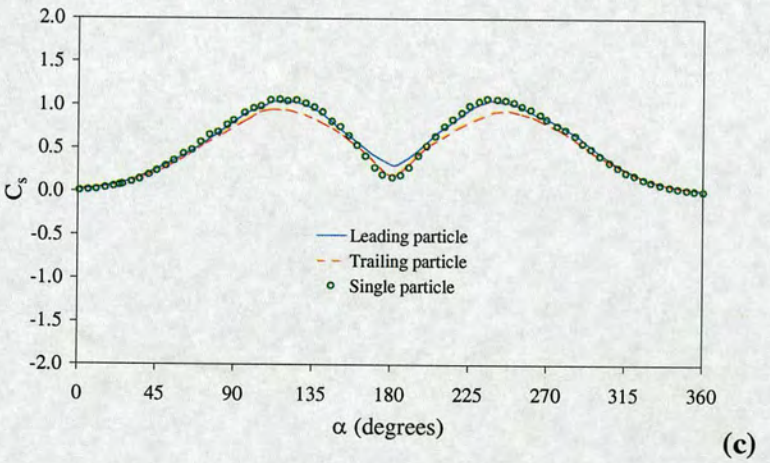

(c)

Fig. 3A.11 (a) Streamwise velocity profiles, (b) pressure coefficients and (c) wall shear stress coefficients for a single spherical particle and two fixed spherical particles at $D_o = 15.0$, $\theta = 0^o$ and $Re_p = 15$.

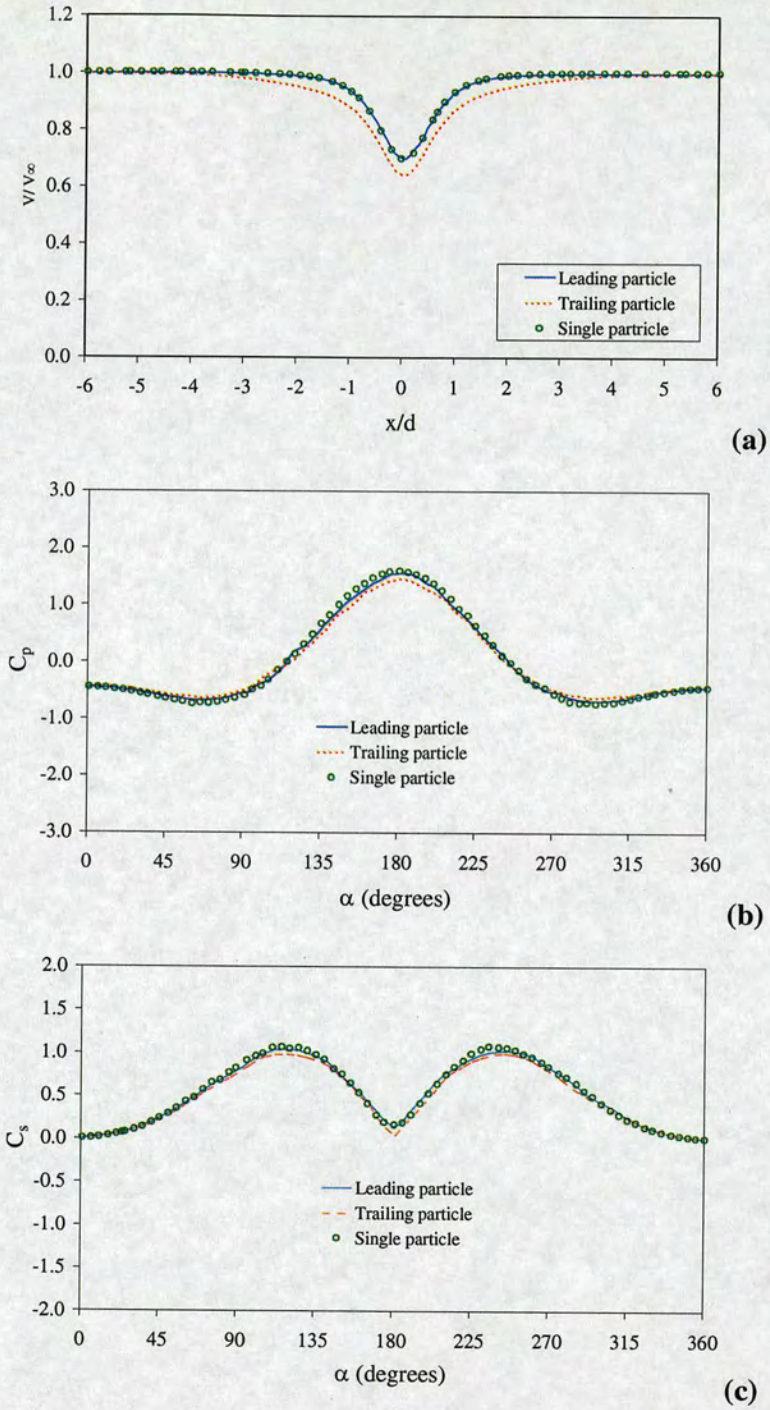

Fig. 3A.12 (a) Streamwise velocity profiles, (b) pressure coefficients and (c) wall shear stress coefficients for a single spherical particle and two fixed spherical particles at $D_o = 20.0$, $\theta = 0^o$ and $Re_p = 15$.

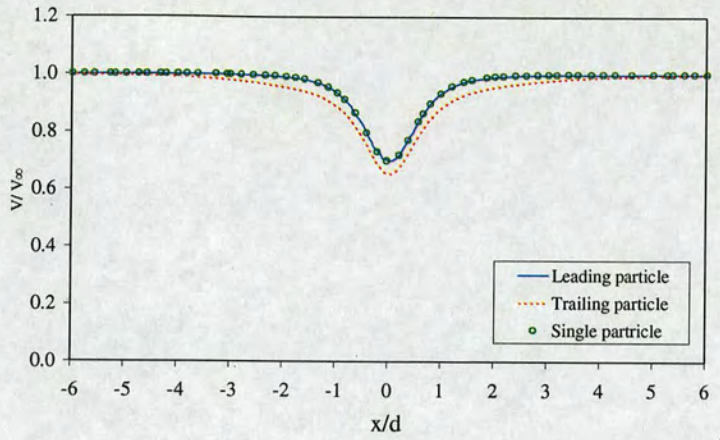

(a)

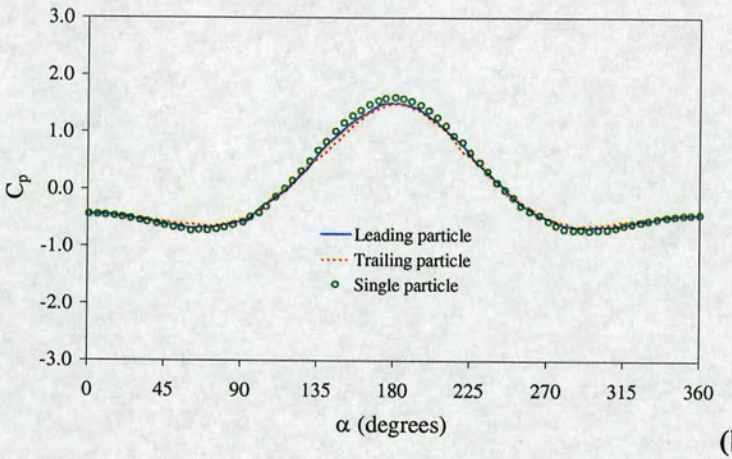

(b)

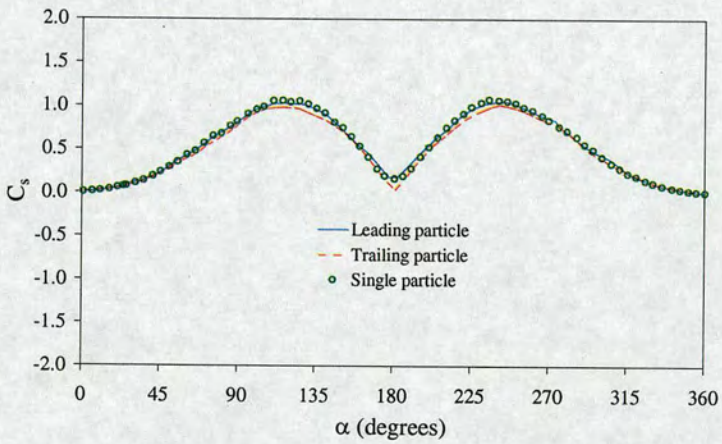

(c)

Fig. 3A.13 (a) Streamwise velocity profiles, (b) pressure coefficients and (c) wall shear stress coefficients for a single spherical particle and two fixed spherical particles at $D_o = 25.0$, $\theta = 0^o$ and $Re_p = 15$.

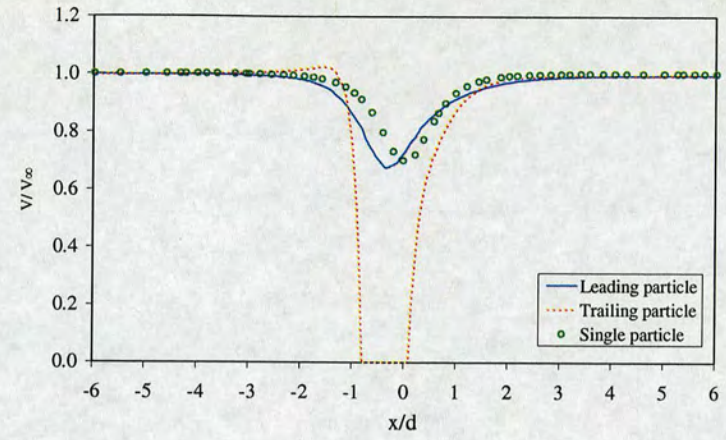

(a)

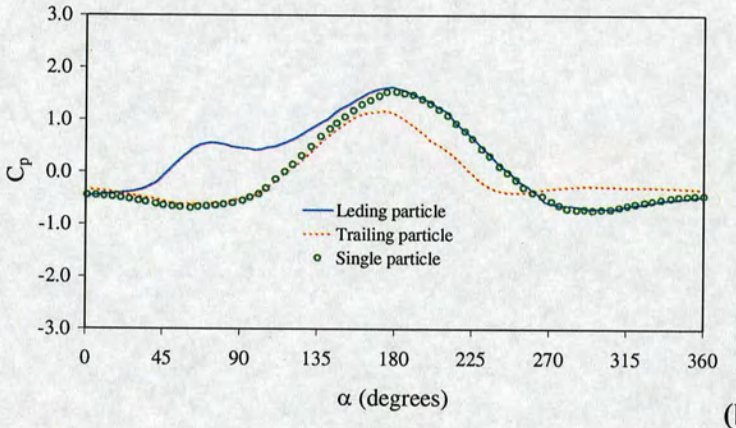

(b)

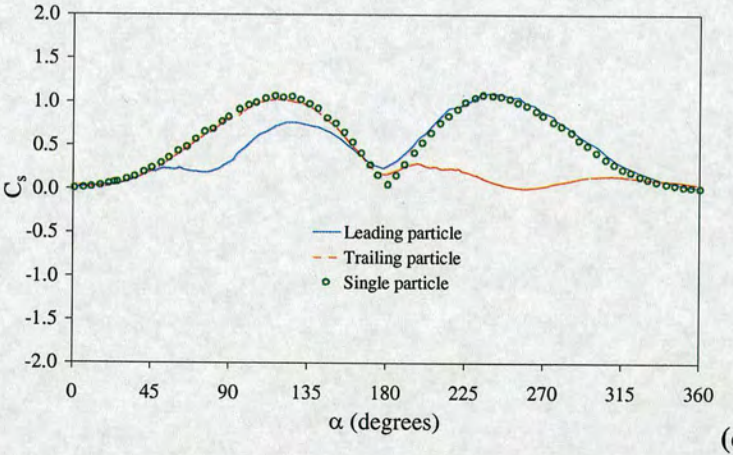

(c)

Fig. 3A.14 (a) Streamwise velocity profiles, (b) pressure coefficients and (c) wall shear stress coefficients for a single spherical particle and two fixed spherical particles at $D_o = 1.10$, $\theta = 45^o$ and $Re_p = 15$.

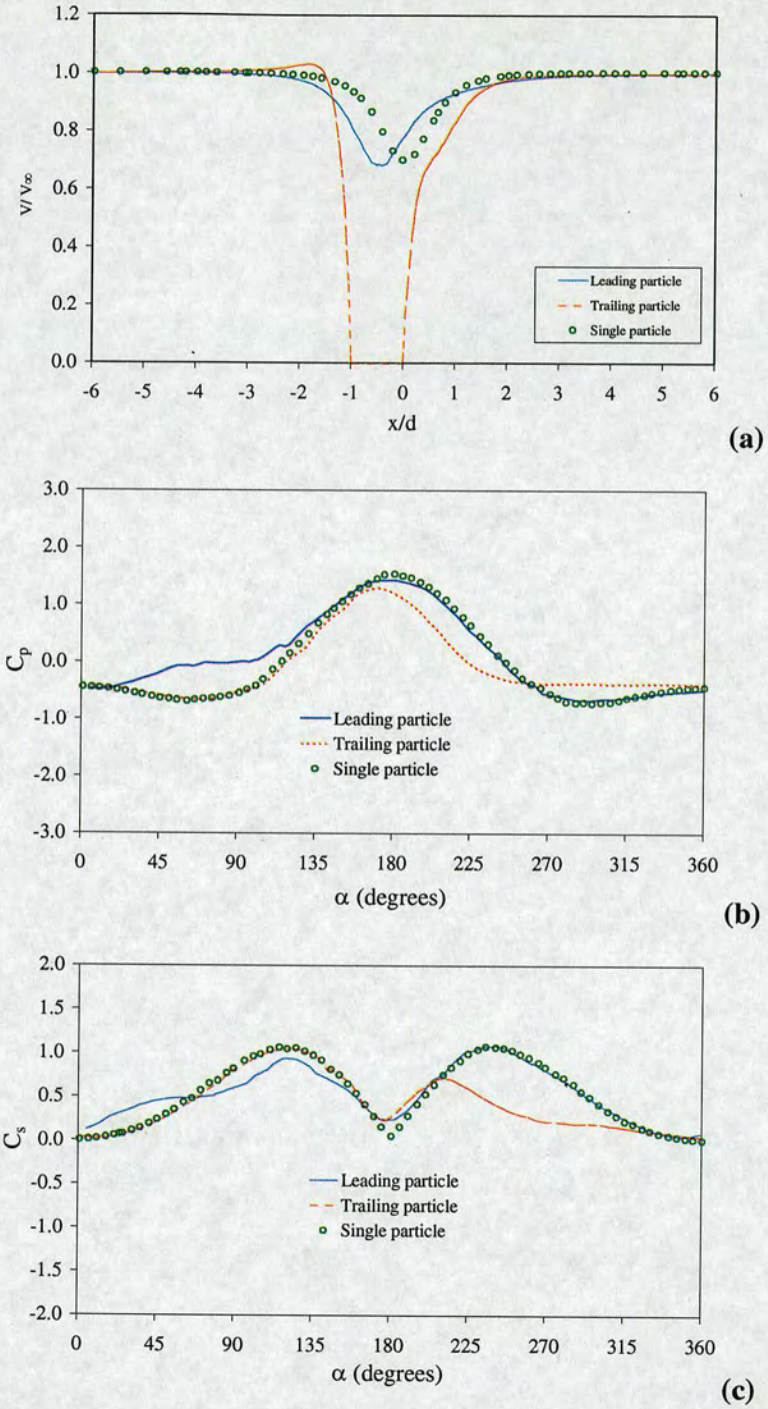

Fig. 3A.15 (a) Streamwise velocity profiles, (b) pressure coefficients and (c) wall shear stress coefficients for a single spherical particle and two fixed spherical particles at $D_o = 1.50$, $\theta = 45^o$ and $Re_p = 15$.

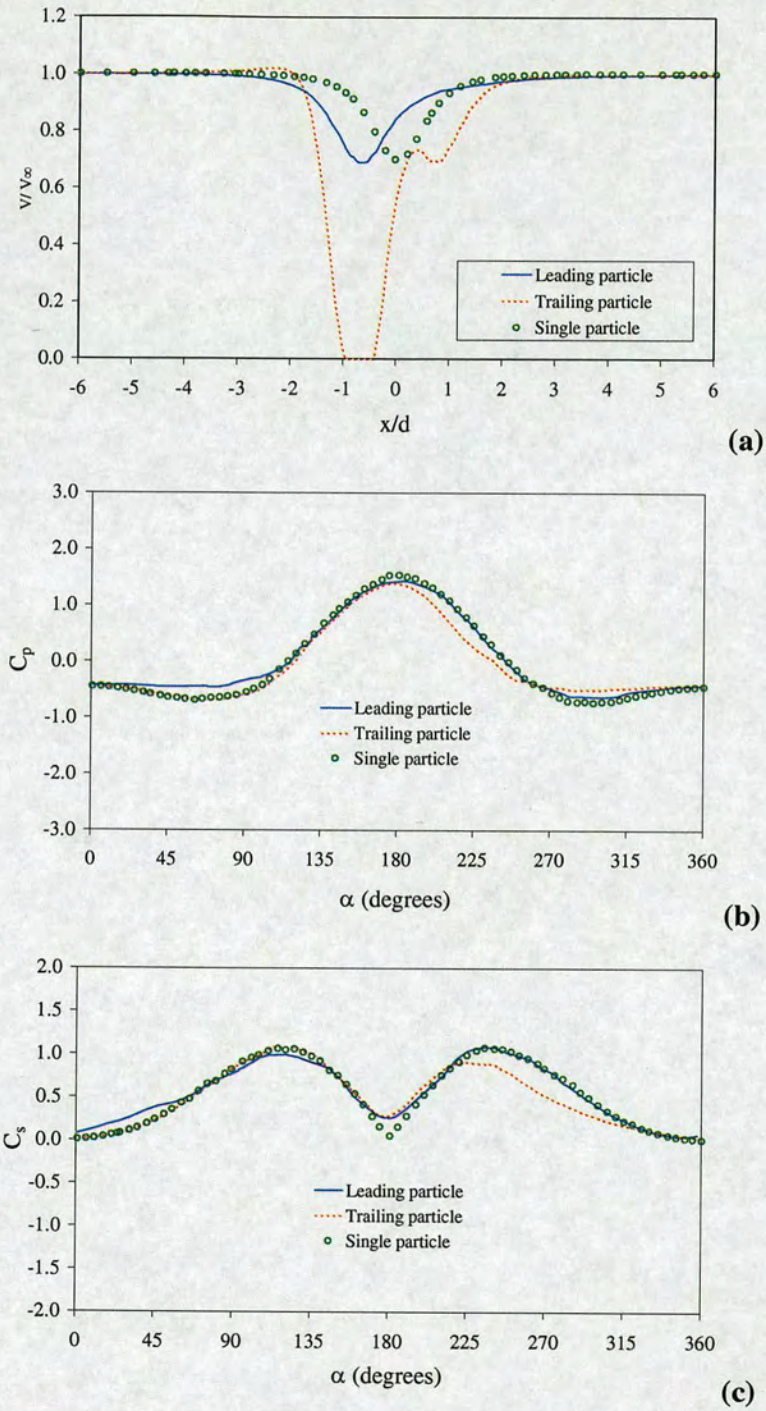

Fig. 3A.16 (a) Streamwise velocity profiles, (b) pressure coefficients and (c) wall shear stress coefficients for a single spherical particle and two fixed spherical particles at $D_o = 2.0$, $\theta = 45^o$ And $Re_p = 15$.

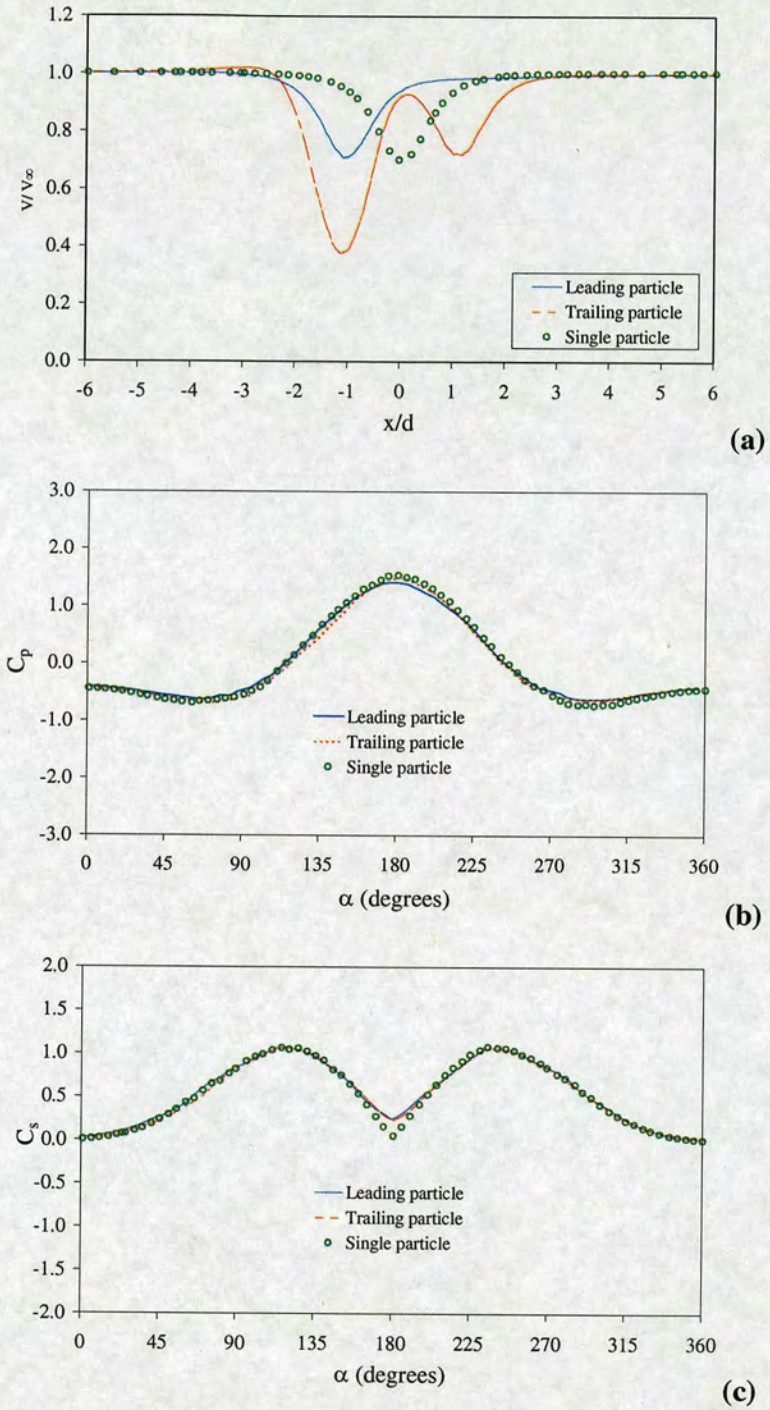

Fig. 3A.17 (a) Streamwise velocity profiles, (b) pressure coefficients and (c) wall shear stress coefficients for a single spherical particle and two fixed spherical particles at $D_o = 3.0$, $\theta = 45^o$ and $Re_p = 15$.

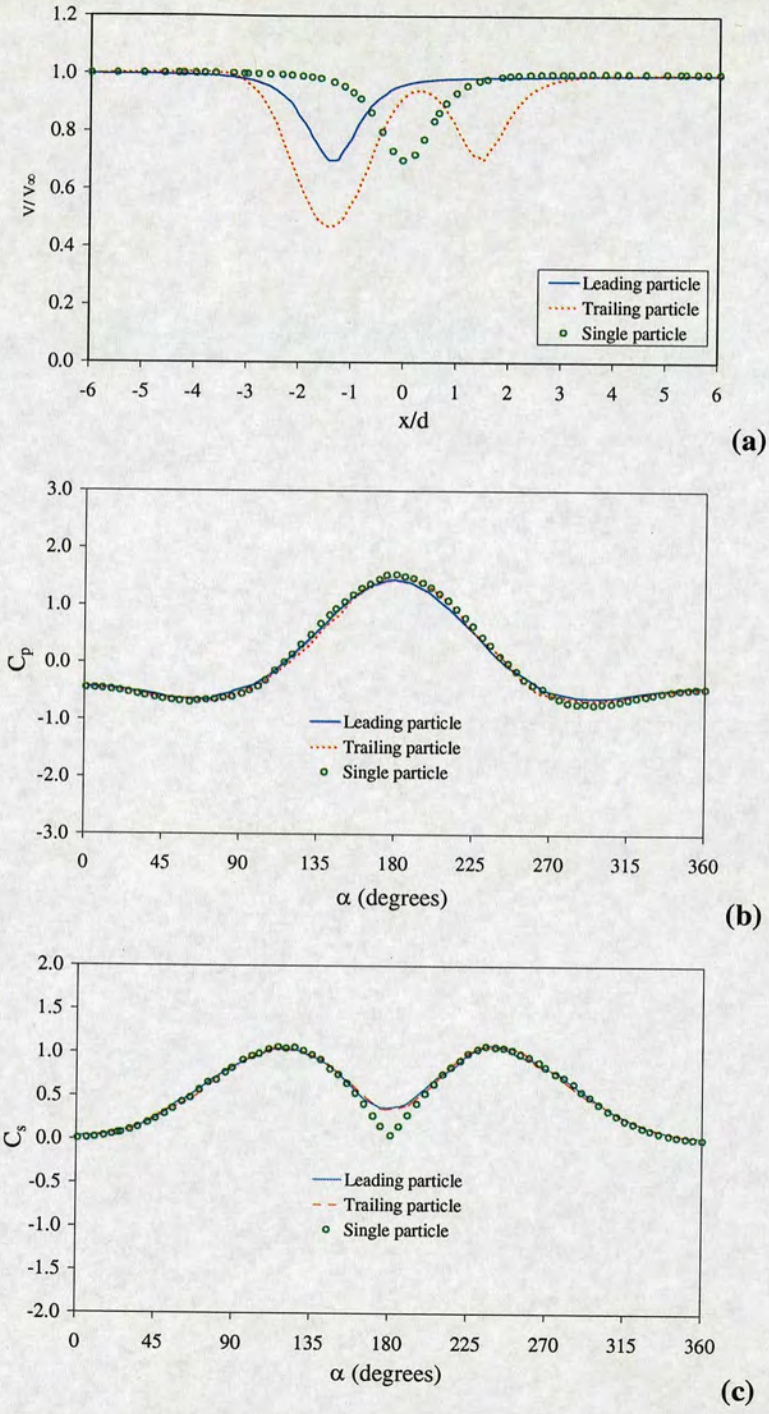

Fig. 3A.18 (a) Streamwise velocity profiles, (b) pressure coefficients and (c) wall shear stress coefficients for a single spherical particle and two fixed spherical particles at $D_o = 4.0$, $\theta = 45^o$ and $Re_p = 15$.

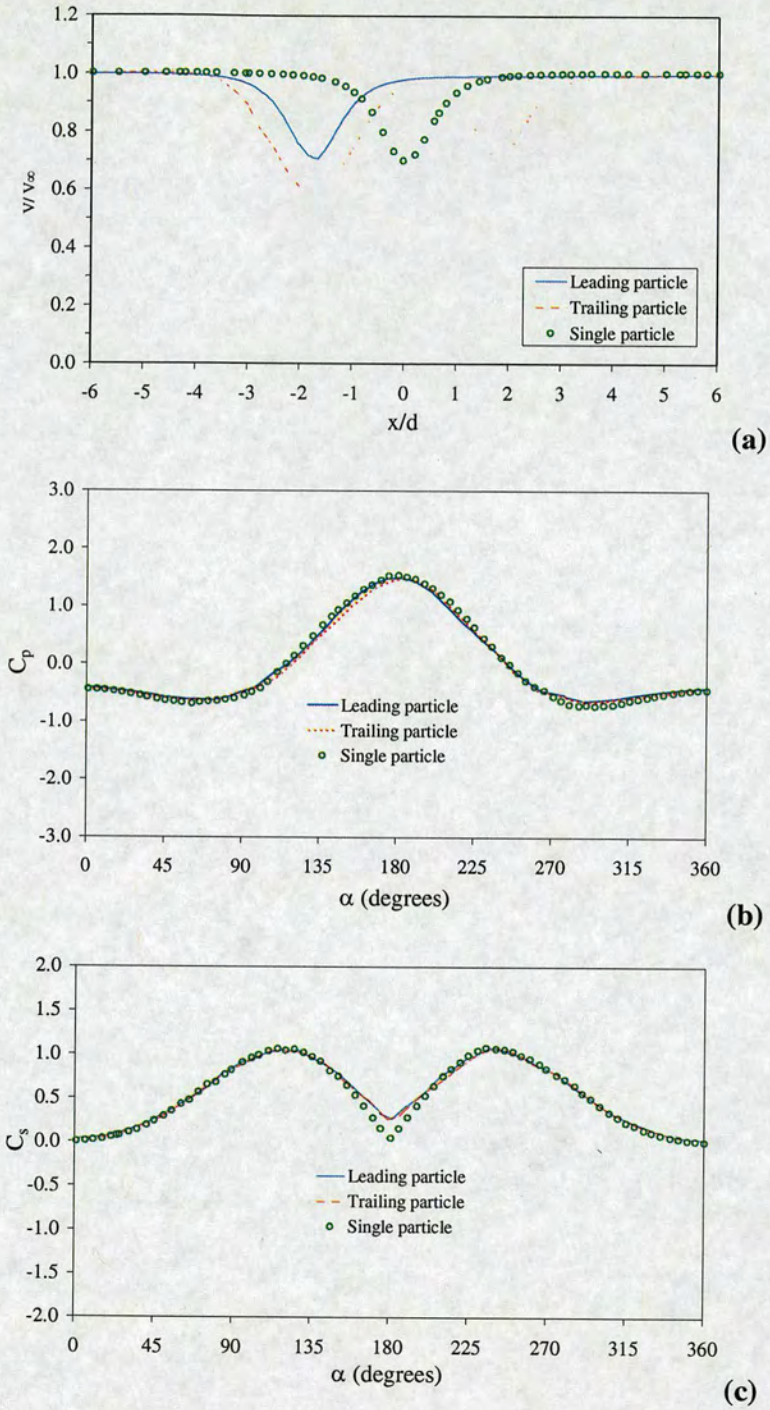

Fig. 3A.19 (a) Streamwise velocity profiles, (b) pressure coefficients and (c) wall shear stress coefficients for a single spherical particle and two fixed spherical particles at $D_o = 5.0$, $\theta = 45^o$ and $Re_p = 15$.

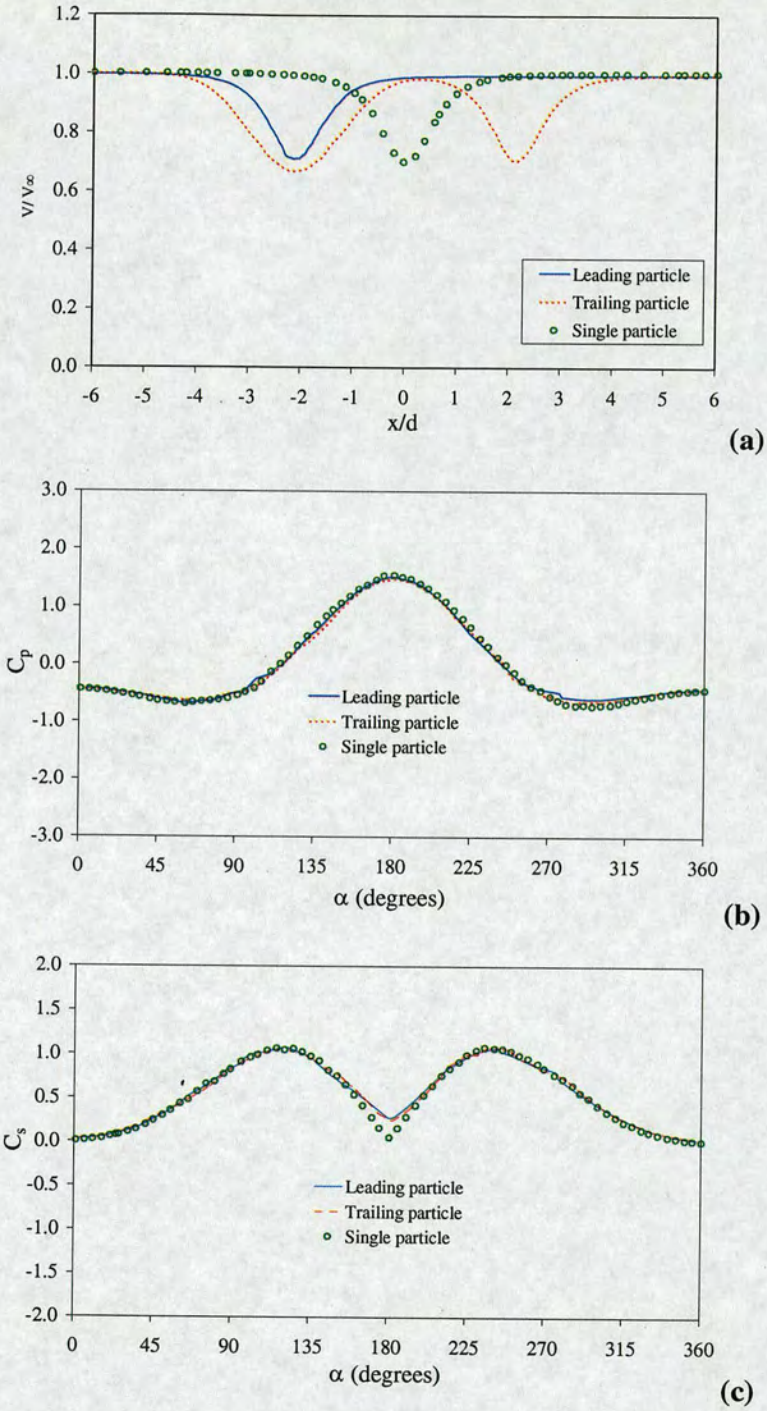

Fig. 3A.20 (a) Streamwise velocity profiles, (b) pressure coefficients and (c) wall shear stress coefficients for a single spherical particle and two fixed spherical particles at $D_o = 6.0$, $\theta = 45^o$ and $Re_p = 15$.

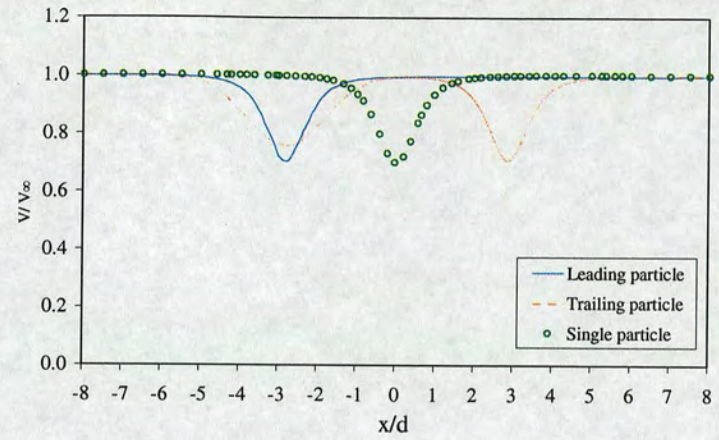

(a)

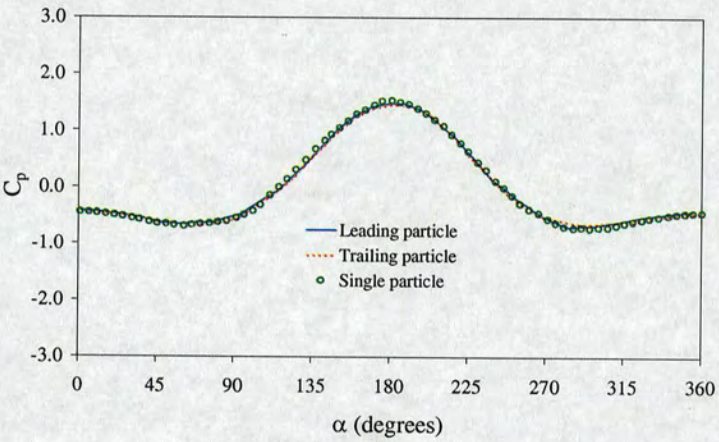

(b)

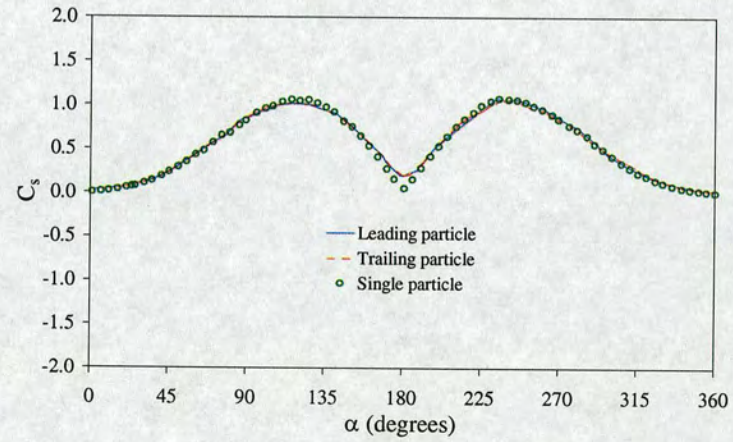

(c)

Fig. 3A.21 (a) Streamwise velocity profiles, (b) pressure coefficients and (c) wall shear stress coefficients for a single spherical particle and two fixed spherical particles at $D_o = 8.0$, $\theta = 45^o$ and $Re_p = 15$.

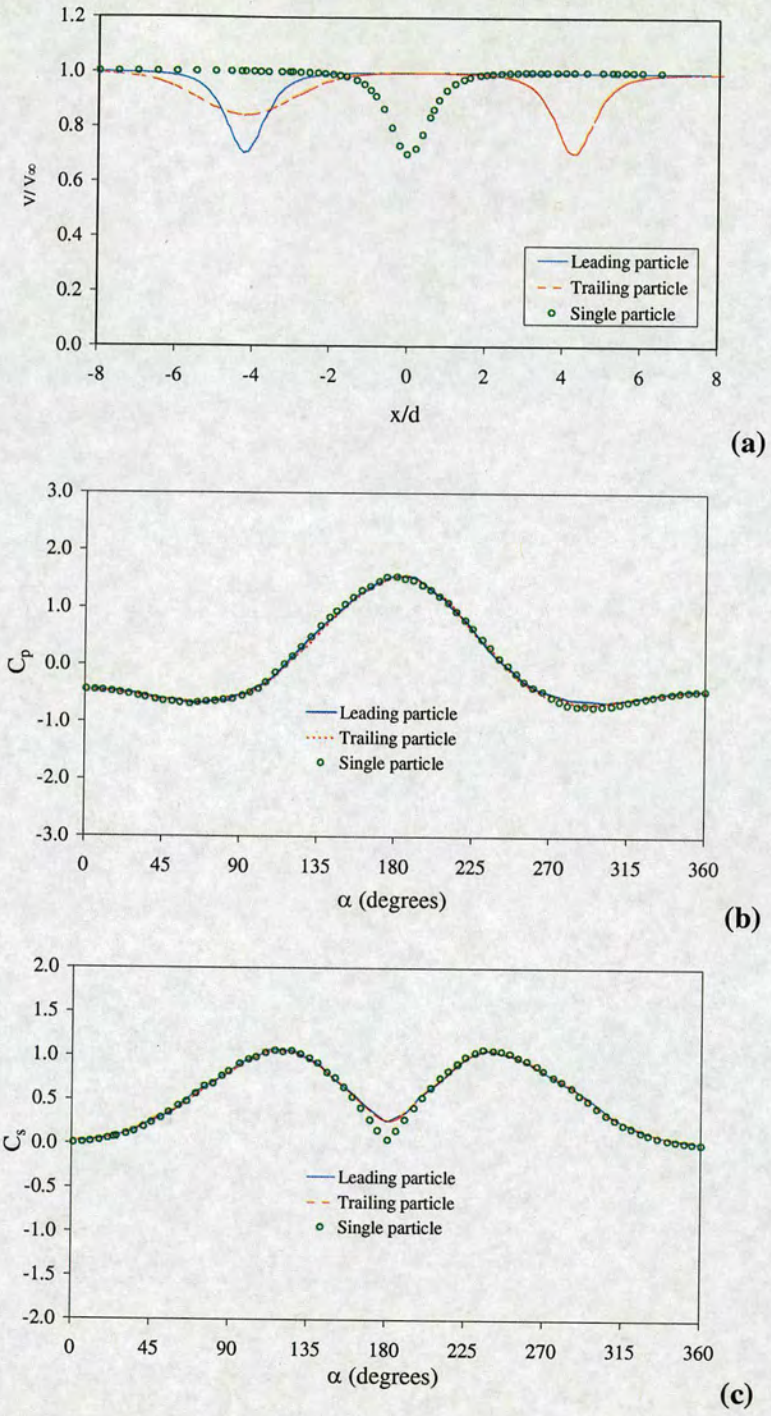

Fig. 3A.22 (a) Streamwise velocity profiles, (b) pressure coefficients and (c) wall shear stress coefficients for a single spherical particle and two fixed spherical particles at $D_o = 12.0$, $\theta = 45^o$ and $Re_p = 15$.

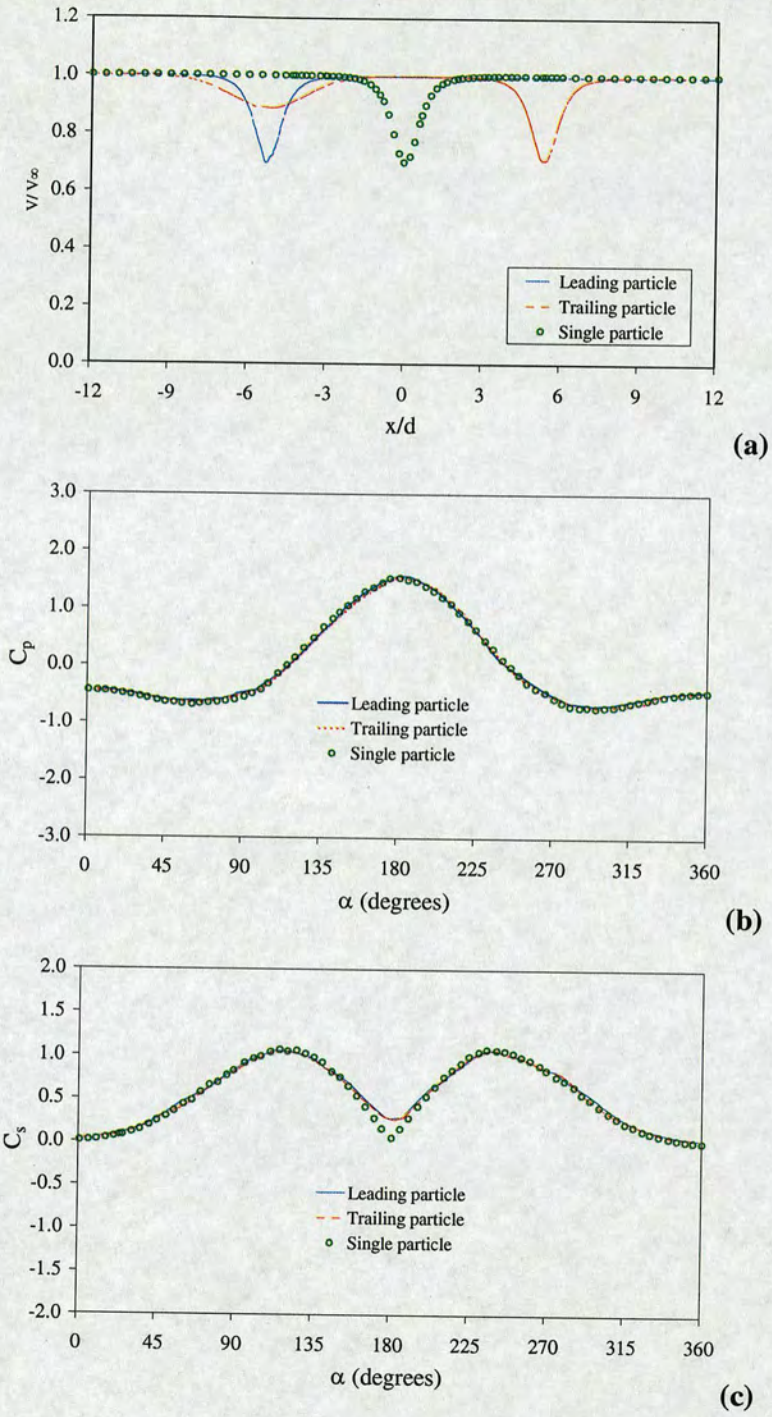

Fig. 3A.23 (a) Streamwise velocity profiles, (b) pressure coefficients and (c) wall shear stress coefficients for a single spherical particle and two fixed spherical particles at $D_o = 15.0$, $\theta = 45^o$ and $Re_p = 15$.

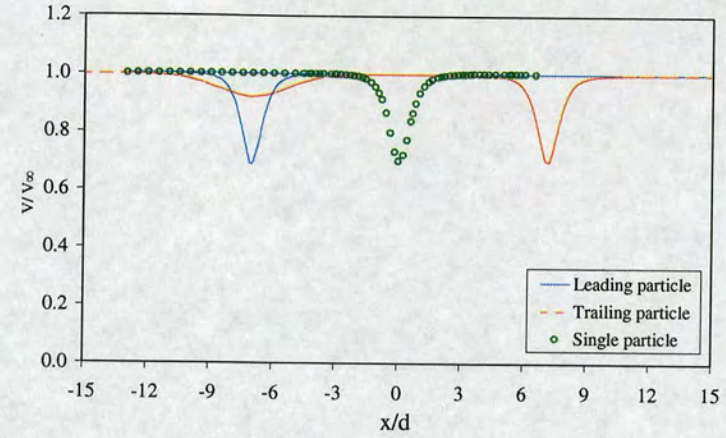

(a)

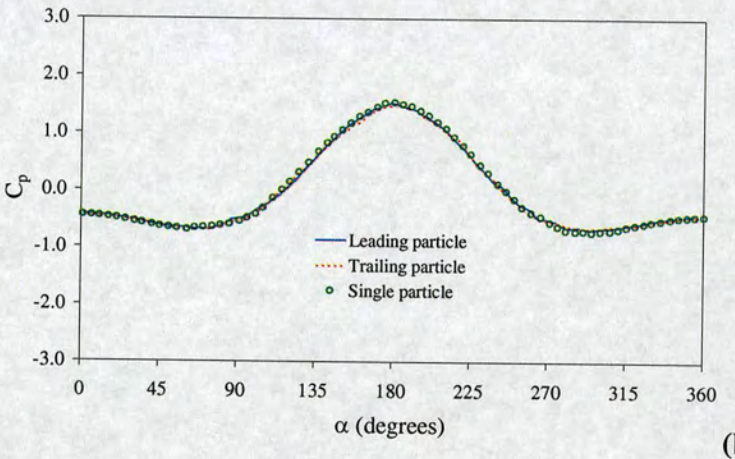

(b)

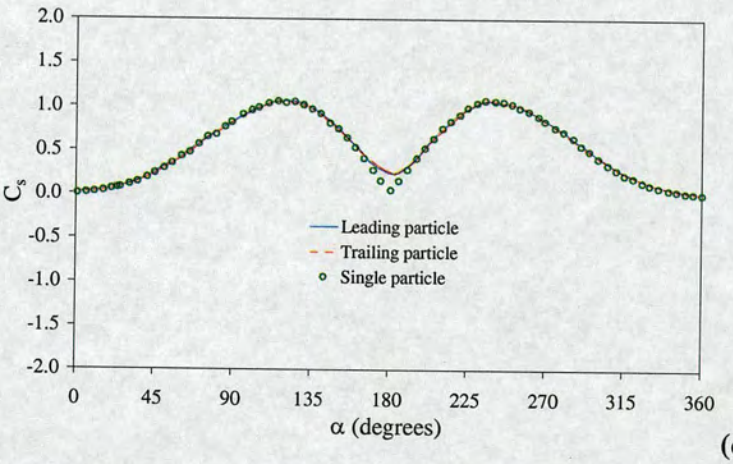

(c)

Fig. 3A.24 (a) Streamwise velocity profiles, (b) pressure coefficients and (c) wall shear stress coefficients for a single spherical particle and two fixed spherical particles at $D_o = 20.0$, $\theta = 45^o$ and $Re_p = 15$.

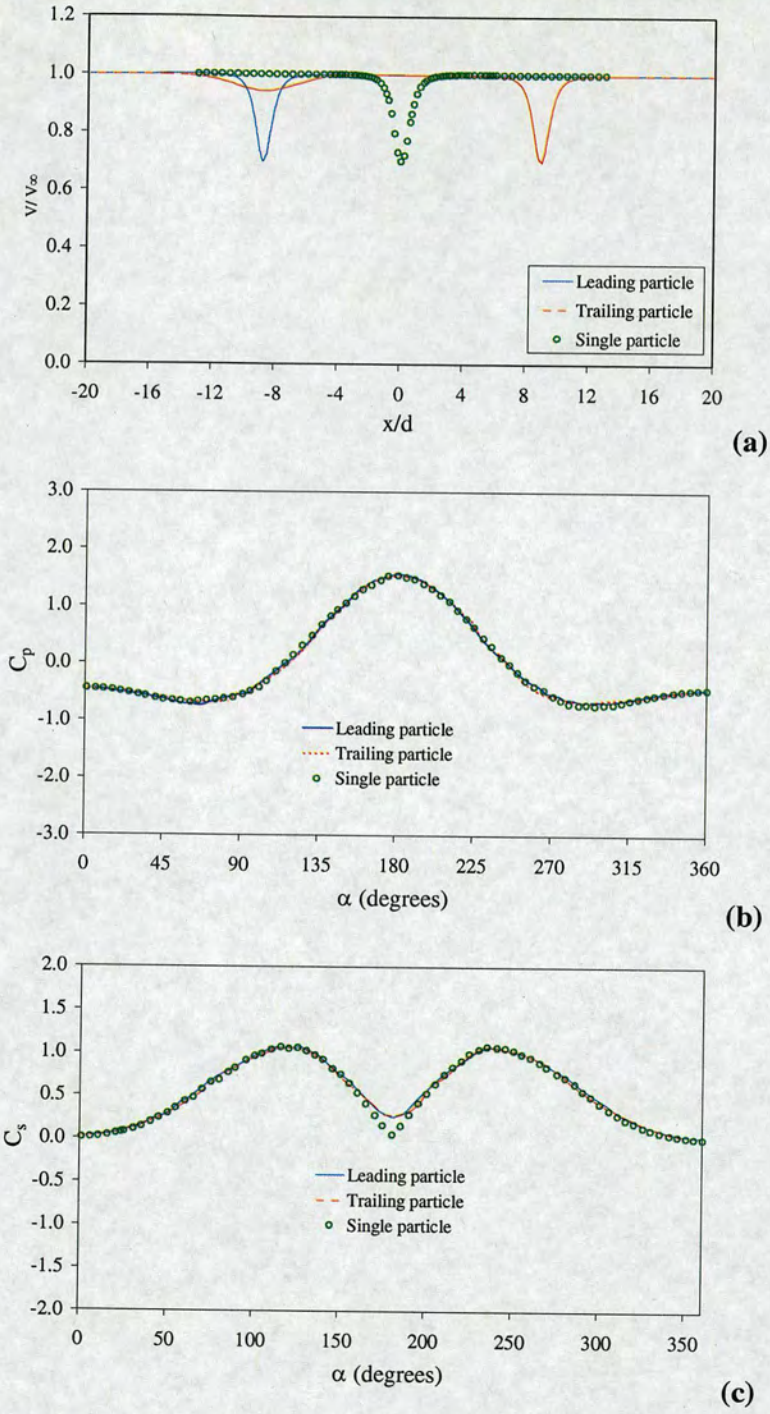

Fig. 3A.25 (a) Streamwise velocity profiles, (b) pressure coefficients and (c) wall shear stress coefficients for a single spherical particle and two fixed spherical particles at $D_o = 25.0$, $\theta = 45^o$ and $Re_p = 15$.

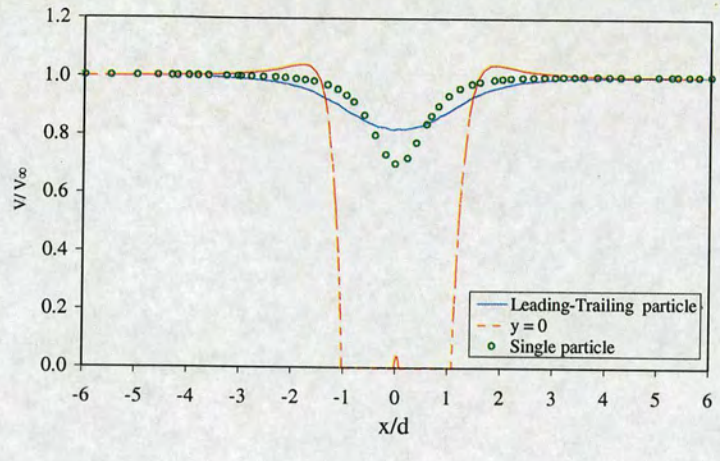

(a)

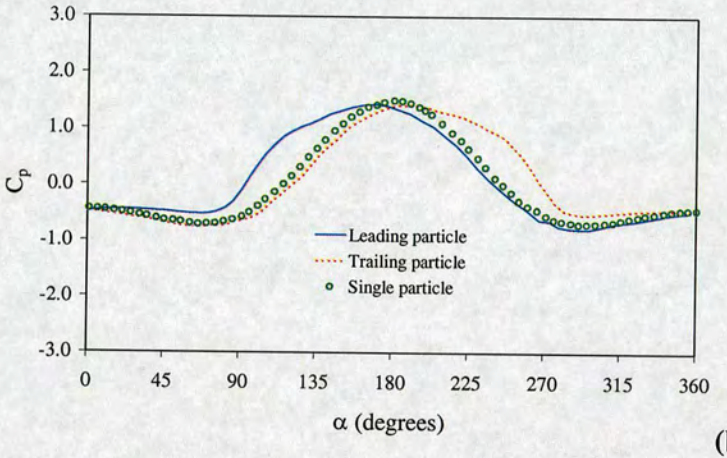

(b)

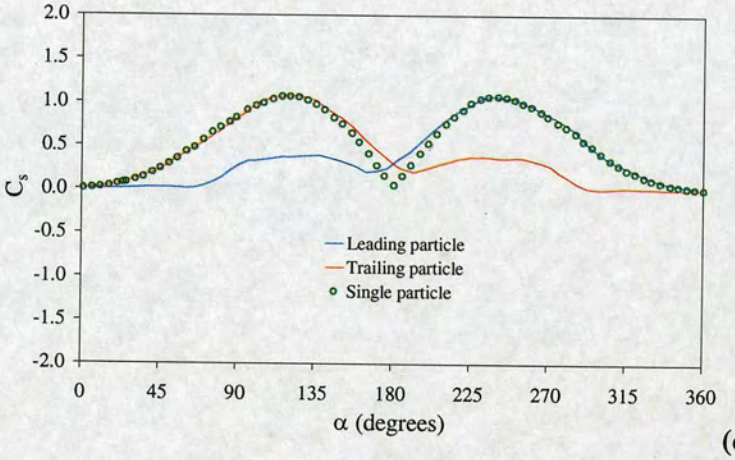

(c)

Fig. 3A.26 (a) Streamwise velocity profiles, (b) pressure coefficients and (c) wall shear stress coefficients for a single spherical particle and two fixed spherical particles at $D_o = 1.1$, $\theta = 90^o$ and $Re_p = 15$.

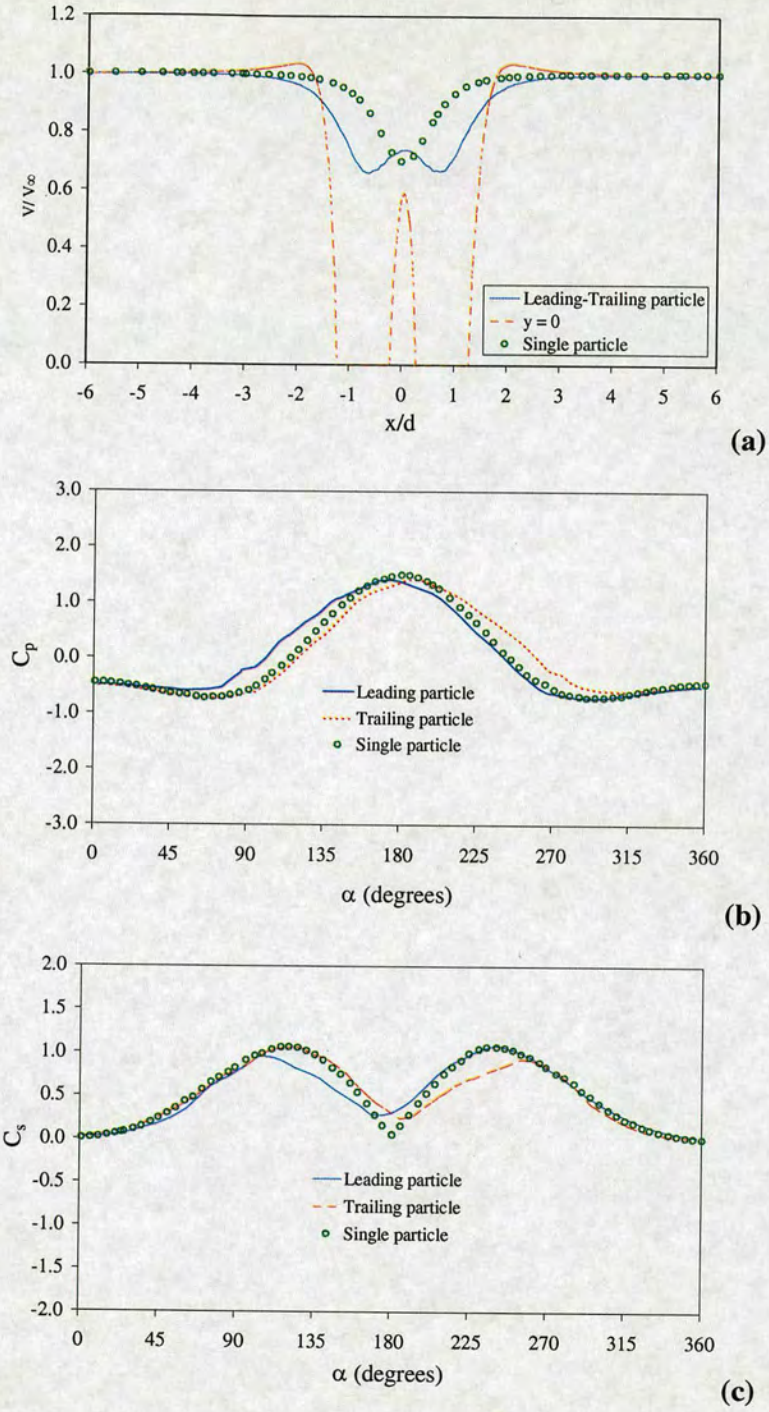

Fig. 3A.27 (a) Streamwise velocity profiles, (b) pressure coefficients and (c) wall shear stress coefficients for a single spherical particle and two fixed spherical particles at $D_o = 1.50$, $\theta = 90^o$ and $Re_p = 15$.

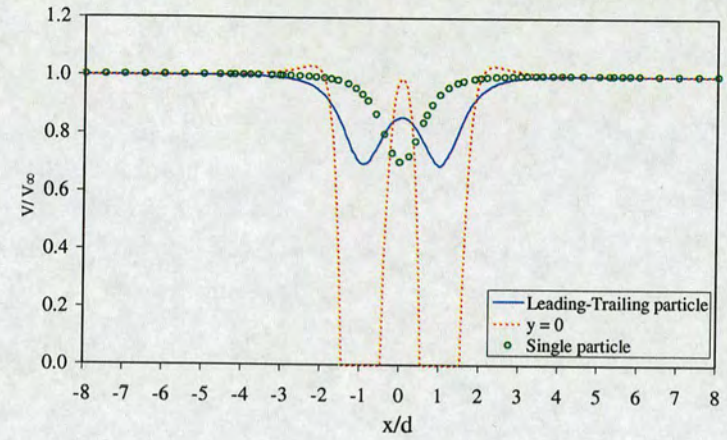

(a)

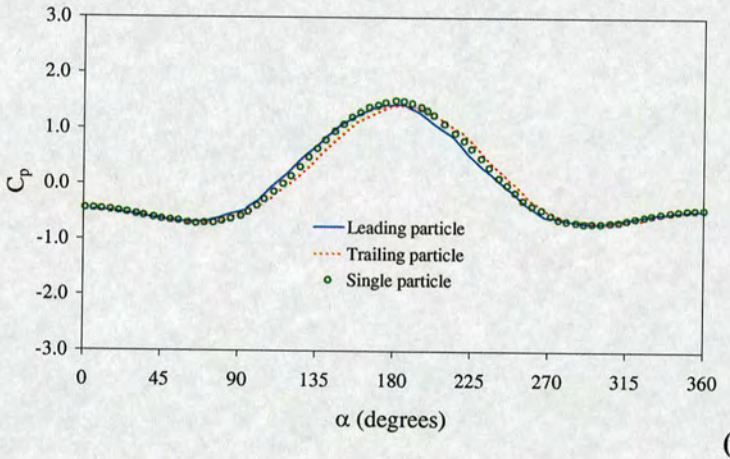

(a)

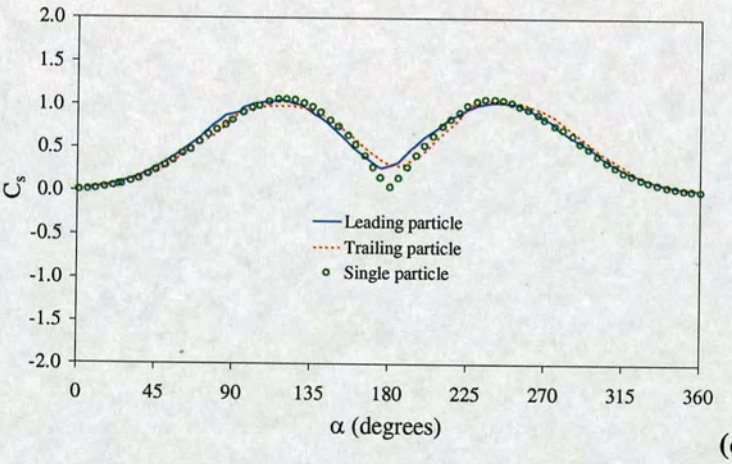

(c)

Fig. 3A.28 (a) Streamwise velocity profiles, (b) pressure coefficients and (c) wall shear stress coefficients for a single spherical particle and two fixed spherical particles at $D_o = 2.0$, $\theta = 90^o$ and $Re_p = 15$.

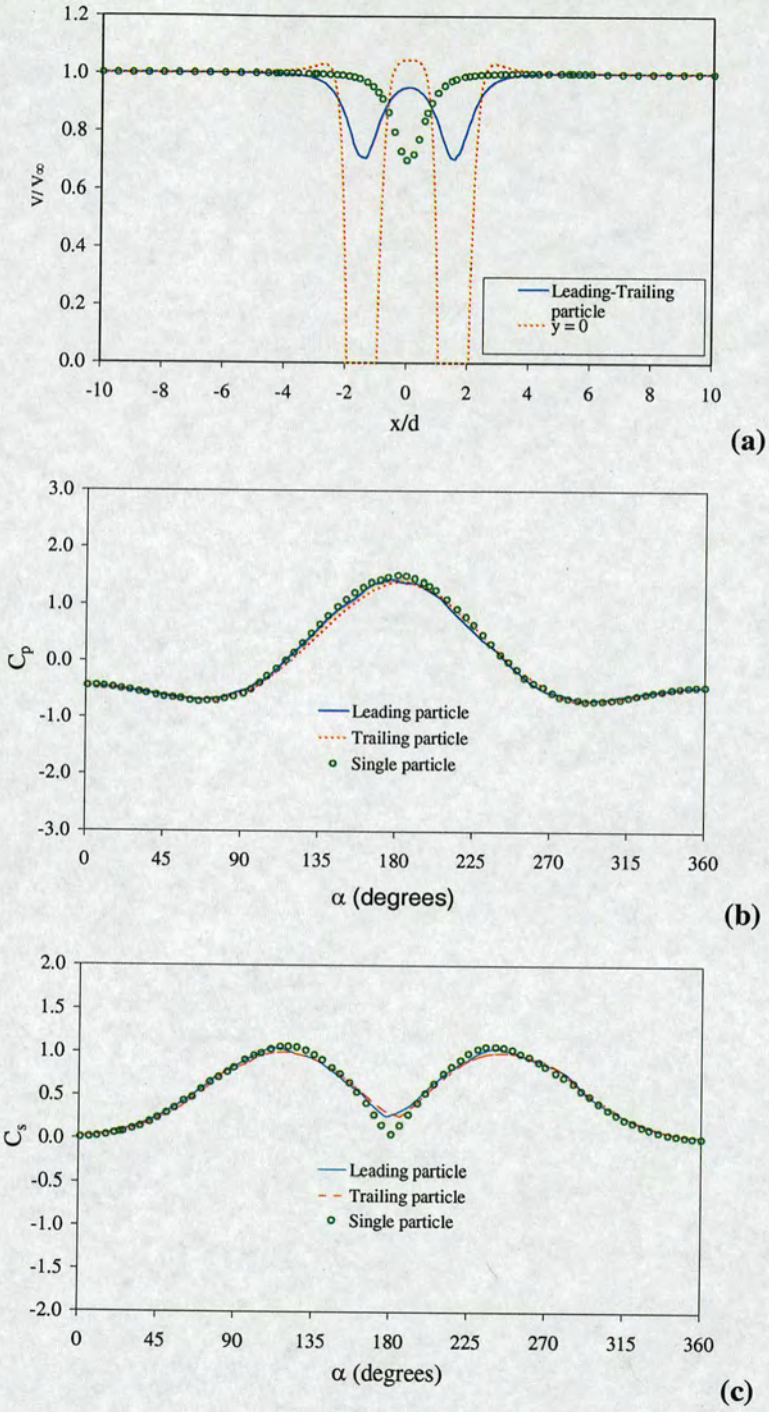

Fig. 3A.29 (a) Streamwise velocity profiles, (b) pressure coefficients and (c) wall shear stress coefficients for a single spherical particle and two fixed spherical particles at $D_o = 3.0$, $\theta = 90^o$ and $Re_p = 15$.

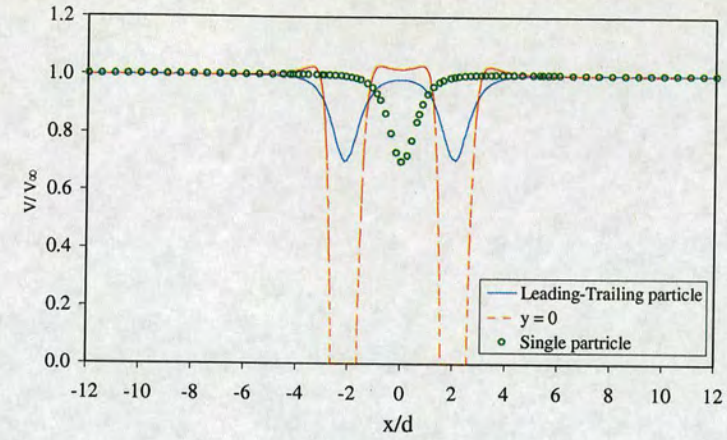

(a)

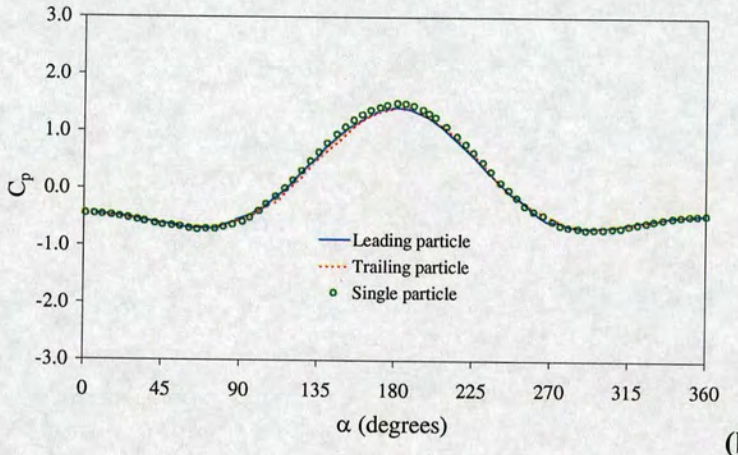

(b)

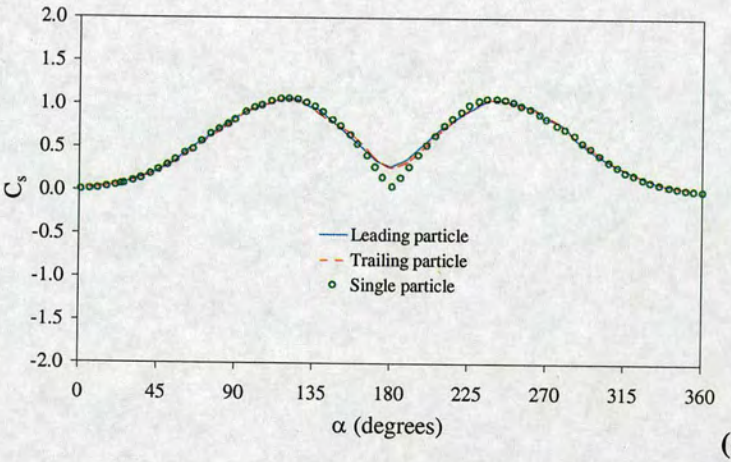

(c)

Fig. 3A.30 (a) Streamwise velocity profiles, (b) pressure coefficients and (c) wall shear stress coefficients for a single spherical particle and two fixed spherical particles at $D_o = 4.0$, $\theta = 90^o$ and $Re_p = 15$.

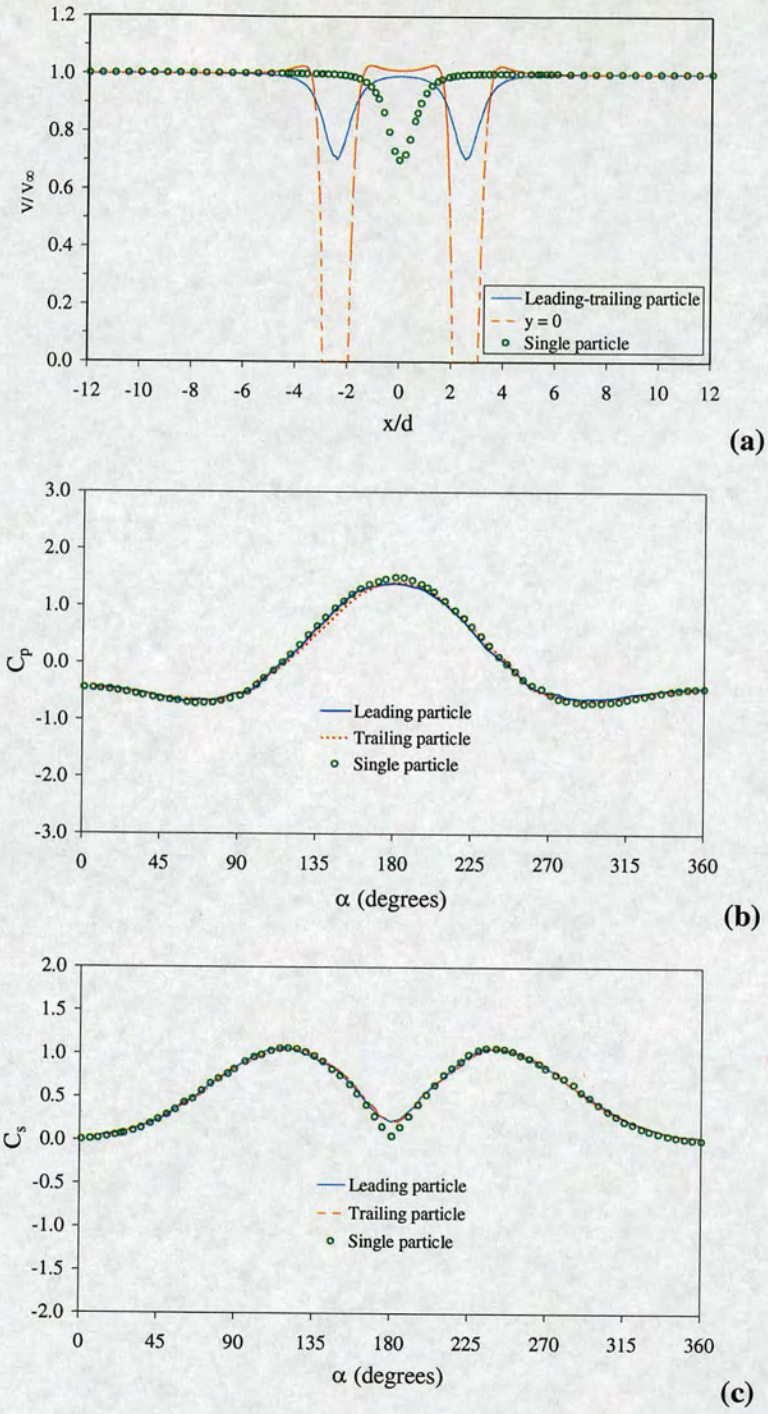

Fig. 3A.31 (a) Streamwise velocity profiles, (b) pressure coefficients and (c) wall shear stress coefficients for a single spherical particle and two fixed spherical particles at $D_o = 5.0$, $\theta = 90^o$ and $Re_p = 15$.

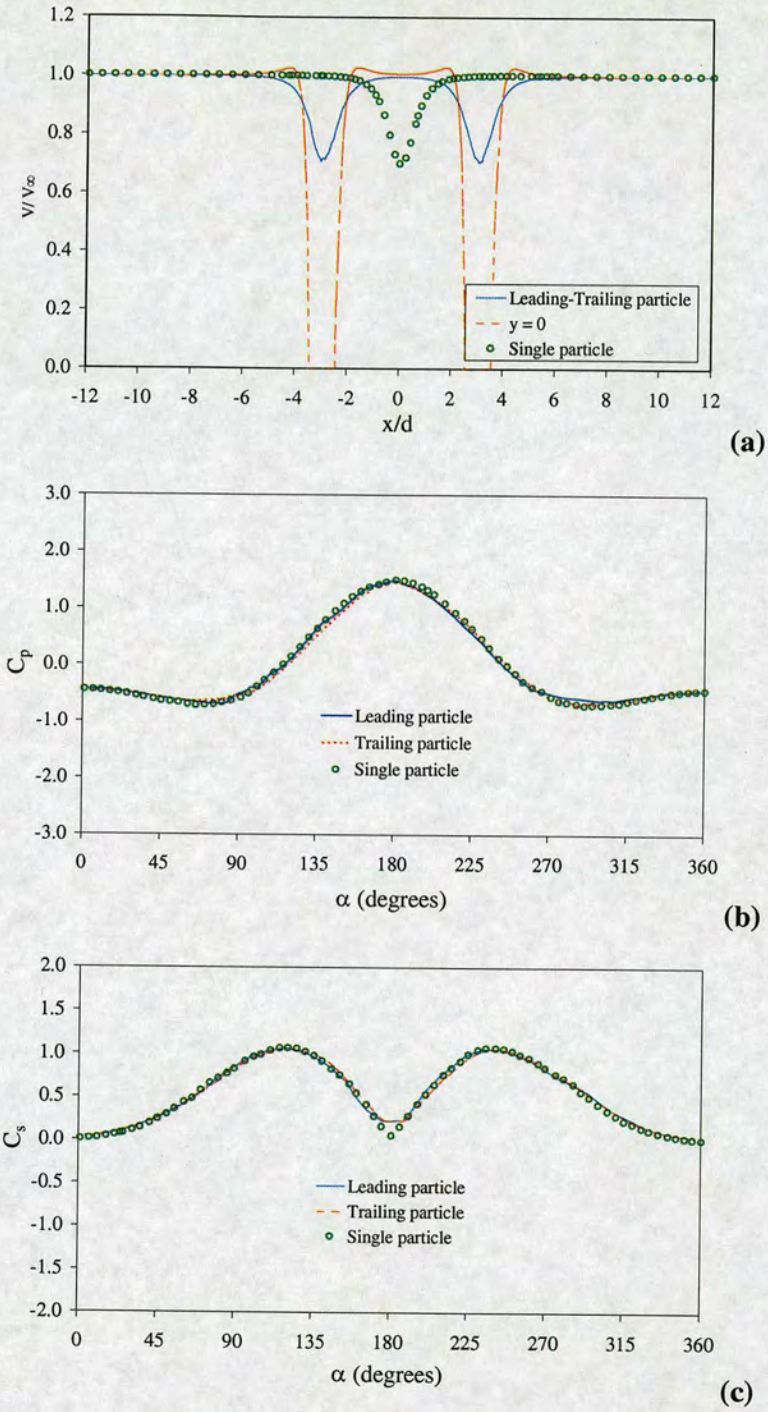

Fig. 3A.32 (a) Streamwise velocity profiles, (b) pressure coefficients and (c) wall shear stress coefficients for a single spherical particle and two fixed spherical particles at $D_o = 6.0$, $\theta = 90^o$ and $Re_p = 15$.

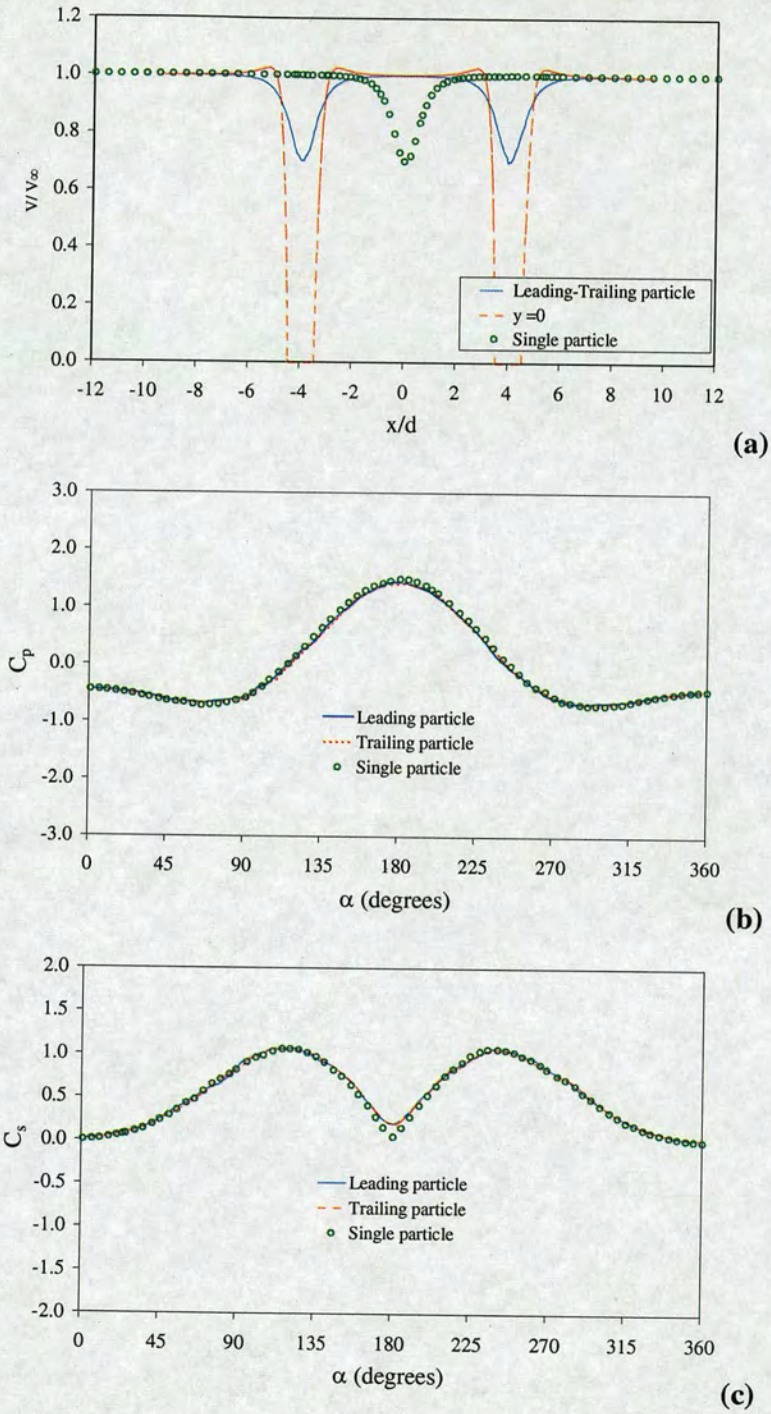

Fig. 3A.33 (a) Streamwise velocity profiles, (b) pressure coefficients and (c) wall shear stress coefficients for a single spherical particle and two fixed spherical particles at $D_o = 8.0$, $\theta = 90^o$ and $Re_p = 15$.

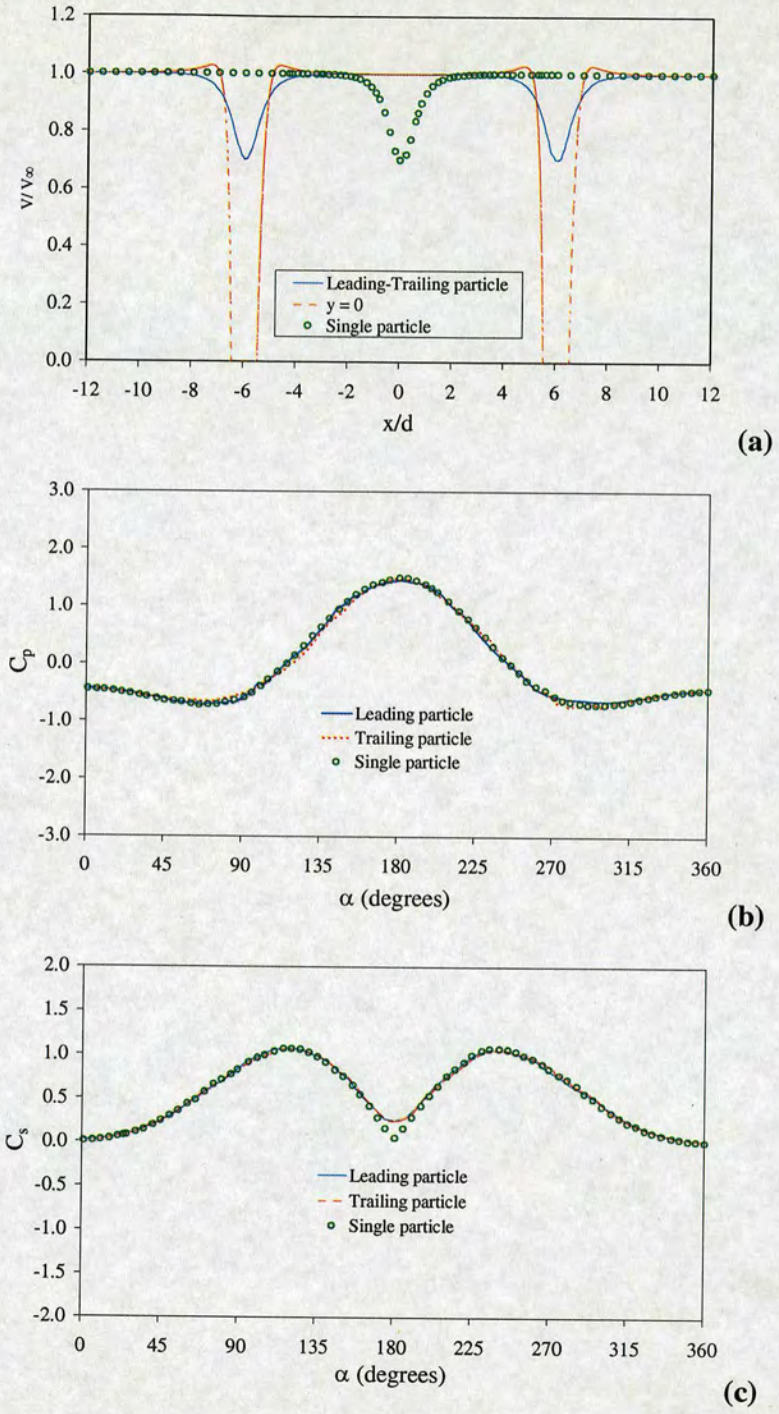

Fig. 3A.34 (a) Streamwise velocity profiles, (b) pressure coefficients and (c) wall shear stress coefficients for a single spherical particle and two fixed spherical particles at $D_o = 12.0$, $\theta = 90^o$ and $Re_p = 15$.

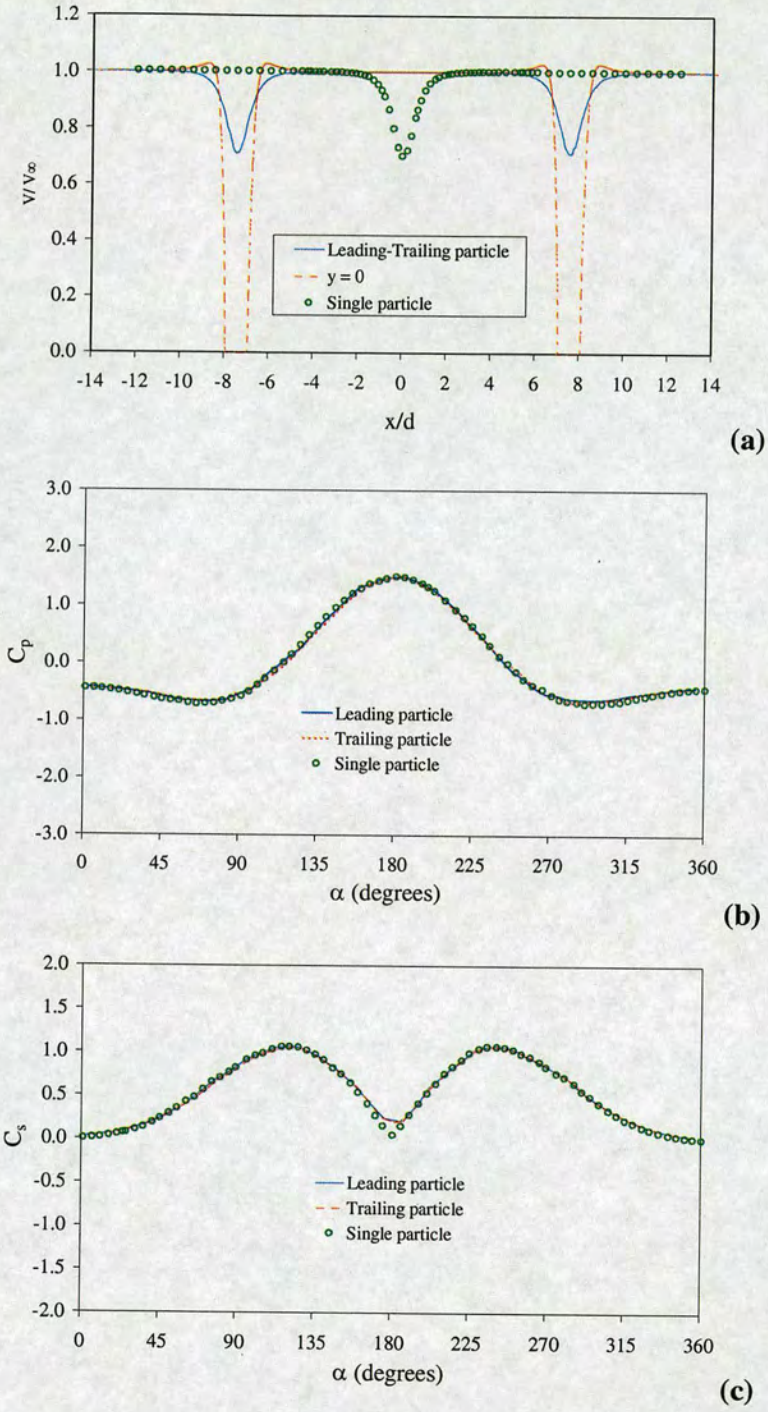

Fig. 3A.35 (a) Streamwise velocity profiles, (b) pressure coefficients and (c) wall shear stress coefficients for a single spherical particle and two fixed spherical particles at $D_o = 15.0$, $\theta = 90^o$ and $Re_p = 15$.

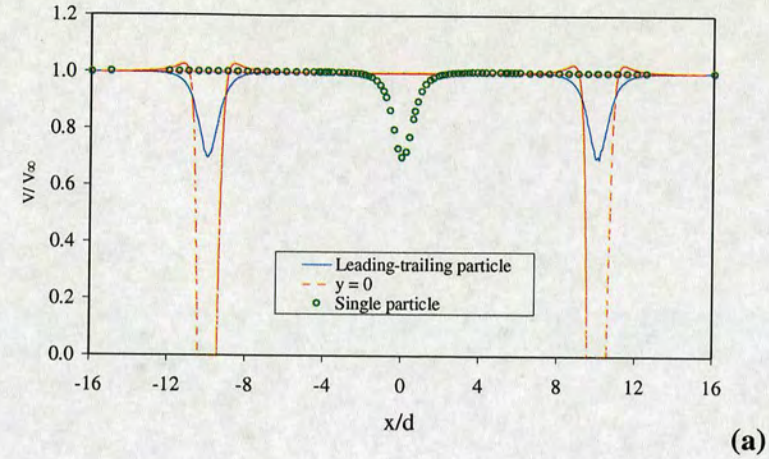

(a)

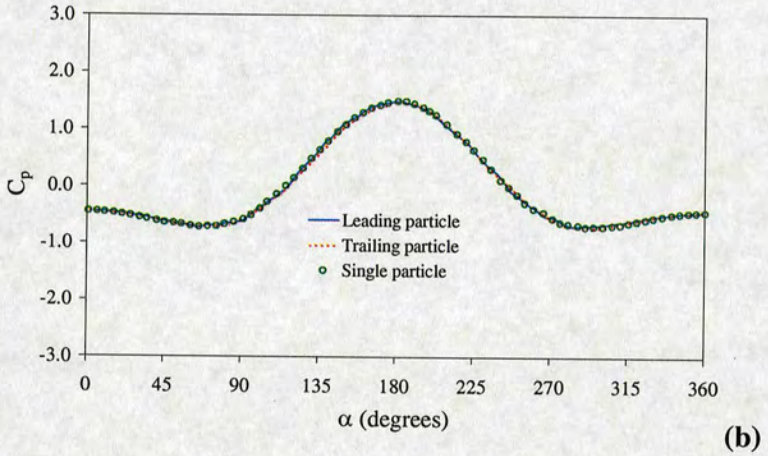

(b)

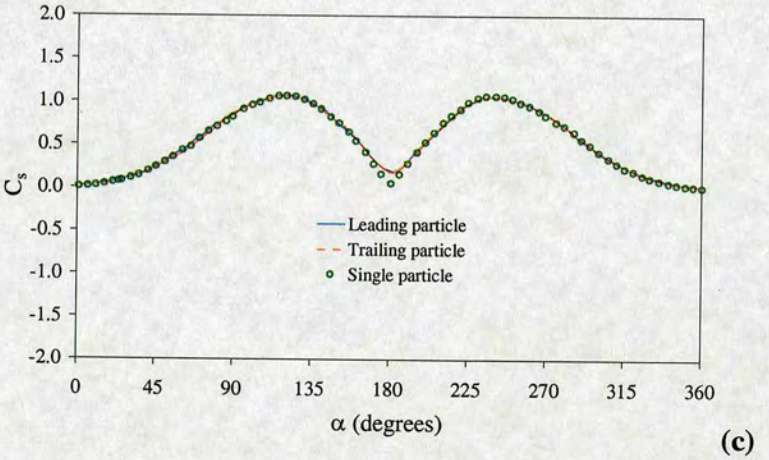

(c)

Fig. 3A.36 (a) Streamwise velocity profiles, (b) pressure coefficients and (c) wall shear stress coefficients for a single spherical particle and two fixed spherical particles at $D_o = 20.0$, $\theta = 90^o$ and $Re_p = 15$.

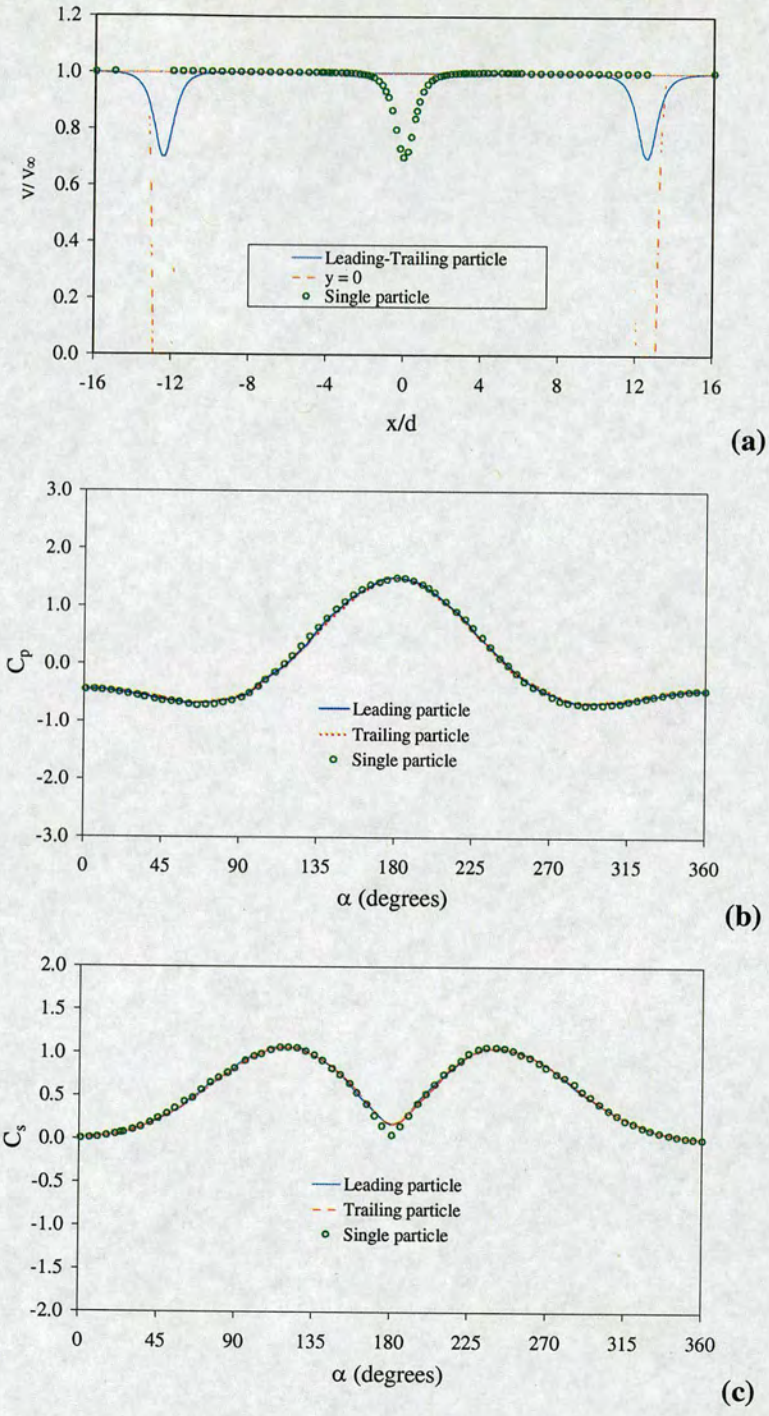

Fig. 3A.37 (a) Streamwise velocity profiles, (b) pressure coefficients and (c) wall shear stress coefficients for a single spherical particle and two fixed spherical particles at $D_o = 25.0$, $\theta = 90^o$ and Rep = 15.

APPENDIX TO CHAPTER 4

4 HYDRODYNAMIC INTERACTION FORCES IN ONE, TWO AND THREE-PARTICLE SYSTEM

This appendix reports a simple way to compare the influence of hydrodynamic interacting forces on a three-particle system (3-b) with the influence of hydrodynamic interacting forces from a two-particle system (2-b), which mimics a three-particle system. The first section summarises the hydrodynamic forces over one and two-particle systems, which will help to find useful expressions to compare the three-particle system with the "virtual" three-particle system obtained from a two-particle system. In the second section the method to calculate three particle hydrodynamic forces from two interacting particle systems mimicking a three interacting particles is explained.

A4.1 Hydrodynamic forces over one and two-particle systems

Figure A4.1 shows the hydrodynamic forces on a single particle and the forces for two interacting particle system immersed in a three-dimensional flow. Figure A4.1(a) show the forces $F_s^{1-b;x}$, $F_s^{1-b;y}$ and $F_s^{1-b;z}$ stand for the total hydrodynamic forces over a spherical single particle in the x, y and z direction, respectively. Figure A4.1(b) illustrate the forces $F_1^{2-b;x}$, $F_1^{2-b;y}$ and $F_1^{2-b;z}$ represent the total hydrodynamic forces over particle 1 due to hydrodynamic influence of particle 2 in the x, y and z direction, respectively. Finally in the same figure, $F_{2(1)}^{2-b;x}$, $F_{2(1)}^{2-b;y}$ and $F_{2(1)}^{2-b;z}$ define the

forces over particle 2 as a result of the hydrodynamic influence of particle 1. The forces over a single particle are only due to the hydrodynamic interaction between the flow and the particle itself. However, in two-phase flows at relative high particle concentration, the particles are close enough that the velocity field generated by one of the particles is transmitted through the fluid and influence the hydrodynamic forces on the other particles.

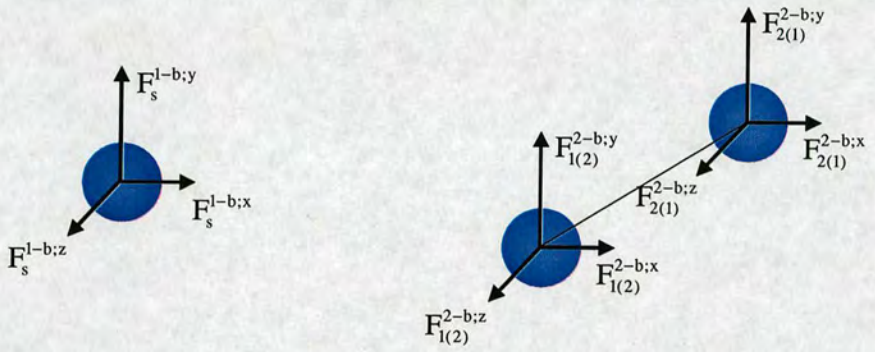

(a) (b)

Fig. 4A.1 Forces over a particle in a three-dimensional flow, (a) one particle system and (b) two particles system.

Although there are many forces that affect the particle movement in a three-dimensional flow, the dominant forces in this study is the total drag force, which include the form drag (pressure) and wall shear stress.

In the single particle simulations carried out in this work, the force in the x direction ($F_s^{1-b;x}$) and the force in the z direction ($F_s^{1-b;z}$) are found to be at least four orders of magnitude smaller than the force in the y direction ($F_s^{1-b;y}$). Therefore, under the specific conditions on this study, the force in the y direction is considered as the only dominant force in the one particle system:

$$\text{One particle system} \begin{cases} F_s^{1-b;x} \approx 0 \\ F_s^{1-b;y} \neq 0 \\ F_s^{1-b;z} \approx 0 \end{cases} \tag{A4.1}$$

On the other hand, series of CFD simulations of two fixed spherical particles placed relative to each other were also carried out. The results indicated that the presence of a second particle interacts with the other particle and the force in the x-axis direction becomes significant for some particle positions. However, because of the centres of the two particles are located in the x-y plane, the main hydrodynamic interactions between the two particles are held in this plane. The force in the z direction remains too small, at least four orders of magnitude smaller than the force in the y direction. Hence, for this specific conditions the interactive force between the two particles in the z direction could be also consider as zero. Thus, the force system in the y direction for particle 1 in a two-particle system can be expressed as follows:

$$\text{Two particle system} \begin{cases} F_{1(2)}^{2-b;x} \neq 0 \\ F_{1(2)}^{2-b;y} \neq 0 \\ F_{1(2)}^{2-b;z} \approx 0 \end{cases} \tag{A4.2}$$

where $F_{1(2)}^{2-b;x}$, $F_{1(2)}^{2-b;y}$ and $F_{1(2)}^{2-b;z}$ represent the total force on particle 1 due to the presence of particle 2 in the x, y and z direction, respectively. Similar expressions can be obtained for particle 2 because of the hydrodynamic interaction of particle 1.

A4.2 Hydrodynamic forces in a three-particle system

A4.2.1 Forces in a three-particle system

Figure A4.2 shows the forces in a three-particle system for the two configurations used in this study: three collinear particle system and three particles placed at the corners of an equilateral triangle.

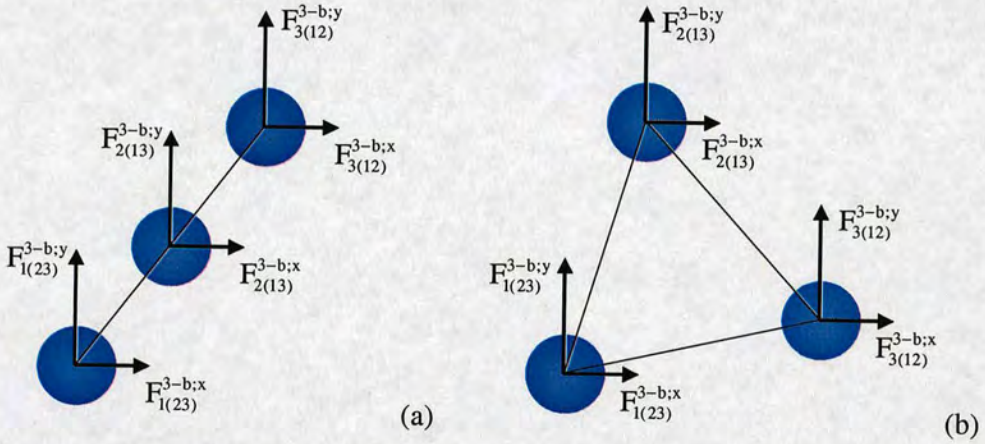

Fig. 4A.2 Forces on three interacting particles in x-y plane, (a) collinear configuration and (b) equilateral triangular formation.

The centre of the particles are located at z = 0 and same numerical and dynamic conditions as in two-particle system are used, the only significant forces on the three particle are those in the x and y direction. The forces system over particle 1 in a three-particle system can be expressed as:

$$\text{Three particle system} \begin{cases} F^{3-b;x}_{1(23)} \neq 0 \\ F^{3-b;y}_{1(23)} \neq 0 \\ F^{3-b;x}_{1(23)} \approx 0 \end{cases} \qquad \text{(A4.5)}$$

where $F^{3-b;x}_{1(23)}$, $F^{3-b;y}_{1(23)}$ and $F^{3-b;z}_{1(23)}$ stand for the total hydrodynamic forces over particle 1 in the x, y and z directions. Similar expressions for particle 2 and 3 can be written.

A4.2.2 Forces in a "virtual" three-particle system

In order to compare the forces from a two-particle system with the forces from a three-particle system, the forces from two-particle system are obtained mimicking a three-particle system as show in Figure A4.3. One of the two particles is kept in one position ("fixed" particle) whilst the other particle is placed in two different positions ("moving" particle); the "moving" particle is named as particle 2 in one position and as particle 3 in the other position as show in Figure A4.3(a) and A4.3(b), respectively. Finally, from the two positions of the "moving" particle a "virtual" three-particle system can be created.

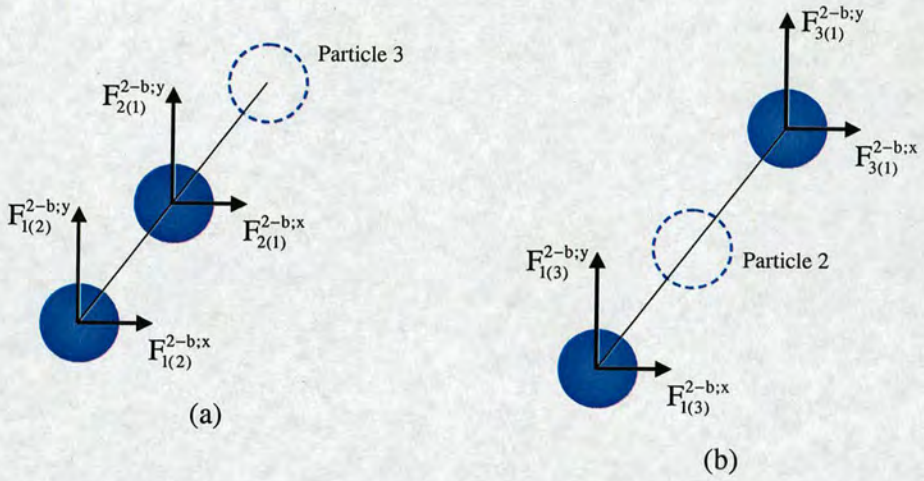

Fig. 4A.3 Interacting particles in a "virtual" three-particle system in line configuration, (a) particles 1 and 2 and, (b) particles 1 and 3.

From CFD simulations it was observed that the main (drag and lift) forces over the particle in this study are due to the fluid interaction only but the forces over one of the particles in a two-particle system depend on the fluid interaction and the interaction of the other particle. Thus, the main forces over one of the particles in a two-particle system could be expressed as a function of the force on a single particle and the force due to some dynamic interaction due to the other particle. For example, the force over particle 1 due to the fluid and particle 2 interactions could be expressed as:

$$F_{1(2)}^{2-b;y} = \begin{cases} F_s^{1-b;y} - F_{1(2)dyn}^{2-b;y} & \text{for } F_{1(2)}^{2-b;y} < F_{1(2)dyn}^{2-b;y} \\ F_s^{1-b;y} + F_{1(2)dyn}^{2-b;y} & \text{for } F_{1(2)}^{2-b;y} > F_{1(2)dyn}^{2-b;y} \end{cases} \quad \text{(A4.3)}$$

where

$F_{1(2)}^{3-b;y}$ is the force over particle 1in the y direction due to fluid and particle 2 interaction.

$F_s^{1-b;y}$ is the force over a single particle in the y direction and,

$F_{1(2)dyn}^{2-b,y}$ is the dynamic interaction due to particle 2.

Similar expressions can be obtained for particle 2, and analogous expressions can be found for the two particles in the x direction also.

In a three-particle system the main forces over one of the particles could be expressed as a function of the force on a single particle and the force due to some dynamic interaction due to the other 2 particles. Thus, applying this concept the forces over one of the particles in a mimic three-particle system are computed. Table A4.1 shows the methodology to obtain the force in the y-axis direction for a mimicking three-particle system; the force is expressed in terms of the forces on a single particle and the hydrodynamic interaction due to the other particle placed at two different positions.

3-b system	2-b system			1-b system	3-b forces = ∑(1-b forces ± 2-b dynamic interactions)
	Particles 1-2	Particle 2-3	Particle 1-3		
$F_{3(12)}^{3-b;y}$	–	$F_{3(2)dyn}^{2-b;y}$	$F_{3(1)dyn}^{2-b;y}$	$F_s^{1-b;y}$	$F_{3(12)}^{3-b;y} = F^{1-b;y} \pm F_{3(2)dyn}^{2-b;y} \pm F_{3(1)dyn}^{2-b;y}$
$F_{2(13)}^{3-b;y}$	$F_{2(1)dyn}^{2-b;y}$	$F_{1(3)dyn}^{2-b;y}$	–	$F_s^{1-b;y}$	$F_{2(13)}^{3-b;y} = F^{1-b;y} \pm F_{2(1)dyn}^{2-b;y} \pm F_{2(3)dyn}^{2-b;y}$
$F_{1(23)}^{3-b;y}$	$F_{1(2)dyn}^{2-b;y}$	–	$F_{2(3)dyn}^{2-b;y}$	$F_s^{1-b;y}$	$F_{1(23)}^{3-b;y} = F^{1-b;y} \pm F_{1(2)dyn}^{2-b;y} \pm F_{1(3)dyn}^{2-b;y}$

Table 4A.1 Hydrodynamic forces over a particle in a mimicking three-particle system obtained from a two-particle system in the y axis direction.

The final expression from table A4.1 for the forces over a particle 1 in a mimicking three-particle system is

$$F_{1(23)}^{3-b;y} = F^{1-b;y} \pm F_{1(2)dyn}^{2-b;y} \pm F_{1(3)dyn}^{2-b;y} \tag{A4.4}$$

Considering equation A4.3, equation A4.4 could be expressed as:

$$F_{1(23)}^{3-b;y} = F_s^{1-b;y} - \left(F_s^{1-b;y} - F_{1(2)}^{2-b;y}\right) - \left(F_s^{1-b;y} - F_{1(3)}^{2-b;y}\right) \text{ for } F_{1(2)}^{3-b;y} < F_s^{1-b;y} \tag{A4.5}$$

Rearranging terms for $F_{1(2)}^{2-b;y} < F_s^{1-b;y}$ and $F_{1(3)}^{2-b;y} < F_s^{1-b;y}$, the equation A4.5 can be written as:

$$F_{1(23)}^{3-b;y} = F_{1(2)}^{2-b;y} + F_{1(3)}^{2-b;y} - F^{1-b;y} \tag{A4.8}$$

Similar expressions can be found for the other two particles and also in the x direction. Equation A4.7 or equation A4.8 could be used to compare the forces obtained from a three-particle mimicking system with forces obtained from a "real" three-particle system as those shown in Figure A4.2. The methodology can be applied to any three interacting particle configuration.

APPENDIX TO CHAPTER 5

5A SNAPSHOTS OF PARTICLE STRUCTURES

A series of snapshots from canonical (NVT) Monte Carlo computer simulations in a multiple particle system are presented in this appendix to support the conclusions in chapter 5. The snapshots depicted here correspond to MC simulations using a non-dimensional temperature $\left(T^* = T_g / |U_{min}|\right)$ *varying from 0.5 to 4.0 and at the range of particle volume fraction* $\left(\alpha_p = \pi / 6D_0^3\right)$ *ranging from 2% to 0.05%. Figure 5.1A – 5.4A show the snapshots obtained from MC simulations with 512 spherical particles, whist Figure 5.5A – 5.8A illustrate the snapshots obtained from simulations with 1000 spherical particles. In all figures presented here the flow direction is from the bottom to the top.*

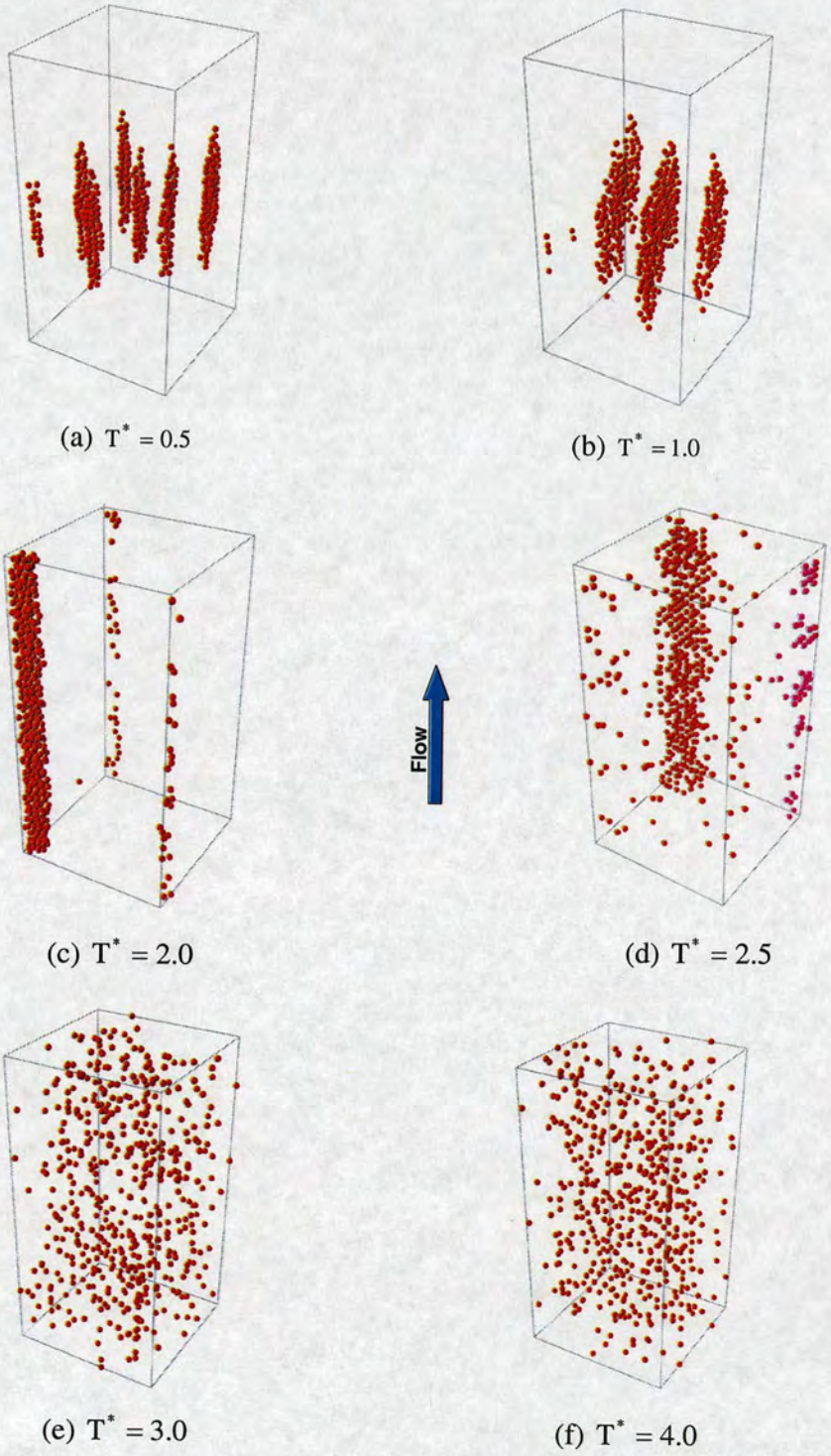

(a) $T^* = 0.5$ (b) $T^* = 1.0$

(c) $T^* = 2.0$ (d) $T^* = 2.5$

(e) $T^* = 3.0$ (f) $T^* = 4.0$

Fig. 5A.1 Particle snapshots at $\alpha_p = 0.008$ ($D_o = 4$) with $N_p = 512$.

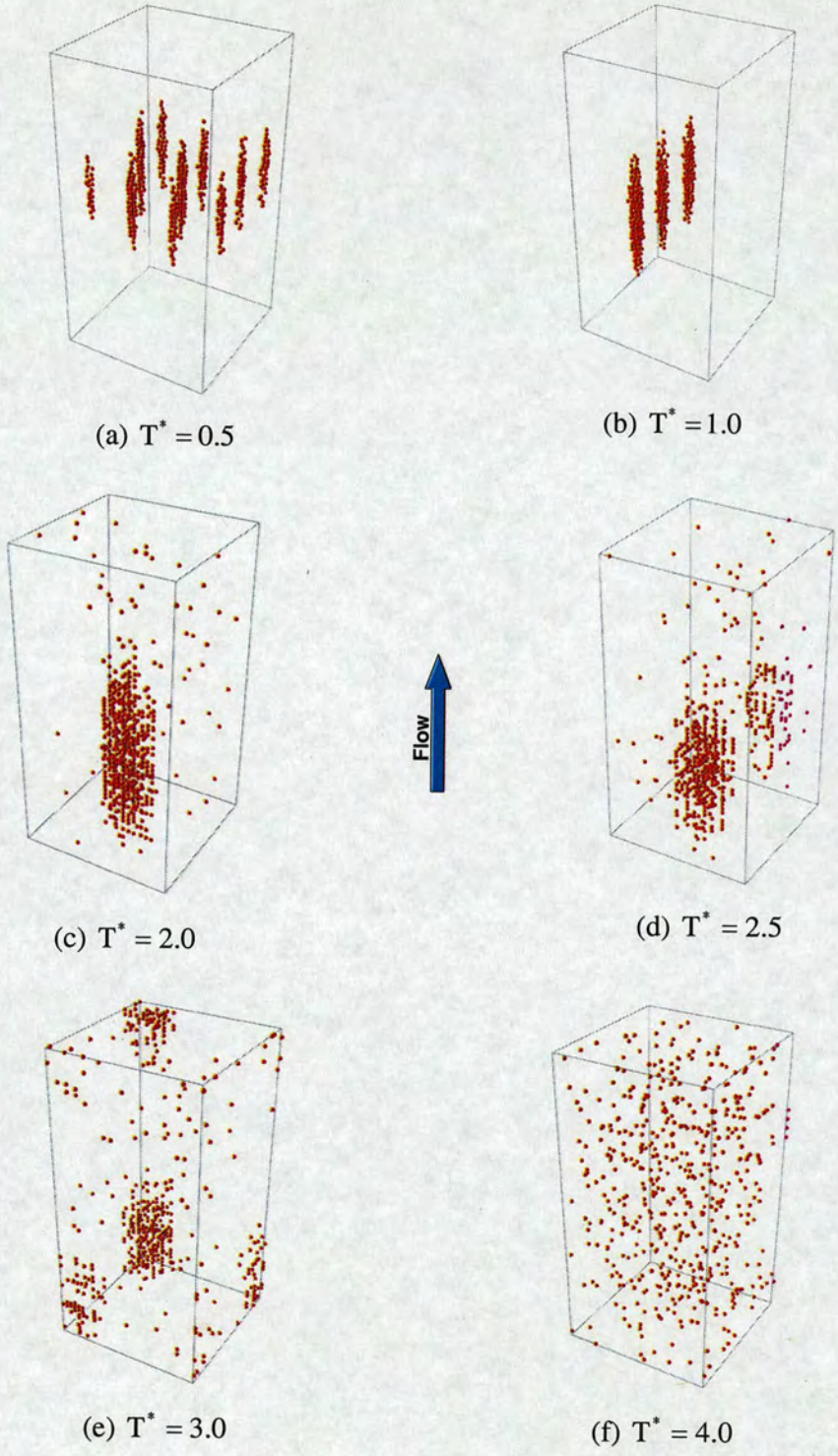

(a) $T^* = 0.5$

(b) $T^* = 1.0$

(c) $T^* = 2.0$

(d) $T^* = 2.5$

(e) $T^* = 3.0$

(f) $T^* = 4.0$

Fig. 5A.2 Particle snapshots at $\alpha_p = 0.002$ ($D_o = 6$) with $N_p = 512$.

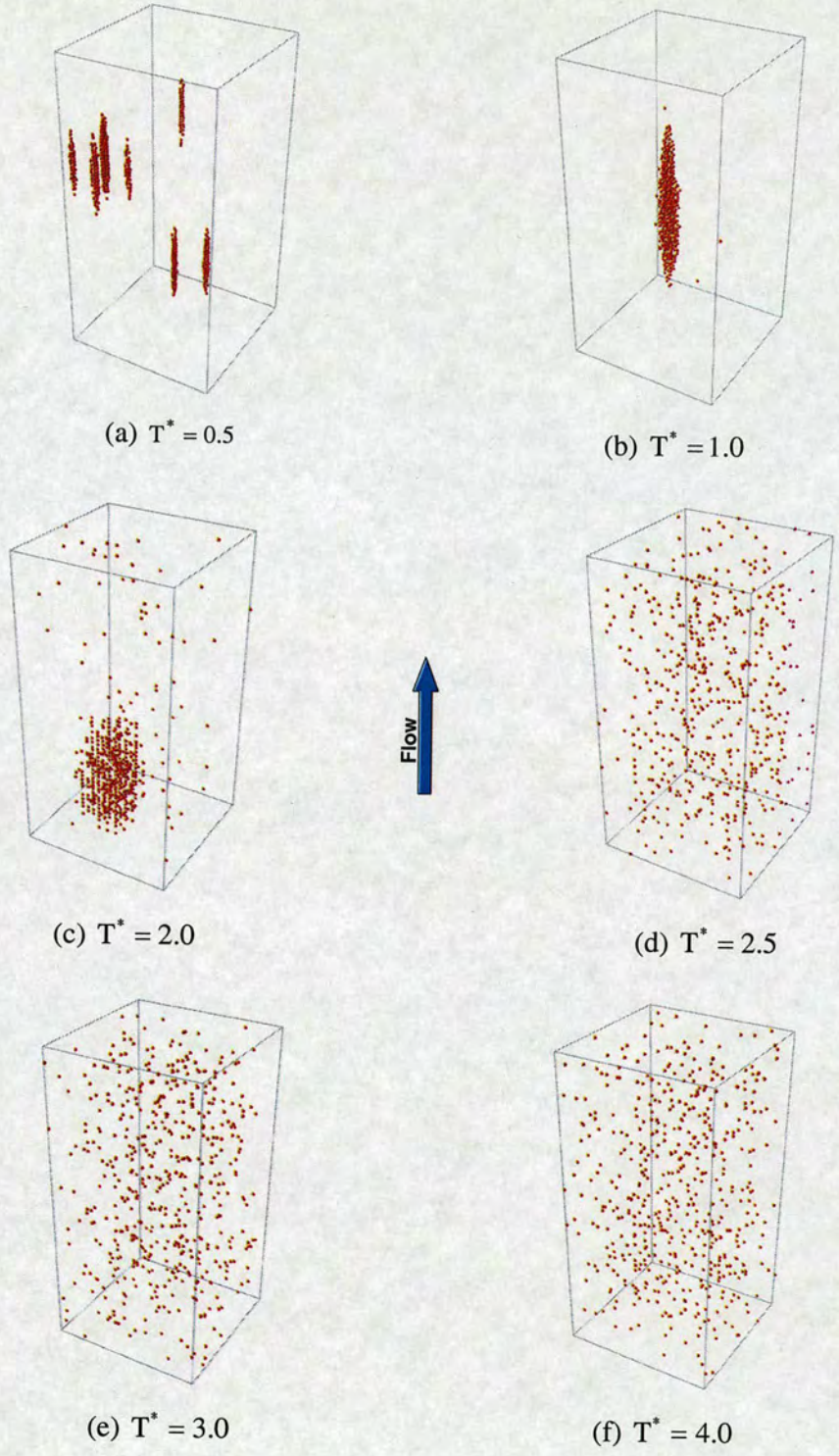

(a) $T^* = 0.5$

(b) $T^* = 1.0$

(c) $T^* = 2.0$

(d) $T^* = 2.5$

(e) $T^* = 3.0$

(f) $T^* = 4.0$

Fig. 5A.3 Particle snapshots at $\alpha_p = 0.001$ ($D_o = 8$) with $N_p = 512$.

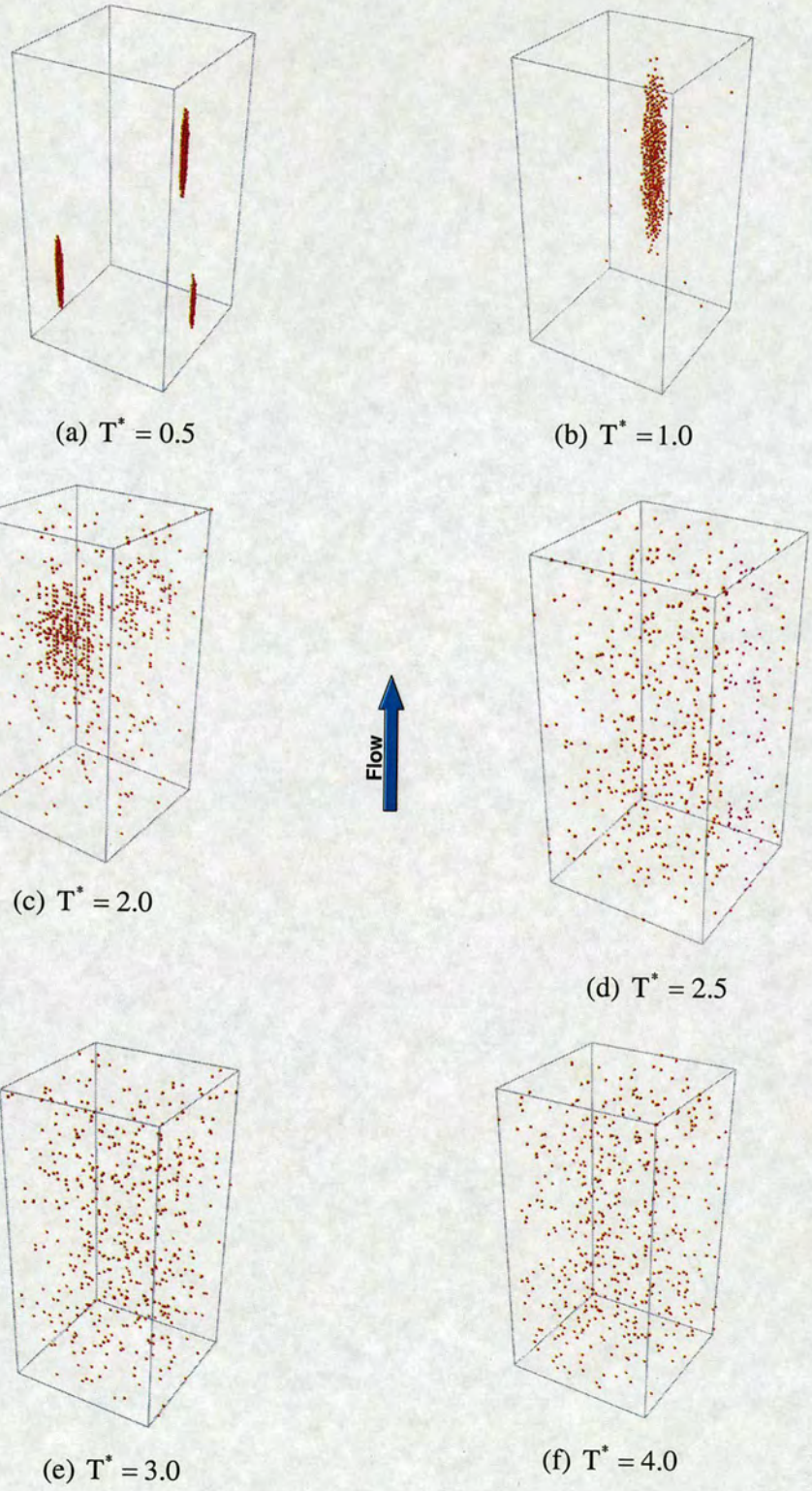

Fig. 5A.4 Particle snapshots at $\alpha_p = 0.0005$ ($D_o = 10$) with $N_p = 512$.

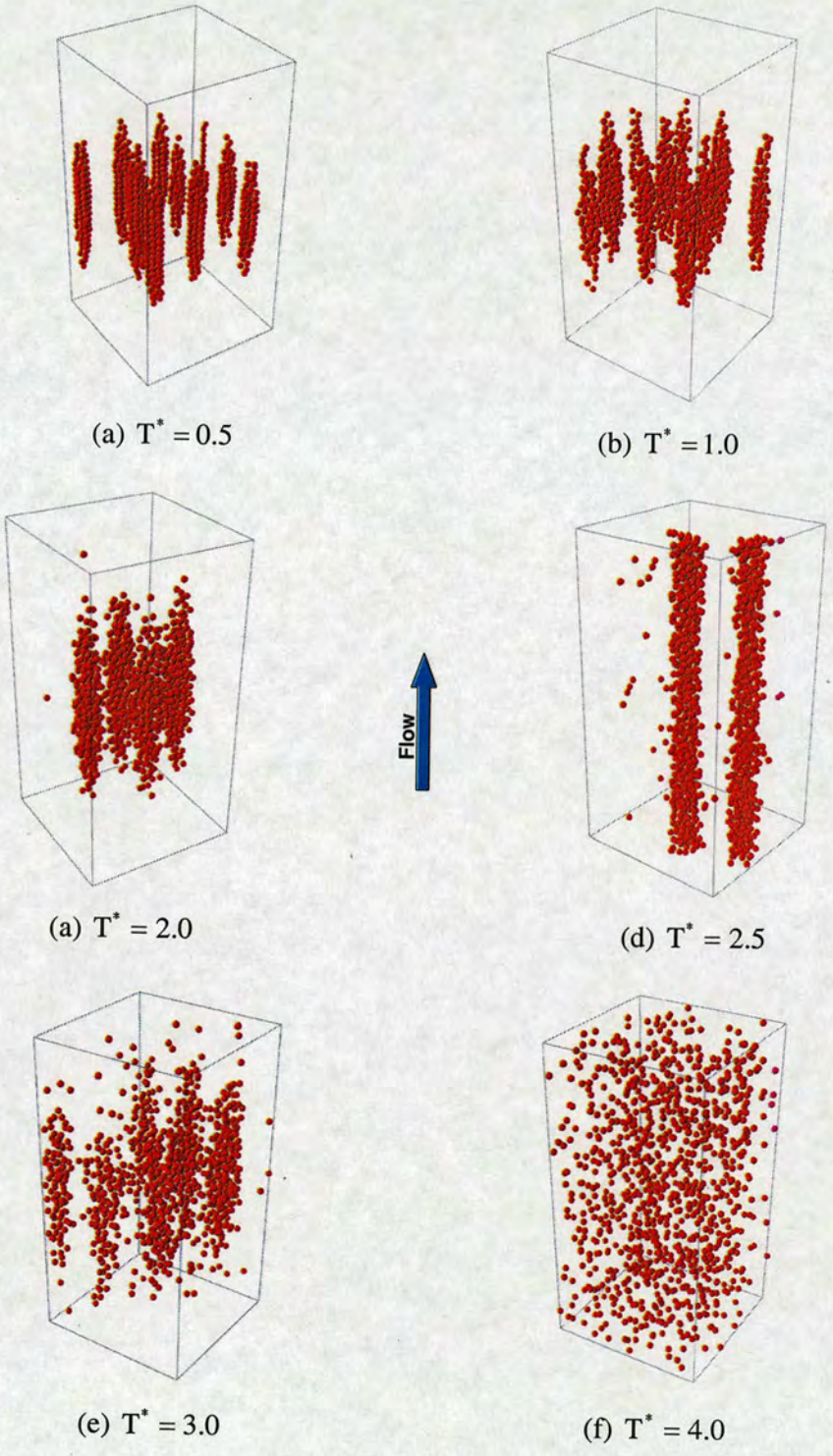

(a) $T^* = 0.5$ (b) $T^* = 1.0$

(a) $T^* = 2.0$ (d) $T^* = 2.5$

(e) $T^* = 3.0$ (f) $T^* = 4.0$

Fig. 5A.5 Particle snapshots at $\alpha_p = 0.02$ ($D_o = 3$) with $N_p = 1000$.

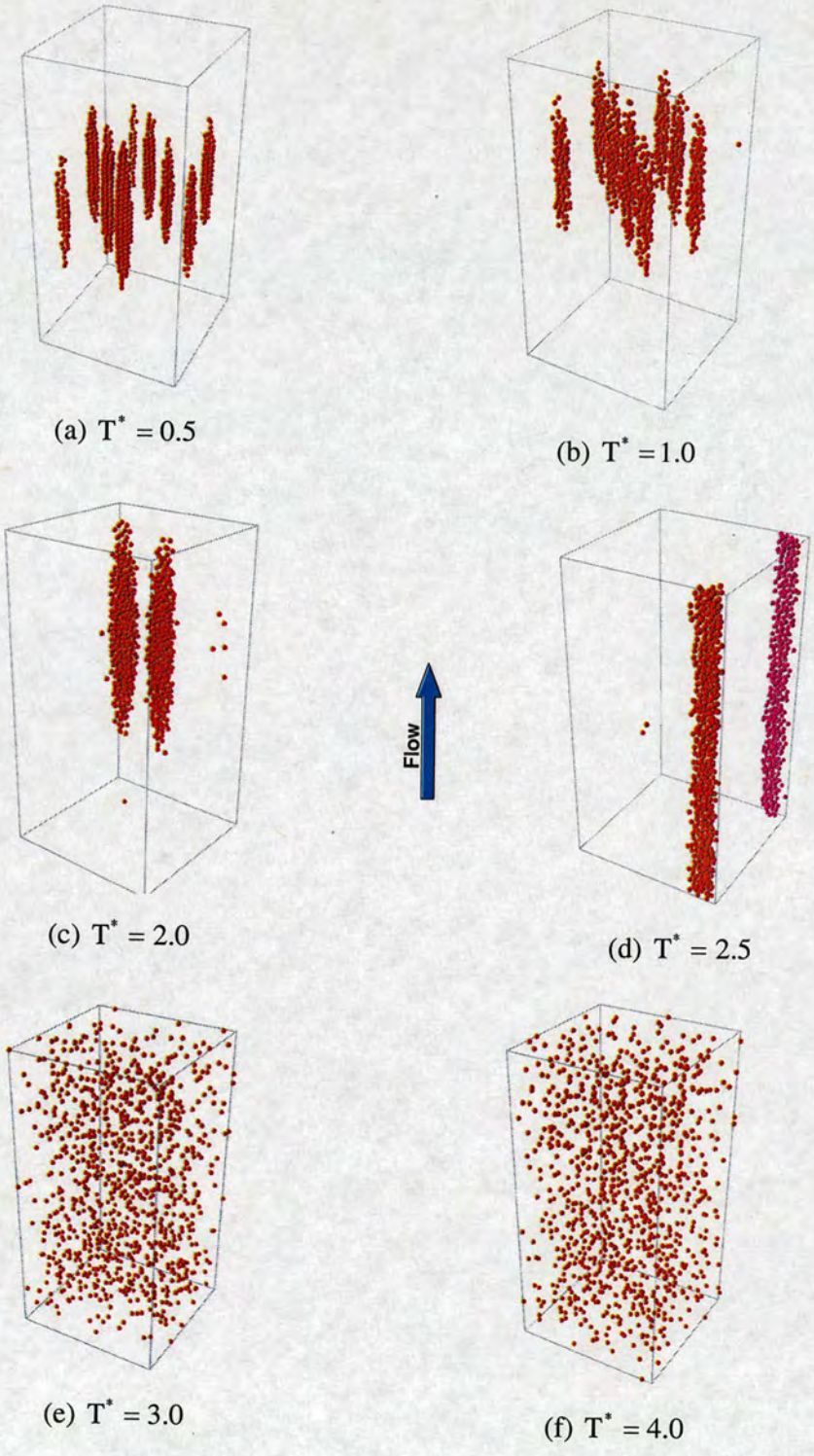

(a) $T^* = 0.5$

(b) $T^* = 1.0$

(c) $T^* = 2.0$

(d) $T^* = 2.5$

(e) $T^* = 3.0$

(f) $T^* = 4.0$

Fig. 5A.6 Particle snapshots at $\alpha_p = 0.008$ ($D_o = 4$) with $N_p = 1000$.

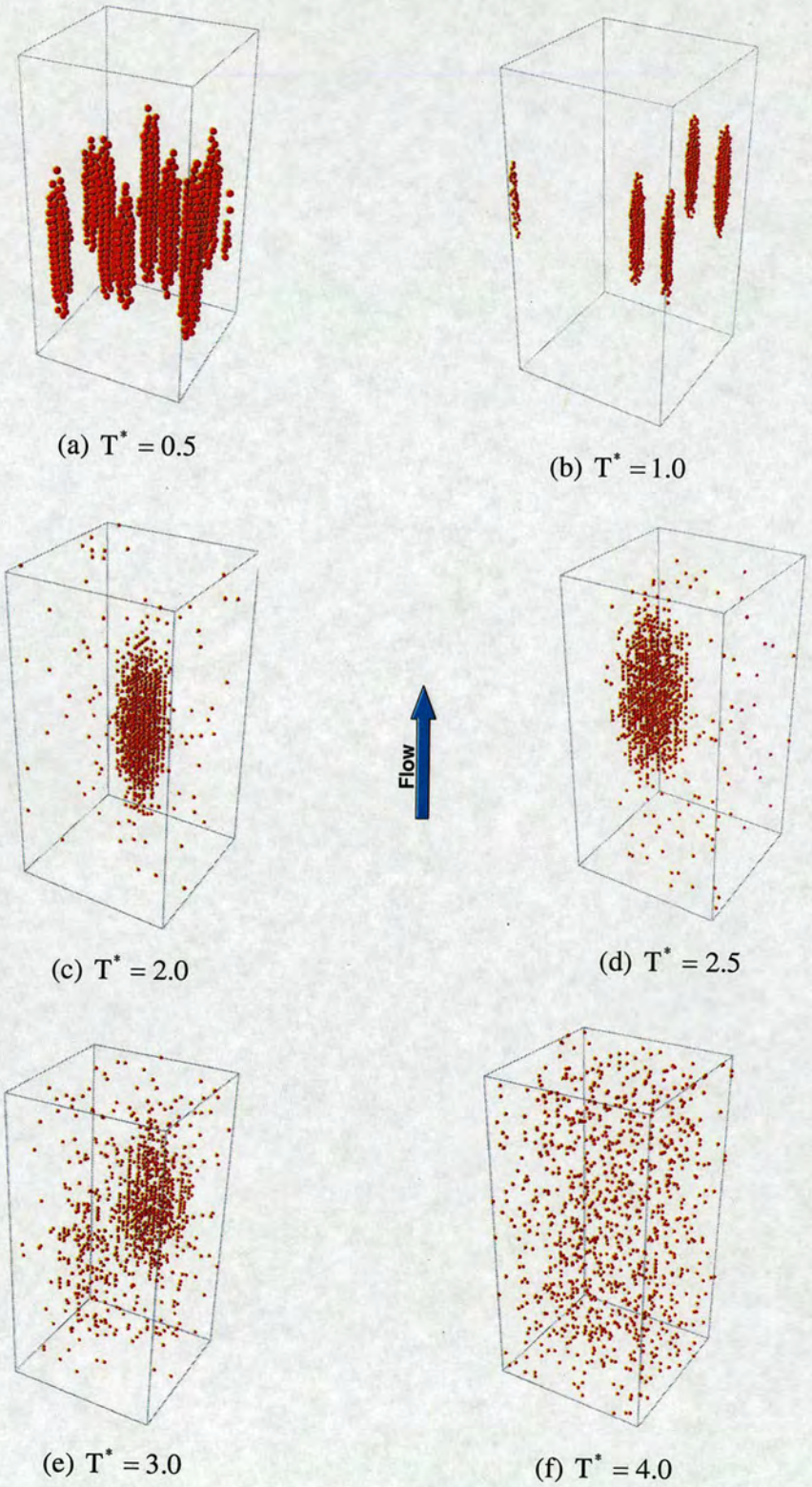

(a) $T^* = 0.5$

(b) $T^* = 1.0$

(c) $T^* = 2.0$

(d) $T^* = 2.5$

(e) $T^* = 3.0$

(f) $T^* = 4.0$

Fig. 5A.7 Particle snapshots at $\alpha_p = 0.002$ ($D_o = 6$) with $N_p = 1000$.

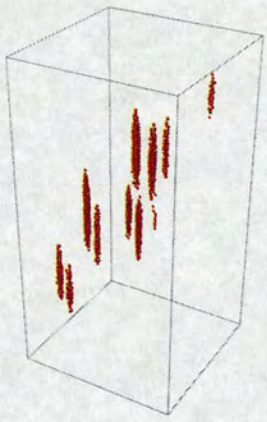

(a) $T^* = 0.5$

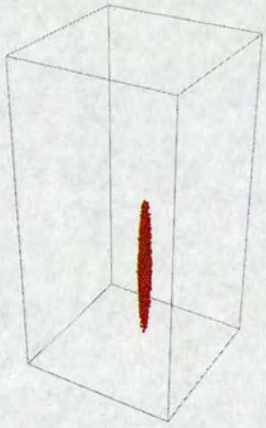

(b) $T^* = 1.0$

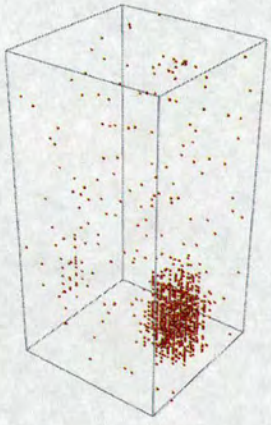

(a) $T^* = 2.0$

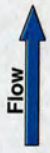

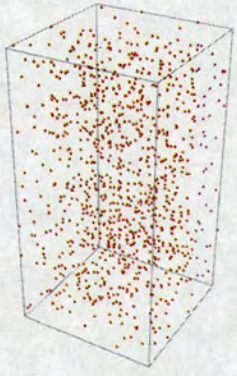

(b) $T^* = 2.5$

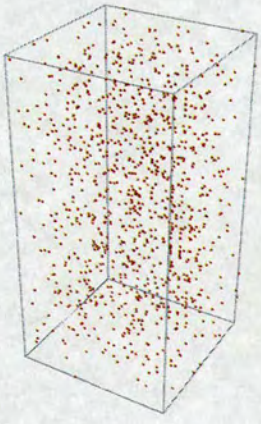

(e) $T^* = 3.0$

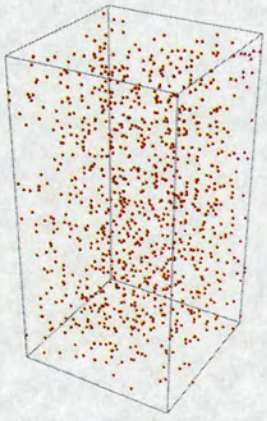

(f) $T^* = 4.0$

Fig. 5A.8 Particle snapshots at $\alpha_p = 0.001$ ($D_o = 8$) with $N_p = 1000$.